Late Quaternary Depositional History, Sedimentary Geochemistry, and Organic Carbon Burial at Mississippi Canyon 118: A Deep-sea Site on the Northern Gulf of Mexico Slope Containing a Gas-Hydrate and Cold-Seep Field

Wesley Clint Ingram

A dissertation submitted to the faculty of the University of North Carolina at Chapel Hill in partial fulfillment of the requirements for the degree of Doctor of Philosophy in the Department of Marine Sciences.

Chapel Hill

2013

Approved by

Dr. Stephen Meyers

Dr. Larry Benninger

Dr. Christopher Martens

Dr. Brent McKee

Dr. Donna Surge

ABSTRACT

WESLEY INGRAM: Late Quaternary Depositional History, Sedimentary Geochemistry, and Organic Carbon Burial at Mississippi Canyon 118: A Deep-sea Site on the Northern Gulf of Mexico Slope Containing a Gas-Hydrate and Cold-Seep Field
(Under the direction of Dr. Stephen Meyers)

This dissertation investigates late Quaternary sediments surrounding a gas-hydrate and cold-seep field situated on the northern Gulf of Mexico slope, to reconstruct depositional history, document sedimentary geochemistry, and evaluate organic carbon burial. The study locale encompasses the first Gas Hydrate Seafloor Observatory in the Gulf of Mexico, located within offshore federal lease block Mississippi Canyon 118 (MC118). Sediments recovered in 10 gravity cores surround the MC118 gas-hydrate and cold-seep field and yield a record spanning 20 Ka-present. Three related studies document the depositional history at MC118, through assessment of: (1) lithostratigraphy, biostratigraphy, chronostratigraphy, (2) sedimentary geochemistry and organic carbon burial, and (3) redox processes, with a focus on manganese cycling. A central objective is evaluation of the impact of global (deglacial sea level rise), regional (delta lobe switching), and local (gas hydrates, seeps, salt diapirism) influences on sedimentation surrounding the MC118 field.

A litho-bio-chronostratigraphic framework is developed using X-ray fluorescence (XRF) core scanning (Ca/Ti), biostratigraphy, and radiocarbon dating. Four stratigraphic units are identified; within each mapped stratigraphic unit, sedimentation rates generally increase with distance from the MC118 field and with age at each core site. This framework

is integrated with a chemical stratigraphy (inorganic and organic geochemical data) to assess terrigenous versus pelagic sediment burial fluxes, and to evaluate the controls on organic carbon burial. Results indicate that terrigenous sediment burial flux is the primary control on temporal changes in sedimentation rate, bulk sediment composition and organic carbon burial, linked to factors such as deglacial sea level rise and delta lobe switching. All geochemical burial fluxes generally increase with distance from the MC118 field, suggesting a stable spatial pattern of deposition throughout the late Quaternary. The final study evaluates authigenic manganese layers, which vary in frequency and concentration with distance from the field. The manganese record is interpreted as indicating intermittent periods of steady state and non-steady state conditions during formation within dysoxic sediments, providing a novel means to assess stability of sedimentation. The results from this dissertation research provide an important paleoenvironmental context for ongoing geochemical and geophysical monitoring at the MC118 field.

Acknowledgements

This dissertation was supported by multiple funding sources including (1) university and departmental funds to Stephen Meyers (UNC-Chapel Hill and UW-Madison), (2) the UNC-Chapel Hill Marine Science department, and (3) the Gulf of Mexico Gas Hydrate Research Consortium (HRC grants 300212198E (UM 07-01-071) and 300212260E (UM 08-11-047) to C.S. Martens). I thank the Duke/UNC Oceanographic Consortium for funding the first cruise (onboard R/V Hatteras) to the Mississippi Canyon research site (MC118), which was part of a joint proposal with Kai Ziervogel, Drew Steen and Carol Arnosti. A subsequent cruise onboard the R/V Pelican was provided by Minerals Management Services (now Bureau of Ocean Energy) and NOAA's National Institute for Undersea Science and Technology, with funding from the Gas Hydrate Research Consortium. Both of these cruises provided the equipment, time and support needed to obtain all the core material used in this dissertation research. I thank David Hollander (University of South Florida) for providing oxygen and carbon isotope analyses free of charge and Weatherford Geochemistry Lab (Houston, Texas) for providing Rock Pyrolysis data using their Source Rock Analyzer at a discounted rate. I would like to thank Chris Martens for providing full intellectual freedom to pursue my interest and finally, I would like to thank Steve Meyers for his enthusiasm, dedication, and for providing a great set of geochemical instruments, which we fully exploited in this research.

Table of Contents

List of Tables vii

List of Figures viii

Dissertation Introduction..... 1

References 11

Late Pleistocene-Holocene sedimentation surrounding an active seafloor gas-hydrate and cold-seep field on the Northern Gulf of Mexico Slope.....16

Abstract.....16

Introduction 18

Methods.....22

Results.....28

Discussion.....32

Conclusions 38

References 39

Chemostratigraphy of Deep-sea Quaternary Sediments along the Northern Gulf of Mexico Slope: Quantifying the Source and Burial of Sediments and Organic Carbon at Mississippi Canyon 118.....57

Abstract.....57

Introduction 59

Methods.....65

Results 70

Discussion 73

Conclusions 79

References 80

Authigenic Manganese deposits surrounding the Mississippi Canyon 118 Gas Hydrate and Cold Seep Field: Their documentation, interpretation and utility for evaluating redox state and stability of sedimentation 96

Abstract 96

Introduction 98

Methods 104

Results 109

Discussion 115

Conclusions 120

References 121

Dissertation Conclusion 135

Appendix A 142

Appendix B 156

Dissertation References 189

List of Tables

Cores collected at MC118 by the *R/V Hatteras* and *R/V Pelican* 45

AMS radiocarbon dating of planktonic foraminifera at MC118. 46

Average coefficient of variation and concentrations (HAT-03 and PEL-04) 86

ICP, XRF and CO_2 coulometry calibration data (HAT-03 and PEL-04).....87

Manganese calibration, concentration data and coefficient of variations 126

Manganese wet chemistry results and SGS reported concentrations 128

Depth and concentration of authigenic Mn-layers 127

Average concentrations for each stratigraphic unit 143

Density data (dry bulk) from Core PEL-15 146

Average burial flux values for each stratigraphic unit 147

ICP data from Hat-03 of calibrated elements 150

ICP data from PEL-04 of calibrated elements 151

Average coefficient of variation of XRF and Coulometry 153

Authigenic manganese concentration data 154

Estimated time to form Mn-layers 155

List of Figures

Bathymetric map of MC118 with regional inset and depth contours.....47

Bathymetric map of MC118 site with core locations 48

Stratigraphic correlation of all MC118 sediment cores.....49

Hatteras Cruise Ca/Ti profile and chronostratigraphic cross section.....50

Pelican Cruise Ca/Ti profile and chronostratigraphic cross section 51

Reworked nannofossils at MC118 correlated to Orca Basin. 52

Isopach and sedimentation map from ~14 kilo-years BP to present 53

Isopach and sedimentation map from ~2.3 kilo-years BP to present 54

Isopach and sedimentation map from ~9.5 to ~2.3 kilo-years BP.....55

Isopach and sedimentation map from ~14 to ~9.5 kilo-years BP.....56

Two-panel bathymetric map and core location map 88

Chronostratigraphic Correlation MC118 Cores 89

XRF profiles with ICP data (Cores HAT-03 and PEL-04).....90

Calibration XRF Ca/Ti counts to CO_2 Coulometry.....91

Hatteras Cruise cross section of $CaCO_3$ and TOC 92

Pelican Cruise cross section of $CaCO_3$ and TOC.....93

Burial Flux Plots MAR, Ti, R. Clay, TOC and $CaCO_3$ 94

Rock Pyrolysis results for Core HAT-03.....95

Conceptual model of manganese cycling 131

Hatteras Cruise cross section of manganese..... 132

Pelican Cruise cross section of manganese 133

XRF-manganese profile and wet chemistry (PEL-07) 134

Hatteras Cruise cross section of Al 157

Pelican Cruise cross section of Al 158

Hatteras Cruise cross section of Ti 159

Pelican Cruise cross section of Ti 160

Hatteras Cruise cross section of Si 161

Pelican Cruise cross section of Si 162

Hatteras Cruise cross section of Fe 163

Pelican Cruise cross section of Fe 164

Hatteras Cruise cross section of Ba 165

Pelican Cruise cross section of Ba 166

Hatteras Cruise cross section of S 167

Pelican Cruise cross section of S 168

Hatteras Cruise cross section of S and TOC 169

Pelican Cruise cross section of S and TOC 170

Ti burial flux for each stratigraphic unit 171

Ba burial flux for each stratigraphic unit 172

Al burial flux for each stratigraphic unit 173

Fe burial flux for each stratigraphic unit 174

Mn burial flux for each stratigraphic unit 175

$CaCO_3$ burial flux for each stratigraphic unit 176

TOC burial flux for each stratigraphic unit 177

Cross-plots of Barium to other inputs (1) 178

Cross-plots of Barium to other inputs (2) 179

Cross-plots of Barium to other inputs (3) 180

Cross-plots of Barium to other inputs (4) 181

Cross-plots of Manganese to other inputs (1) 182

Cross-plots of Manganese to other inputs (2) 183

Age-depth plot (HAT-03) 184

Stable carbon and oxygen isotope profile (HAT-03) 185

Composite Age-Depth from AMS carbon-14 dates 186

Correlation Ca/Ti and “reworked” nannofossils at MC118 187

Cross-plot of weight percent TOC and $CaCO_3$ data 188

Dissertation Introduction

1.1 Research Overview

This research comprised of multiple studies ultimately focuses on the (1) deposition of deep-sea sediments, (2) their solid-phase geochemical composition, and (3) redox processes as recorded by authigenic manganese deposits (Mn-layers). Each of these topics are organized into three separate chapters and are considered in the context of global, regional and local geologic factors such as sea-level rise, delta lobe switching, interactions with a nearby "active" cold-seep and gas-hydrate field and seafloor warping from salt diapirism as part of the field. By the description "active", it is implied that gas and fluids (brine fluids, natural gas and petroleum) expel from the seafloor at the site, which has been observed as oil sheen at the ocean surface (Sleeper and Lutken, 2008). This description is also supported by outcrops of gas hydrate, at the seabed, which can detach and release into the water column (Chris Martens, personal communication). The site is described in more detail herein (Chapter 1, Ingram et al., 2010). In summary, it is an area of the seafloor (~1 km^2) that contains a large gas-hydrate and cold-seep field, which is located ~200 km South of Gulfport Mississippi on the Gulf-of-Mexico slope in ~890 m water depth and within federal offshore lease block Mississippi Canyon 118 (MC118). A total of ten sediment cores were collected from the MC118 site while onboard two separate research cruises, during which 38.6-m of

sediments were recovered spanning the Late Pleistocene to recent (20 Ka to present) (Ingram et al., 2010). Results from these deep-sea sediment cores are included in three separate chapters that considered different and related research topics. A summary of the broader research goals and objectives are outlined below.

1.2 Summary of Research Goals

Several research themes are investigated separately and address inter-related research questions, some of which are considered very important to gas-hydrate and cold-seep research. This research includes objectives specific to MC118, which provides the context for the broader research questions (and MC118 consortium efforts). These objectives sequentially characterize MC118 (and geologic processes) and can be summarized as follows, (1) chronostratigraphy and depositional environment, (2) sedimentary geochemistry and (3) redox processes, all of which, reveal many interesting conclusions about sedimentation at this dynamic setting.

On a broader context, one key research effort involves understanding how gas hydrates, cold seeps and/or salt diapirs (all part of MC118 field) are connected to slope failure and/or erosion along continental slopes (Maslin et al., 2004; 1998, Minert et al., 2005, Paull et al., 1996; 2003). The inherent "stability" of the field as well as the seafloor at this location is a central theme. The term "stability" as it is used herein, specifically in reference to the MC118 field, refers to the nature, rate, and frequency of hydrocarbon expulsion from the gas hydrates and cold seeps, as well as disruption from salt tectonics. Stated as question, does release of gas (methane) and fluids from the MC118 field occur frequently with little disruption to the seafloor or rarely with sufficient energy causing

changes to the local environment or surrounding sediments? It has been implied that gas hydrates and cold seeps can modulate marine sedimentation, particularly along continental margins in a substantial and sometimes catastrophic way, generating submarine slides, slumps and debris flows (Paull et al., 1996; 2003). Hence this research attempts to address substantial and controversial scientific topics. Other research has also considered the impact of these expulsion processes on broader context, such as their role in the erosion of continental margins on geologic timescales (Haq, 1998). This still debated question can be summarized as follows: can gas hydrates and/or cold seep fields catastrophically destabilize the seafloor or influence deep-sea sedimentation in substantial way? This question is addressed in the first study (Chapter 1), specifically as it relates shallow sediments surrounding the MC118 seeps and gas hydrates.

The initial study (see Chapter 1) considers additional research goals relating to the site, where a large gas-hydrate and cold-seep field persists. More specifically, several objectives are considered in the context of the depositional environment at MC118 and are as follows: (1) to document the spatial and temporal variability of sedimentation surrounding the MC118 field during the late Pleistocene and Holocene, (2) to investigate spatial scales over which processes associated with gas hydrate formation and/or cold seeps influence sedimentation, seafloor erosion, mass wasting and/or seabed morphology (Paull et al., 1996, 2003; Mienert et al., 2005), and finally (3) to consider the sensitivity of sedimentation to other processes such as seafloor warping due to salt tectonics (Galloway et al., 2000; Winker and Booth, 2000; Diegel et al., 1995 Jackson, 1995), along with sea-level rise and Mississippi delta lobe switching from the latest Pleistocene and Holocene (Blum and Roberts, 2009).

In addition to a chronostratigraphy for MC118 (Chapter 1), continuous 1-cm scale X-ray Fluorescence (XRF) core scanning for a suite of elements was also performed on this deep-sea record comprising more than 38-m of sediment. This dataset was combined with the established chronostratigraphy from Ingram et al. (2010), to then determine mass accumulation rates (burial fluxes) for several geochemical proxies across MC118. With these burial fluxes (Chapter 2), additional research topics were investigated, (1) quantification of the components of sedimentation at MC118, (2) the relationship of the geochemical fluxes to global, regional and local factors (sea-level rise, Mississippi deltaic shifting, salt diapirism) and finally, (3) burial of organic carbon at MC118. With regards to the last topic, the accumulation of organic carbon at MC118 is considered in the context of terrigenous and pelagic (biogenic) inputs, which provides documentation of probable sources of the organic matter. This topic has particular importance in the field of sedimentary geochemistry as it relates to depositional factors that promote enhanced organic carbon burial in similar settings, which relate to formation of ancient organic-rich shale and mudstones (Hunt, 1972).

Finally, the last chapter deals with redox processes, inferred through a detailed record of sedimentary manganese. Given the Ingram et al., (2010) chronostratigraphy and detailed sedimentary geochemistry, it is apparent that the highly-concentrated manganese deposits (Mn-layers) are authigenic. Hence, one of the main goal of this final study is to establish the probable composition of these authigenic deposits, which are well-documented by cm-scale X-ray fluorescence (XRF) core scanning. Multiple working hypotheses are considered regarding the origin of the Mn-layers at MC118 in this final study (Chapter 3), and are as follows: (1) Mn-layers are reworked authigenic minerals

derived from the MC118 field, (2) Mn-layers are oxides/oxyhydroxides forming *in-situ* near the seafloor in association with normal marine sedimentation and a transient, redox boundary, (3) Mn-layers are Mn-rich carbonates (Ca-$Mn(CO_3)_2$), or rhodochrosite ($MnCO_3$) formed by Mn cycling where conditions are also saturated with respect to carbonate ($CaCO_3$) content, or finally (4) are Mn oxides, which are then converted to carbonates in the sediment column.

The location of the core sites around the MC118 field provides the opportunity to also consider how this redox-sensitive element may be responding to sedimentary processes associated with the field or the effects of salt diapirism. Hence, manganese may be a geochemical proxy sensitive to redox conditions and by extension stability of sedimentation and this concept is proposed as a hypothesis in Chapter 3. This idea has clear implications for interpreting the geologic record and past redox conditions at a dynamic seafloor setting such as MC118. The final study (Chapter 3) presents the following question: are authigenic manganese deposits linked to gas hydrates, cold seeps and/or salt diapirism by influencing conditions (steady state versus non-steady state conditions) of state and redox processes?

1.3 Central Research Topics

The following section provides a background of central and ongoing topics in gas hydrate and cold seep research. This section provides an outline of concepts considered important in the field. Key research themes are summarized, which account for a substantial proportion of the published literature. Some of these key topics include

investigations of gas-hydrate formation/dissociation and the cycling of (methane) carbon. Some have focused on localized scales at modern seep sites (Lapham et al., 2010; Castellini et al., 2006), and others have focused on global, deep-time events (Dickens et al., 1995; Katz et al., 1999; Kennett et al., 2000, 2003). Another topic of interest includes evaluation of gas hydrate occurrence and potential as a hydrocarbon energy source, including estimates of natural-gas contained within these hydrated deposits (Milkov, 2003; Collett, 1992; 2002). Additionally, many have also speculated on the connection of gas hydrates to past submarine slope failures, interactions with deep-marine slope sedimentation and margin erosion (Paull et al., 1996, 2003; Maslin et al., 1998, 2004; Haq, 1998; Mienert et al., 2005). This synopsis of gas hydrate research is discussed at times in the subsequent studies (chapters), and below in greater detail to provide context for the MC118 research.

The potential for gas hydrates to influence the global carbon cycle receives considerable attention for the primary reason that the estimated amount of methane contained with this hydrated reservoir is so immense (Milkov, 2003). It has been suggested that the sudden transfer of carbon from this reservoir to the oceans and atmosphere was a factor in both Recent (Quaternary) and in deep-time climatic events (Kennett et al., 2000; Dickens et al., 1995). Kennett et al. (2000) argued that the driver of rapid methane variability in the atmosphere during the Quaternary observed primarily in the Greenland ice-core record was due to destabilization of marine gas hydrates. However, others have argued that the increase in methane was derived from terrestrial sources such as expansion of tropical wetland environments during warmer periods (Lorius et al., 1990; Chappellaz et al., 1990; Raynaud et al., 1998; Servinghaus et

al., 1998). The idea that marine clathrates contribute to methane in the ice-core record is known as the “Clathrate Gun Hypothesis”, which states that abrupt warming following glacial periods and more-recent stadial terminations are a consequence of hydrate dissociation due to interactions between sea level change and ocean temperatures. This subsequently causes destabilization of the hydrated deposits and releases methane to the oceans and atmosphere (Kennett et al. 2000). More recently, this hypothesis has been questioned due to careful re-evaluation of methane-deuterium isotopes from Greenland ice cores (Sowers, 2006). In summary, the deuterium isotopic values from methane impart a distinct signal based on their source (wetlands are isotopically heavy relative to marine clathrates). Temperature proxies such as oxygen isotopes, measured methane concentrations and methane-deuterium values are correlative in the ice-core record across key Quaternary warming (inter-stadial) events. Coincident across these events a simple numerical model demonstrates that the isotopic signal of methane-deuterium is from the heavier isotope, and thus is not consistent with a marine clathrate origin (Sowers, 2006). Thus, gas hydrates as a source (and driver) of Quaternary Climate change has diminished.

Variations in the deep-time global carbon cycle and their connection to extreme climatic events have also received much attention in gas-hydrate research, the Paleocene-Eocene Thermal Maximum (PETM) event occurring at ~55 Ma (Dickens et al., 1995, 1997; Kaiho et al., 1996; Zachos et al., 2001; Katz et al., 1999; Norris and Röhl, 1999). This global carbon-isotopic excursion (-2 to -3‰ shift in organic carbon and marine carbonates) is thought to represent a massive transfer of isotopically-light methane from gas hydrates to the oceans and atmosphere (Dickens et al., 1995, 1997;

Kaiho et al., 1996). The isotopic excursion and associated climate event is coincident with what is considered to be the warmest interval during the entire Cenozoic Era (65 - 0 Ma). It is so substantial, that it is recognizable globally and has been chosen to mark the Paleocene-Eocene boundary in the geologic timescale (Zachos et al., 2001). Previous investigators have suggested that the transfer of terrestrial organic carbon to the oceanic reservoir is not sufficient to account for the magnitude of the PETM isotopic excursion (Dickens et al. 1995, 1997).

The topic of estimating the present size, extent and potential carbon resource contained with the hydrate reservoir has also been the focus of research. Extreme volumes of natural gas (over 10,000 trillion cubic feet of gas) are thought to exist as "frozen" hydrated deposits, mostly occurring within less than 1 km of the shallow geosphere beneath continental margins and permafrost regions, together comprising a massive proportion (approximately a third) of the total amount of organic carbon (Collett, 1992, 1995, 2002). Substantial amounts of free and dissolved natural gas also likely exist beneath the solid gas hydrate deposits which act to trap natural gas beneath the solid-phase interval (Dickens and Quinby-Hunt, 1994, 1997). Methane and other natural gases continually cycle between free gas and frozen hydrate where this boundary occurs (Castellini et al., 2006; Kvenvolden 1995, 1998). Gas hydrates are also widely distributed, outcropping along the seafloor in water depths exceeding 600 m in the lower latitudes and at shallower depths. With sufficiently cold temperatures hydrates may be stable under lower pressure conditions, terrestrial deposits occur beneath permafrost in Polar Regions (Kvenvolden 1995, 1998; Lerche and Bagirov, 1998). Natural gas reserves from hydrates have been detected and even completed for

gas-bearing zones along the North Slope of Alaska (Collett, 1993). More recently, appraisal wells have demonstrated successful production test from gas-hydrate reservoirs along the north slope of Alaska and Canadian Arctic (personal communication, Timothy Collett). Due to the extensive global distribution, gas hydrates likely greatly exceed conventional petroleum reserves based on carbon equivalence (Kvenvolden, 1998). Alternatively, when compared to other unconventional carbon resources, many currently under exploitation (shale oil, shale gas, tight oil and gas sands, heavy oil sands, and oil shales), gas hydrates are likely not substantially larger (personal communication, Larry Meckel). Given economic factors (find and development cost), gas hydrates are also generally not competitive with other unconventional fossil carbon resources, and may not be for quite some time, when/unless these other sources are depleted.

World-margin stability, as it relates to submarine gas hydrate deposits, has been an ongoing topic since the realization that exchange occurs between solid hydrates and free gases along specific boundaries beneath the continental margins. This situation increases the risk of slope failure (slumps and debris flows) by reducing sediment mechanical strength, and thus may have contributed to past margin failures (McIver, 1982; Jansen et al., 1987; Piper et al., 1997; Paull et al., 1996, 2003; Mienert et al., 2005; Haq et al., 1998; Maslin et al., 1998, 2004; Kennett et al., 2000, 2003). Many have speculated on the connection of gas hydrates to submarine slope failures and continental margin erosion on geologic time scales (Paull et al., 1996, 2003; Maslin et al., 1998, 2004; Haq, 1998; Mienert et al., 2005). Some have even speculated of the sequence of events leading to gas-hydrate induced slope failures (McIver, 1982).

Additionally, the presence of frozen hydrates in sediment pore spaces also inhibits compaction; hence where and when these hydrates dissociate into water and gas, weak fluidized layers can develop in the subsurface and further destabilize the mechanical strength of the slope (McIver, 1982). Although gas hydrates may contribute to the erosion of continental slopes in some way, other processes substantially impact continental margin erosion on geologic scales as well, they include (1) canyon incision, (2) rapid sedimentation and over-steepening, (3) current erosion or (4) mass wasting (from slumps/debris flows) initiated by a trigger such as seismic activity (Lang et al. 1987; Mountain et al., 1987, 1996). It is hypothesized that the frequency and magnitude of submarine slope failures contributing to margin erosion increased globally after polar ice sheets became permanent and when sea-level amplitude increased substantially (Haq, 1987). It is not quantitatively known how the expansion of the hydrate reservoir within the most recent ice-house climate transition (past ~35 million years) has contributed to major Cenozoic continental margin erosion if at all.

References

Blum, M.D. and Roberts, H.H., 2009. Drowning of the Mississippi Delta due to insufficient sediment supply and global sea-level rise. *Nature Geoscience*, v. 2, p. 488-491.

Castellini, D.G., Dickens, G.D., Snyder, G.T., Ruppel, C.D., 2006. Barium cycling in shallow sediments above active mud volcanoes in the Gulf of Mexico. *Chemical Geology,* v. 226, p. 1–30.

Chappellaz, J., Barnola, J.M.m Raynaud, D., Korotkevich, Y.S. and C. Lorius 1990. Ice-core record of atmospheric methane over the past 160,000 years. *Nature*, v. 345, p. 127-131.

Collett, T.S. 1992. Potential of gas hydrates outlined. *Oil and Gas Journal*, v. 9025, p. 84-87.

Collett, T.S. 1993. Natural Gas Hydrates of the Prudhoe Bay and Kuparuk River Area, North Slope, Alaska. *The AAPG Bulletin*, v. 77, no. 5, p. 795-812.

Collett, T.S. 1995. Gas hydrate resources of the United States, in Gautier, D.L., Dolton, G.L., Takahashi, K.I., and Varnes, K.L., (eds.) 1995 National assessment of United States oil and gas resources-results, methodology, and supporting data: U.S. Geological Survey Digital Data Series 30 (on CD-ROM).

Collett, T.S., 2002. Energy resource potential of natural gas hydrates. American Association of Petroleum Geologists, v. 86, no. 11, p. 1971-1992.

Dickens, G.R. and Quinby-Hunt, M.S. 1994. Methane hydrate stability in seawater. *Geophysical Research Letters*, v. 21, no. 19, p. 2115-2118.

Dickens, G.R., O'Neil, J.R., Rea, D.K. and Owen, R.M.(1995. Dissociation of oceanic methane hydrate as a cause of the carbon isotope excursion at the end of the Paleocene. *Paleoceanography*, v. 10, p. 965-971.

Dickens, G. and Quinby-Hunt, M.S 1997. Methane hydrate stability in pore water: a simple theoretical approach for geophysical applications. *Journal of Geophysical Research*, v. 102, p. 773-783.

Diegel, F.A., Karlo, J.F., Schuster, D.C., Shoup, R.C., Tauvers, P.R., 1995. Cenozoic structural evolution and tectono-stratigraphic framework of the northern Gulf Coast continental margin, in: Jackson, M.P.A., Roberts, D.G., Snelson, S., (eds.), Salt Tectonics: *A Global Perspective: American Association of Petroleum Geologist Memoir* v. 65, p. 109-151.

Galloway, W.E., Ganney-Curry, P.E., Li, X., Buffler, R.T., 2000. Cenozoic depositional history of the Gulf of Mexico Basin. *American Association of Petroleum Geologist Bulliten*, v. 84, no. 11, p. 1743-1774.

Haq, B.U., Hardenbol, J. and Vail P.R., 1987. Chronology of fluctuating sea levels since the Triassic (250 million years ago to present), *Science*, v. 235, p. 1156-1167.

Haq, B.U., 1998. Natural gas hydrates: searching for the long-term climatic and slope-stability records. *In*: Henriet, J.P and J. Mienert (eds.) *Gas Hydrates: Relevance to World Margin Stability and Climate Change*. Geological Society, London Special Publications, v. 137, p. 303-318.

Hunt, J. M., 1972. Distribution of carbon in crust of Earth, *AAPG Bulletin*, v. 56, p. 2273-2277.

Ingram, W.C., Meyers, S.R., Brunner, C.B., and Martens, C.S. 2010. Late Pleistocene-Holocene sedimentation surrounding an active seafloor gas-hydrate and cold-seep field on the Northern Gulf of Mexico Slope, *Marine Geology*, v. 278, p. 43-53.

Jackson, M.P.A., 1995. Retrospective Salt Tectonics, in: Jackson, M.P.A., Roberts, D.G., Snelson, S. (eds.), Salt Tectonics: A Global Perspective. *AAPG Memoir*, v. 65, p. 1-28.

Jansen, E., Befring, S., Bugge, T. et al. 1987. Large submarine slides on the Norwegian continental margin: sediments, transport and timing. *Marine Geology*, v. 78, p. 77-107.

Kaiho, K., Arinobu, T., Ishiwatari, R., Morgans, H.E.G., Okada, H., Takeda, N., Tazaki, K., Zhou, G., Kajiwara, Y., Matsumoto, R., Hirai, A., Niitsuma, N. and H. wada (1996), Latest Paleocene benthic foraminiferal extinction and environmental changes at Tawanui, New Zealand: *Paleoceanography*, v. 11, p. 447-465.

Katz, M.E., Pak, D.K., Dickens, G.R. and K.G. Miller 1999. The source and fate of massive carbon input during the latest Paleocene Thermal Maximum, *Science*, v. 286, p. 1531-1533.

Kennett, J.P., Cannariato, K.G., Hendy, I.L. and Behl, R.J. 2000. Carbon Isotopic Evidence for Methane Hydrate Instability During Quaternary Interstadials. *Science*, v. 288, p. 128-133.

Kennett J.P., K.G. Cannariato, I.L. Hendy and Behl, R.J. 2003. Methane hydrates in Quaternaryclimate change, The Clathrate Gun Hypothesis. *American Geophysical Union*, Washington DC, 216 pp.

Kvenvolden, K.A. 1995. A review of the geochemistry of methane in natural gas hydrate. Organic Geochemistry, v. 23, no. 12, p. 997-1008.

Kvenvolden, K.A. 1998. A primer on the geological occurrence of gas hydrate. *In*: Henriet, J.P and J. Mienert (eds.) *Gas Hydrates: Relevance to World Margin Stability and Climate Change*. Geological Society, London Special Publications, v. 137, p. 9-30.

Lang, T. H. and Wise, S.W. 1987. Neogene and Paleocene-Maestrichtian calcareous nannofossil stratigraphy, Deep Sea Drilling Project Sites 604 and 605, upper continental rise off New Jersey: Sedimentation rates, hiatuses, and correlation with seismic stratigraphy. *Initial Reports of the Deep Sea Drilling Project*, v. 93, p. 661-683.

Lapham, L.L., Chanton, J.P., Chapman, R. and Martens, C.S. 2010. Methane under-saturated fluids in deep-sea sediments: Implications for gas hydrate stability and rates of dissolution. Earth and Planetary Science Letters, v. 298, (3-4), p. 275-285.

Lerche, I., Bagirov, E., 1998. Guide to gas hydrate stability in various geological settings. Marine and Petroleum Geology 15 (5), 427–437.

Lorius, C., Jousel, J., Raynaud, D., Hansen, J. and H. Le Treut 1990. The ice-core record: climate sensitivity and future greenhouse warming. *Nature*, v. 347, p. 139-145.

Sleeper, K.A. Lutken, C., 2008. Activities Report for Cruise GOM1-08-MC118 aboard the R/V Pelican Sampling and Deployment Cruise Mississippi Canyon Federal Lease Block 118 Northern Gulf of Mexico April 22-28, 2008. Supported by, Center for Marine Resources and Environmental Technology and Seabed Technology Research Center University of Mississippi.

Maslin, M., Mikkelsen, N., Vilela, C. and Haq, B. 1998. Sea-level and gas-hydrate-controlled catastrophic sediment failures of the Amazon Fan. *Geology*, v. 26 no. 12, p. 1107-1110.

Maslin, M., Owen, M., Day, S. and Long, D. 2004. Linking continental-slope failures and climate change: Testing the clathrate gun hypothesis. *Geology*, v. 32, p. 53-56.

McIver, R.D. 1982. Role of naturally occuring gas hydrates in sediment transport. *AAPG Bulletin*, v. 66, p. 789-792.

Milkov, A.V., 2003. Global estimates of hydrate-bound gas in marine sediments: how much is really out there? *Earth-Science Reviews*, v. 66, p. 183-197.

Minert, J., Vanneste, M., Bünz, S., Andreassen, K., Haflidason, H., and Sejrup, H.P 2005. Ocean warming and gas hydrate stability on the mid-Norwegian margin at the Storegga Slide. *Marine and Petroleum Geology*, v. 22, p. 233-244.

Mountain, G.S., Damuth, C.M.G., McHugh, Lorenzo, J.M. and Fulthrope, C.S. 1996. Origin, reburial, and significance of a middle Miocene canyon, New Jersey continental slope. *Proceedings of the Ocean Drilling Program, Scientific Results*, v. 150, no. 15, p. 283-292. Ocean Drilling Program, Texas A&M University, College Station TX, USA

Mountain, G.S. 1987. Cenozoic Margin Construction and Destruction Offshore New Jersey. *Cushman foundation for Foraminiferal Research, Special Publication*, v. 24, 57-83.

Norris, R.D. and Röhl, U. 1999. Carbon Cycling and chronology of climate warming during the Paleocene-Eocene transition, *Nature*, v. 401, p. 775-778.

Paull, C.K., Brewer, P.G., Ussler III, W., Peltzer, E.T., Rehder, G., and Clague, D. 2003. An experiment demonstrating that marine slumping is a mechanism to transfer methane from gas-hydrate deposits into the upper ocean and atmosphere. *Geomarine letters*, v. 22, p. 198-203.

Paull, C.K., Buelow, W.J., Ussler III, W., Borowski, W.S. 1996. Increased continental-margin slumping frequency during sea-level lowstands above gas hydrate-bearing sediments. *Geology*, v. 24, no. 2, p. 143-146.

Piper, D.J.W., C. Pirmez, P. L. Manley, D. Long, R.D. Flood, W.R. Normark, and Showers W. 1997. Mass-Transport of the Amazon Fan: Proceedings of the Ocean Drilling Program, Scientific Results, v. 155, p. 109-146. Ocean Drilling Program, Texas A&M University, College Station TX 77845-9547, USA

Raynaud, D., J. Chappellaz, J. M. Barnola, Y. S. Korotkevich, and C. Lorius 1988. Climatic and CH4 cycle implications of glacial-interglacial CH4 change in the Vostok core, *Nature*, v. 333, p. 655–657.

Severinghaus, J.P., Sowers, T., Brook, E.J., Alley, R.B. and Bender, M.L. 1998. Timing of abrupt climate change at the end of the Younger Dryas interval from thermally fractionated gases in polar ice. *Nature*, v. 391, p. 141-146.

Sowers, T., 2006. Late Quaternary Atmospheric CH_4 Isotope Records Suggests Marine Clathrates Are Stable. *Science*, v. 311, p. 838-840.

Winker, C.D. and Booth, J.R. 2000. Sedimentary dynamics of the salt-dominated continental slope, Gulf of Mexico: integration of observations from the seafloor, near surface and deep subsurface. GCS SEPM Foundation 20th Annual Research Conference Deep-Water Reservoirs of the World, Dec. 3-6, pp. 1059-1086.

Zachos, J.C., Pagani, M., Sloan, L., Thomas, E. and Billups, K. 2001. Trends, Rhythms and Aberrations of in Global Climate 65 Ma to Present. *Science*, v. 292, p. 686-693.

Chapter 1

Late Pleistocene-Holocene sedimentation surrounding an active seafloor gas-hydrate and cold-seep field on the Northern Gulf of Mexico Slope

Abstract

A chronostratigraphic framework is constructed from sediments surrounding an active gas-hydrate and cold-seep field, situated on the northern Gulf of Mexico slope within federal offshore lease block Mississippi Canyon 118 (MC118). Accelerator mass spectrometer (AMS) radiocarbon dating, foraminiferal biostratigraphy and nannofossil biostratigraphy are used to constrain the age of sediments from 10 gravity cores collected around the field. X-ray fluorescence (XRF) core scanning is employed to develop continuous down-core elemental profiles, which are used to evaluate biogenic calcium and siliciclastic titanium sediment inputs, and provide a means to correlate sediments across the study area and infer changes in sedimentation through time. Spatial reconstruction of sedimentation surrounding the field indicates the following: (1) a consistent pattern of stratigraphic thinning in close proximity to the field over the past 14,000 yrs and (2), temporal changes in sedimentation that primarily reflect deglacial sea-level rise as well as regional factors such as Mississippi delta lobe switching. These results highlight the variability of sedimentation along a continental slope setting where

marine cold seeps and gas hydrate persist, yet do not suggest slope failure or destabilization of the seafloor at this site, at least during the past 14,000 yrs. The evaluation of sedimentation at this location provides an important context for ongoing biogeochemical and geophysical monitoring of the MC118 site, which has been designated the first National Gas Hydrate Seafloor Observatory by the Gulf of Mexico Hydrate Research Consortium.

Introduction

Marine gas hydrate formation represents an important process that can influence sedimentation in continental slope settings, and potentially contributes to continental margin slope failures on geologic time scales (Paull et al., 1996, 2003; Maslin et al., 1998, 2004; Haq, 1998; Mienert et al., 2005). The rapid dissociation of gas hydrates has also received much attention as a driver of past climate change, due to the potency of methane as a greenhouse gas, and the potential for destabilization of large hydrate deposits (e.g., Dickens et al., 1997; Katz et al., 1999; Kennett et al., 2000, 2003). In addition, gas hydrate deposits and natural-gas/petroleum seepage at the seafloor are a shallow depth hazard for deep-water petroleum exploration (Solheim et al., 2005). As a consequence, all offshore blocks leased to the petroleum industry must undergo an extensive shallow hazard assessment and site survey of the seafloor prior to any operations, to mitigate the risk of unintended hydrate degassing or disturbances to the seafloor biological communities often present at these sites.

This study investigates sediments surrounding a gas-hydrate cold-seep field within the Mississippi Canyon offshore federal lease block 118 (MC118) (Fig. 1) and is a component of a larger multi-disciplinary consortium effort to study the MC118 field (e.g., Sassen et al., 2006; Lutken et al., 2006; Sleeper et al., 2006; Sleeper and Lutken, 2008; Brunner 2007a; Lapham et al., 2008, in press). The MC118 site has been designated as the first National Gas Hydrate Seafloor Observatory by the Gulf of Mexico Hydrate Research Consortium jointly funded by NOAA, DOE and MMS (McGee, 2006).

Several inter-related objectives specific to the MC118 field are addressed by this study and include the following: (1) to document the spatial and temporal variability of sedimentation surrounding the MC118 field during the late Pleistocene and Holocene, (2) to investigate the spatial scale over which processes associated with gas hydrates and cold seepage influence sedimentation, seafloor erosion, mass wasting and seabed morphology (e.g., Maslin et al., 1998, 2004; Paull et al., 1996, 2003; Mienert et al., 2005), and (3) to evaluate the sensitivity of sedimentation at the site to processes such as seafloor warping due to salt tectonics (e.g., Galloway et al., 2000; Winker and Booth, 2000; Diegel et al., 1995 Jackson, 1995), changes in sea level, Mississippi delta lobe switching, and other regional/global processes that have potentially influenced sediment accumulation and redistribution during the latest Pleistocene and Holocene.

Ten sediment gravity cores, collected during two separate cruises, have been collected around the gas-hydrate/cold-seep field to investigate sediments within the MC118 block and possible sedimentation disturbances in proximity to the field (Fig. 2). Biostratigraphic, sedimentologic and X-ray fluorescence core scanning analyses are used to define unique sedimentary packages, and chronologic control is achieved using biostratigraphy and AMS 14C dating. Correlative horizons are utilized to construct sedimentation and isopach maps at various time intervals for the past 14,000 yrs. The comparison of sediment thicknesses and sedimentation rates surrounding the MC118 field (upslope and downslope) provides a means to infer processes that influence sedimentation at the seafloor in this location, and aids in the interpretation of the Late Pleistocene and Holocene depositional history at the MC118 site.

1.1 Geological Setting: MC118

The bathymetry of the Gulf of Mexico continental slope is heavily influenced by the extensive Louann (Jurassic in age) subsurface salt formation (e.g., Diegel et al., 1995; Jackson, 1995; Galloway et al., 2000). Deformation of the salt through time has contributed to the present-day hummocky bathymetry of the northern Gulf of Mexico slope. On a local scale, movement of subsurface salt deposits may generate shallow faults that extend up to the seafloor, thereby providing migration pathways for hydrocarbons sourced by leaky oil and gas reservoirs at depth. As a consequence, there are numerous deep-water petroleum seeps, gas vents, methane cold seeps and thermogenic gas-hydrate fields within the Gulf of Mexico (Sassen et al., 2001). Hydrocarbons are rapidly cycled and oxidized in shallow sediments at these sites (Castellini et al., 2006). In particular, gas hydrates of a thermogenic origin form where upward-migrating hydrocarbon-rich fluids and gasses encounter cool bottom water temperatures (Milkov and Sassen, 2002).

A gas-hydrate/cold-seep field centered at 28.8523°N and 88.4920°W lies in approximately 890 m water depth within the MC118 offshore block (Figs. 1 and 2). Visible outcroppings of gas hydrates, faulted carbonate “hard-grounds” and pockmark features consistent with gas and petroleum seepage (e.g., Figs. 1 and 2) cover approximately 1 km^2 of the seafloor (e.g., Sassen et al., 2006; Sleeper et al., 2006). The seaward slope across the study area typically ranges from 3° to 4°, but slopes of 10° to 12° are present locally across pockmark features (Sleeper et al., 2006). The field is underlain by a salt diapir 200 to 300 m below the seafloor, which contributes to subsurface fluid migration, seafloor warping and irregular bathymetry at the site (Sassen

et al., 2006). The supply of hydrocarbons (natural gas and petroleum) to the seafloor supports an active biological seep community (e.g., Sassen et al., 2006) and microbial chemolithotrophy in the immediate vicinity of active gas-fluid seepage.

Methods

2.1 Core Collection

Gravity coring was conducted from the surface ships R/V Hatteras in August 2007 and R/V Pelican in April 2008. Five sediment gravity cores were recovered during the R/V Hatteras, in a depositional dip orientation, oriented along 88°29'30" W (Fig. 2; Table 1). Coring operations onboard the cruise encountered "hard-grounds" at one location (failed core site) adjacent to the field resulting in recovery of only a few carbonate nodules. Five additional cores were recovered along the Pelican transect in a NW to SE orientation across the field (Fig. 2; Table 1). Small amounts of gas-hydrate cement were recovered during coring onboard the Pelican along the flanks of the field (Sleeper and Lutken, 2008; Fig. 1).

2.2 Core Processing

After transport of the sediment cores to a land-based laboratory at the University of North Carolina, Chapel Hill, cores were split and prepared for sedimentological, biostratigraphic and geochemical analyses. One half of the split core was prepared for X-ray fluorescence scanning by applying a thin (4 µm) Ultralene film across the top of the sediment surface. The remaining material was described visually (Fig. 3) and then used for destructive sampling. All core material was placed in sealed plastic core sleeves and D-tubes, and stored in the core laboratory refrigerator at ~3 °C.

2.3 X-ray fluorescence core scanning

X-ray fluorescence (XRF) core scanning was used to evaluate down-core changes in the bulk geochemical composition of MC118 sediments, specifically focusing on calcium and titanium (Figs. 4 and 5) as measures of biogenic and terrigenous clastic sediment inputs, respectively. Split cores were analyzed using an Avaatech XRF core scanner with an Oxford 50W X-ray source (rhodium target), and a Canberra X-PIPS detector with a 1500-micrometer silicon crystal. Continuous down-core X-ray fluorescence core scanning was conducted at a 1-cm resolution.

Calcium was measured using a 5 kV source voltage, 900 mA, without a filter, using a 90 s measurement time. Titanium was measured using a 10 kV source voltage, 1000 mA, with a cellulose filter, using a 90 s measurement time. To measure error and reproducibility, duplicate scans were performed at a 10-cm resolution using the same scanning parameters yielding highly reproducible results, with an average error < 5%.

2.4 Foraminiferal biostratigraphy

A detailed planktonic foraminiferal biostratigraphy was performed on Core HAT-03 (Figs. 3 and 6). A total of 29 samples each at ~40 cm^3 were taken at 10-cm or less depth intervals and prepared for microscopic examination of the sand-size fraction. Sediment samples were dried at 50 °C for 48 h, soaked in a 1% Calgon solution to disaggregate clay-rich sediment, and washed on a screen with 63-µm openings until only the sand-sized fraction remained. The sand-size residue was examined for foraminifera

under a (90×) Olympus SZX12 dissecting microscope. The Gulf of Mexico biostratigraphy of Kennett and Huddlestun (1972) was applied as modified by Kennett et al (1985).

Several key biostratigraphic boundaries, Y/Z~10 ka and Y1/Y2~15 ka calendar kilo-yrs BP, respectively (Flower and Kennett, 1990), were identified and used for age control in this core. Biostratigraphic boundaries used in this study are based partly on the disappearance of *Globorotalia inflata* and the reappearance of the *G. menardii* plexus, which correspond to sea-level and temperature changes in the Gulf of Mexico during deglaciation and the subsequent interglacial period (Flower and Kennett, 1990). The Y1/Y2 (~15 ka) boundary is defined by the disappearance of *G. inflate* and corresponds to the transition from the last glacial to the deglacial. The Y/Z (~10 ka) boundary is defined by the First Occurrence (FO) of *G. menardii*, a warm water species, absent until 9.8 ka corresponding to the early Holocene.

2.5 Nannofossil biostratigraphy

An unconventional nannofossil biostratigraphy was performed on the cores at MC118 in an effort to tie into a previously documented chronology from the Orca Basin in the Gulf of Mexico (Fig. 6). The Orca Basin is an anoxic salt mini-basin that is ~290 km southwest of the Mississippi Delta at 2300 m water depth. The depression is a natural sediment catch with high sedimentation rates and no bioturbation, yielding a detailed sedimentary record, and providing isotopic and biostratigraphic evidence for deglacial flooding events into the Gulf of Mexico during the Late Pleistocene and Holocene transition (e.g., Marchitto and Wei, 1995; Kennett et al., 1985; Broecker et al., 1988, 1989; Flower and Kennett, 1990). Marchitto and Wei (1995) discovered an increase in

the abundance of reworked (pre-Quaternary) nannofossils at the Orca Basin during meltwater pulse 1a (between 14 and 15 Ka), which they attributed to scouring of epicontinental sediments by glacial meltwater outflow down the Mississippi River drainage basin and into the Gulf of Mexico. A similar biostratigraphic "event" of highly reworked nannofossils was also observed in cores from the MC118 study area (Fig. 6).

Analysis of the percentage of reworked nannofossils in MC118 sediments followed the procedure of Marchitto and Wei (1995). Samples were taken at variable stratigraphic resolution to focus on intervals that tie into the Orca Basin record, yet were always less than 10-cm spacing. Sample smear slides were prepared from the unlithified marine sediments, and cover slips were mounted to slides using Norland-81 optical adhesive. Slides were viewed at 1250× on a Zeiss Axioscope under cross-polarized light. A total of at least 750 nannofossils were identified and counted in each sample. The percent reworked was obtained by counting the number of Pre-Quaternary nannofossils relative to the total number in a sample of at least 750; this ratio multiplied by 100 yielded the percent reworked, plotted on a log scale (Figs. 4, 5 and 6). The vast majority of the reworked (Pre-Quaternary) nannofossils are Cretaceous in age.

2.6 Radiocarbon dating

Planktonic foraminifera were picked for AMS radiocarbon dating to provide chronologic constraints for the recovered sediments. A total of 20 AMS radiocarbon dates were obtained from six different cores at various stratigraphic horizons with a focus on constraining the age of key correlative horizons, e.g., the $CaCO_3$-rich and

reworked nannofossil interval (see Results section; Figs. 3–5). Approximately 5 mg of foraminiferal tests, mostly the white variety of Globigerinoides ruber, were handpicked from sieved sediment samples (see Foraminiferal biostratigraphy section). Microfossil tests were then sonicated in deionized water prior to processing for radiocarbon analysis.

Radiocarbon dating was performed by the National Ocean Science Accelerator Mass Spectrometry Facility (NOSAMS) at Woods Hole Oceanographic Institute. δ13C values were determined to correct for fractionation effects. NOSAMS reports ages according to the convention outlined by Stuiver and Polach (1977) and Stuiver (1980). Radiocarbon ages are calculated using a 5568-year half-life of radiocarbon and are reported by NOSAMS without reservoir corrections or calibration to calendar years. The provided radiocarbon ages were converted to calendar years before present (BP) using a recently updated calibration curve spanning 0 to 50,000 yrs from Fairbanks et al. (2005). A 400-year reservoir correction was applied to each radiocarbon age prior to conversion to calendar years, as utilized in previous investigations also using planktonic foraminifera of similar age in the Gulf of Mexico (e.g., Richey et al., 2007).

2.7 Isopach mapping

A total of four isopach maps are generated based on the thickness between key chronostratigraphic horizons that define unique sedimentary packages at MC118. Isopach thickness was mapped for each interval using the Surfer mapping program and contours are based on an inverse square to distance algorithm. Thickness maps are converted to sedimentation rate maps for each isopach interval using age control

provided by biostratigraphy and radiocarbon dating (Sections 3.4–3.6); assume continuous sedimentation between the chronostratigraphic horizons.

Results

Analyses of the MC118 sediment cores (Table 1; Figs. 3–5) identify three distinct stratigraphic intervals that are continuous across the entire study area. These stratigraphic units are similar in overall character to those previously documented within the study area (Lutken et al., 2006; Brunner, 2007a), and in a piston core ~90 km to the west of the field recovered from the western flank of the Mississippi Canyon bathymetric feature (Brunner, 2007b). The thickness of several stratigraphic units discussed below is also represented by isopach reconstructions (Figs. 7–10).

3.1 Stratigraphic Unit I

This stratigraphic interval is the shallowest unit observed in all of the collected cores. The unit is primarily uniform calcareous nannofossil silty clay, with abundant foraminiferal microfossils and exhibits a high Ca/Ti ratio (Figs. 3–5). Both XRF core scanning (e.g., Figs. 4 and 5) and visual appearance (e.g., Fig. 3) indicate that this is the most $CaCO_3$-rich interval sampled. The color is light olive gray, visually lighter than sediments at greater depth. Sediments of Unit I appear homogenous and contain little sedimentary structures.

Stratigraphic Unit I is particularly well identified by the XRF Ca/Ti core scanning data, and is Holocene (~9500 calendar yrs BP to present) in age based on AMS radiocarbon dating (Figs. 3–5; Table 2). Foraminiferal biostratigraphic data further constrains the age of this stratigraphic unit. Core Hat-03 contains the Y/Z Subzone

boundary, positioned at 60–70 cm sub-bottom depth, approximately 20 cm below the onset of the Ca/Ti peak. This places sediments above this position within the Holocene, dated to ~10 kilo-yrs BP using biostratigraphy (e.g., Flower and Kennett, 1990; Poore et al., 2003).

Unit I is defined to encompass the entire interval from the base of Ca/Ti peak to the core tops (HAT-03), and is informally divided into two subunits: an upper interval that is laterally discontinuous (Unit IA), and a lower laterally continuous interval represented by a broad Ca/Ti peak (Unit IB). Unit IA is calcareous ooze that is late Holocene in age (~2300 calendar yrs BP to present; e.g., Fig. 4). These sediments are similar to the subjacent $CaCO_3$-rich sediments (Unit IB) and the contact between them is visually gradational making distinction difficult. However, these sediments are clearly distinguishable with the aid of XRF core scanning. Ca/Ti values of this most shallow interval (Unit IA) are low relative to the $CaCO_3$-rich interval (Unit IB), yet exhibit higher Ca/Ti values than mud-rich sediments at depth (Units II and III; Figs. 4 and 5). The top of some cores also preserve a second minor Ca/Ti peak within Unit IA (e.g. see HAT-02 and HAT-05). The very shallow sediments of Unit IA, though discontinuous, provide yet another correlative horizon at the site. Thickness and sedimentation rate maps for Units IA and IB sediments are based on the ~2300-calendar-year datum placed at the end of the sub-adjacent Ca/Ti peak (Unit IB), and extended to the core tops (Figs. 8 and 9).

3.2 Stratigraphic Unit II

This unit is a mottled hemipelagic nannofossil silty clay, and the stratigraphic top of the unit ranges from as shallow as 10 cm to as deep as 120 cm below seafloor (Fig. 3). The base of the unit extends from ~100 cm depth in some cores to over 200 cm in others (Fig. 3). This unit displays visual mottling of dark olive brown colors and light olive gray colors with tubular structures (resembling borrows). The color mottling is observed in each core, and gradually decreases with depth to the base of the unit.

XRF core scans indicate that Unit II sediments are markedly more mud-rich, displaying low Ca/Ti ratios (Figs. 4, 5, and 10). The stratigraphic top of the unit is defined by an increase in Ca/Ti values associated with the more $CaCO_3$-rich Unit I (Figs. 4 and 5) and its base is defined by the first distinct presence of reddish banding (Figs. 3–5, see Section 4.3). Its age ranges between 9500 yrs and 15,500 calendar yrs BP based on radiocarbon and nannofossil biostratigraphy (Marchitto and Wei, 1995; Figs. 3–6). Chronologic constraint thus indicates that these sediments represent the late Pleistocene to earliest Holocene transition.

3.3 Stratigraphic Unit III

Sediments of Unit III are well-laminated hemipelagic nannofossil silty clay, olive to dark olive brown in color, containing numerous reddish bands that increase in frequency with depth (Fig. 3). In places, Unit III exhibits irregular contacts across the reddish bands. The top of the unit is marked by a single distinctive red band of nannofossil silty clay that varies in depth from 115 cm below seafloor in Core HAT-03 to

255 cm below seafloor in Core HAT-05 (Fig. 3). Evaluation of the abundance of pre-Quaternary nannofossils at MC118 indicates that the position of this red band closely corresponds to the first peak in reworked nannofossils (Figs. 3–6). Several cores exhibit a double peak of pre-Quaternary nannofossils across the red band interval. Core HAT-01 lacks the highly reworked nannofossil peak, the red band, or clear laminations, indicating the absence of Unit III sediments (Figs. 3 and 4).

Marchitto and Wei (1995) described an increase in reworked nannofossil abundance in sediments from the Orca Basin during meltwater pulse 1a (Fig. 6; see Discussion). Supporting chronologic constraints supports correlation of the reworked nannofossil peak observed to the Orca Basin and MC118 (e.g., Marchitto and Wei, 1995; Fig. 6). Using the chronology of Marchitto and Wei (1995) from the Orca Basin (Fig. 6), the stratigraphic top of Unit III is approximately 14 kilo-yrs.

Foraminiferal biostratigraphy indicates that the Y1/Y2 subzone boundary (~15 kilo-yrs BP) is located between 120 and 122 cm below sea floor (cmbsf) in Core HAT-03, just below the red band and the reworked nannofossil peak. Sediments of Unit III are at least latest Pleistocene in age, and no younger than 14 Ka based on nannofossil biostratigraphy, 15 Ka based on foraminiferal biostratigraphy, and 15.5 Ka based on radiocarbon dating (Table 2, Fig. 3). Stratigraphic Unit III lacks a clear basal horizon across the study area; hence, neither the total thickness nor the average sedimentation rate can be determined for these latest Pleistocene sediments.

Discussion

The results of this study indicate pronounced changes in sedimentation at MC118 during the latest Pleistocene–Holocene, with respect to the rate and pattern of deposition, as well as the geochemistry of the sediments. This is well documented by the observed variability in XRF-scanning Ca/Ti profiles. Sedimentologic observations from the MC118 cores indicate that carbonate content is primarily attributable to the abundance of microfossils (e.g., foraminifers and nannofossils), and thus elevated calcium concentration in MC118 sediments is primarily attributable to an increase in biogenic $CaCO_3$ (Brunner, 2007a, b). Terrigenous contributions are inferred from the relative abundance of titanium, supplied to the Gulf of Mexico shelf and slope from lithogenic sources and primarily derived from ilmenite (FeTiO3), closely followed by rutile (TiO_2), minerals mostly associated with sand- and silt-size grains (Woolsey, 1984; Appelbaum and Bouma, 1972). Hence, in the Gulf of Mexico, the Ca/Ti ratio generally reflects relative changes in biogenic versus lithogenic sedimentation.

The most obvious geochemical feature in sediments at MC118 is elevated $CaCO_3$ concentration from 2300 to 9500 calendar yrs BP (Unit IB, Ca/Ti curve; Figs. 4 and 5). The onset of this $CaCO_3$-rich sedimentation may largely represent decreased clay flux associated with Holocene sea-level rise and retreat of the paleo-shoreline. While it seems the shelf here was exposure at times, cross-shelf transport to the slope break and associated canyon incision was not pervasive everywhere (Törnqvist et al., 2006). Holocene delta lobe switching provides a second mechanism to explain observed trends in biogenic carbonate versus lithogenic components of sedimentation at the MC118 site.

The timing and relative positions of the Holocene Mississippi River deltaic lobes have been previously considered in several investigations (Törnqvist et al., 1996; Roberts, 1997; Aharon 2006; Blum and Roberts, 2009), and show consistency with the Ca/Ti data from MC118. For example, during the period from 7500 to 5000 calendar yrs BP, the early Holocene Louisiana deltas prograded far to the west, approximately 300 km from the modern Mississippi River outflow (Blum and Roberts, 2009). The positioning of the delta at that time is coincident with $CaCO_3$-rich sedimentation at MC118, suggesting that the location of the delta to the west diminished terrigenous sedimentation at MC118. A third interpretation is that of elevated biological $CaCO_3$ production during the deposition of Unit IB, and consequent dilution of the lithogenic components. However, a reduction in sedimentation rate at MC118 from the latest Pleistocene to Holocene transition (Section 5.1; Figs. 7–10) argues against the hypothesis of enhanced biological production. Hence, past sea-level change and movement of the Mississippi Delta seem to be the most likely explanation for the observed changes in the Ca/Ti ratio.

Deltaic shifting to the east (towards MC118) by the Teche delta complex (5.5–3.5 Ka) and especially the St. Bernard delta complex (4.0–2.0 Ka), should have resulted in an increase in lithogenic sedimentation at MC118 (Blum and Roberts, 2009). Consistent with this, we observe a decrease in the Ca/Ti ratio commencing by at least 2.9 Ka (see PEL-15 in Fig. 5). This interval is followed at the very top (20 cmbsf) in Cores HAT-02 and HAT-05 by a short-lived Ca/Ti peak (Fig. 4), perhaps marking higher frequency changes in the Mississippi River outflow. The general position of the modern Plaquemines–Balize delta and Mississippi River mouth was established by 1.3 Ka, and reaches directly

toward the MC118 study area. This positioning likely contributes to lithogenic dilution of carbonate content at the very top of the MC118 cores.

4.1 Isopach Mapping

The stratigraphic intervals observed at MC118 are summarized and mapped by isopach thickness and associated sedimentation rate (e.g., Figs. 7–10). These maps reveal an overall decrease in sedimentation rate from ~14 Ka to present, yet spatial patterns of deposition surrounding the field are consistent across all intervals (Figs. 7–10). The general pattern of sedimentation at MC118 is summarized by an isopach from the red band at the top of Unit III (~14 Ka) to the present, indicating stratigraphic thickening and elevated sedimentation rate with distance from the field (Fig. 7). The shallowest isopach exhibits a similar pattern (Unit IA; Fig. 8), as does the Holocene $CaCO_3$-enriched interval (Unit IB; 2.3–9.5 Ka; Fig. 9), and the mottled nannofossil silty clay of Unit II (9.5–14 Ka; Fig. 10).

The isopach map reconstructions indicate that the location of stratigraphic thinning (adjacent to the gas-hydrate and cold-seep field) shifts from a more offshore position during the latest Pleistocene–Early Holocene (14 to 9.5 Ka; Fig. 10) to a more landward location during the Holocene (Unit IB; 2.3–9.5 Ka; Fig. 9). This observation is suggestive of migration of fluid seepage and hydrate activity along the seafloor in a northward upslope direction from the latest Pleistocene to the Holocene. The change in position of stratigraphic thinning through time may be a result of subtle changes in bathymetry and movement of paleo-highs induced by seafloor warping from subsurface salt, potentially including alteration of the subsurface plumbing. Cold seeps and mud

volcanoes alike can shift their position through time and this phenomenon has been observed in terrestrial mud volcanoes that produce numerous mounds and craters that collapse, change shape, and shift position (Dimitrov, 2002). On a localized scale, the seafloor near the MC118 gas vents and petroleum seeps exhibit slight depressions and craters (Figs. 1 and 2), although the density of coring does not permit evaluation of sedimentation trends inside the field. It should be emphasized that sedimentation controlled by salt tectonics is important on geologic timescales and ultimately is a key factor in controlling deposition along the Gulf of Mexico continental slope (Galloway et al., 2000; Winker and Booth, 2000; Diegel et al., 1995; Jackson, 1995). Complex interactions between subsurface salt deposits, fluid migration and sedimentation seem likely at MC118.

Shifting of the MC118 field due to changes in hydrate stability associated with rising sea level is an alternative hypothesis to explain observations, but is not consistent with theoretical prediction. The MC118 site has remained at sufficient water depth and beneath the zone of potential methane-hydrate instability since the Late Pleistocene as predicted by stability in seawater (e.g., 400–600 m water depth; Lerche and Bagirov, 1998; Dickens and Quinby-Hunt, 1994), however, advection of warm fluids from the subsurface complicate the base of the hydrate stability zone. Furthermore, gas hydrate at the MC118 site formed in close proximity to petroleum seepage, which hosts a mixture of thermogenic gases, and therefore is more stable than pure methane hydrate (e.g., Lerche and Bagirov, 1998; Sassen et al., 2001).

Finally, the similarity of Cores HAT-02 and HAT-05 is striking (Fig. 4; Figs. 7–10) with respect to the shape of the Ca/Ti profiles and thickness of each interval, suggesting

that these sites record undisturbed background sedimentation. In total, the results of this study are consistent with localized remobilization of sediment or reduced sedimentation over the gas-hydrate/cold-seep field, yet are not suggestive of significant seafloor failure across a widespread area (~1 km), at least during the past ~14,000 yrs. However, given the location of the core sites outside the field, it is difficult to detect minor (meter-scale) remobilization events (e.g., Figs. 1 and 2).

4.2 The "red band"

The reddish-colored interval ("red band") that defines the top of Unit III has previously been observed at MC118 (Lutken et al., 2006; Brunner, 2007a; Sleep et al., 2008). The red band level is approximately concurrent with the most recent interval of reworked nannofossils (also typically the highest magnitude peak of reworked nannofossils; Figs. 4–6). Although no unique elemental composition was observed across the red band, it is, however, associated with a negative $\delta^{18}O$ excursion from a series of planktonic foraminifera from Core HAT-03 (W. Ingram, unpublished data). Marchitto and Wei (1995) also discovered a similar coincidence of highly reworked nannofossils and strongly negative $\delta^{18}O$ isotopic values from planktonic foraminifera, which they attributed to scouring of epicontinental sediments by glacial meltwater outflow down the Mississippi River drainage basin and into the Gulf of Mexico.

It is possible that highly weathered, subaerially exposed sediments spanning the midcontinent of North America were delivered to MC118 by meltwater discharge events that drained large pro-glacial lakes as described by Marchitto and Wei (1995). Interestingly, the frequency of red banding increases with depth below the initial, most

prominent red band that defines the top of stratigraphic Unit III. At these depths, well below the initial red band, sediments are most certainly latest Pleistocene, up to ~19,000 calendar yrs BP, based on radiocarbon dating (Figs. 3–5). The chronostratigraphy developed in this study indicate latest Pleistocene laminated sediments were deposited rapidly and were perhaps derived from weathered, subaerially exposed and oxidized sediments of the North American midcontinent, bypassing the shelf during the latest Pleistocene sea-level low stand. Constans and Parker (1986) have established the percentage of reworked (extinct) nannofossils as a proxy indicator for enhanced erosion of terrestrial epicontinental sediments and subsequent delivery to the continental slope of the northern Gulf of Mexico during sea-level low stands on glacial–interglacial cycles. Nannofossil biostratigraphic results of this study suggest similar processes were involved during the time the red band interval was deposited. Additionally, previous investigators (e.g., Aharon 2006) have suggested hyperpycnal flow of meltwater into the Gulf of Mexico during the period from 14.7 to 14.2 calendar kilo-yrs coincident with the timing of the red band at MC118. Thus the observed red band may represent a proxy indicator for a significant erosional event perhaps connected to the draining of large terrestrial pro-glacial lakes and the delivery of oxidized sediments to the Gulf of Mexico. Although the proposed hypothesis for the formation of the red band is speculative, this interval is nonetheless highly continuous in sediments around the MC118 study area. Hence, the red band provides a new chronostratigraphic marker for sediments in the vicinity of MC118.

Conclusions

This study establishes a chronostratigraphic framework for late Pleistocene-Holocene sedimentation surrounding the MC118 gas-hydrate and cold-seep field. The results provide compelling evidence for enhanced sediment erosion, remobilization and/or non-deposition in close proximity to the MC118 field. Isopach reconstructions clearly indicate greater stratigraphic thickness and higher sedimentation rates with distance from the gas-hydrate/cold-seep field. The evolution of sedimentation patterns over the past 14 Ka reveals lateral shifting in the position of stratigraphic thinning, which likely reflects migration of the locus of hydrate outcropping and cold seepage and/or movement of subtle paleo-bathymetric highs through time. The ultimate cause of the observed stratigraphic patterns likely involves complex interactions between subsurface salt deposits, fluid migration and sedimentation.

The MC118 stratigraphic record reveals similar sedimentation and bulk geochemistry far upslope and downslope from the field. This result is inconsistent with catastrophic slope failure or major disruptions to sedimentation over a large portion of the seafloor at MC118, at least since the end of the last deglacial. Changes in the sedimentation rate and consistent variability in geochemistry through time at MC118 at each core site is most likely a consequence of deglacial sea-level rise and regional factors such as Mississippi delta lobe switching.

References

Aharon, P., 2006. Entrainment of meltwaters in hyperpycnal flows during deglaciation superfloods in the Gulf of Mexico. Earth and Planetary Science Letters 241 (1–2), 260–270.

Appelbaum, B.S., Bouma, A.H., 1972. Geology of the upper continental slope in the Alaminos Canyon region. Gulf Cost Association of Geological Societies Transactions 22, 157–164.

Blum, M.D., Roberts, H.H., 2009. Drowning of the Mississippi Delta due to insufficient sediment supply and global sea-level rise. Nature Geoscience 2, 488–491.

Broecker, W.S., Andreé, M., Wolfli, W., Oeschger, H., Bonani, G., Kennett, J.P., Peteet, D., 1988. The chronology of the last deglaciation: implications to the causes of the Younger Dryas event. Paleoceanography 3, 1–19.

Broecker, W.S., Kennett, J.P., Flower, B.P., Teller, J.T., Trumbore, S., Bonani, G., Wolfli, W., 1989. Routing of meltwater from the Laurentide ice sheet during the Younger Dryas cold episode. Nature 341, 318–321.

Brunner, C.A., 2007a. Stratigraphy and paleoenvironment of shallow sediments from MC118. Proceedings of the Annual Meeting of the Gulf of Mexico Hydrates Research Consortium, October 10–11, 2007, Oxford, Ms. [one CD].

Brunner, C.A., 2007b. Qualitative planktonic foraminiferal biostratigraphy of core MD02-2570, of late Quaternary age, from the northern Gulf of Mexico. In: Winters, W.J., Lorenson, T.D., Paull, C.K. (Eds.), Initial report of the gas hydrate and paleoclimate cruise on the R/V Marion Dufresne in the Gulf of Mexico, 2–18 July 2002: USGS Open-File Report 2004-1358, one DVD. online at http://www.pubs.usgs.gov/of/2004/1358/.

Castellini, D.G., Dickens, G.D., Snyder, G.T., Ruppel, C.D., 2006. Barium cycling in shallow sediments above active mud volcanoes in the Gulf of Mexico. Chemical Geology 226, 1–30.

Constans, R.E., Parker, M.E., 1986. Calcareous nannofossil biostratigraphy and paleoclimate indices for the Late Quaternary, Deep Sea Drilling Project Leg 96, Gulf of Mexico. In: Bouma, A.H., Coleman, J.M., Meyer, A.W., et al. (Eds.), Initial Reports of the Deep Sea Drilling Project 96. U.S. Government Printing Office, Washington, D.C., pp. 601–630.

Dickens, G.R., Quinby-Hunt, M.S., 1994. Methane hydrate stability in seawater. Geophysical Research Letters 21, 2115–2118.

Dickens, G.R., Castillo, M.M., Walker, J.C.G., 1997. A blast of gas in the latest Paleocene: simulating first-order effects of massive dissociation of methane hydrate. Geology 25, 259–262.

Diegel, F.A., Karlo, J.F., Schuster, D.C., Shoup, R.C., Tauvers, P.R., 1995. Cenozoic structural evolution and tectono-stratigraphic framework of the northern Gulf Coast continental margin, in: Jackson, M.P.A., Roberts, D.G., Snelson, S., (Eds.), Salt Tectonics: A Global Perspective: American Association of Petroleum Geologist Memoir 65, pp. 109–151.

Dimitrov, L.I., 2002. Mud volcanoes—the most important pathway for degassing deeply buried sediments. Earth Science Reviews 59, 49–76.

Fairbanks, R.G., Mortlock, R.A., Chiu, T.-C., Cao, L., Kaplan, A., Guilderson, T.P., Fairbanks,T.W., Bloom, A.L., Grootes, P.M., Nadeau, M.-J., 2005. Radiocarbon calibration curve spanning 0 to 50, 000 years BP based on paired 230Th/234U/238U and 14C dates on pristine corals. Quaternary Science Reviews 24, 1781–1796.

Flower, B.P., Kennett, J.P., 1990. The Younger Dryas cool episode in the Gulf of Mexico. Paleoceanography 5 (6), 949–961.

Galloway, W.E., Ganey-Curry, P.E., Li, X., Buffler, R.T., 2000. Cenozoic depositional history of the Gulf of Mexico basin. American Association of Petroleum Geologists Bulletin 84 (11), 1743–1774.

Haq, B.U., 1998. Natural gas hydrates: searching for the long-term climatic and slopestability records. In: Henriet, J.P., Mienert, J. (Eds.), Gas Hydrates: Relevance to World Margin Stability and Climate Change: Geological Society, London Special Publications, 137, pp. 303–318.

Jackson, M.P.A., 1995. Retrospective Salt Tectonics, in: M.P.A. Jackson, D.G. Roberts, S. Snelson, (Eds.), Salt Tectonics: a Global Perspective. AAPG Memoir 65, pp. 1–28.
Katz, M.E., Pak, D.K., Diskens, G.R., Miller, K.G., 1999. The source and fate of massive carbon input during the latest Paleocene thermal maximum. Science 286, 1531–1533.

Kennett, J.P., Huddlestun, P., 1972. Late Pleistocene paleoclimatology, foraminiferal biostratigraphy and tephrochronology, Western Gulf of Mexico. Quaternary Research 2, 38–69.

Kennett, J.P., Elmstrom, K., Penrose, N.L., 1985. The last deglaciation in Orca Basin, Gulf of Mexico: high-resolution planktonic foraminifera changes. Paleogeography, Paleoclimatology, Paleoecology 50, 189–216.

Kennett, J.P., Cannariato, K.G., Hendy, I.L., Behl, R.J., 2000. Carbon isotopic evidence for methane hydrate instability during Quaternary interstadials. Science 288 (5463), 128–133.

Kennett, J.P., Cannariato, K.G., Hendy, I.L., Behl, R.J., 2003. Methane Hydrates in Quaternary Climate Change: The Clathrate Gun Hypothesis. American Geophysical Union, Washington, DC. 216 pp.

Lapham, L.L., Chanton, J.P., Martens, C.S., Sleeper, K., Woolsey, J.R., 2008. Microbial activity in surficial sediments overlying acoustic wipeout zones at a Gulf of Mexico cold seep. Geochemistry, Geophysics, Geosystems 9 (4), 1–17.

Lapham, L.L., Chanton, J.P., Chapman, R., Martens, C.S., (in press). Methane undersaturate fluids in deep-sea sediments: implications for gas hydrate stability and rates of dissolution. Manuscript for Earth and Planetary Science Letters

Lerche, I., Bagirov, E., 1998. Guide to gas hydrate stability in various geological settings. Marine and Petroleum Geology 15 (5), 427–437.

Lutken, C.B., Brunner, C.A., Lapham, L.L., Chanton, J.P., Rogers, R., Sassen, R., Dearman, J., Lynch, L., Kuykendall, J., Lowrie, A., 2006. Analyses of core samples from Mississippi Canyon 118, paper OTC 18208, Offshore Technology Conference, American Association of Petroleum Geologist, May 1–4, Houston, TX.

Marchitto, T.M., Wei, K.-Y., 1995. History of the Laurentide meltwater flow to the Gulf of Mexico during the last deglaciation, as revealed by reworked calcareous nannofossils. Geology 23, 779–782.

Maslin, M., Mikkelsen, N., Vilela, C., Haq, B., 1998. Sea-level and gas-hydrate-controlled catastrophic sediment failures of the Amazon Fan. Geology 26 (12), 1107–1110.

Maslin, M., Owen, M., Day, S., Long, D., 2004. Linking continental-slope failures and climate change: testing the clathrate gun hypothesis. Geology 32, 53–56.

McGee, T., 2006. A seafloor observatory to monitor gas hydrates in the Gulf of Mexico. The Leading Edge 25 (5), 644–647.

Mienert, J., Vanneste, M., Bunz, S., Andreassen, K., Haflidason, H., Sejrup, H.P., 2005. Ocean warming and gas hydrate stability on the mid-Norwegian Margin at the Storegga Slide. Marine and Petroleum Geology 22, 233–244.

Milkov, A.V., Sassen, R., 2002. Thickness of gas hydrate stability zone, Gulf of Mexico, continental slope. Marine and Petroleum Geology 17, 981–991.

Paull, C.K., Brewer, P.G., Ussler III, W., Peltzer, E.T., Rehder, G., Clague, D., 2003. An experiment demonstrating that marine slumping is a mechanism to transfer methane from gas-hydrate deposits into the upper ocean and atmosphere. Geomarine Letters 22, 198–203.

Paull, C.K., Buelow, W.J., Ussler III, W., Borowski, W.S., 1996. Increased continental margin slumping frequency during sea-level lowstands above gas hydrate-bearing sediments. Geology 24 (2), 143–146.

Poore, R.Z., Dowsett, J.J., Verardo, S., 2003. Millennial- to century-scale variability in Gulf of Mexico Holocene climate records. Paleoceanography 18 (2), 1–13.

Richey, J.N., Poore, R.Z., Flower, B.P., Quinn, T.M., 2007. 1400 yr multiproxy record of climate variability from the northern Gulf of Mexico. Geology 35 (5), 423–426.

Roberts, H.H., 1997. Dynamic changes of the Holocene Mississippi river delta plain: the delta cycle. Journal of Coastal Research 13, 605–627.

Sassen, R., Sweet, S.T., Milkov, A.V., DeFreitas, D.A., Kennicutt, M.C., 2001. Thermogenic vent gas and gas hydrate in the Gulf of Mexico slope: is gas hydrate decomposition significant? Geology 29 (2), 107–110.

Sassen, R., Roberts, H.H., Jung, W., Lutken, C.B., DeFreitas, D.A., Sweet, S.T., Guinasso Jr., N.L., 2006. The Mississippi Canyon 118 gas hydrate site: a complex natural system. Paper OTC 18132, Offshore Technology Conference, May 1–4, Houston, TX.

Sleeper, K.A., Lowrie, A., Bosman, A., Macelloni, L., Swann, C.T., 2006. Bathymetric mapping and high resolution seismic profiling by AUV in MC 118 (Gulf of Mexico). Paper OTC 18133, Offshore Technology Conference, May 1–4, Houston, TX.

Sleeper, K.A., Lutken, C., 2008. Activities Report for CruiseGOM1-08-MC118 aboard the R/V Pelican Sampling and Deployment Cruise Mississippi Canyon Federal Lease Block 118 Northern Gulf of Mexico April 22–28, 2008. The Center for Marine Resources and Environmental Technology and the Seabed Technology Research Center, University of Mississippi. http://www.olemiss.edu/depts/mmri/programs/ppt_list.html, 16 pp.

Solheim, A., Bryn, P., Berg, K., Mienert, J., 2005. Ormen Lange — an integrated study for the safe development of a deep-water gas field within the Storegga Slide Complex, NE Atlantic continental margin. *Marine and Petroleum Geology* 22 (1–2), 221–318.

Stuiver, M., Polach, H.A., 1977. Discussion: reporting of 14C data. Radiocarbon 19, 355–363. Stuiver, M., 1980. Workshop on 14C data reporting. *Radiocarbon* 22, 964–966.

Törnqvist, T.E., Wortman, S.R., Mateo, Z-R.P., Milne, G.A. and Swenson, J.B., 2006. Did the last sea level low stand always lead to cross-shelf valley formation and source to sink sediment flux? *Journal of Geophysical Research*, v. 111, p. 1-13.

Törnqvist, T.E., Kidder, T.R., Austin, W.J., van der Borg, K., de Jong, A.F.M., Klerks, C.J.W., Snijders, E.M.A., Storms, J.E.A., van Dam, R.L., Wiemann, M.C., 1996. A revised chronology for Mississippi River subdeltas. *Science* 273 (5282), 1693–1696.

Winker, C.D., Booth, J.R., 2000. Sedimentary dynamics of the salt-dominated continental slope, Gulf of Mexico: integration of observations from the seafloor, near surface, and deep subsurface. GCSSEPM Foundation 20th Annual Research Conference Deep-Water Reservoirs of the World, Dec. 3–6, pp. 1059–1086.

Woolsey, J.R., 1984. Exploration for industrial minerals in Mississippi Sound and adjacent offshore territories of Mississippi and Alabama. Mississippi–Alabama Sea Grant Consortium, Project No. R/ER-11, Grant No. NA81AA-D-00050. 22 pp.

Date Core taken	Aug. 2007	Aug. 2007	Aug. 2007	Aug. 2007	Aug. 2007
Cruise (Research Vessel)	*Hatteras*	*Hatteras*	*Hatteras*	*Hatteras*	*Hatteras*
Core I.D.	HAT-01	HAT-02	HAT-03	HAT-04	HAT-05
Core Locations:					
Latitude (N)	28 52' 10.0"	28 51' 50.0"	28 50' 29.5"	28 50' 29.3"	28 50' 28.3"
Longitude (W)	88 29' 30.0"	88 29' 30.0"	88 29' 30.0"	88 29' 30.0"	88 29' 30.0"
Water Depth (m)	840	873	960	965	1061
Gross Thickness					
Sub-bottom depth (cm)	226	275	272	283	269
Net thickness (cm)	222	261	258	282	255

Date Core taken	April. 2008	April. 2008	April. 2008	April. 2008	April. 2008
Cruise (Research Vessel)	*Pelican*	*Pelican*	*Pelican*	*Pelican*	*Pelican*
Core I.D.	PEL-02	PEL-15	PEL-04	PEL-07	PEL-08
Core Locations:					
Latitude (N)	28 51' 34.0"	28 50' 59.6"	28 50' 49.5"	28 50' 42.8"	28 50' 37.7"
Longitude (W)	88 30' 16.2"	88 29' 37.5"	88 28' 23.6"	88 27' 53.3"	88 27' 49.1"
Water Depth (m)	873	869	920	981	971
Gross Thickness					
Sub-bottom depth (cm)	440	460	405	600	711
Net thickness (cm)	438	445	400	597	703

Table 1. Shallow gravity cores that recovered deep-sea sediments at the MC118 study site during two separate cruises onboard surface ships the *R/V Hatteras* and *R/V Pelican*, the tabulated data includes (1) when the cores where collected, (2) core labels, (3) their location and (4) sediment recovery (net thickness).

Core I.D.	Sub-bottom Depth (cm)	Radiocarbon Age (yr)	Gulf of Mexico Correction	Calendar-Age (y BP)	Error (yr)
HAT-02	12	1270	870	773	47
	25	1940	1540	1418	53
	50	2720	2320	2336	22
	120	10300	9900	11280	56
	245	13750	13350	15544	121
	265	14100	13700	15946	132
HAT-03	10	2550	2150	2146	66
	30	4190	3790	4162	48
	115	11650	11250	13086	67
	270	16450	16050	19182	103
HAT-04	20	2870	2470	2565	90
HAT-05	6	1460	1060	960	25
	20	1780	1380	1296	28
	120	8920	8520	9513	21
PEL-15	4	3210	2810	2901	39
	30	9660	9260	10441	91
	453	15800	15400	18632	98
PEL-04	4	1480	1080	978	38
	40	7660	7260	8067	55
	406	15200	14800	17702	216

Table 2. AMS radiocarbon dating of planktic foraminifera from sediments recovered at the MC118 site, tabulated data includes AMS dates from "picked" foraminifera indicating, the location (depth) of the sample in each core, radiocarbon years, reservoir correction, reservoir-corrected age and error. Note: Core Hat-03, with a sample depth of 115 cm, is anomalously young by approximately 1000 calendar yrs, and thus is not utilized in the final chronostratigraphy. Error in calendar years is 1 standard deviation.

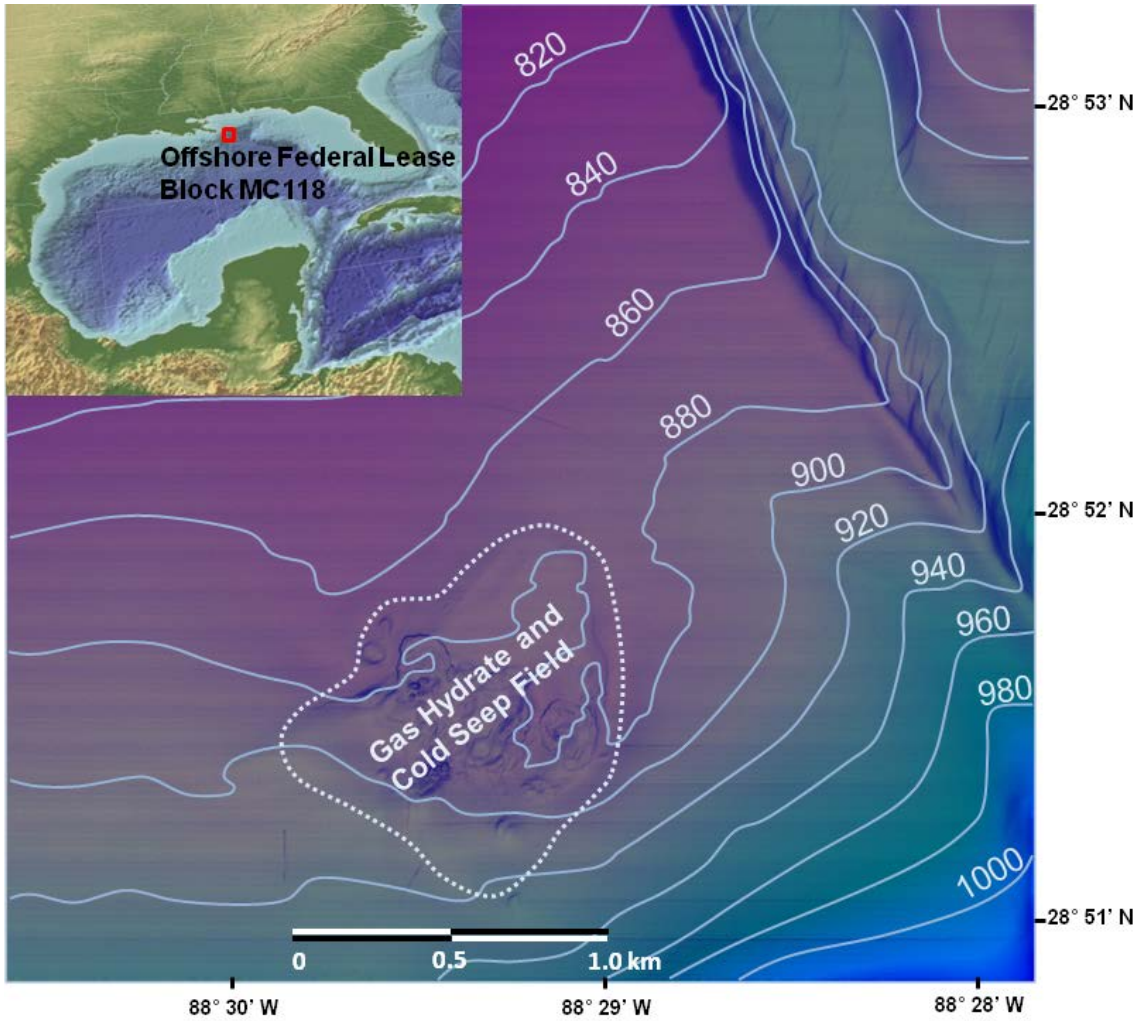

Figure 1. Bathymetric map of the study area (Block MC118), labeled contours (light blue) in meters water depth (e.g., Sleeper and Lutken, 2008) with inset digital elevation and bathymetry map (top left; cropped NOAA geophysical data center image) of the Gulf of Mexico region. Bathymetry provided by the Gulf of Mexico Hydrate Research Consortium, modified after figure from Ken Sleeper. The location of MC118 offshore federal lease block is indicated by the red box in the inset map. The extent of the studied gas-hydrate and cold-seep field is outlined by the light blue dashed line and is characterized by an area containing gas vents, seafloor pockmark features, petroleum seepage, shallow faults, carbonate hard-grounds and gas hydrate deposits. The study area is ~150 km South of Gulfport Mississippi in 800 to 1000 m water depth.

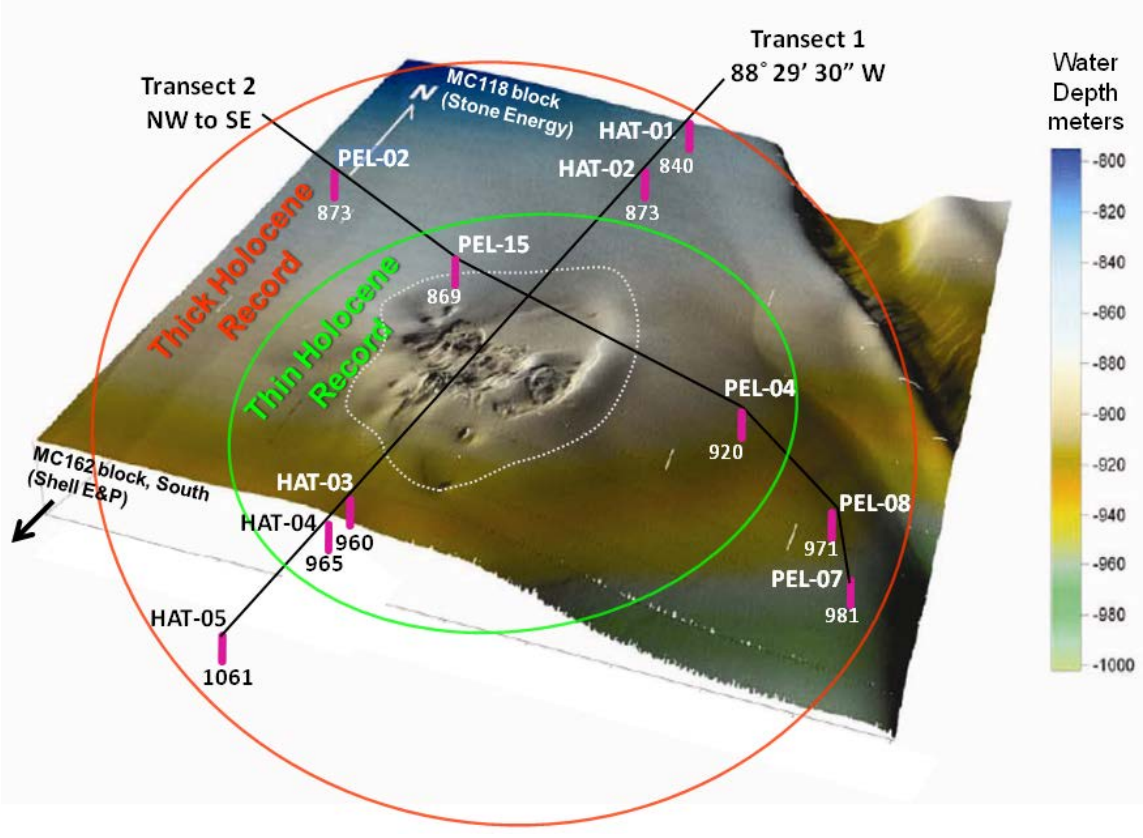

Figure 2. Bathymetric map of the study site with the location of cores collected during cruises on the R/V Hatteras and R/V Pelican; base map image is from the Gulf of Mexico Hydrate Research Consortium (Sleeper et al., 2006). Cores are indicated by vertical magenta lines, with core identification (above) and water depth in meters (below). The edge of the gas-hydrate and cold-seep field is outlined by a thin dashed white line, black lines connecting cores indicate transects taken by the R/V Hatteras (Transect 1) and R/V Pelican (Transect 2). Cores within the green circle near the field exhibit a thin Holocene section, and cores outside the green circle and within the orange circle contain a thicker Holocene section. The color bar on the far right indicates water depth in meters.

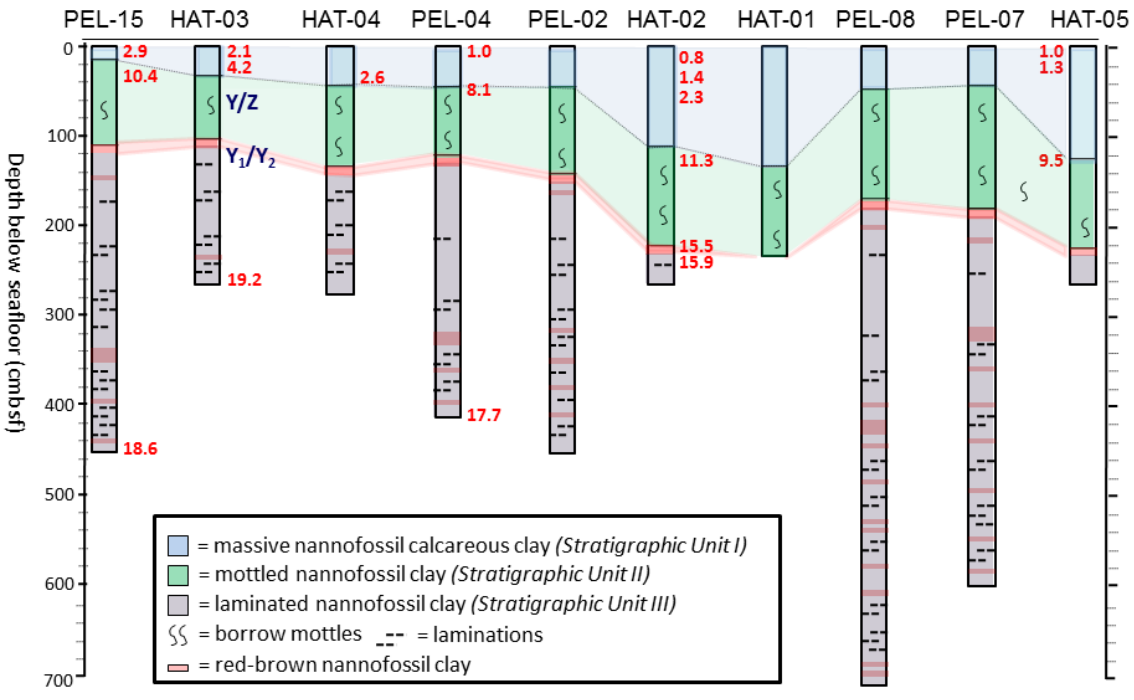

Figure 3. Stratigraphic correlation of marine sediments collected for this study. Cores are arranged by increasing distance (left to right) from the gas-hydrate and cold-seep field. Dates obtained via AMS radiocarbon analysis of planktonic foraminifera (red, Ka) and foraminiferal biostratigraphic boundaries (dark blue, Y/Z ~10 Ka and Y1/Y2 ~15 Ka) are shown alongside their stratigraphic position; all reported ages are in calendar kilo-yrs BP. Three distinct stratigraphic units (see Results for detailed descriptions) are identified as follows: Unit I (light blue) massive nannofossil calcareous silty clay; Unit II (light green) mottled nannofossil clay; Unit III (gray) laminated nannofossil clay containing reddish-brown nannofossil clay layers (red lines). A distinct ~5-cm thick reddish clay layer with highly “reworked” (pre-Quaternary) nannofossils defines the top of Unit III.

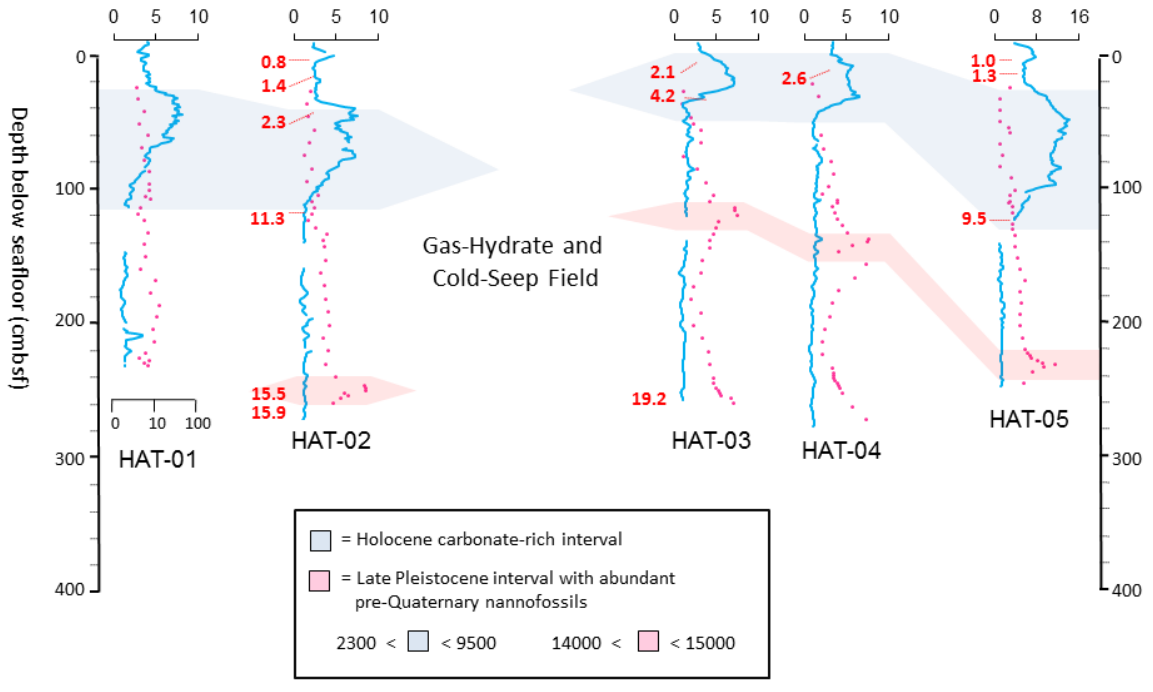

Figure 4. X-ray fluorescence (XRF) core scanning Ca/Ti results (blue line), and the percentage of reworked nannofossils (red dots), for cores collected on the R/V Pelican (Transect 2). The Ca/Ti data is plotted as a 3-cm moving average, and the reworked nannofossil data are plotted on a log scale (1 to 100%) shown at the bottom of the Core PEL-02 on far left. Two correlative horizons are identified as discussed in the text: a Holocene (Unit IA; 2300–9500 yrs) $CaCO_3$-rich interval (blue) and late Pleistocene (14,000–15,000 yrs) reworked nannofossil interval (red). Radiocarbon ages are in Ka (calendar kilo-yrs BP).

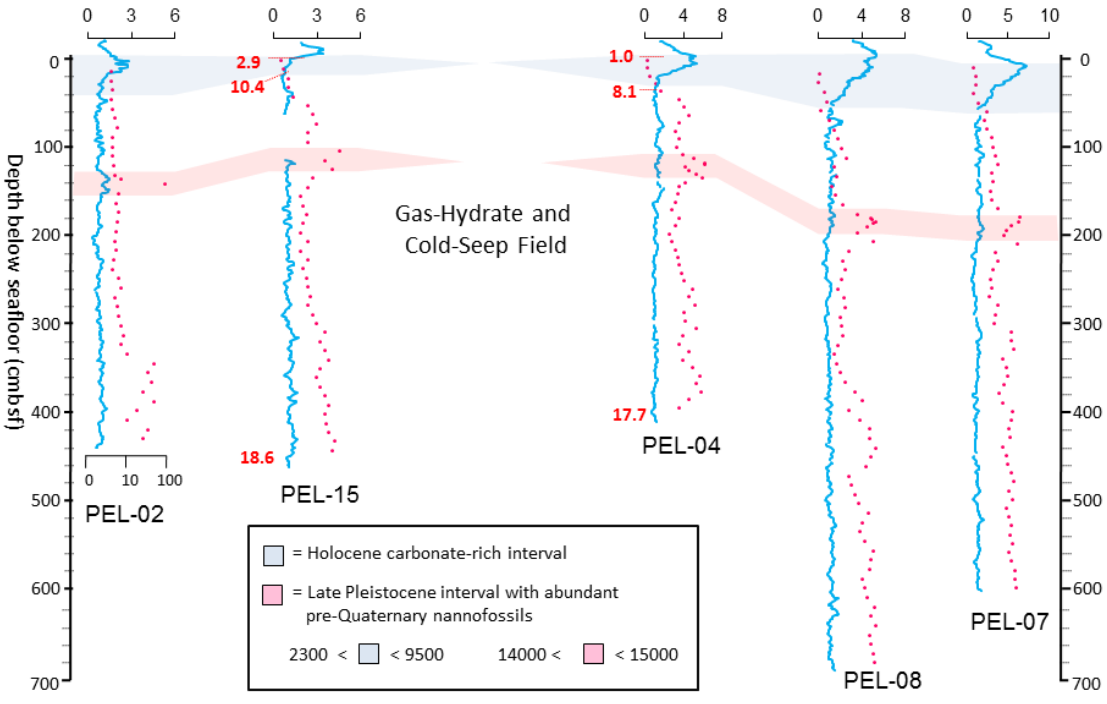

Figure 5. X-ray fluorescence (XRF) core scanning Ca/Ti results (blue line), and the percentage of reworked nannofossils (red dots), for cores collected on the R/V Pelican (Transect 2). The Ca/Ti data is plotted as a 3-cm moving average, and the reworked nannofossil data are plotted on a log scale (1 to 100%) shown at the bottom of the Core PEL-02 on far left. Two correlative horizons are identified as discussed in the text: a Holocene (Unit IA; 2300–9500 yrs) $CaCO_3$-rich interval (blue) and late Pleistocene (14,000–15,000 yrs) reworked nannofossil interval (red). Radiocarbon ages are in Ka (calendar kilo-yrs BP).

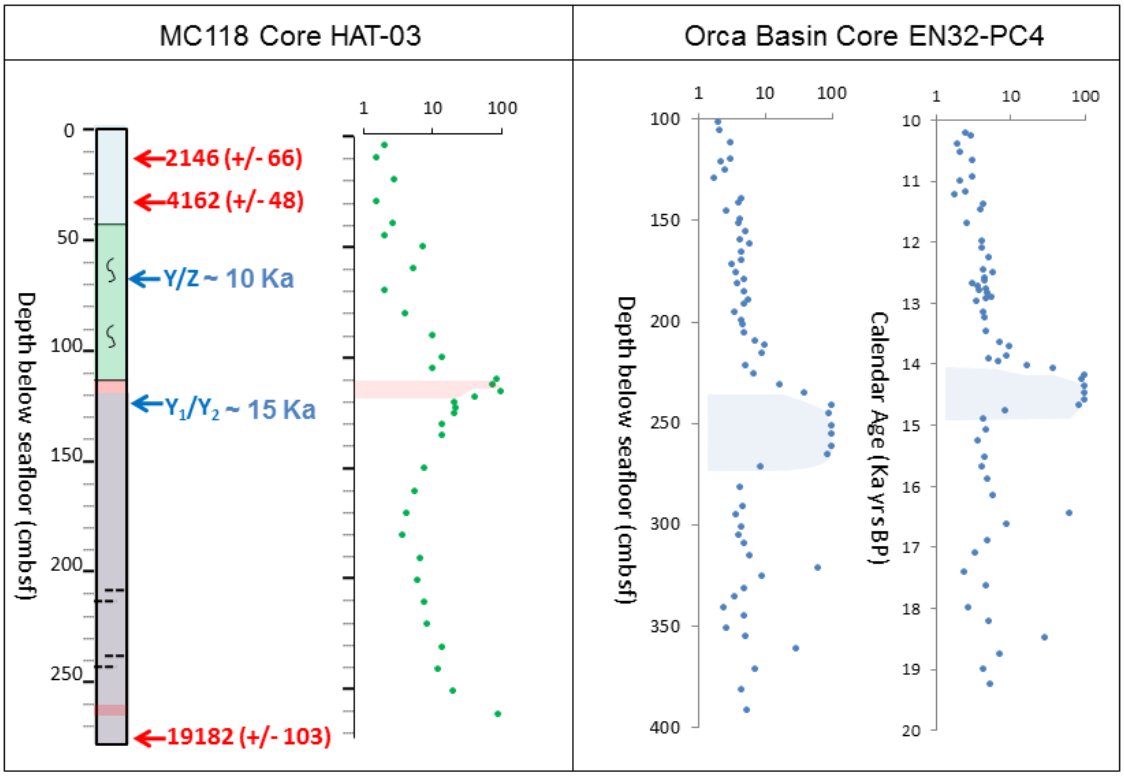

Figure 6. Percentage of reworked nannofossils for MC118 (left panel) and the Orca Basin (right panel; data from Marchitto and Wei, 1995). The original Marchitto and Wei (1995) timescale for the EN32-PC4 core, derived from Flower and Kennett (1990) includes a 400-yr reservoir correction already applied to their radiocarbon ages. It is converted here to calendar kilo-yrs BP using the Fairbanks et al. (2005) calibration. This previous work places the most prominent peak of reworked nannofossils between 14 and 15 Ka calendar kilo-yrs BP. Age control for Core HAT-03 includes AMS radiocarbon ages (red), in calendar yrs BP, and foraminiferal biostratigraphic boundaries (dark blue, Y/Z~10 Ka and Y1/Y2~15 Ka), also in calendar kilo-yrs BP. The aforementioned, biostratigraphic events used in this study are based partly on the disappearance of *Globorotalia inflata* (14 to 15 Ka) and reappearance of the *G. menardii plexus* (~10 Ka), which correspond to sea-level and temperature changes in the Gulf of Mexico during deglaciation and the subsequent interglacial period (Flower and Kennett, 1990). The age of the highly reworked nannofossil interval, constrained by biostratigraphy and radiocarbon age dates, is between 14,000 and 15,000 calendar kilo-yrs BP. Hence, the initial shallow peak of reworked nannofossils in Core HAT-03 (left plot) is coincident in age with the peak identified in Core EN32-PC4 (far right plot). Percentage of reworked nannofossils is plotted on a log scale in all three profiles.

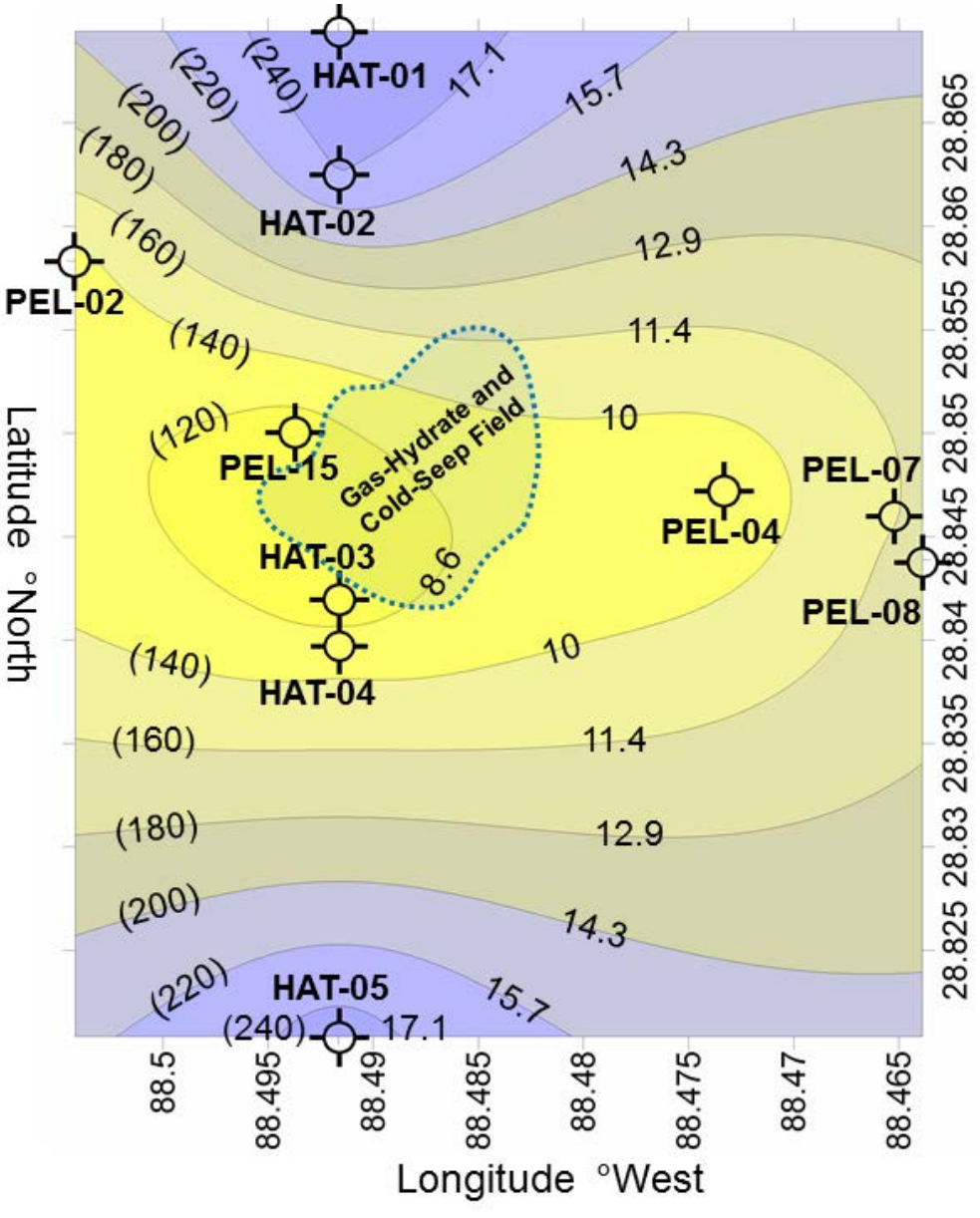

Figure 7. Isopach thickness and sedimentation rate map of the MC118 area for the interval above the red band, ~14 kilo-yrs BP to the present (core tops), which includes sediments of stratigraphic Units I and II. Very shallow latest Holocene sediments may be missing in some cores. Core locations are identified by open circles. The area of the present-day gas-hydrate and cold-seep field is indicated by the transparent blue shading within the dotted outline. Contour lines are labeled using sedimentation rate (cm/kyr) and thickness (cm) shown in parentheses.

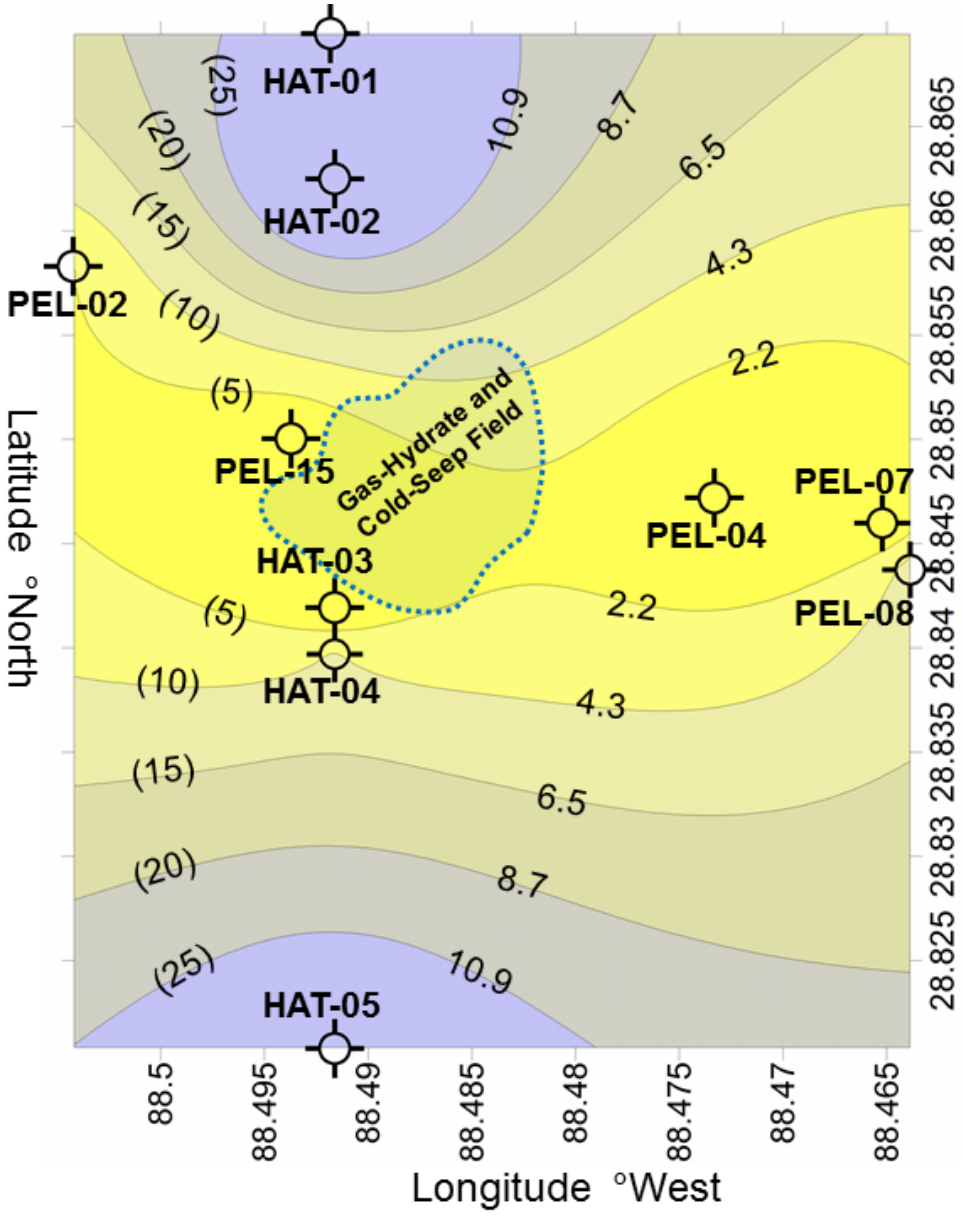

Figure 8. Isopach thickness and sedimentation rate map of the MC118 area for the interval from ~2.3 kilo-yrs BP to present (Unit IA). These very shallow sediments are only distinguishable with the aid of XRF core scanning and are partially missing in some cores. Core locations are identified by open circles. The area of the present-day gas-hydrate and cold-seep field is indicated by the transparent blue shading within the dotted outline. Contour lines are labeled using sedimentation rate (cm/kyr) and thickness (cm) shown in parentheses.

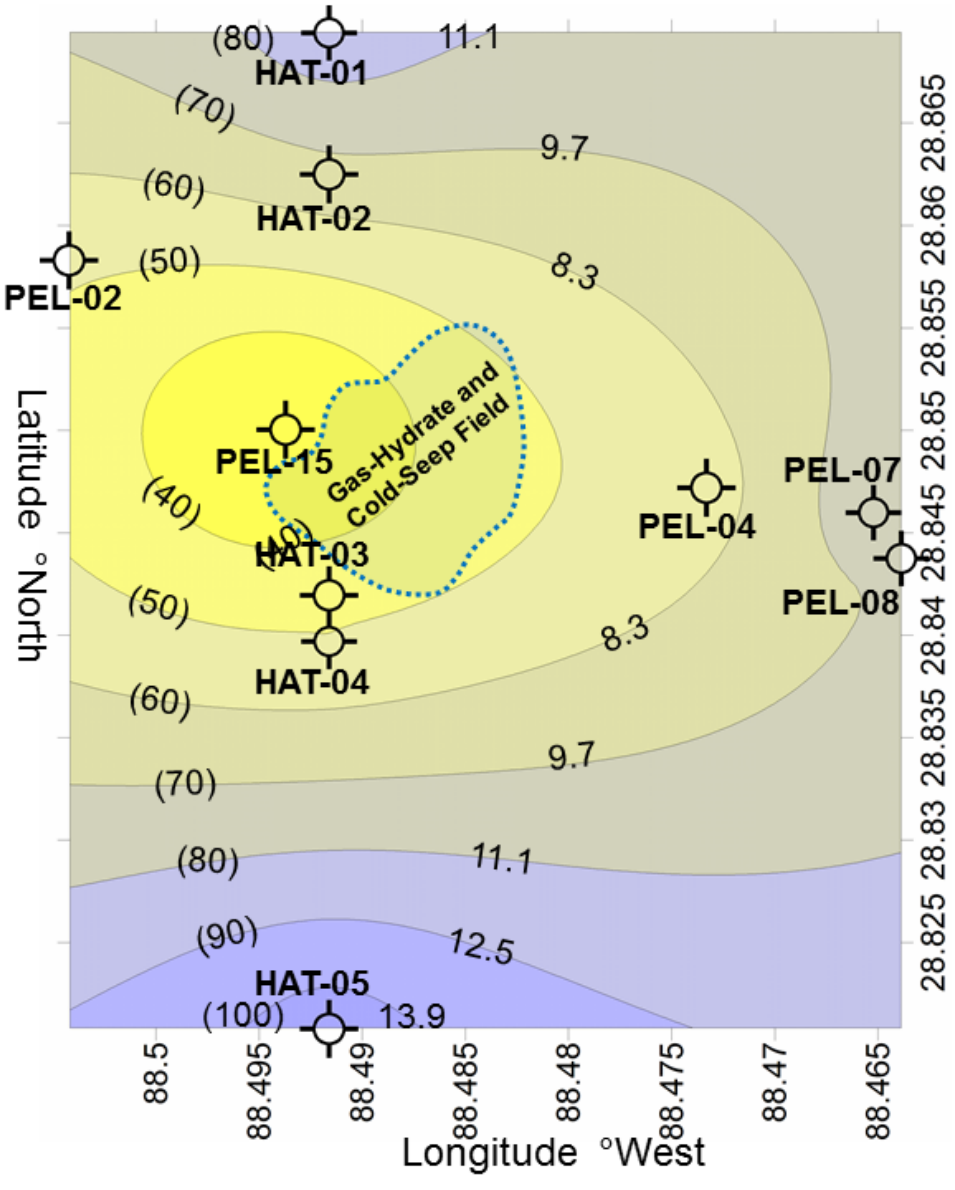

Figure 9. Isopach thickness and sedimentation rate map of the MC118 area from the top to the base of the $CaCO_3$-rich interval of stratigraphic Unit IB, ~9.5 to ~2.3 kilo-yrs BP, identified by the Ca/Ti data, and visually by its light olive gray color. Core locations are identified by open circles. The area of the present-day gas-hydrate and cold-seep field is indicated by the transparent blue shading within the dotted outline. Contour lines are labeled using sedimentation rate (cm/kyr) and thickness (cm) shown in parentheses.

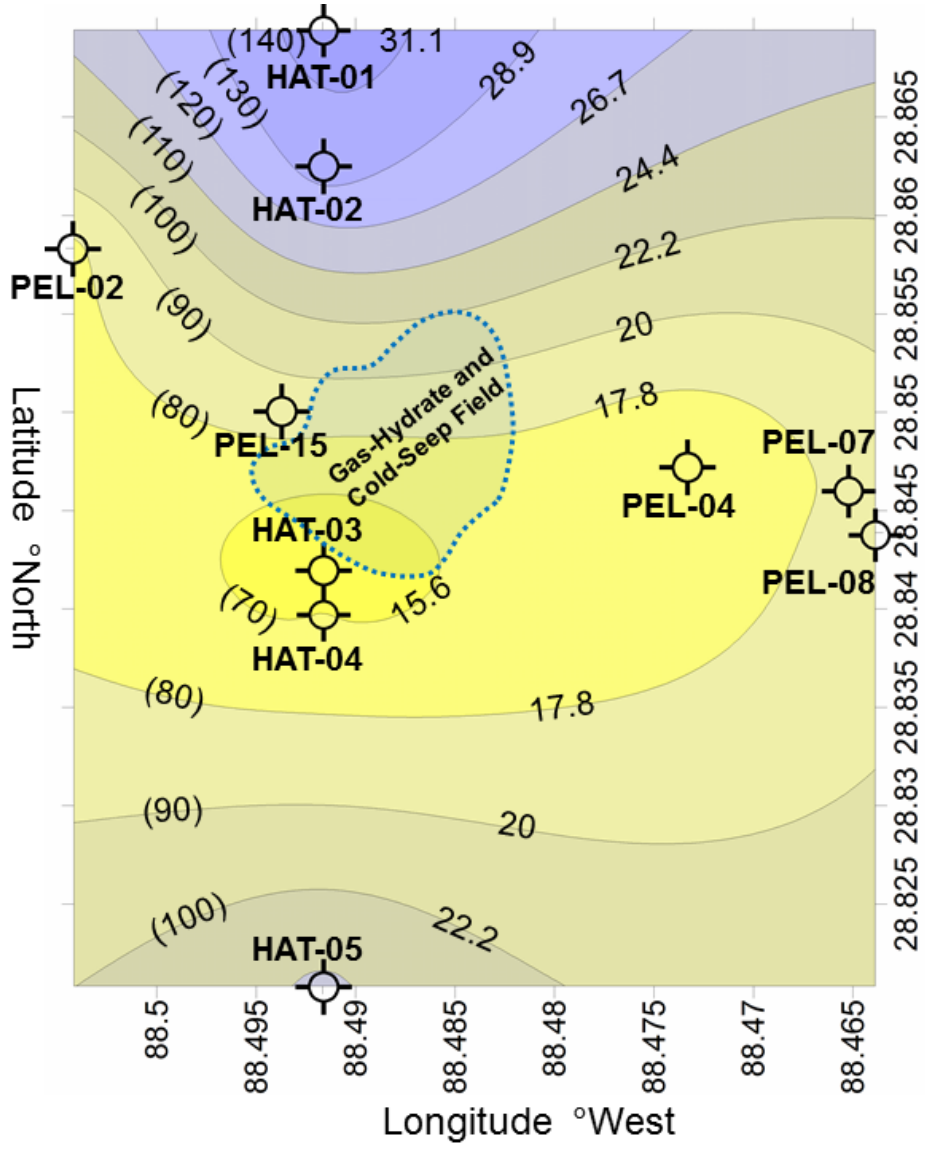

Figure 10. Isopach thickness and sedimentation rate map of the MC118 area for Unit II, from the base of the $CaCO_3$-rich interval of Unit I, ~9.5 kilo-yrs BP, to the red band interval, ~14 kilo-yrs BP, marking the top of Unit III. Core locations are identified by open circles. The area of the present-day gas-hydrate and cold-seep field is indicated by the transparent blue shading within the dotted outline. Contour lines are labeled using sedimentation rate (cm/kyr) and thickness (cm) shown in parentheses.

Chapter 2

Chemostratigraphy of Deep-sea Quaternary Sediments along the Northern Gulf of Mexico Slope: Quantifying the Source and Burial of Sediments and Organic Carbon at Mississippi Canyon 118

Abstract

This study investigates late Pleistocene to Holocene sedimentation, sedimentary geochemistry, and organic-carbon burial near the Mississippi Canyon 118 (MC118) gas-hydrate and cold-seep field - the first National Gas Hydrate Seafloor Observatory - to reconstruct depositional history and provide a paleoenvironmental context for ongoing geochemical and geophysical monitoring. A chemical stratigraphy is established from sediments that were recovered in 10 shallow gravity cores surrounding the MC118 field on the Northern Gulf of Mexico Slope. Geochemical data (from X-ray fluorescence core scanning, CO_2 coulometry, and inductively coupled plasma emission spectrometry) are evaluated within the context of a detailed chronostratigraphy to map geochemical burial fluxes across MC118 during distinct stratigraphic intervals, each of which represents substantial changes in the depositional environment. These measurements are supplemented by Rock Eval pyrolysis data to aid in the evaluation of organic matter source contributions.

The new dataset provides a means to quantitatively assess temporal and spatial changes in geochemistry and deposition surrounding the MC118 field. Results indicate that terrigenous sediment burial flux is the primary control on temporal changes in sediment composition and organic carbon burial, which are linked to sea level change and Mississippi delta lobe switching. Terrigenous proxy burial fluxes (titanium and insoluble residue) and organic carbon accumulation (primarily "type III" organic matter) are elevated during the interval spanning 14 to 9.5 kilo-years BP, compared to more recent deposition at MC118. Conversely, $CaCO_3$ accumulation (due to pelagic biogenic sources) is more consistent through time, although $CaCO_3$ concentration displays pronounced changes due to variable dilution by clay. The gas-hydrate and cold-seep field itself forms a bathymetric high from salt diapirism, which is reflected in spatial patterns recorded in the chemostratigraphy. Analyses of geochemical burial fluxes indicate an increase of all sedimentary components (pelagic and terrigenous, including total organic carbon) with distance from the field. The results suggest a relatively stable spatial pattern of sedimentation with respect to MC118 during the latest Pleistocene and Holocene, but also the dynamic nature of deposition near the salt diapirism-induced bathymetric high that hosts the present day gas-hydrate and cold-seep deposits.

Introduction

The Mississippi Canyon 118 (MC118) gas-hydrate and cold-seep field is situated on the northern Gulf of Mexico slope in approximately 890 m water depth, 150 km south of Gulfport Mississippi (Figure 1). This study investigates the chemistry of late Pleistocene to Holocene deep-sea sediments surrounding the MC118 field, to evaluate controls on organic matter burial, reconstruct depositional history, and provide a paleoenvironmental context for ongoing geochemical and geophysical monitoring (Macelloni et al., 2010; 2012, Lapham et al., 2008, McGee, 2006). This new geochemical dataset is integrated with a recently published chronostratigraphy at MC118 (Ingram et al. 2010) to specifically address the following inter-related research questions: (1) How have terrigenous and pelagic inputs, including organic matter burial, varied during the late Pleistocene and Holocene at MC118?, (2) How have global sea-level changes and regional delta-lobe switching influenced deposition during this time interval?, (3) How has the spatial pattern of deposition surrounding the MC118 field evolved, and (4) What is the influence of the gas-hydrate and cold seep field - including seafloor warping associated with salt diapirism - on temporal and spatial changes in pelagic and terrigenous sedimentation over the studied area?

To address these research questions, a multi-proxy geochemical approach is employed. X-ray fluorescence (XRF) core scanning (Richter et al., 2006) is conducted on a total of 10 shallow gravity cores strategically distributed across the seafloor (Ingram et al., 2010; Figure 1), to generate nearly continuous down-core profiles of Al, Ti, K, Si, Fe

and Ca. XRF core scans (counts) are calibrated to concentration data using Inductively Coupled Plasma Atomic Emission Spectrometry (ICP-AES; wt.% Al, Ti, K, Si, Fe, Ca) and CO_2 Coulometry (wt.% $CaCO_3$; Huffman, 1977). These measurements are supplemented by wt.% total organic carbon (wt.% TOC, via CO_2 coulometry), wt.% insoluble residue (wt.% residue, via CO_2 coulometry) and Rock Eval pyrolysis data for organic matter typing. This new geochemical data set is integrated with the MC118 chronostratigraphy established by Ingram et al., (2010), to evaluate spatial and temporal variability in burial fluxes of key geochemical components. The elemental proxies used herein reflect pelagic and terrigenous contributions ($CaCO_3$, Ti, insoluble residue) as well as organic carbon burial (TOC accumulation). In total, the study comprises 33,849 unique geochemical measurements, providing an extensive documentation of sediment geochemistry, and an important context for ongoing monitoring at the first National Gas Hydrate Seafloor Observatory (as designated by the US Department of Energy; McGee, 2006).

1.1 Geologic Setting: MC118

The MC118 field is the focus of a large multi-disciplinary effort to document physical and biogeochemical processes associated with gas hydrates and marine hydrocarbon systems, jointly funded by NOAA, DOE and MMS (Lutken et al., 2006; Sassen et al., 2006). The field is located on the upper continental slope of the northern Gulf of Mexico, centered at 28.8523^{o}N and 88.4920^{o}W, at approximately 890 m depth along an overall gently sloping seafloor. Locally, the seafloor within the vicinity of the

hydrate and cold seep field is influenced by numerous factors including gas hydrate formation, hydrocarbon (gas and petroleum) seepage and apparent seafloor warping from shallow salt deposits. Visible outcroppings of gas hydrates, faulted carbonate "hard-grounds" and pockmark features consistent with gas and petroleum seepage (Figure 1) cover approximately 1 km^2 of the seafloor (Sassen et al., 2006; Sleeper et al., 2006; Macelloni et al., 2010; 2012). While the seaward slope across the study area typically ranges from 3^o to 4^o, slopes of 10^o to 12^o are present locally across the area of gas-hydrate formation and cold seepage where pockmarks exists (Sleeper et al., 2006).

Regionally, the bathymetry of the Gulf of Mexico continental slope is heavily influenced by the extensive Louann (Jurassic in age) salt formation (Diegel et al., 1995; Galloway et al., 2000; Jackson, 1995). Deformation of salt within the basin has contributed to the present-day hummocky bathymetry of the northern Gulf of Mexico slope (Jackson et al., 1995). At MC118, a salt diapir lies approximately 300 m below the ocean floor and is a probable migration pathway for hydrocarbons sourced by "leaky" oil and gas reservoirs at depth (Macelloni et al., 2012), such diapirs are prolific along the northern Gulf-of-Mexico slope (McBride, 1998).

Ingram et al., (2010) document the lithostratigraphy, biostratigraphy, and chronostratigraphy for MC118 using the same core material as in the present study. Previous analysis identified four distinct stratigraphic intervals: Unit IA, Unit IB, Unit II, and Unit III (Figure 2), which also follow distinct changes in chemostratigraphy (Figure 3). Stratigraphic "Unit IA" is a massive, calcareous nannofossil clay and is Late Holocene (2.3 Ka to present) in age (Figure 2). Unit IA is defined at its top by the shallowest

recovered sediment (core tops), and at its base by the onset of a more $CaCO_3$-rich interval (defining the sub-adjacent "Unit IB"). The higher clay content of Unit IA, while not obvious from visual description, is apparent from published Ca/Ti XRF scans (Ingram et al., 2010; see also Figure 5). Sediments of this unit are relatively thin and extend to 38 cmbsf at its greatest (HAT-02) to less than 5 cm at its shallowest (HAT-03, PEL-04, -15 and -08). At the most "expanded" core sites, Unit IA includes an additional minor and shallower increase in carbonate content, as is visible in Cores HAT-02 and HAT-05 (Figure 5; Figure 4 of Ingram et al., 2010). This minor "peak" occurs at approximately 10-15 cmbsf in the two cores and implies variability in the lithogenic or biogenic inputs in shallow (most recent) Late Holocene sediments.

Stratigraphic "Unit IB" is a more carbonate-rich, massive calcareous nannofossil clay, and is also Holocene (9.5 to 2.3 Ka) in age (Figure 2; Ingram et al., 2010). Sediments are thicker (18 - 83 cm) than the shallower Unit IA and extend down to a maximum depth of 120 cmbsf (Figures 2). This interval is underlain by "Unit II", a mottled nannofossil clay with substantially less carbonate then shallower intervals, which is late Pleistocene to earliest Holocene in age (14 to 9.5 Ka). The base of Unit II is defined by a distinct reddish-brown colored band ("red band") composed of pre-Quaternary nannofossils that have been linked to melt water pulse 1A (Marchitto and Wei, 1995), and thus provides a chronostratigraphic horizon (dated between 14 and 15 kilo-calendar years; Ingram et al., 2010). The depth of the "red band" ranges from 115 cm to 255 cmbsf in Core HAT-03 and -05, respectively

Stratigraphic "Unit III" is a well-laminated, nannofossil clay, and is late Pleistocene (> 14,000 years) in age (Figure 2; Ingram et al., 2010). This unit, similar to Unit II is also carbonate poor relative to Units IA and IB. The unit displays reddish banding that increases in frequency with depth (Figure 2). Unit III has no defined stratigraphic base in the cores, and extends down to the deepest recovered sediments at 711 cmbsf in Core PEL-08. Further details on MC118 lithostratigraphy, biostratigraphy and chronostratigraphy are available in Ingram et al. (2010).

1.2 The Marine Sedimentary Geochemistry Archive

Numerous geochemical proxies are utilized in the present study, and thus a brief review relevant to their application at MC118 is provided here. The elements K, Al, Ti (Figure 3) serve as lithogenic indicators in the hemipelagic deposits at MC118, derived from terrigenous alumino-silicate clays and silts (Kujau et al., 2010; Pattan et al., 2005). Titanium exists in low concentrations (< 1%) in marine sediment, yet it is also relatively chemically unreactive in such settings, providing a particularly robust "conservative" lithogenic indicator. In the Gulf of Mexico, titanium is primarily derived from ilmenite ($FeTiO_3$), closely followed by rutile (TiO_2), minerals associated with sand- and silt-size grains (Appelbaum and Bouma, 1972; Woolsey, 1984). Ingram et al. (2010) established that lithogenic sand-sized grains are not readily apparent in MC118 sediments, thus titanium inputs are likely fine-grained silts. The elements Fe and Si are also potential indicators of lithogenic inputs at MC118, but can be substantially influenced by

authigenic and pelagic biogenic processes in slope settings (Kasten et al., 1998; DeMaster, 1981).

It is generally assumed that the $CaCO_3$ content in deep marine sediments is primarily derived from biogenic skeletal material such as tests of calcareous nannoplankton, foraminifera and pteropods (Bralower and Thierstein, 1984, 1987; Sageman and Lyons, 2004). The use of wt.% $CaCO_3$ as a measure of pelagic biogenic carbonate contribution is most useful at oceanographic sites well above the lysocline, and localities where carbonate dissolution is not substantial. The detailed sedimentologic and biostratigraphic evaluation of MC118 sediments by Ingram et al. (2010) revealed no evidence for authigenic carbonate (or dissolution) in the 10 cores studied here, hence wt.% $CaCO_3$ should be a reliable pelagic biogenic indicator. Finally, the accumulation of organic carbon (TOC) is also associated with multiple sources, and refractory terrestrial organic matter can even dominate along “deltaic” continental margins (Snowdon and Meyers, 1992), which may be the case at MC118 (see Discussion).

Methods

2.1. Core collection and processing

Gravity coring was conducted from the surface ships R/V *Hatteras* in August 2007 and R/V *Pelican* in April 2008. Five sediment gravity cores were recovered by the R/V *Hatteras* in a depositional dip orientation, and five additional cores were collected onboard the R/V *Pelican* along a NW to SE transect (Figure 1). For details of shipboard and land-based core collection and processing methods see Ingram et al. (2010) and Sleeper and Lutken (2008).

2.2 X-ray fluorescence core scanning and calibration

Cores were analyzed using an Avaatech-XRF core scanner (Richter et al., 2006) with an Oxford 50 W X-ray source (rhodium target), and a Canberra X-PIPS detector with a 1500-micrometer silicon crystal. Continuous XRF scanning was conducted at 1-cm resolution and was used to evaluate changes in the bulk geochemical composition of MC118 sediments, with a focus on the elements Ca, Al, Si, K, Ti, and Fe (Figure 3). Analysis of these elements was based on both their reproducibility and their utility as proxies for sedimentary inputs (biogenic vs. lithogenic). The elements Ca, Al, and Si were measured using a 5 kV source voltage, 900 mA, without a filter, using a 90 second measurement time. Heavier elements, K, Ti and Fe were measured using a 10 kV source voltage, 1000 mA, with a cellulose filter, using a 90 second measurement time. To

quantify reproducibility, duplicate scans were performed at 10-cm resolution using the same scanning parameters (Table 1).

Sediment samples from cores were collected to measure wt.% composition of the studies elements to calibrate XRF data (counts) to down-core concentration profiles. Samples were taken at numerous stratigraphic intervals to span the full range of geochemical variability detected using the XRF core scanning. All samples were prepared by extracting 1-cm thick intervals of the un-scanned core half, which were then placed in 100-mL beakers, dried at 50˚ C for 48 hours, and pulverized to a 100 mesh (< 0.064 mm) fraction. Remaining dried and crushed sediments were placed into vials, and subsamples were taken from the homogenized powdered fraction for subsequent geochemical measurements via CO_2 Coulometry and ICP-AES.

2.3 CO_2 Coulometry, ICP-AES, and XRF calibration

Standard coulometry procedures (Huffman, 1977) were used to determine inorganic carbon (CO_3^{2-}), total organic carbon (TOC), and insoluble residue (% residue) concentration. A total of 836 measurements, including duplicates, were performed on 9 cores using the acid digestion and combustion steps of the coulometry technique. Duplicate measurements of percent carbon for acid digestion and combustion measurements yield errors of less than 5% for inorganic carbon and less than 10% for organic carbon (coefficient of variation; Table 1). Percent total organic carbon (TOC) is calculated by subtracting the inorganic portion (CO_3^{2-}) from total carbon content. Weight percent $CaCO_3$ is calculated by multiplying percent inorganic carbon (from acid

digestion) by 8.333, the stoichiometric conversion, assuming all carbonate is present as either calcite or aragonite. Insoluble residue (primarily clay and silt) is determined as the residual percentage after accounting for TOC and $CaCO_3$.

Calibration equations (least-squares linear fits) for conversion of the XRF data (counts) to wt. % $CaCO_3$ are displayed in Figure 4. The ratio of Ca/Ti was found to provide a better predictor of wt. % $CaCO_3$ than Ca counts. This is likely due to correction for minor changes in bulk density, which influence both Ca and Ti XRF measurements. While the calibration results are excellent, some disagreement is expected given that the two analytical methods are measuring somewhat different sample substrates: CO_2 coulometry is conducted on a homogenized powder from a 1-cm thick interval with a volume of approximately 10 cm^3, and the XRF analysis is conducted over a 1-cm^2 area of the split-core surface with detection effective to a depth of <100 microns for light elements.

In addition, sediment samples from two cores, one from each transect (HAT-03 and PEL-04), were selected to calibrate XRF scans using ICP-AES (SGS Laboratory, Toronto). Crushed sediment samples were prepared using the XRF calibration procedure (see Section 2.2) and analyzed for a suite of elements for calibration purposed (Table 2). A summary of the ICP-AES method is as follows, samples are dissolved in acids (HF, HNO_3 and HCL), pumped into a nebulizer to convert the liquid into an aerosol, carried with Ar gas into a plasma chamber, where light from excited elements is detected using a photomultiplier tube. For a detailed explanation of the method (for major and trace elements in rocks and sediments) see Murray et al., (2000). Duplicate measurements

from the MC118 cores yield low errors of 0.7 to 1.8% (coefficient of variation), depending upon the specific element and core investigated (Table 1). A summary of derived calibration equations (least-squares linear fits) are provided for conversion of XRF count data to mass composition (Table 2).

2.4 Rock-Eval Pyrolysis

Ten powdered dried sediment samples were analyzed by Weatherford Geochemistry Laboratory using a Source Rock Analyzer (SRA), to determine the type of organic matter deposited under changing sedimentation regimes. The samples are from core HAT-03, and span all stratigraphic units (IA, IB, II and III). Determination of the pyrolysis combustion peaks is similar to prior generation instrumentation (Claypool and Reed, 1976; Espitalié et al., 1985). In summary, pyrolysis peaks are as follows: (S1) measures free hydrocarbons (volatile bitumen), (S2) hydrocarbons cracked during programed pyrolysis, (S3) oxygen content of the organic matter. Rock pyrolysis using the SRA method may encounter problems with respect to TOC determination when dealing with unstable carbonates (Espitalié et al., 1985); for this reason along with elevated carbonate concentrations in MC118 sediments, CO_2-coulometry TOC values are considered more reliable, and were used in all calculations.

2.5 *Bulk Density Determination and Mass Accumulation Rates*

Sediment dry-bulk density is determined from laboratory measurements of physical properties and is based on 9 samples from Core Pel-15. The procedure follows that used by Dadey et al. (1992), which includes a correction for marine sediments with saline pore fluids. The following calculation is used (Dadey et al., 1992): $M_s = M - M_f = (M_d - s * M) / (1 - s)$, where M = wet mass, M_s = corrected dry mass, M_f = pore-fluid mass, M_d = dry mass uncorrected and s = salinity (0.035). The mass accumulation rate (or "burial flux") for each geochemical proxy of interest is determined by multiplying the dry bulk density (g/cm^3), sedimentation rate (Ingram et al., 2010), and average concentration for each stratigraphic unit (IA, IB and II) at individual core sites. Rates were calculated for proxies diagnostic of biogenic ($CaCO_3$) and terrigenous inputs (Ti, insoluble residue; Figures 7), as well as for organic carbon (Figure 8). Uncertainty of the burial fluxes was estimated by calculation of one standard deviation between maximum and minimum flux values (see error bars in Figure 7). The maximum and minimum flux values were determined by combining variability in concentration of each proxy from duplicates with a chronologic error of 216 (+/-) calendar years, which was the maximum error encountered from AMS C-14 dating (Table 2 in Ingram et al., 2010).

Results

The four stratigraphic intervals (Unit IA, IB, II, III) previously described by Ingram et al. (2010) at MC118 are considered here (see section 1.1). The new data set quantifies pronounced changes in wt. % $CaCO_3$, lithogenic elements, and TOC (Table 1; Figures 3, 5-6). The most obvious feature at all core sites is a substantial reduction in wt.% Fe, K, Al, Si and Ti and organic carbon content during deposition of Unit IB (9.5-2.3 ka), associated with elevated wt.% $CaCO_3$ content (Figures 3, 5-6). In contrast, Unit II (14-9.5 ka) and Unit III (> 14 ka) are the most enriched in lithogenic elements and organic carbon. Based on this compositional data, the depositional history at MC118 can be characterized as one progressing from more organic-carbon and clay-rich during the latest Pleistocene, to more carbonate-rich and organic carbon-poor during the early-mid Holocene (9.5 – 2.3 ka). A reversal of this trend is observed in latest Holocene sediments of Unit IA (2.3 ka – present). This reversal is most apparent at core sites farthest from the MC118 field (HAT-01, -02 and -05; Figures 1, 5), which also display a transient increase ("pulse") in wt.% $CaCO_3$ at some sites (HAT-02 and -05; Figure 5). A summary of the geochemical results are presented in Table 1, and these data are also used in burial flux calculations of select geochemical proxies (Figure 7). Mass accumulation rates (burial fluxes) are estimated using the chronostratigraphy of Ingram et al. (2010), concentrations of geochemical proxies ($CaCO_3$, TOC, Ti and Residual Clay; Table 1), and average bulk density measurements for each unit (1.716 g/cm^3 for Unit I) and (1.828 g/cm^3 for Unit II).

3.5 Geochemical Mass Accumulation Rates

The mass accumulation rate of bulk sediment is characterized by a general increase with distance from the gas-hydrate and cold-seep field (Figure 7A). However, core sites above the field often display elevated rates for a given distance, as compared to sites below the field (Figure 7A), a feature that is especially obvious for Unit II and Unit IB. At all sites, the mass accumulation rate of bulk sediment during Unit II (14-9.5 ka) is markedly higher than Unit IA (2.3 ka-present) and Unit IB (9.5-2.3 ka). These general spatial and temporal patterns of sediment accumulation are also observed in the burial flux of organic carbon (Figure 7C), titanium (Figure 7B), and insoluble residue (Figure 7B). In contrast, the temporal changes in mass accumulation rate of $CaCO_3$ (Figure 7D) are often less pronounced, although spatial trends show some similarity. To further illustrate these differences, note that $CaCO_3$ accumulation rates vary from 4 to 50 g m^{-2} yr^{-1} across the seafloor in Unit IA (Figure 7D), an increase by a factor of 12. However, $CaCO_3$ burial fluxes at any given core site demonstrate much less temporal variability (some sites yield almost no change such as HAT-01, -02 and -05; Figure 7D). This contrasts with TOC burial fluxes, which exhibit much greater temporal variability (0.36 - 3.0 g m^{-2} yr^{-1} for HAT-03), as opposed to the spatial variability (0.32 - 1.8 g m^{-2} yr^{-1} within Unit IB), and this trend is also quite consistent across MC118 (Figure 7C). Hence, the most important observation for $CaCO_3$ mass accumulation is that, despite substantial changes in sedimentation rate through the Late Pleistocene to the Holocene (Ingram et al., 2010), its burial flux is more stable, as compared to TOC burial flux which changes dramatically (Figures 5-7).

The mass accumulation of lithogenic components (Ti and insoluble residue) exhibits similar spatial patterns and temporal changes as TOC burial flux (Figures 7C). In other words, lithogenic components display dramatically increased burial during deposition of Unit II at all sites, and a pattern of generally higher burial fluxes at sites farther from the gas-hydrate and cold-seep field (Figures 7C). Hence, while spatial heterogeneity is, at times, considerable at MC118, the temporal variability is even larger for lithogenic elements and replicated at every core site across the Pleistocene-Holocene transition (Figure 7).

3.6 Rock-Eval Pyrolysis

Sediments spanning the late Pleistocene and Holocene at MC118 demonstrate markedly different *Tmax* and hydrogen index values. Samples from the Holocene (20-40 cmbsf) are mixed type II/III, while those from the late Pleistocene (70-250 cmbsf) yield a type-III signature (Figure 8). All samples are immature with low *Tmax* values, which is not unexpected for such shallow-buried sediments. These analyses suggest that organic matter within Unit II (14-9.5 ka) is predominantly terrigenous in origin, a result consistent with enhanced accumulation of lithogenic elements as observed at MC118 (Figure 7C).

Discussion

5.1 Pelagic versus Terrigenous sedimentation

The most important observation with respect to pelagic (marine biogenic) sedimentation at MC118 is the mass accumulation of $CaCO_3$ remains relatively stable through time (Figures 7, 8) despite dramatic changes in down-core concentration of wt.% $CaCO_3$ (Figures 5-6). For example, elevated $CaCO_3$ concentrations are a distinctive feature of Unit IB sediments (Figures 5-6), yet this increase is not reflected in the $CaCO_3$ burial flux across this same interval (Figure 7). In fact, the highest $CaCO_3$ accumulation rates almost uniformly occur in the more carbonate-poor Unit II interval (Figure 7). Interestingly, the site with the most consistent rate of $CaCO_3$ accumulation across Units IA to II (49.7 to 51.8 g m^{-2} yr^{-1}, Core HAT-01) is located furthest upslope from the MC118 field (Figure 1, 6-7). Despite the consistency of $CaCO_3$ accumulation here (Core HAT-01), there is still substantial changes in wt. % $CaCO_3$ across this same interval (11.1 to 25.6 wt. %; Figure 5). It is reasonable to assume that this coring site is one of the least likely to be influenced by the field (or salt diapirism), due to its distal and upslope position from the seep site (Figure 1). Thus, geochemical burial fluxes at this location most likely represent "background" sedimentation, undisturbed by process associated with the MC118 field or salt diapir (Ingram et al., 2010; Figure 1).

The terrigenous lithogenic signal is documented at the MC118 site by titanium and insoluble residue accumulation (largely clay and silt). Results indicate rapid deposition of lithogenic material in Unit II (14-9.5 ka), followed by much slower

accumulation rates during the later Holocene intervals (Unit IA and IB) (Figure 7C). The reduction in accumulation of the lithogenic fraction is most likely tied to a retreating shoreline and diminished terrestrial influence at the site. This interpretation has been invoked to explain a similar trend at DeSoto Canyon (Winn et al., 1995), ~100 km to the east MC118. In both locations along the eastern Gulf of Mexico Margin, glacial low-stands exposed parts of the shelf (Törnqvist et al., 2006), thereby increasing proximity to the shoreline and enhancing terrigenous sedimentation.

In summary, $CaCO_3$ burial flux (pelagic component of sedimentation) from the Late Pleistocene (14 - 9.5 Ka) to Holocene (9.5 – 2.3 Ka), was relatively stable despite considerable changes in depositional environment at MC118 associated with post-glacial sea-level rise (Figures 5-6). Thus, elevated $CaCO_3$-content in shallow (Unit IB) sediments is due to a reduction in the dilution effect from lithogenic inputs, and not from substantial change in primary productivity. These results imply that primary production in the water column has remained relatively consistent in the northern Gulf of Mexico from the late Pleistocene to the Present, with perhaps slightly elevated carbonate production during the latest Pleistocene (Figure 7D). In contrast, changes in lithogenic inputs appear to be the controlling factor on chemical composition of sediments. It is reasonable to conclude that post-glacial sea-level rise and Mississippi Delta lobe shifting drove bulk chemical composition of sediments at MC118 by modulating terrigenous sedimentation (lithogenic inputs). The supply of lithogenous sediments to MC118 are clays and silts eroded from the Mississippi drainage basin or delta, which are then discharged into the Northern Gulf of Mexico. It has been shown that the suspended sediment load (siliciclastic material) from the Mississippi River is

initially deposited within 30 km offshore from the delta, then dispersed over a much larger area by wind and wave energy (Corbett et al., 2004; Gordon and Goni, 2004). Silt and sands are potentially remobilized (including turbidity flows) farther down the Gulf-of-Mexico Slope where they may accumulate in seafloor depressions and at MC118 (Prather et al., 1998; Winkler, 1996).

5.3 Organic Matter Type and Burial

The spatial and temporal patterns of organic matter burial at the study site are clearly influenced in a way similar to overall sedimentation (Ingram et al., 2010), and more specifically the lithogenic components (Figures 3, 7D). The MC118 record exhibits TOC concentrations that are substantially lower in early-late Holocene Units IA (2.3 ka-present) and IB (9.5-2.3 ka) as compared to late Pleistocene Unit II (14-9.5 ka). The burial flux displays a similar trend of reduced accumulation in Units IA and IB (Figures 5-6, 7C). These temporal changes in the accumulation of TOC are not correlative to that of $CaCO_3$ burial flux changes - and inferred productivity - but rather follow lithogenic burial flux changes. This dataset is consistent with the hypothesis that organic matter deposited at MC118 is predominantly terrestrial in origin, or, at the very least, its burial is somehow influenced by greater terrigenous sedimentation linked to sea-level change and delta lobe switching (see below).

It has been suggested that the degree of organic matter oxidation and its preservation into the geologic record is proportional to the time spent within oxygenated sediments and associated aerobic decomposition (Hartnett et al., 1998).

Then, it is also possible that the observed increase in accumulation of organic matter in Unit II (Figure 7) is driven by rapid sedimentation, followed by slower accumulation in the later Holocene intervals (Ingram et al., 2010). This slower sedimentation during Units IA and IB may have provided sufficient time for organic matter to undergo greater aerobic decomposition, yielding lower present-day TOC concentration and a reduced burial flux (Figures 5, 6, 7B). However, changes in sedimentation rate alone are unlikely to account for the enhanced organic carbon burial flux at MC118. For instance, a 10-fold increase in sedimentation (open-marine setting) equates to a 2-fold increase in TOC (Müller and Seuss, 1979), yet MC118 displays a 2-fold increase in TOC (Figure 5-6) and only a 2 to 3-fold increase in sedimentation (Ingram et al., 2010). Hence, this effect is much more pronounced at MC118, or alternatively, some other mechanism is at work, such as a change in the composition of the organic matter.

To evaluate changes in the proportion of labile versus refractory organic matter though time, Rock Eval Pyrolysis results are presented using a Hydrogen Index (HI)-T_{max} cross-plot to determine kerogen type (Figure 8). Kerogen is operationally defined as insoluble in organic solvents (Durand, 1980; Tissot and Welte, 1984), comprising a partially-converted, complex mixture of sedimentary organic matter, such as geopolymers (organic geomacromolecules) that have been subjected to early diagenesis (Schulz, 2000). However, in very shallow sediments such as cores from MC118, this process is generally not complete. In these settings organic matter is only partially converted to kerogen, and the term “proto-kerogen” seems appropriate (Hollander et al., 1993). Holocene sediments spanning the seafloor to 55 cmbsf in Core HAT-03 plot in the mixed type II/III field, well above those from Unit II (below 55 cmbsf), which are

found in the type III field on the cross-plot (Figure 10). Thus, while allochtonous (terrigenous) organic matter is likely present throughout, the older Unit II sediments contain far more Type III organics (Figure 8), and at the same time greater lithogenic inputs (Figure 3, Figure 7C). It seems likely that the type III signal is derived from terrestrial biogenic material eroded from the continent within the Mississippi River drainage basin.

It is also possible that organic matter at greater depth yields a lower hydrogen index due to selective biodegradation. In this scenario, hydrogen-rich (labile), organic matter is preferentially diminished with prolonged exposure to microbial decomposition, for instance Type I and II "proto-kerogens" can change their geochemical signal by moving down alteration pathways towards lower H/C and O/C ratios (Hollander et al., 1993). Thus, without changing the initial portion of marine to terrigenous organic matter reaching the seafloor, it may be possible to preserve more "refractory" organic matter and change the geochemical signal by this process. Additionally, it is also possible that the MC118 seep field itself is a potential source of bitumen (not kerogen) contributing to the surrounding MC118 sediments, thereby altering the geochemical signal, yet this is not apparent from pyrolysis data (lack of S1 peak). It also seems likely that tar deposits and/or authigenic carbonates would have been observed, yet there is no evidence for either based on sedimentological analysis of the cores (Ingram et al., 2010). If the Rock Eval results are interpreted as a degradation signal, this would suggest that Unit II sediments experienced greater degradation than Unit IA and IB, despite higher sedimentation rates. This observation is inconsistent with

oxygen exposure time serving as the primary control on temporal changes in organic matter accumulation at MC118.

In conclusion, rock pyrolysis results are consistent with inorganic geochemistry (titanium and insoluble residue accumulation). Together, these results suggest terrigenous-dominated sedimentation characterizes the late Pleistocene of Unit II (14 - 9.5 Ka), then transitioning to enhanced pelagic sedimentation during the early-mid Holocene (9.5 - 2.3 Ka). This is not surprising given the location of study area on the northern Gulf of Mexico slope, offshore from a major delta that was in closer proximity to MC118 during deposition of Unit II (a time of lower sea level). However, we cannot rule out the possibility that Unit II contains a higher proportion of degraded Type II organic matter, thereby resulting in lower hydrogen indices through organic matter alteration (Hollander et al., 1990).

Conclusions

This study reveals several key conclusions specific to the late Pleistocene to Holocene depositional history at MC118. The most important observation is that the flux of lithogenic inputs and organic carbon decreases with time (from the late Pleistocene to late-Holocene), and burial rates for all components generally increases with greater distance from the gas hydrate and cold-seep field at each core site. Sediments shift from clay-rich during the late Pleistocene-earliest Holocene (14 to 9.5 Ka) to $CaCO_3$-rich during a period approximating the Holocene (9.5 Ka to present). This change is connected to post-glacial sea-level rise and proximity to the Mississippi delta, which are important controls on the delivery of terrigenous sediments to MC118. The mass accumulation rates of lithogenic proxies and Rock Eval data are consistent with an enhanced delivery of terrigenous organic matter during the late Pleistocene-earliest Holocene (14 to 9.5 Ka), a time of greater proximity of MC118 to terrigenous sources. In contrast, carbonate accumulation rates, and inferred carbonate productivity at MC118, show less pronounced temporal variability. Taken together, the new results suggest a complex depositional history at MC118, yet relatively stable spatial patterns of deposition around the nearby field, which reflect the salt diapir-induced bathymetric high that hosts present-day gas hydrates and cold seeps.

References

Appelbaum, B.S., Bouma, A.H., 1972. Geology of the upper continental slope in the Alaminos Canyon region. Gulf Cost Association of Geological Societies Transactions v. 22, p. 157–164.Bralower, T.J. and Thierstein, H.R., 1984. Low productivity and slow deep water circulation in mid-Cretaceous oceans. *Geology*, v. 12, p. 614-618.

Bralower, T.J. and Thierstein, H.R., 1987. Organic carbon and metal accumulation rates in Holocene and mid-Cretaceous sediments: paleoceanographic significance. *in* Marine Petroleum Source Rocks (eds. J. Brooks and A.J Fleet), *Geological Society of London Special Publication*, v. 26. p. 345-369.

Claypool, G.E., and Reed, P.R., 1976. Thermal analysis technique for source rock evaluation: quantitative estimate of organic richness and effects of lithologic variation, *AAPG Bulletin*, v.60, pp. 608-626.

Corbett, R.D., McKee, B., Duncan, D., 2004. An evaluation of mobile mud dynamics in the Mississippi River deltaic region. *Marine Geology*, v. 209, p. 91-112.

DeMaster, D.J., 1981. The supply and accumulation of silica in the marine environment, *Geochimica et Cosmochimica Acta*, v. 45, pp. 1715-1732.

Dadey, K.A., Janecek, T., Klaus, A., 1992. Dry-Bulk Density: Its use and determination. Proceedings of the Ocean Drilling Program, *Scientific Results*, v. 126, p. 551-554.

Diegel, F.A., Karlo, J.F., Schuster, D.C., Shoup, R.C., Tauvers, P.R., 1995. Cenozoic structural evolution and tectono-stratigraphic framework of the northern Gulf Coast continental margin, in: Jackson, M.P.A., Roberts, D.G., Snelson, S., (eds.), Salt Tectonics: *A Global Perspective: American Association of Petroleum Geologist Memoir* v. 65, p. 109-151.

Durand, B., 1980. Kerogen. Insoluble organic matter from the sedimentary rocks? Editions Technip., Paris, 519 pp.

Espitalié, J., Deroo, G. and Marquis, F. 1985. La pyrolyse Rock-Eval et ses applications. Rev. Inst. Fr. Pét., v. 40, pp. 755-784.

Galloway, W.E., Ganey-Curry, P.E., Li, X., Buffler, R.T., 2000. Cenozoic depositional history of the Gulf of Mexico basin. *American Association of Petroleum Geologist Bulletin* v. 84, no. 11, p. 1743-1774.

Gordon, E.S., Goni, M.A., 2004. Controls on the distribution and accumulation of terrigenous organic matter in sediments from the Mississippi and Atchafalaya river margin. *Marine Chemistry*, v. 92, p. 331-352.

Hartnett, H. E., Keil, R.G., Hedges, J.I., Devol, A.H., 1998. Influence of oxygen exposure time on organic carbon preservation in continental margin sediments, *Nature*, v. 391, p. 572– 574.

Hollander, D.J., McKenzie, J.A., Hsu, K.J., Huc, A.Y. 1993. Application of a eutrophic lake model to the origin of ancient organic-carbon-rich sediments. *Global Biogeochemical Cycles*, v. 7, p. 157-179.

Huffman, E.W.D., Jr., 1977. Performance of a new carbon dioxide coulometer. *Microchemistry Journal* v. 22, p. 567-573.

Jackson, M.P.A., 1995. Retrospective Salt Tectonics, in: M.P.A. Jackson, D.G. Roberts, S. Snelson, (eds.), Salt Tectonics: a global perspective. *AAPG Memoir* v. 65, p. 1-28.

Ingram, W.C., Meyers, S.R., Brunner, C.B., Martens, C.S., 2010. Late Pleistocene-Holocene sedimentation surrounding an active seafloor gas-hydrate and cold-seep field on the Northern Gulf of Mexico Slope, *Marine Geology*, v. 278, p. 43-53.

Kasten, S., Freudenthal, T., Gingele, F.X., Schulz, H.D., 1998. Simultaneous formation of iron-rich layers at different redox boundaries in sediments of the Amazon deep-sea fan. *Geochimica et Cosmochimica Acta*, v. 62, no. 13, p. 2253–2264.

Kujau, A., D. Nurnberg, C. Zielhofer, A. Bahr, Rohl, U., 2010. Mississippi River discharge over the last ¡-560,000 years.Indications from X.ray fluorescence core.scanning, *Palaeogeography, Palaeoclimatology, Palaeoecology*, v. 298, 311.318, doi:10.1016/j.palaeo.2010.10.005.

Lapham, L.L., Chanton, J.P., Martens, C.S., Higley, H., Jannasch, H.W., and Woolsey, J.R., 2008. Measuring long term changes in dissolved ion and gas concentrations and stable isotopes at a hydrate site: Mississippi Canyon 118, Gulf of Mexico. *Environmental Science and Technology*, v. 42, p. 7368-7373.

Lutken, C.B., Brunner, C.A., Lapham, L.L, Chanton, J.P., Rogers, R., Sassen, R., Dearman, J., Lynch, L., Kuykendall, J., Lowrie, A., 2006. Analyses of core samples from Mississippi Canyon 118, paper OTC 18208. Presented at the Offshore Technology Conference, American Association of Petroleum Geologist, Houston, TX

Macelloni, L., Caruso, S., Lapham, L., Lutken, C., Brunner, C., Lowrie, A., 2010. Spatial distribution of seafloor bio-geological and geochemical processes as proxy to evaluate fluid-flux regime and time evolution of a complex carbonate/hydrates mound, northern Gulf of Mexico. *Gulf Coast Association of Geological Societies Transactions* v. 60, p. 461-480.

Macelloni, L., Simonetti, A., Knapp, J.H., Knap, C.C., Lutken, C.B. and Lapham, L.L., 2012. Multiple resolution seismic imaging of a shallow hydrocarbon plumbing system, Woolsey Mound, Northern Gulf of Mexico. *Marine and Petroleum Geology*, v. 38, p. 128-142.

Marchitto, T.M., Wei, K-Y., 1995. History of the Laurentide meltwater flow to the Gulf of Mexico during the last deglaciation, as revealed by reworked calcareous nannofossils. *Geology*, v. 23, p. 779-782.

McBride, B.C., 1998. The evolution of allochthonous salt along a megaregional profile across the northern Gulf of Mexico, *AAPG Bulletin*, v. 82, p. 1037-1054.

McGee, T., 2006. A seafloor observatory to monitor gas hydrates in the Gulf of Mexico. *The Leading Edge* v. 25, no. 5, p. 644–647.

Müller, P.J and Seuss, E., 1979. Productivity, sedimentation rate, and sedimentary organic matter in the oceans – Organic carbon preservation. *Deep-Sea Research*, v. 26, p. 1347-1362.

Murray, R.W., Miller, D.J., and Kryc, K.A., 2000. Analysis of major and trace elements in rocks, sediments, and interstitial waters by inductively coupled plasma-atomic emission spectrometry (ICP-AES). *ODP Technical Note, 29,* [Online] Available from World Wide Web: http://www-opd.tamu.edu/publications/tnotes/tn29/INDEX.HTM [Cited 2002-07-23]

Pattan, J.N., Masuzawa, T., Borole1, D.D., Parthiban, G., Jauhari, P., Yamamoto, M., 2005. Biological productivity, terrigenous influence and noncrustal elements supply to the Central Indian Ocean Basin: Paleoceanography during the past » 1 Ma. *Journal of Earth System Science,* v. 114, no. 1, February 2005, p. 63-74.

Prather, B.E., Booth, J.R., Steffens, G.S., Craig, P.A., 1998. Classification, lithologic calibration, and stratigraphic succession of seismic facies of intra-slope basins, deep-water Gulf of Mexico: *American Association of Petroleum Geologists Bulletin*, v. 82, p. 701-728.

Richter et al., 2006. The Avaatech Core Scanner: Technical description and applications to NE Atlantic sediments. *In*: Rothwell, R.G. (eds.), New ways of looking at sediment core and core data. *Geological Society Special Publication*, London, pp. 39-50.

Sageman, B.B., Lyons, T.W., 2004. Geochemistry of Fine-grained Sediments and Sedimentary Rocks, in: MacKenzie, F., (eds.) Sediments, Diagenesis, and Sedimentary Rocks, Treatise on Geochemistry v. 7, pp. 115-158.

Sassen, R., Roberts, H.H., Jung, W., Lutken, C.B., DeFreitas, D.A., Sweet, S.T., Guinasso Jr., N.L., 2006. The Mississippi Canyon 118 Gas Hydrate Site: A complex natural system. paper OTC 18132 presented at the Offshore Technology Conference, Houston, TX.

Schulz, H. D., and Matthias, Z. (eds.) 2000. Marine Geochemistry, Springer-Verlag, v. 1, 455 p. DM149. ISBN 3-540-66453-X.

Sleeper, K.A., Lowrie, A., Bosman, A., Macelloni, L., Swann, C.T., 2006. Bathymetric mapping and high resolution seismic profiling by AUV in MC 118 (Gulf of Mexico). paper OTC 18133 presented at Offshore Technology Conference, Houston, TX

Sleeper, K.A. Lutken, C., 2008. Activities Report for Cruise GOM1-08-MC118 aboard the R/V Pelican Sampling and Deployment Cruise Mississippi Canyon Federal Lease Block 118 Northern Gulf of Mexico April 22-28, 2008. Supported by, Center for Marine Resources and Environmental Technology and Seabed Technology Research Center University of Mississippi.

Snowdon, L.R., Meyers, P.A., 1992. Source and maturity of organic matter in sediments and rocks from Sites 759, 760, 761 and 764 (Wombat Plateau) and Sites 762 and 763 (Exmouth Plateau). *Proceedings of the Ocean Drilling Program, Scientific Results*, (eds.,) von Rad, U., Haq, B.U., et al., v. 122 pp. 309-315.

Tissot, B.P. and Welte, D.H., 1984. Petroleum formations and occurrences: Springer and Verlag, Berlin, 2nd edition, 699 pp.

Törnqvist, T.E., Wortman, S.R., Mateo, Z.R.P., Milne, G.A., and Swenson, J.B., 2006. Did the last sea level lowstand always lead to cross-shelf valley formation and source-to-sink sediment flux? *Journal of Geophysical Research*, v. 111, p. 1-13, F04002.

Winn Jr., R.D., Roberts, H.H., Kohl, B., Fillon, R.H., Bouma, A.H., Constans, R.E., 1995. Latest Quaternary deposition on the outer shelf, northern Gulf of Mexico: facies and sequence stratigraphy from the Main Pass Block 303 shallow core. *Geological Society of America Bulletin*, v. 107, p. 851-866.

Winkler, C.D., 1996. High Resolution Seismic Stratigraphy of a late Pleistocene submarine fan pounded by salt-withdrawal mini-basins of the Gulf of Mexico continental slope: Offshore technology Conference Proceedings, OTC 8024, pp. 619-628.

Woolsey, J.R., 1984. Exploration for industrial minerals in Mississippi Sound and adjacent offshore territories of Mississippi and Alabama. Mississippi–Alabama Sea Grant Consortium, Project No. R/ER-11, Grant No. NA81AA-D-00050. 22 pp.

(A) Average Coefficient of Variation

Proxy	XRF CV	ICP-AES CV	CO_2-C CV	Samples (N)
Al	0.038	0.012	NA	52 | 6
Ti	0.049	0.018	NA	52 | 6
K	0.037	0.012	NA	52 | 6
Fe	0.020	0.007	NA	52 | 6
Ca	0.024	0.009	NA	52 | 6
TOC	NA	NA	0.087	20
$CaCO_3$	NA	NA	0.037	20

(B) Average Concentrations by interval

Core	Proxy	Unit IA	Unit IB	Unit II	Units I&II
HAT-03	wt.% $CaCO_3$	19.21	26.58	12.56	18.94
" "	wt.% TOC	0.36	0.26	1.19	0.73
" "	wt.% Ti	0.21	0.20	0.24	0.22
" "	wt.% R. Clay	80.41	73.15	86.24	80.31
PEL-04	wt.% $CaCO_3$	12.79	25.39	11.06	14.67
" "	wt.% TOC	0.95	0.81	1.37	1.10
" "	wt.% Ti	0.24	0.22	0.25	0.25
" "	wt.% R. Clay	86.25	73.79	87.55	84.22

(C) Range of values each proxy by interval

Core	Proxy	Unit IA	Unit IB	Unit II	Units I&II
HAT-03	wt.% $CaCO_3$	NA	38.75 - 13.24	15.37 - 12.11	38.75 - 13.11
" "	wt.% TOC	NA	0.23 - 0.36	1.95 - 0.38	0.23 - 1.95
" "	wt.% Ti	0.22 - 0.20	0.26 - 0.16	0.26 - 0.22	0.26 - 0.16
" "	wt.% R. Clay	NA	86.45 - 60.93	85.30 - 83.32	86.45 - 60.93
PEL-04	wt.% $CaCO_3$	16.08	35.05 - 18.88	18.37 - 9.05	35.05 - 9.05
" "	wt.% TOC	0.95	1.04 - 0.50	1.79 - 1.38	1.79 - 0.5
" "	wt.% Ti	0.25 - 0.23	0.24 - 0.20	0.29 - 0.24	0.29 - 0.20
" "	wt.% R. Clay	82.95	80.27 - 64.26	89.41 - 80.20	89.41 - 64.26

Table 1. (A) Average coefficient of variation (CV) for each geochemical proxy considered in this study (Cores HAT-03 and PEL-04) based on duplicate analyses from each method, (1) X-ray fluorescence (XRF), (2) Inductively Coupled Plasma Atomic Emission Spectrometry (ICP-AES) and (3) CO_2 coulometry (CO_2). For samples (N), values on left are duplicates from XRF and CO_2 coulometry on right. (B) Average concentration values (wt.%) are determined for each proxy and used to determine mass accumulation rates (see Figure 7) across each respective stratigraphic time interval, Unit IA, IB, II, and for the combine 14-ka record (Units I&II). (C) The range of values from CO_2 coulometry data for wt.% $CaCO_3$, TOC and R. Clay, along with wt.% Ti from calibrated XRF is provided here and at times in the text.

XRF-ICP Elemental Calibration Data

Core	Proxy	Calibration Eqn.	R^2 Value	Samples (N)
HAT-03	Al	$y = 5*10^{-4}(x) + 3.3396$	0.7319	15
" "	Ti	$y = 6*10^{-6}(x) + 0.0847$	0.9222	15
" "	K	$y = 2*10^{-5}(x) + 0.435$	0.7643	14
" "	Fe	$y = 6*10^{-6}(x) + 0.589$	0.8941	16
" "	Ca	$y = 2*10^{-4}(x) - 1.4069$	0.9154	14
PEL-04	Al	$y = 7*10^{-4}(x) + 3.8955$	0.6754	30
" "	Ti	$y = 4*10^{-6}(x) + 0.1584$	0.8302	32
" "	K	$y = 8*10^{-5}(x) + 0.7941$	0.7449	30
" "	Fe	$y = 6*10^{-6}(x) + 1.0749$	0.8112	30
" "	Ca	$y = 3*10^{-5}(x) - 1.7188$	0.9232	32

ICP-CO_2 Coulometry Calibration Data

HAT-03	$CaCO_3$	$y = 0.932(x) + 1.6417$	0.9926	12
PEL-04	$CaCO_3$	$y = 0.884(x) + 1.9768$	0.9871	17

Table 2. Calibration equations (least-squares linear fits) for each element, where down-core concentrations were determined for Cores HAT-03 and PEL-04, these equations were used to convert XRF counts into weight percent composition (wt. %). The correlation coefficients and number of samples are also shown. See figure 3 for graphical representation of ICP data plotted with the calibrated XRF core scans, and figure 4 for the wt.% $CaCO_3$ calibrations.

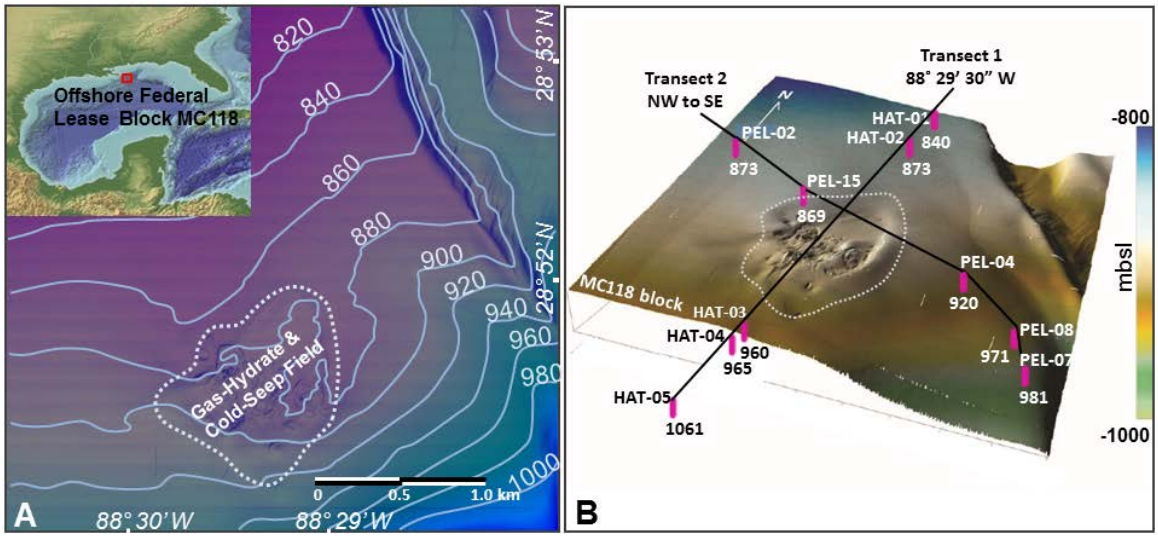

Figure 1. *Panel A*: Bathymetric map of the study area (Block MC118) with labeled contours (light blue) in meters water depth (base map courtesy of Ken Sleeper) with inset digital elevation and bathymetry map (top left; NOAA geophysical data center image) of the Gulf of Mexico Region. Bathymetry provided by the Gulf of Mexico Hydrate Research Consortium, (modified after Sleeper et al., 2006). The location of MC118 offshore federal lease block is indicated by the red box in the inset map. The extent of the studied gas hydrate-cold seep field is outlined by the dashed line and is characterized by an area with gas vents, seafloor pockmark features, petroleum seepage, shallow faults, carbonate hard-grounds and gas hydrate deposits. *Panel B*: Bathymetric map of the study site with the location of cores collected during cruises on the R/V *Hatteras* and R/V *Pelican*; base map image is courtesy of the Gulf of Mexico Hydrate Research Consortium. Cores are indicated as vertical magenta lines, with core identification (above) and water depth (in meters) below the core symbol. The edge of the gas hydrate-cold seep field is outlined by a thin dashed white line, black lines connecting cores indicate transects taken by the R/V *Hatteras* ("Hatteras Transect") and R/V *Pelican* ("Pelican Transect"). The color bar on the far right indicates water depth.

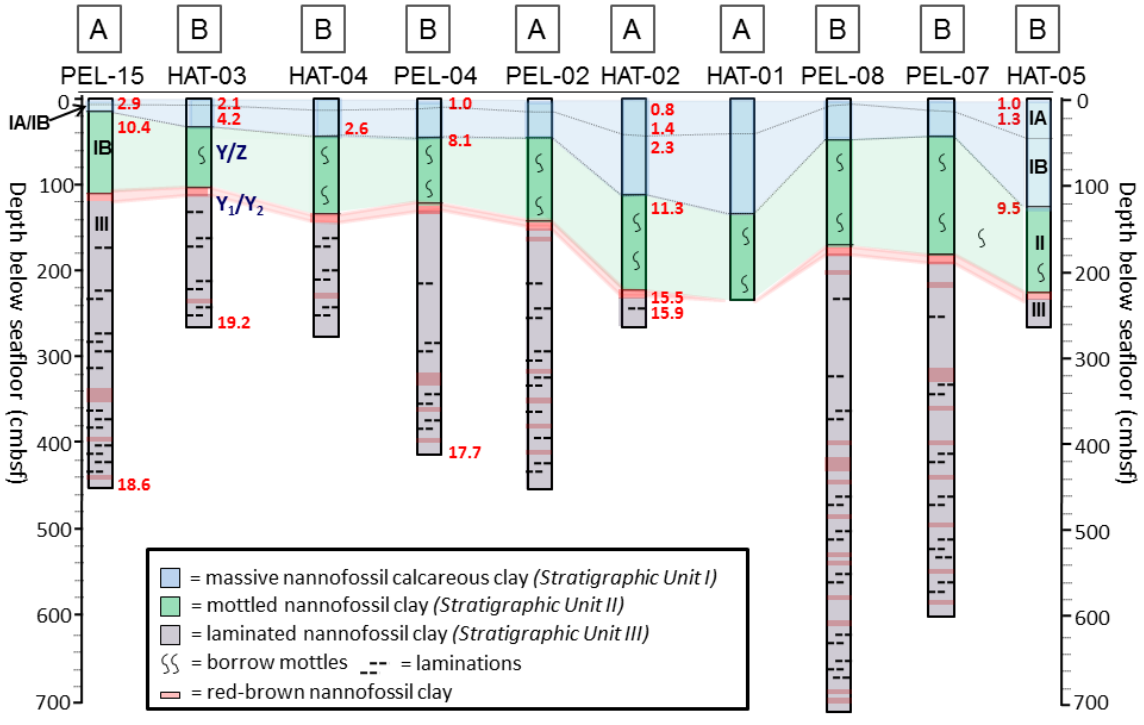

Figure 2. Stratigraphic correlation of marine sediments collected across the MC118 study area. Cores are arranged by increasing distance (left to right) from the gas hydrate-cold seep field. The "A" and "B" designation at the top of each core indicate whether the site is located above or below (respectively) the hydrate/cold-seep field. Dates obtained via AMS radiocarbon analysis of planktonic foraminifera (red, Ka) and foraminiferal biostratigraphic boundaries (dark blue, Y/Z ~ 10 Ka and Y_1/Y_2 ~ 15 Ka) are shown alongside their stratigraphic position; all reported ages are in calendar kilo-years BP. Three distinct stratigraphic units are identified as follows: Unit I (light blue) = massive nannofossil calcareous clay; Unit II (light green) = mottled nannofossil clay; Unit III (gray) = laminated nannofossil clay containing reddish-brown nannofossil clay layers (red lines). A distinct ~5-cm thick reddish clay layer with highly "reworked" (pre-Quaternary) nannofossils defines the top of Unit III.

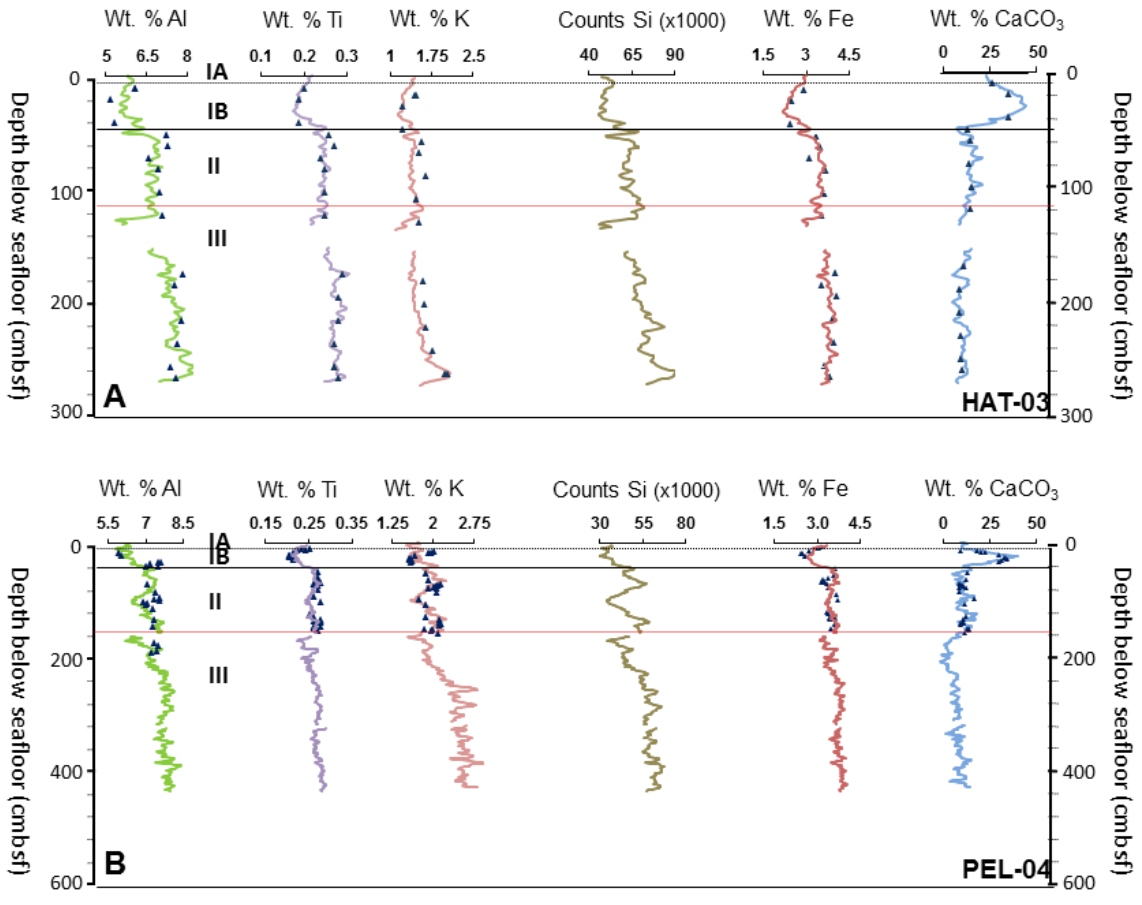

Figure 3. *Panel A* (top): XRF results (calibrated and un-calibrated) for Core HAT-03. From left to right: Al, Ti, K, Si, Fe and $CaCO_3$. The above calibrated and un-calibrated XRF core scans are smoothed using a 3-point moving average. The ICP and CO_2 coulometry data is plotted on the same scale, and Si is un-calibrated. The calibrated XRF core scans are a smoothed 3-point moving average. Stratigraphic Units IA, IB, II and III are as described in the text. *Panel B* (bottom): same as above, for Core PEL-04 and with a condensed depth scale (0 to 600 cmbsf).

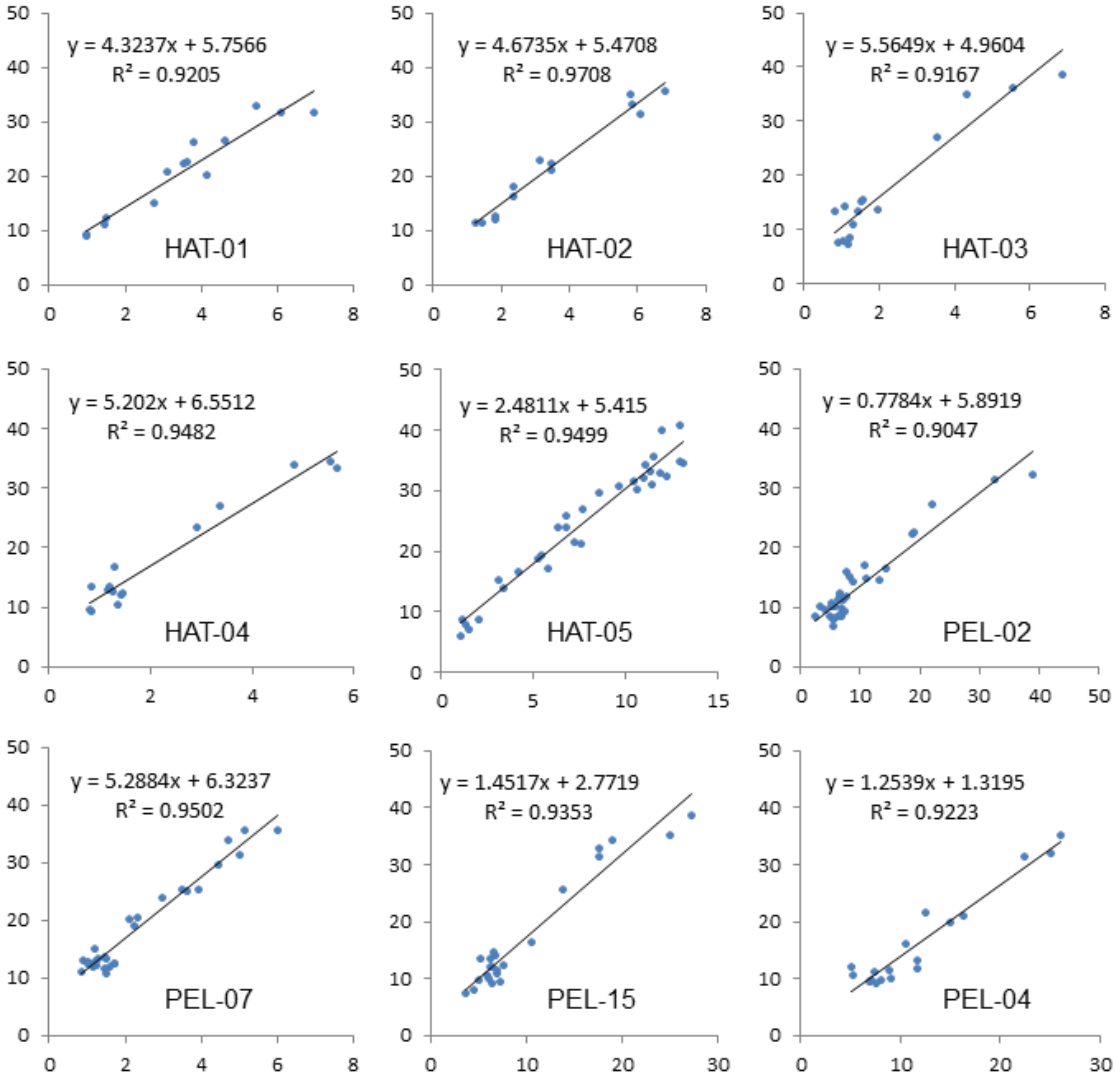

Figure 4. Cross plots of XRF Ca/Ti data (x-axis) and wt. % $CaCO_3$ measured using the CO_2 Coulometry acid digestion method (y-axis), for each of the nine calibrated cores. Correlation coefficients and least-squares linear fits for each calibration equation are also presented.

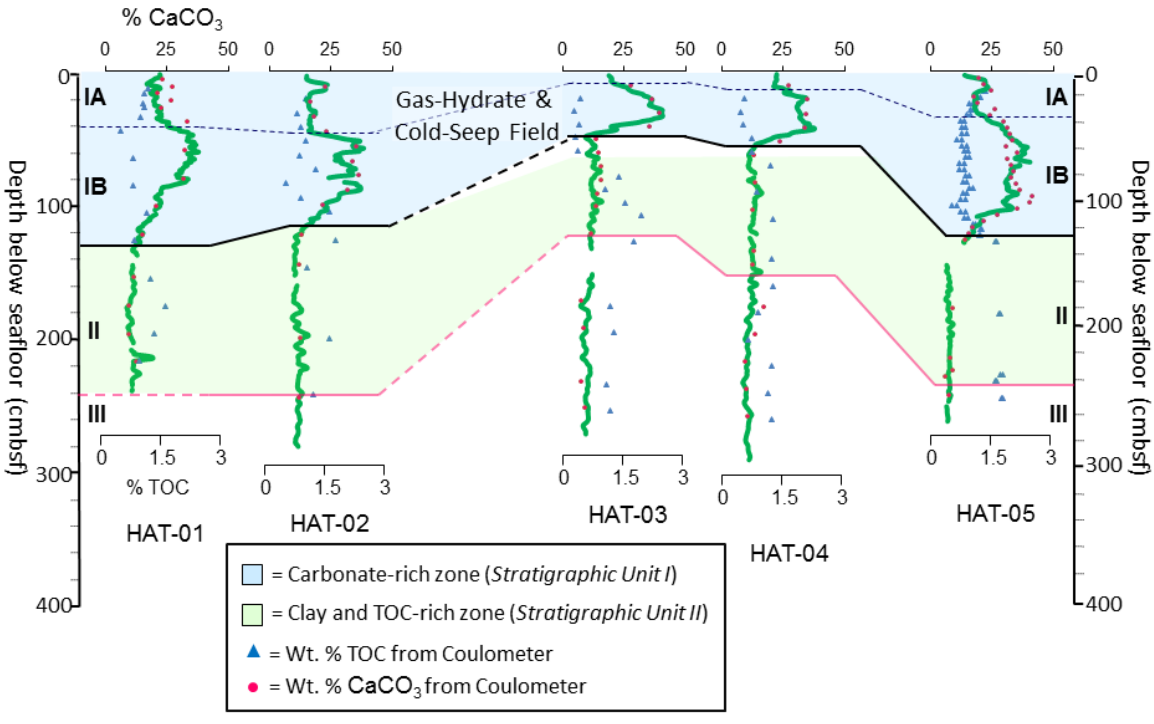

Figure 5. Calibrated weight percent calcium carbonate (solid green curve) derived from XRF scanning of cores from the Hatteras Transect (Figures 1, 2). The data represented by the green curve is smoothed using a 3-point moving average. Total organic carbon (blue triangles) and wt. % $CaCO_3$ (red dots) from CO_2 Coulometry (see legend) is also plotted. Stratigraphic Units IA, 1B, II and III are as defined in the text.

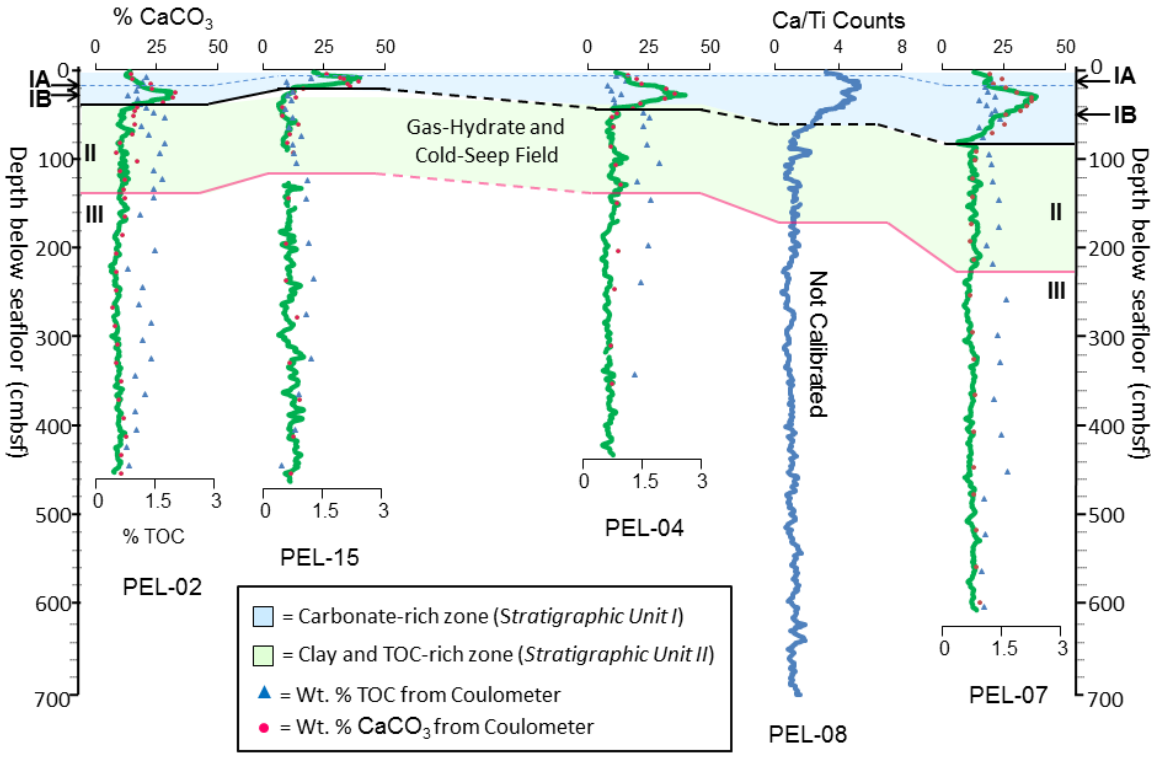

Figure 6. Calibrated weight percent calcium carbonate (solid green curve) derived from XRF scanning of cores from the Pelican Transect (Figures 1, 2). The data represented by the green curve is smoothed using a 3-point moving average. Total organic carbon (blue triangles) and wt. % $CaCO_3$ (red dots) from CO_2 Coulometry (see legend) is also plotted. Stratigraphic Units IA, 1B, II and III are as defined in the text.

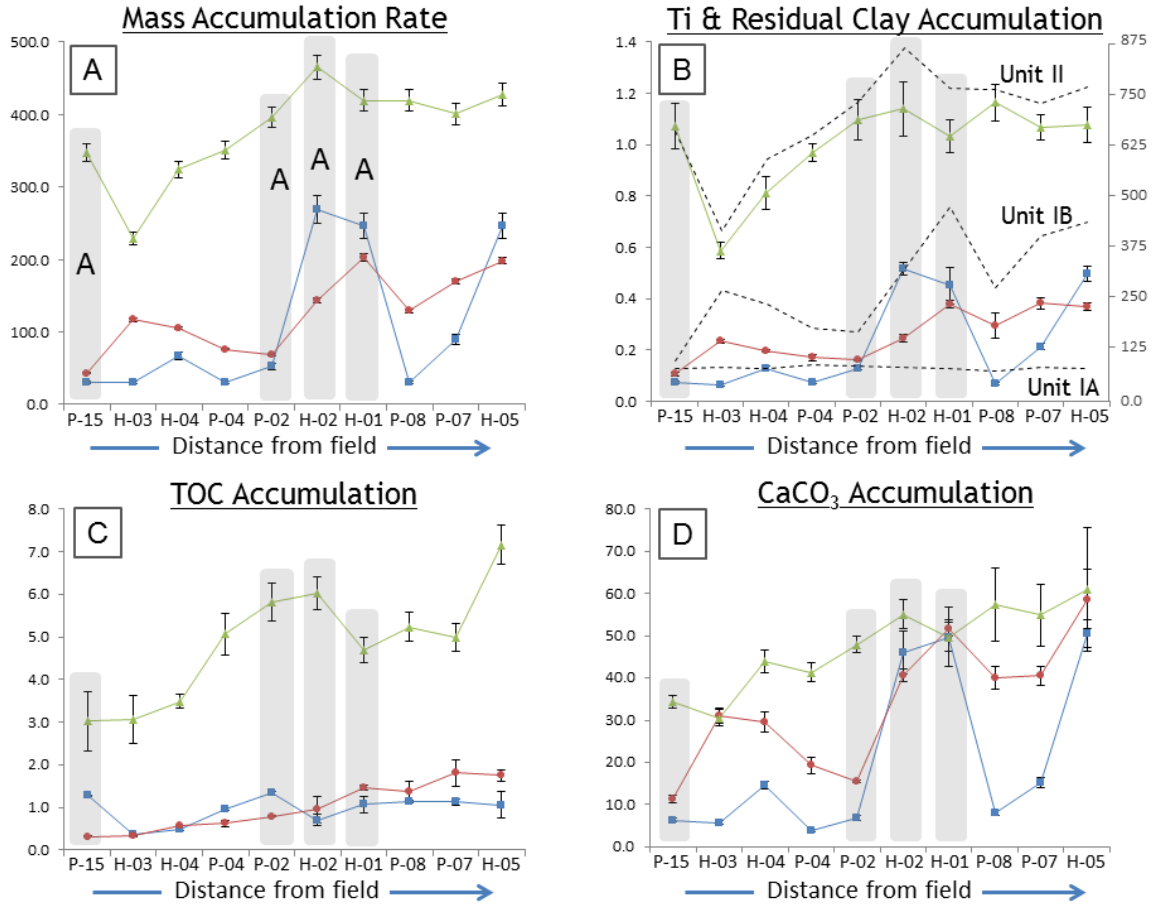

Figure 7. Mass accumulation rate (g m^{-2} yr^{-1}), along with Titanium (Ti), Total Organic Carbon (TOC), carbonate ($CaCO_3$), and insoluble residue (residue) accumulation rates calculated for each stratigraphic unit at each core site (Unit IA: blue, Unit IB: red and Unit II: green). The cores are arranged from left to right by increasing distance from the MC118 field (see Figure 2) and are labeled on the x-axes to denote the cruise (P = Pelican and H = Hatteras) and core number. Errors are calculated using one standard deviation of duplicate measurements (XRF scans for Ti; CO_2 Coulometry for TOC, $CaCO_3$) and a chronologic error of 216 calendar years, maximum error encountered from carbon-14 dating (Table 2 in Ingram et al., 2010). Error bars for residual clay (1 - $CaCO_3$ + TOC) are not calculated as respective errors are represented by other plots. Note the consistent increase of Mass Accumulation Rate, Ti, TOC, and insoluble residue accumulation between Unit I (red IA and blue IB) and Unit II (green), which is not replicated by $CaCO_3$, see discussion for interpretation of this key observation.

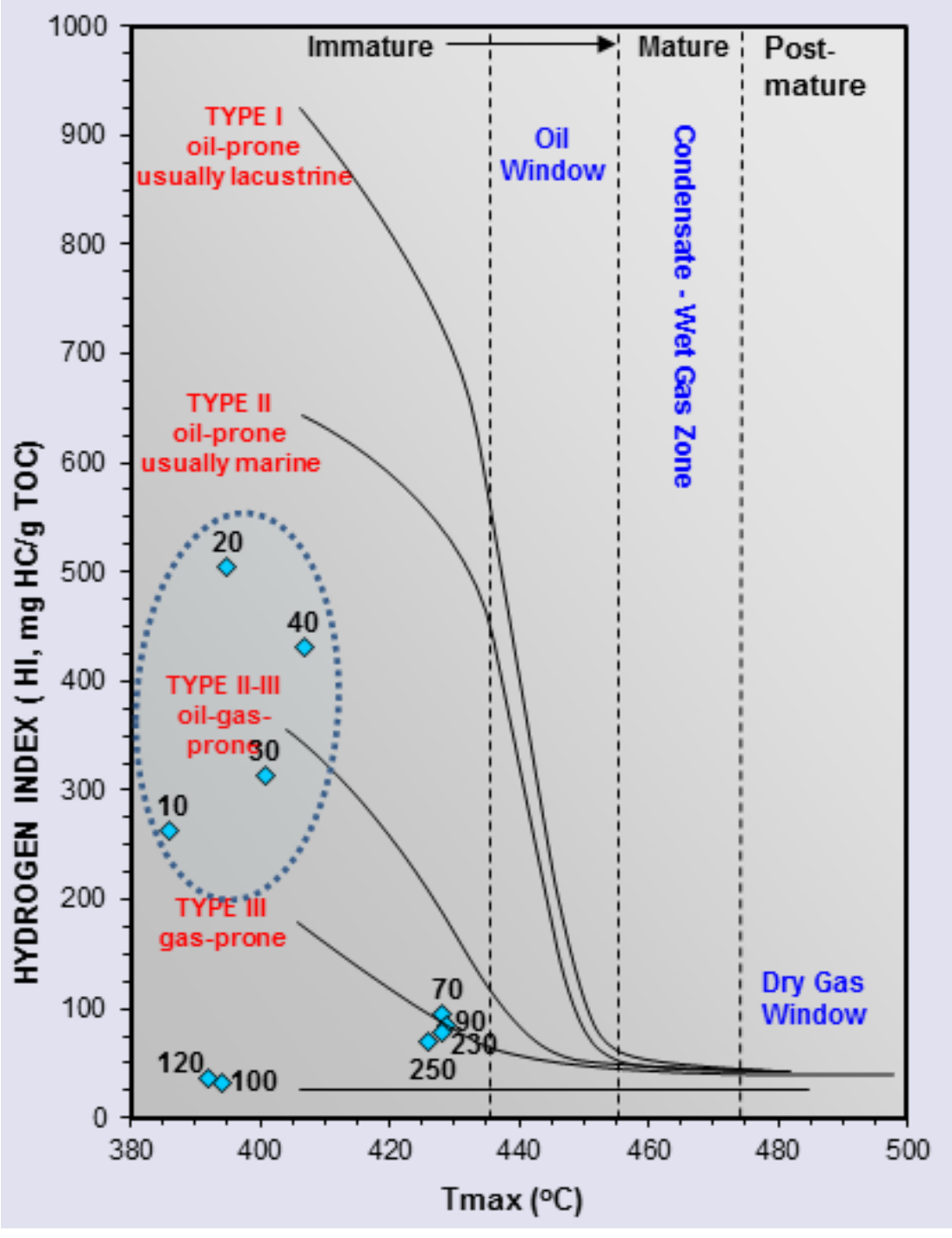

Figure 8. Rock Eval pyrolysis results from 10 samples of Core HAT-03 spanning Units I and II. Hydrogen Index (y-axis) plotted against *Tmax* (x-axis) for each sample (blue diamonds). *Tmax* (°C) is the temperature of maximum release of hydrocarbons from cracking of kerogens during pyrolysis (S_2 peak) and is an indication of maturation of the organic matter. All samples are immature, and thus plot left of the dashed lines. The hydrogen index is indicative of kerogen source, e.g. marine (oil prone) or terrestrial (gas prone), see discussion for interpretation.

Chapter 3

Authigenic manganese deposits surrounding the Mississippi Canyon 118 Gas Hydrate and Cold-Seep Field: Their documentation, interpretation, and utility for evaluating redox state and stability of sedimentation

Abstract

This study investigates a unique deep-sea manganese (Mn) record obtained from ten sediment cores surrounding a large gas-hydrate and cold-seep field situated on the northern Gulf of Mexico Slope (Mississippi Canyon 118; MC118), the first National Gas Hydrate Seafloor Observatory. The distribution of Mn with depth is highly variable and occurs as numerous discrete highly-enriched layers (ranging from 1-10 cm thick; henceforth "Mn-layers"), which are well documented by high-resolution (1-cm scale) X-ray fluorescence core scanning. Evaluation of the Mn record within the context of the established litho and chronostratigraphic framework demonstrates that the Mn-layers are generally not stratigraphically correlative, nor are they linked to original deposition. Thus, these Mn-layers are interpreted as authigenic deposits.

Evaluation of the Mn-layers using reductive dissolution and acidification procedures indicates they are primarily authigenic Mn carbonate. This Mn record is qualitatively interpreted as indicative of intermittent periods of steady state and non-steady state conditions during formation within dysoxic sediments. The individual Mn-

layers also vary in concentration both spatially and temporally with relation to the position of gas-hydrate and cold-seep field, generally more frequent in occurrence yet less concentrated with increased proximity to the MC118 field. This study investigates the possibility that the Mn-layers are connected to stability of sedimentation (duration and frequency of steady state versus non-steady state conditions), which is in turn linked to the field itself (potentially via salt diapirism) and variable redox conditions though time.

Introduction

This study documents and evaluates a detailed manganese (Mn) record from shallow marine sediments surrounding a large gas-hydrate and cold-seep field in the northern Gulf of Mexico (the first National Gas Hydrate Seafloor Observatory; McGee, 2006). The study site, an area of the seafloor with active gas hydrate formation and cold seepage, is located within offshore Federal Lease Block Mississippi Canyon 118 (MC118) in 890 m water depth (Figure 1). Ingram et al., (2010) describe the site and geologic context (chronostratigraphic framework; Figure 2) in more detail.

Manganese is sensitive to redox cycling in natural (pore) waters, and in turn, is influenced by sedimentation rate, erosion, organic carbon burial, among other processes in marine sediments (Gingele and Kasten, 1994; Calvert and Pedersen, 1993; Canfield 1993; Canfield et al., 1993; Burdige, 1993; Burdige and Gieskes, 1983; Froelich, 1979). This study investigates the hypothesis that Mn deposits at the MC118 site are a sensitive indicator of steady state versus non steady state sedimentation, which in turn is connected to the nearby gas-hydrate and cold-seep field (and associated salt diapirism). Redox chemistry at this site, as in many similar settings, is potentially influenced by numerous factors (sedimentation rate, supply and reactivity of organic matter, pore-water oxygen content, and bioturbation, etc.). By substantially varying these factors, it is possible to disrupt steady-state conditions, controlling the time over which authigenic minerals may form in dysoxic sediments (Mn-oxides or carbonates) across a discrete stratigraphic position. In other words, when the (pore-water) system is

in balance and available metals (Mn, Fe) are remobilized, redox fronts will form in the subsurface within dysoxic sediments (Calvert and Pedersen, 1993; Canfield 1993; Canfield et al., 1993; Burdige, 1993) and continue to form authigenic minerals until such redox fronts are disrupted by paleoenvironmental changes.

As discussed below, a unique Mn record is recovered from the MC118 site by shallow gravity coring, and is documented by fine resolution (cm-scale) X-Ray Fluorescence (XRF) core scanning (Richter et al., 2006). Presented here for the first time at the MC118 National Gas Hydrate Seafloor Observatory, this Mn record exhibits numerous highly-enriched layers (ranging from 1-10 cm thick; henceforth "Mn-layers"). The Mn-layers vary in magnitude and frequency with proximity to the field, yet with an apparent (approximate) conservation of total manganese mass across the different core sites. The specific objectives of this study are to provide a detailed documentation of the Mn-layers, determine their mineral composition, evaluate their formation mechanism, and investigate their interpretive value with respect to understanding sedimentation surrounding the gas-hydrate and cold-seep field. This record is evaluated within the context of multiple (potentially interrelated) working hypotheses: (1) the Mn-layers are oxides or oxyhydroxides formed *in situ*, associated with normal marine sedimentation, formed by a conditionally stable, yet transient, redox boundary, (2) the Mn-layers are Mn-rich carbonates (Ca-Mn$(CO_3)_2$), formed by Mn cycling where conditions are also saturated with respect to carbonate minerals, (3) the Mn-layers are reworked authigenic minerals originating from the MC118 field, and finally, (4) the Mn-layers are sensitive to changes in sedimentation rate; thus linked to the presence of the MC118 field and associated salt diapirism. The first two hypotheses pertain to the composition

of the Mn-layers, and the latter (hypotheses 3 and 4) to the paleoenvironmental implications of these authigenic deposits.

As will be documented herein, litho and chronostratigraphic study of MC118 reveals no clear depositional event(s) that can explain the occurrence of the highly enriched Mn-layers, nor do the layers follow consistent chronostratigraphic trends. Furthermore, application of a reductive cleaning (dissolution) and acidification procedure indicates that the Mn-layers are primarily associated with authigenic Mn carbonate. Given that the Mn-layers are authigenic, it seems likely that their concentration and frequency of occurrence are related to conditions of state (steady-state verses non steady-state) at the site, which could be connected to sedimentation, and by extension the MC118 field and associated salt diapirism.

1 Background: Manganese Geochemistry

A review of Mn geochemistry in marine systems is presented here to better interpret the MC118 record. Mn enrichments may form on the seafloor and in shallow marine sediments as oxides, oxyhydroxides or other complex minerals. Mn-oxide nodules occur in the deep-ocean basins, typically in clay-rich sediments with low-accumulation rates and minimal carbonates (Burdige, 1993; Schulz and Zabel 2000; Gingle and Kasten, 1994). It has been estimated that deep-sea Mn-oxides comprise 16 times the total manganese within terrestrial deposits, and that they are geologically recent, formed during ventilation of the deep oceans by oxygen-rich bottom waters (Schulz and Zabel 2000). The oceans and pore waters in the sediment column are also a

large repository of dissolved Mn^{2+} both now and in the past. Within oxygenated seawater (~Eh +0.4 V, ~pH ~8.1), Mn exists in the dissolved phase as Mn^{2+} (Bruland 1983), yet it is also unstable in the presence of oxygen (Chun, et al., 2010). The Mn is derived from geologic sources such as hydrothermal systems, where some 90 percent originates from vents and seafloor spreading centers (Glasby, 1988); a much smaller proportion derives from cold seeps (Schulz and Zabel 2000).

On average, the oceans contain enough dissolved Mn to exceed saturation with respect to MnO_2 (Bruland, 1983), though precipitation from seawater occurs very slowly (Martin, 2005). Still, Mn-oxides may form much more rapidly via surface catalysis (Murray and Brewer 1977) or bacterial oxidation (Cowen and Bruland 1985; Ehrlich, 1996). While interesting, Mn-oxide nodules were not observed at the studied site. This is mostly likely due to the higher sedimentation rates at the MC118 site, which is greater than deep-sea locations more distal from continental margins. MC118 also contains higher carbonate content, which is not ideal for forming Mn-oxide nodules.

Authigenic Mn minerals forming beneath the seafloor or along redox boundaries occur across a wide range of sediment depths and are found in a variety of settings, including continental shelf to the deep ocean within oxygenated to anoxic sediments (Chun et al., 2010; Gingele and Kasten, 1994; Calvert and Pedersen, 1993; Burdige and Gieskes, 1983). Sediment pore-water Mn profiles typically exhibit rapid increases in the dissolved phase just beneath the maximum solid-phase enrichment, then gradually decreasing again at greater depths (Figure 3; Froelich et al., 1979, Aller 1990; 1994; Canfield, 1993; Canfield et al., 1993). The depth to layer(s) of Mn enrichment and the

associated pore-water gradient is highly variable, yet the sequence of higher concentrations beneath the authigenic "front" is quite repeatable, generally occurring where oxygen is depleted (Figure 3; Froelich et al., 1979). Multiple factors can control the depth where this occurs, including, (1) sedimentation rates, (2) availability of reactive metals such as Fe and Mn, (3) bottom-water oxygen concentration, (4) intensity of bioturbation and irrigation, as well as (4) variation in the supply or type of organic matter (Aller 1990; 1994; Schulz and Zabel, 2000). These factors must balance for a period of time in the sediment column for continued growth of authigenic minerals along a redox front (Figure 3). Given steady-state conditions, such deposits may appear as discrete layers of elevated concentrations in the elemental record marking the modern redox transition, or alternatively, a "paleo-redox" boundary.

In summary, the cycling of Mn occurs through repeated steps of Mn-oxide burial into dysoxic pore waters, reducing MnO_2 (Mn IV) to Mn^{2+} (Mn II) followed by remobilization and upward diffusion of dissolved-phase Mn^{2+}, which then re-precipitates across a redox front where oxygen increases, thereby continually forming authigenic Mn at that front until it shifts (Froelich et., 1979; Calvert and Pedersen, 1993; Stum and Morgan, 1996; Sageman and Lyons, 2004). Hem et al. (1981) states that in marine sediments (pH ~8.1), multiple phases of Mn are possible e.g., Eh values of 0.5 V, favors soluble Mn (II) and Eh values greater than 0.5 V favors insoluble Mn (IV). Hence, within the shallow sediment column beneath an oxygenated water column, Mn-oxides are stable while in reducing conditions they dissolve. Given this, pure Mn-oxides should not persist at greater depths unless preserved by some other mechanism (Piper 1994). Repeated cycling of Mn, referred to as a "Mn pump" (Sageman and Lyons, 2004), can

concentrate enough dissolved Mn within sufficiently alkaline pore waters to form Mn-rich carbonates (Ca-$Mn(CO_3)_2$). The very reduction of MnO_2 commencing after oxygen depletion increases alkalinity by acid consumption via the following reaction

$$CH_2O + 2MnO_2 + 4H^+ \rightarrow CO_2 + 2Mn^{2+} + 3H_2O$$

and continues until Mn^{2+} becomes saturated with respect to Mn-Ca carbonates (Lynn and Bonatti 1965; Froelich et al., 1979). Mn-rich carbonates are more resistant to anoxic pore waters; thus they can be preserved in deep marine sediments, and ultimately into the geologic record (Gingele and Kasten, 1994; Pedersen and Price, 1982). The formation of authigenic Mn carbonates in marine sediments is more complex than simplistic models might suggest and is a topic of active research, but may be occurring at MC118 (See Discussion).

Methods

2.1. Core Collection and Processing

Gravity coring was conducted from the surface ships R/V *Hatteras* in August 2007 and R/V *Pelican* in April 2008 (Sleeper and Lutken, 2008). A total of 10 sediment gravity cores (5 from each cruise) were recovered (Ingram et al., 2010; Figure 1). Cores were transported to and processed at a shore-based laboratory at the University of North Carolina, Chapel Hill, where they were split and prepared for destructive and non-destructive geochemical analyses (see Ingram et al., 2010, for detailed description of coring and processing methods).

2.2 X-Ray Fluorescence (XRF) Core Scanning

Cores were analyzed using an Avaatech-XRF core scanner with an Oxford 50 W X-ray source (rhodium target), and a Canberra X-PIPS detector with a 1500-micrometer silicon crystal. Continuous down-core XRF scanning was conducted at 1-cm resolution to evaluate changes in the Mn composition of the sediments. Specifically, Mn was scanned using a 10 kV source voltage, 1000 mA, with a cellulose filter, using a 90 second measurement time, with duplicate scans every 10 cm, which yielded highly reproducible results. The XRF scanning 'count' data is calibrated (least-squares linear fits; Table 1) to manganese concentration data obtained from three cores (HAT-03, PEL-04, PEL-07; 54 samples), determined via Inductively Coupled Plasma Emission Spectrometry (ICP-AES;

SGS Laboratory method ICP-AES 40B). Duplicate samples were also analyzed, which yielded low average coefficient of variation values for Mn (Table 1).

2.3 Wet Chemistry: Reductive Dissolution and Acidification

Targeted samples were subjected to a two-step "wet chemistry" analytical procedure to operationally determine probable Mn minerals (following Chun et al., 2010). This procedure employed a reductive cleaning (dissolution) to first remove oxides and oxyhydroxides from the sample, followed by an acid dissolution to remove carbonate content from the sample, with the remaining sample presumably comprising "insoluble" clay content. Samples from 5 different depth intervals came from Core PEL-07 and were selected from locations where XRF core scanning demonstrated high Mn content (Mn-layers). Details on the manganese oxide and manganese carbonate extraction are provided below.

Inductively Coupled Plasma Emission Spectrometry (ICP-AES; SGS Laboratory method ICP-AES 40B) was used to determine the Mn and Ti content of three resulting fractions at each of the five Mn-layers: untreated (total Mn), manganese carbonate, and insoluble residue. Mn concentration of the "insoluble" residue represents unreactive aluminosilicates (Chun et al., 2010; Dickens and Owen, 1993; Schenau et al., 2002). Results are reported in terms of an Mn enrichment factor (EF), EF = $(metal/Ti)_{sample}/(metal/Ti)_{crust}$, which normalizes authigenic Mn to a conservative detrital element (Table 2; Chun et al., 2010). "Excess" Mn (not the detrital component) is also determined using the following equation from Chun et al., (2010) [Mn excess = Mn_{total} –

(Ti_{sample} * $(Mn/Ti)_{crust}$)]. The bulk crustal Mn/Ti (mol/mol) = 0.156 (from Rudnick and Gao, 2003) is used in both equations.

2.5 Manganese oxide extraction and carbonate extraction

A reductive cleaning procedure was carried out on each of the 5 sample depths to operationally quantify wt.% Mn comprised of Mn-oxide and Mn-oxyhydroxide minerals. Sediment from each depth was pulverized into 100-mesh powder, weighed to 100 mg and placed into 15 ml centrifuge tubes. The reduction was carried out by adding 10 ml of 0.033 M sodium dithionite, complexation with 0.22 M sodium citrate and 1.0 M sodium bicarbonate solution (pH = 7.55) to prevent unintended dissolution of Mn carbonates. The dissolution and extraction of oxides and oxyhydroxides occurred by (1) continuously shaking the samples in the solution for 6 hours, (2) centrifuging the mixture, (3) decanting the supernatants, then (3) adding 10 ml of 1 M magnesium chloride ($MgCl_2$) at pH = 8.0, (4) shaking for another 2 hours, (5) centrifuging the mixture again, (6) decanting the supernatant, and finally (7) rinsing the sediment residue with 10 ml of distilled water and shaking for an additional 6 hours.

After the above procedure, remaining solid residue was removed from the centrifuge tubes, dried on a hotplate, re-pulverized and a fraction of this was measured for Mn concentration by SGS laboratories using the ICP-AES 40B method. This method (reductive cleaning) has been previously employed for the same purpose to operationally determine the proportion of Mn in (1) oxides and oxyhydroxides, (2)

carbonates and/or (3) aluminosilicates in marine sediment samples (Dickens and Owen, 1993; Schenau et al., 2002).

An acid digestion procedure was performed sequentially after the oxide extraction procedure. The remaining residue contained in the 15 ml centrifuge tubes from the previous procedure was rinsed with distilled water prior to performing the acid digestion, in an effort to further clean the sample and avoid unintended complexation during sequential dissolution. The dissolution and extraction of Mn in carbonates was performed by (1) adding 10 ml of sodium acetate (pH = 3.96), (2) shaking for 6 hours, (2) centrifuging the mixture, (3) decanting the supernatant, (4) rinsing with 10 ml of distilled water, and (5) shaking for an additional 6 hours, then (6) decanting the supernatant again. The remaining solid was removed from the centrifuge tubes, dried on a hotplate, re-pulverized and then sent to SGS and measured for Mn concentration using the ICP-AES 40B method. This procedure sufficiently dissolves carbonates found in marine sediments, while minimizing unintended dissolution of the mostly "insoluble" aluminosilicates clay residue.

Results from the above 2-step dissolution procedures (Table 2) yield the relative proportion of Mn (% of total) contained with the (1) oxide and oxyhydroxides, (2) carbonate and (3) aluminosilicates fractions. Mn-ppm values are provided along with the enrichment factor and excess Mn for each step (Table 3). To determine the proportion of oxide and oxyhydroxides, measured Mn concentration (ppm) after reductive dissolution was subtracted from the untreated concentration. For the carbonate fraction, Mn measured from the "insoluble" fraction was then subtracted

from that of the reductive cleaning step. Finally, by removing carbonate only the "insoluble" clay residue remains (Table 2). It should be noted that some of the change in Mn concentration associated with carbonate and insoluble clay fractions may be due to the change in total sample mass associated with the extraction procedure. This is of particular concern for sediments with high carbonate content. However, the samples investigated here (for sequential dissolution in PEL-07) are from the clay-rich stratigraphic units II and III (less than 13 wt.% carbonate). Thus, this effect of variable mass change is not substantial here and certainly not large enough to change the observed trends in the data. To address this issue, the Mn enrichment factor and excess Mn is also determined for each step following the equations used by Chun et al., (2010), and bulk Mn/Ti crustal values (Rudnick and Gao, 2003).

Results

Analysis of 10 shallow gravity cores, comprising 38.6 m of total recovered sediment (Table 1), reveal a highly detailed Mn record (Figures 4-5). Mn concentrations and their occurrence vary dramatically between the different core sites (Figure 4-5; Table 1). The fine (cm-scale) resolution of the XRF core scans provides the ability to document (in detail) the variability in this record, and the numerous Mn-layers. Results are presented here by grouping sediments into their respective stratigraphic units and considering the Mn deposits within the context of the MC118 paleoenvironmental and depositional history (for chronostratigraphic context, see Ingram et al. 2010).

3.1 Stratigraphic Unit I

Shallow sediments of Unit I are informally broken into Units IA and IB, the former extends from the seafloor to onset of higher Ca/Ti-XRF counts, coincident with increased wt.% $CaCO_3$ (Ingram et al., 2010). These sediments are late Holocene in age (~2.3 kilo-calendar years BP to present), described as calcareous nannofossil silty clays, and are laterally discontinuous across the study area. Beneath Unit IA, sediments of Unit IB are also described as calcareous nannofossil silty clays, differentiated from the overlying unit by a consistent increase in wt.% $CaCO_3$. Unit IB is thicker, on average, then Unit IA above, and accumulated over a longer time period (~2.3 to 9.5 kilo-calendar years). Sediments of Unit IB are lighter in color with fewer sedimentary structures, and

when examined under high-magnification transmission-light microscopy, yield the greatest concentration of calcareous microfossils (Ingram et al., 2010).

Unit IA exhibits fewer Mn-layers (Figures 4-5), with some exceptions. For example, Cores HAT-04 and PEL-04 display an increase in Mn concentration in the shallowest portion of the XRF-core scans. Core HAT-04 displays a complete, well developed Mn-layer near the top of the core; however the record appears relatively constant through this interval, lacking Mn-layers (except HAT-04 and PEL-04). Concentrations within Unit IA are, on average, 430 ppm based on XRF calibration to ICP-ES data. In contrast, the Mn concentrations for Cores HAT-04 and PEL-04, measuring 635 and 653 ppm, respectively are both approximately 50 percent higher than average, due to the presence of Mn-layers within this section (Figures 4-5). The Mn record within Unit IB also contains few authigenic Mn-layers (Figures 4-5), with one notable exception Core HAT-03, which displays two (nearly synchronous) Mn-layers, near the base of unit. Calibrated concentrations here are 585 ppm Mn for the shallow layer and 930 ppm Mn for the subjacent layer (Figure 4; Table 2), values that are well above "background" Mn concentrations. There is no clear change in the occurrence of Mn-layers between Units IA and IB, despite 10-wt. % increase in $CaCO_3$ content.

3.2 Stratigraphic Unit II

Unit II beneath the shallower carbonate-rich interval is a mottled, hemipelagic, nannofossil silty clay (Ingram et al., 2010). Sediments here are markedly more clay rich with substantially lower $CaCO_3$-content. This unit appears visually darker with

sedimentary structures that are disturbed by burrows in places (Ingram et al., 2010). Sediments are early Holocene to late Pleistocene in age ranging from 9.5 to 14 kilo-calendar years from the top to the base of the unit.

This interval extends through the clay-rich sediments, which contains more authigenic Mn accumulations than any other stratigraphic interval recovered, with at least 15 visible Mn-layers (Table 2; Figure 4-5); average Mn here is approximately 580 ppm Mn, which is greater than shallow sediments. The most prominent Mn-layers also occur here, for example, Cores HAT-01, -05 and PEL-02 contain the most concentrated accumulations, 3356, 3066 and 3463 ppm Mn respectively, all within Unit II (Table 2). One very important observation, cores with the most pronounced Mn-layers also exhibit only one, yet highly discrete Mn-layer (narrow depth interval). Alternatively, cores exhibiting multiple authigenic Mn-layers (Table 2) are less discrete in appearance (Figures 4-5). In addition, even the more concentrated layers (in cores containing multiple layers) are still 1000 ppm less concentrated than the single and most prominent Mn-layers in cores displaying only one (Figure 4-5).

3.3 Stratigraphic Unit III

A continuation of clay-rich sediments comprises Unit III, well-laminated hemipelagic nannofossil silty clay, and is differentiated from the overlying sediments by the numerous red-brown laminations contained within it. Sediments are chemically and lithologically similar to the above unit, yet with slightly higher concentrations of lithogenic-derived elements. The top of this unit is defined by a prominent 1 to 2-cm

thick red-brown colored band ("red band"), also observed by previous investigators (Lutken et al., 2006; Brunner, 2007; Sleeper et al., 2008; Ingram et al., 2010). It is also coincident with a highly "reworked" pre-Quaternary nannofossil interval dated between 14 and 15 kilo-calendar years (Ingram et al., 2010). The unit lacks a defined base and thus extends to the maximum depth recovered by gravity coring. Based on rates of deposition at the site and radiocarbon dating (Ingram et al., 2010), sediments are latest Pleistocene in age and certainly older than the "reworked" nannofossils (14 to 15 kilo-calendar years BP).

This interval (Unit III) contains fewer prominent Mn-layers (Figures 4-5), yet recovery of this stratigraphic unit was incomplete (see Cores HAT-01, -02 and -05 of the Hatteras transect). The Pelican transect recovered more of Unit III, yet still does not display prominent Mn-layers at depth. Yet, several less pronounced Mn-Layers are apparent, for example 20 "smaller" Mn-layers can be identified (Table 2; Figure 4-5). However, this stratigraphic unit is thicker and sediments deposited here more quickly (Ingram et al., 2010). Hence, there is a higher frequency of Mn-layers in Unit III with respect to time (Figures 4-5). The Pelican transect also reveals a similar Mn record in places within this unit (PEL-04, -08 and -07), more specifically the similarity occurs near the base of the Unit II and the top of Unit III in PEL-15 and -08 (Figure 5). By plotting the XRF Mn profile with chronostratigraphic marker beds, it is apparent that the Mn-layers (while similar in appearance, see Figures 4-5) are not chronostratigraphically equivalent. The position of the most concentrated Mn-layers in Core PEL-08 are clearly shifted relative to the adjacent cores (PEL-04 and -07; Figure 5), which confirms that the layers are not depositional. They occur in sediments of different age and do not follow litho or

chronostratigraphic trends across the MC118 sites, and hence their characterization as authigenic deposits formed *in situ* through redox processes (see Discussion).

3.5 Manganese Composition

To evaluate the probable composition (mineral phase) of the Mn-layers, a 2-step wet chemistry method was used, which included a reductive cleaning and acid digestion procedure to operationally determine if the Mn-layers are associated with oxides and oxyhydroxides, carbonates or aluminosilicates (Figure 6; Table 3). Results indicate that the Mn-layers are primarily associated with carbonates as opposed to oxides/oxyhydroxides or aluminosilicates (Figure 6; Table 3). Measurements were performed on Mn-layers from Core PEL-07 spanning stratigraphic Units II and III (Table 3; Figure 6). Following the oxide and carbonate extractions presumably only insoluble clay remains, which was also measured for Mn concentration. The insoluble clay residue is a reflection of terrestrial-derived material, and should be very similar to background accumulation of Mn where the authigenic peaks are missing, and, in fact, this seems to be the case (Figure 6).

In summary, wet chemistry results indicate that the Mn deposits (Mn-layers) at MC118 are predominately carbonates at all depths. Using the ppm values, just of over 80 percent of the total concentration (on average) is comprised of either Mn-rich calcite ($Ca\text{-}Mn(CO_3)_2$) or rhodochrosite ($MnCO_3$). Wet chemistry results also reveal Mn oxides account (on average) for less than 10 percent of the total and only slightly more within the “insoluble” clay fraction (Table 3). Hence, Mn within these layers is by far

predominately associated with carbonates, followed by aluminosilicates and small amounts of Mn-oxides. This observation is further verified by determination of an enrichment factor and “excess” Mn (Table 3), which reveals (1) higher Mn enrichment and (2) “excess” Mn (not associated with clay) associated almost entirely within the carbonates and not oxides. This can be shown by determining the percentage of “excess” Mn in each respective fraction (oxide verses carbonate) where the clay fraction is already removed (via calculation of “excess” Mn). The following expression:

((untreated-carbonate / untreated) *100)

indicates that that only 7.75 % of the Mn is contained with the oxide component, based on the average of all the measured peaks (Table 3). Hence, the vast majority of the “excess” Mn in the Mn-layers is associated with carbonates (over 90% on average).

Discussion

A detailed (well-preserved) deep-sea Mn record containing authigenic accumulations, and complicated by a nearby cold-seep field, is used to evaluate several hypotheses specific to the authigenic deposits (Mn-layers). Results clearly indicate that the Mn-layers are authigenic forming *in situ* at the site; this is based on the observation that the Mn-layers are not stratigraphically correlative nor linked to original deposition. Redox processes and conditions of state are recorded by the Mn-layers and are possibly reflective of variable sedimentation controlled by the cold-seep field itself or salt diapirism. It is suggested that more consistent sedimentation on the flanks of the field (either due to the cold seeps or salt diapirism) yields prolonged periods of steady-state conditions. In turn, prolonged periods of stable redox conditions yield fewer and more concentrated Mn-layers (Figures 4-5). Conversely, periods of non-steady-state conditions generate less concentrated, yet more numerous Mn-layers. Hence, this study presents the possibility that the authigenic Mn deposits (Mn-layers) at MC118 are sensitive to sedimentation, which is linked to the nearby cold seep including seafloor warping from salt diapirism centered under the MC118 field.

4.1 Authigenic Mn Minerals

Wet chemistry methods were used to operationally determine probable mineral composition of the Mn-layers, more specifically to determine amount of Mn associated with oxide-oxyhydroxides, carbonates and/or “insoluble” clay. Authigenic Mn in marine

sediments ranging from oxygenated to dysoxic conditions predominantly consists of carbonate or oxide minerals (Burdige, 1993; Schulz and Zabel, 2000); in more unique settings (hydrothermal vents) Mn sulfides may also form (Canfield, 1993; Schulz and Zabel, 2000). Sulfide minerals are not considered here yet may exist in closer proximity to the seep site where sulfate reduction is more prevalent (Lapham et al., 2008). However, Mn-oxides are considered and generally occur in shallow marine sediments, where reactive MnO_2 is dissolved and remobilized during early oxidation of organic matter, followed by remobilization and re-precipitation along a redox front (Aller, 1990; 1994; Froelich et al., 1979; Schulz and Zabel, 2000). The observed Mn-layers here are authigenic (Figures 4-5), yet are not associated with oxides.

Ingram et al. (2010) demonstrated that $CaCO_3$-content is a substantial component of MC118 sediments (at least from the Late Pleistocene to Holocene); hence it seems probable that sufficient carbonate is available to form Mn-carbonates. It seems that Mn accumulates diagenetically through precipitation of Mn-rich carbonates (Ca-$Mn(CO_3)_2$), perhaps very quickly after redox fronts (Mn-oxides) form near the sediment-water interphase. Alternatively, Mn carbonates may form a protective crust or layer around oxides formed earlier, thereby diminishing their dissolution within dysoxic pore waters (Burdige, 1993). Presumably, further precipitation stops once the Mn-layer is buried beneath the depth of maximum oxygen penetration depth (see below), and the position of *in situ* growth of authigenic Mn then shifts to a shallower depth. It seems that the Mn "redoxcline" exists in very shallow sediments and Mn-oxides quickly convert to Mn-carbonates here. Without pore-water concentration data, it is difficult to precisely determine where the active redox boundary is located.

The shallowest peaks are still relatively deep for dissolved oxygen for similar depositional settings (continental slope) and thus consistent with this dataset, which demonstrates that the Mn-layers are predominately carbonate. The depth of the Mn redox front exists where upward diffusion of Mn^{2+} balances with downward diffusion of oxygen, and is positioned at its shallowest at 7-cm depth in Core HAT-04 (Figure 4-5); all other cores demonstrate Mn-layers at greater depth. Hence, Mn-layers at MC118 are apparently deep compared to both observed and predicted depths for Mn-oxides in most organic-rich (greater than 1.0 % TOC), marine sediments (Burdige and Gieskes, 1983; Kalhorn and Emerson, 1984; Heggie et al, 1986; Aller, 1990, 1994; Shaw et al., 1990; Reimers et al., 1992). In summary, the Mn-layers at MC118 are apparently oxide relics undergoing very slow dissolution, or alternatively, are composed of minerals more easily preserved into dysoxic sediments such as Mn-rich calcite (Ca-$Mn(CO_3)_2$) or rhodochrosite ($MnCO_3$). The later (Mn-carbonates) seems very likely given the wet chemistry results. Finally, it seems doubtful that the oxygen penetration depth here extends down to depths of the Mn-layers (in most cores), as others have demonstrated that oxygen depletion occurs at less than 5 cmbsf both in the western Gulf of Mexico (Hu et al., 2011), and within the Mississippi Canyon region (Diaz and Trefry, 2006).

4.2 Manganese: A proxy for steady-state sedimentation

This MC118 dataset suggest the authigenic Mn-layers are potentially useful as a proxy for periods of prolonged steady-state conditions, in other words the concentration and frequency of the authigenic Mn-layers are recording changes in redox

conditions. While, authigenic Mn accumulations are not uncommon in marine sediments, it is the detail of the MC118 record (from high-resolution XRF scans) that reveals steady verses non-steady state redox conditions at different coring locations. It is possible that the occurrence of fewer and more pronounced authigenic Mn-layers at core sites distal from the MC118 cold seep field is linked to the field (and associated salt diapirism) by controlling deposition at the site (Figures 4-5; Ingram et al., 2010). For example, cores exhibiting only one or two very large Mn peaks (Cores HAT-01, -05 and PEL-02) also happened to be positioned farthest from the field (Figure 1), and those with the most numerous peaks (Core HAT-03 and -04) are adjacent to the field (Figures 4-5). Concentrated Mn-layers formed under prolonged periods of steady-state conditions in balance with more rapid sedimentation (Ingram et al., 2010). At these core sites, rapid sedimentation is perhaps more constant due to their position farther from the MC118 field, undisturbed by hiatuses or subtle erosion over the exposed mound.

The stability of sedimentation is just one factor that can influence a redox boundary. Other factors include: (1) supply and reactivity of organic matter to the sediments, (2) downward diffusion of oxygen, partly controlled by concentration in the overlying water column, (3) pore-water oxygen depletion (biogeochemical cycling or oxidation) and (4) intensity of bioirrigation and bioturbation. All of these factors contribute to redox cycling and depth of the various redox boundaries (Figure 3). The rate of deposition along with changes in sedimentary inputs (carbonate versus siliciclastics) is also changing at MC118 (Ingram et al., 2010); hence this is an important factor to consider. The reactivity of the organic matter can also change and substantially influence biogeochemical cycling. A shift towards more labile organic matter with slower

Holocene sedimentation (see Ingram et al., 2010) could drive the redox boundary toward a shallower depth (Figure 3; Burdige, 1993). It is possible that a change in the accumulation rate alone or reversal in sedimentation (erosion) is just as important, which seems more likely for deposition over a bathymetric high (such as the MC118 gas hydrate/cold seep field). Hence, the duration of steady-state conditions and by extension "magnitude" of the Mn-layers is potentially connected to sedimentation among other factors. It is difficult to imagine how bottom-water oxygen concentrations could substantially vary across a localized area, if at all. On the other hand, bioturbation and/or bioirrigation could vary substantially, perhaps more intensely closer to the seeps. Advection of hydrocarbons is likely only important within or immediately adjacent to the cold seeps, where intensity of biogeochemical cycling and oxidation could drive changes in pore-water oxygen depletion. In summary, it is hypothesized that fewer and less concentrated Mn-layers occur in closer proximity the MC118 field due to the presence of the field (and related salt diapirism) as a control on sedimentation. It seems reasonable that slower sedimentation, intermittent erosion or "draping" of sediment over the elevated bathymetric mound (seep field) would favor non-steady-state conditions.

Conclusions

In consideration of the proposed multiple working hypotheses, several conclusion can be made regarding the Mn record surrounding the MC118 gas hydrate/cold seep field. (1) The Mn-layers are authigenic deposits forming *in situ* in association with a variable redox front, and are not directly linked to specific litho- or chronostratigraphic horizons across the site; hence their interpretation as authigenic. (2) Wet-chemistry (sequential multi-step dissolution) indicates that the Mn-layers are composed of Mn-rich carbonates, Ca-$Mn(CO_3)_2$, and/or rhodochrosite, $Mn(CO_3)$, which contribute to nearly all of the "excess" (non siliciclastic) Mn. (3) While, Mn-layers may (or may not) have initially formed as oxides or oxyhydroxides, they are presently carbonates in MC118 sediments. (4) Finally, the Mn-layers are not "reworked" nor do they originate from the MC118 field, yet it is possible that heterogeneity of the record is related to the field (and related salt diapirism). In summary, returning to the fundamental question of this study - the authigenic Mn-layers appear to provide a means to qualitatively evaluate spatially variable redox conditions and spatially variable sedimentation surrounding the MC118 gas hydrate/cold seep field.

References

Aller, R.C., 1990. Bioturbation and manganese cycling at the sediment-water interface. Philos. Trans. R. Soc. London, v. 331, p. 51-68.

Aller, R.C., 1994. The sedimentary cycle in Long Island Sound: Its role as intermediate oxidant and the influence of bioturbation, O_2, and C_{org} flux on diagenetic reaction balances. *Journal of Marine Resources*, v. 52, p. 259-295.

Bruland, K.W., 1983 1983. Trace elements in sea-water. In: Riley J.P. and Chester, R. (eds.), Chemical Oceanography. Academic Press, London, pp. 157-220.

Brunner, C.A., 2007. Stratigraphy and paleoenvironment of shallow sediments from MC118. Proceedings of the Annual Meeting of the Gulf of Mexico Hydrate Research Consortium, October 10-11, 2007, Oxford, Ms. [one CD]

Burdige, D.J., 1993. The biogeochemistry of manganese and iron reduction in marine sediments. *Earth-Science Reviews*, v. 35, pp. 249-284.

Burdige, D.J., and Gieskes, J.M., 1983. A pore water/solid phase diagenetic model for manganese in marine sediment, *American Journal of Science*, v. 283, p. 29-47.

Calvert, S.E. and Pedersen, T.F, 1993. Geochemistry of recent oxic and anoxic marine sediments: Implications for the geological record, *Marine Geology*, v. 113 (1-2), p. 67-88.

Canfield, D.E., Thamdrup, B. and Hansen, J.W., 1993. The anaerobic degradation of organic matter in Danish coastal sediments: Fe reduction, Mn reduction, and sulfate reduction. *Geochim. Cosmochim. Acta*, 57: 3867-3883.

Canfield, D.E., 1993. Organic matter oxidation in marine sediments. Im. Wollast, R., Markenzie, F.T. and Chou, L. (eds.), Interactions of C, N, P and S biogeochemical cycles. NATO ASI Series, 14. Springer, Berlin, Heidelberg, NY, pp. 333-363.

Chun, C.O.J., Delaney, M.L., Zachos, J.C., 2010. Paleoredox changes across the Paleocene-Eocene thermal maximum, Walvis Ridge (ODP Sites 1262, 1263, and 1266): Evidence from Mn and U enrichment factors. *Paleoceanography*, v. 25, p. 1-13.

Cowen, J.P. and Bruland, K.W., 1985. Metal deposits associated with bacteria: implications for Fe and Mn marine geochemistry. *Deep-Sea Research*, 32: 253-272.

Diaz, R. J. and Trefry, J.H., 2006. Comparison of sediment profile image data with profiles of oxygen and Eh from sediment cores. *Journal of Marine Systems* v. 62, p. 164-172.

Dickens, G.R., and Owen, R.M., 1993. Global change and manganese deposition at the Cenomanian-Turonian boundary, Marine Georesources Geotechnology, v. 11(1), p. 27–43, doi:10.1080/10641199309379904.

Ehrlich, H.L., 1996. *Geomicrobiology*. Marcel Dekker, NY, pp. 719.

Froelich, P.N., Klinkhammer, G.P., Bender, M.L., Luedtke, N., Heath, G.R., Cullen, D., Dauphin, P., Hammond, D., Hrtman, B., and Maynard, V., 1979. Early oxidation of organic matter in pelagic sediments of the eastern equatorial Atlantic: suboxic diagenesis. *Geochimica et Cosmochimica Acta*, v. 43, pp. 1075-1090.

Gingele, F.X. and Kasten, S., 1994. Solid-phase manganese in southeast Atlantic sediments: Implications for the paleoenvironment, Marine Geology, v. 121, no. 3-4, p. 317-332.

Glasby, G.P., 1988. Hydrothermal manganese deposits in island arcs and related to subduction processes: A possible model for genesis. *Ore Geology reviews*, 4:145-153.

Heggie, D.T., Kahn, D., and Fischer, K., 1986. Trace metals in metalliferous sediments, MANOP site M: interfacial pore water profiles, *Earth Planetary Science Letters*, v. 80, p. 106-116.

Hem, J.D. 1981. Rates of manganese oxidation in aqueous systems. *Geochemica Cosmochimica Acta*, v. 66, pp. 3811-3826.

Hu, X., Cai, W.J., Wang, Y, Guo, X., and Lou, S., 2011. Geochemical environments of continental shelf-upper slope sediments in the northern Gulf of Mexico. *Paleogeography, Paleoclimatology, Paleoecology*, v. 312, p.265-277.

Ingram, W.C., Meyers, S.R., Brunner, C.B., Martens, C.S., 2010. Late Pleistocene-Holocene sedimentation surrounding an active seafloor gas-hydrate and cold-seep field on the Northern Gulf of Mexico Slope, *Marine Geology*, v. 278, p. 43-53.

Kalhorn, S., and Emerson, S., 1984. The oxidation state of manganese in surface sediments of the deep sea, *Geochemica, Cosmochimica, Acta*, v. 48, p. 897-902.

Lapham, L.L., Chanton, J.P., Martens, C.S., Sleeper, K., Woolsey, J.R., 2008. Microbial activity in surficial sediments overlying acoustic wipeout zones at a Gulf of Mexico cold seep. Geochemisty, Geophysics, Geosystems, v. 9 (4), p. 1-17.

Lutken, C.B., Brunner, C.A., Lapham, L.L., Chanton, J.P., Rogers, R., Sassen, R., Dearman, J., Lynch, L., Kuykendall, J., Lowrie, A., 2006. Analyses of core samples from the Mississippi Canyon 118, paper OTC 18208, Offshore Technology Conference, American Association of Petroleum Geologist, May 1-4, Houston, TX.

Lynn, D.C. and Bonatti, E. 1965. Mobility of manganese in diagenesis of deep-sea sediments. *Marine Geology*, v. 3, pp. 457-474.

Martin, S.T., 2005. Precipitation and Dissolution of Iron and Manganese Oxides. In: Environmental Catalysis (V.H. Grassian, Ed), CRC Press: Boca Raton, pp. 61-81.

McGee, T., 2006. A seafloor observatory to monitor gas hydrates in the Gulf of Mexico. *The leading Edge*, v. 25 (5), p. 644-647.

Murray, J. W. and P. G. Brewer (1977). The mechanisms of removal of iron, manganese and other trace metals from seawater. In: Marine Manganese Deposits, G. P. Glasby, ed., Elsevier, Holland, pp. 291- 325.

Pedersen, T.F. and Price, N.B., 1982. The geochemistry of manganese carbonate in Panama Basin sediments, *Geochimica Cosmochimica Acta*, v. 46, no. 1, p. 59-68.

Piper, D.Z., 1994. Seawater as the major source of minor elements in black shales, phosphorites and other sedimentary rocks. Chemical Geology, v. 114, pp. 95-114.

Reimers, C.E., Jahnke, R.A., and McCorkle, D.C., 1992. Carbon fluxes and burial rates over the continental slope and rise off central California with implications for the global carbon cycle, *Global Biogeochemical Cycles*, v. 6, p. 199-224.

Richter et al., 2006. The Avaatech Core Scanner: Technical description and applications to NE Atlantic sediments. *In*: Rothwell, R.G. (eds.), New ways of looking at sediment core and core data. *Geological Society Special Publication*, London, pp. 39-50.

Rudnick, R. L. and Gao, S. 2003. Composition of the continental crust, in Treatise on Geochemistry, (eds.) Heinrich, D.H. and Karl, K.T., pp. 1–64, Pergamon, Oxford, U. K.

Sageman, B.B., Lyons, T.W., 2004. Geochemistry of Fine-grained Sediments and Sedimentary Rocks, in: MacKenzie, F., (Eds.) Sediments, Diagensis, and Sedimentary Rocks, Treatise on Geochemistry 7, pp. 115-158.

Schenau, S. J., Reichart, G.J. and De Lange, G.J., 2002. Oxygen minimum zone controlled Mn redistribution in Arabian Sea sediments during the late Quaternary, Paleoceanography, v. 17(4), p. 1058, doi:10.1029/2000PA000621.

Schulz, H. D., and Zabel, M. (eds.) 2000. Marine Geochemistry, Springer-Verlag, v. 1, 455 p. DM149. ISBN 3-540-66453-X.

Shaw, T.J., Gieskes, J.M., Jahnke, R.A., 1990. Early diagenesis in differing depositional environments: the response of transitional metals in pore water, *Geochemica, Cosmochimica, Acta*, v. 54, p. 1233-1246.

Sleeper, K.A., Lowrie, A., Bosman, A., Macelloni, L., Swann, C.T., 2006. Bathymetric mapping and high resolution seismic profiling by AUV in MC 118 (Gulf of Mexico). paper OTC 18133 presented at Offshore Technology Conference, Houston, TX

Sleeper, K.A., Lutken, C., 2008. Activities Report for Cruise GOM1-08-MC118 aboard the R/V Pelican Sampling and Deployment Cruise Mississippi Canyon Federal Lease Block 118 Northern Gulf of Mexico April 22-28, 2008. The Center for Marine Resources and Environmental Technology and the Seabed Technology Research Center, University of Mississippi. http://www.olemiss.edu/depts/mmri/programs/ppt_list.html

Stumm W. and Morgan J.J., 1996. *Aquatic Chemistry*. Wiley, New York, 1022 pp.

XRF-ICP Manganese Calibration Data

Core	Element	Calibration Eqn.	R^2 Value	Samples
HAT-03	Mn	$y = 8.31*10^{-2}(x) - 55.268$	$R^2 = 0.84$	13
PEL-04	Mn	$y = 4.5*10^{-2}(x) + 261.57$	$R^2 = 0.79$	32
PEL-07	Mn	$y = 7.25*10^{-2}(x) + 28.554$	$R^2 = 0.85$	9

Average Coefficient of Variation for Mn

Core	XRF CV	ICP-ES CV	Core	XRF CV
HAT-01	0.098	NA	PEL-02	0.116
HAT-02	0.137	NA	PEL-15	0.129
HAT-03	0.035	0.008	PEL-04	0.066
HAT-04	0.12	NA	PEL-08	0.106

Table 1. XRF-ICP Mn Calibration Data: Calibration equations (least-squares linear fits) relating concentration from ICP-ES method to counts from X-Ray fluorescence method, Pearson coefficients (r^2 value) and number of samples used to make the correlation are shown to the right of the equation. Average Coefficient of Variation for Mn: Average coefficient of variation (CV) ratios for Mn XRF counts (XRF CV) based on duplicate scans analyses every ~10 cm of scanned core and duplicates from Inductively Coupled Plasma Emission Spectrometry (ICP-ES) sent to SGS (Section 2.7). Note average errors (CV) for XRF counts of Mn are slightly higher than other elements previously measured (Ingram et al., 2010), likely a result of lower concentration of Mn in these marine sediments.

Depth of Mn Peak in Sediment

HAT-01	HAT-02	HAT-03	HAT-04	HAT-05	PEL-02	PEL-15	PEL-04	PEL-08	PEL-07
188	*172*	*48*	7	*208*	*74*	*53*	7	*126*	*130*
191	*177*	*53*	*78*	*218*	136	197	*78*	*179*	*141*
200	*181*	118	*84*	260	157	359	*84*	201	*189*
	189	151	*96*		236	373	*96*	309	*212*
	238	217	141				*141*	322	277
	243	262	147				*147*	417	402
			162				162	624	575
			166				166		599
			172				174		
			242				242		
			283						

Calculated Concentration of Authigenic Mn Peak

HAT-01	HAT-02	HAT-03	HAT-04	HAT-05	PEL-02	PEL-15	PEL-04	PEL-08	PEL-07
3356	*1541*	*585*	660	*3066*	*3463*	*345*	565	*1138*	*1628*
2806	*1949*	*930*	*1103*	*315*	622	544	*1008*	*441*	*739*
1136	*856*	410	*969*	935	852	618	*874*	1444	*2020*
	495	738	*614*		410	937	*519*	451	*1372*
	1389	512	888				*793*	450	649
	1770	211	1191				*1096*	581	503
			835				740	1013	961
			1230				1135		1406
			1330				1266		
			344				249		
			491						

Table 2. Top: Depth in cm below the seafloor to discrete each Mn-layer for each coring location. Mn-layers are selected using a 50 percent cut-off above background concentration levels. The concentration (in ppm) for each layer (see depth above) is calculated from XRF core scans and using calibration equations for each respective core transect. Mn-layers (within Unit I) are shown in italics. Ideally each core would be calibrated, yet cores from each transect were scanned in rapid succession; hence values above are a reasonable estimate of concentration.

Mn Species Data to solve for Mn Mineral

Core	Depth	Dissolution	Mn (ppm)	Ti (wt.%)	Mn/Ti	Mn EF	E. Mn (ppm)	Composition	Mn (ppm)	% Total (from ppm)
PEL-07	130	Untreated	0.2800	0.29	0.965	5.393	2281	Oxyhydroxides	160	5.7143
PEL-07	130	Step 1	0.2640	0.31	0.851	4.756	2085	Carbonates	2373	84.7500
PEL-07	130	Step 2	0.0267	0.36	0.074	0.414	NA	insoluble clay	267	9.5357
PEL-07	189	Untreated	0.1990	0.28	0.710	3.969	1489	Oxyhydroxides	60	3.0151
PEL-07	189	Step 1	0.1930	0.31	0.622	3.477	1375	Carbonates	1674	84.1206
PEL-07	189	Step 2	0.0256	0.33	0.077	0.433	NA	insoluble clay	256	12.8643
PEL-07	212	Untreated	0.1670	0.28	0.596	3.331	1169	Oxyhydroxides	90	5.3892
PEL-07	212	Step 1	0.1580	0.29	0.544	3.043	1061	Carbonates	1331	79.7006
PEL-07	212	Step 2	0.0249	0.29	0.085	0.480	NA	insoluble clay	249	14.9102
PEL-07	577	Untreated	0.1610	0.27	0.596	3.330	1127	Oxyhydroxides	0	0.0000
PEL-07	577	Step 1	0.1610	0.28	0.575	3.212	1109	Carbonates	1239	76.9565
PEL-07	577	Step 2	0.0371	0.32	0.115	0.648	NA	insoluble clay	371	23.0435
PEL-07	599	Untreated	0.2350	0.27	0.870	4.861	1867	Oxyhydroxides	180	7.6596
PEL-07	599	Step 1	0.2170	0.27	0.803	4.489	1687	Carbonates	1753	74.5957
PEL-07	599	Step 2	0.0417	0.27	0.154	0.863	NA	insoluble clay	417	17.7447
PEL-07	Avg.	Untreated	0.2084	0.278	0.749	4.187	1586	Oxyhydroxides	98	4.3556
PEL-07	Avg.	Step 1	0.1986	0.292	0.680	3.799	1463	Carbonates	1674	80.0247
PEL-07	Avg.	Step 2	0.0312	0.314	0.099	0.555	NA	insoluble clay	312	15.6197

Table 3. Table displays Mn concentrations from ICP-ES (reported by SGS) on sediment samples from authigenic Mn-layers within Core PEL-07. Sufficient sediment was taken from 5 depths, where Mn-layers occur, and subjected to a two-step chemical dissolution procedure to first remove sold-phase oxides, then carbonates (see methods). Mn enrichment factor (Mn-EF) and "excess" Mn (E. Mn) is also determined for each layer (see methods; Chun et al., 2010), note NA for insoluble clay as "excess" Mn is defined as the amount which exceeds the siliciclastic clay fraction. The sample was measured for Mn concentration following each step, and untreated sediment samples. The Mn concentration for oxides, carbonates and insoluble clay, are inferred from that measured after each extraction. The percent of total is ratio of Mn concentration of each component (oxide, carbonate and clay) to the total Mn from the untreated sample (see far right percentages derived from ppm).

.

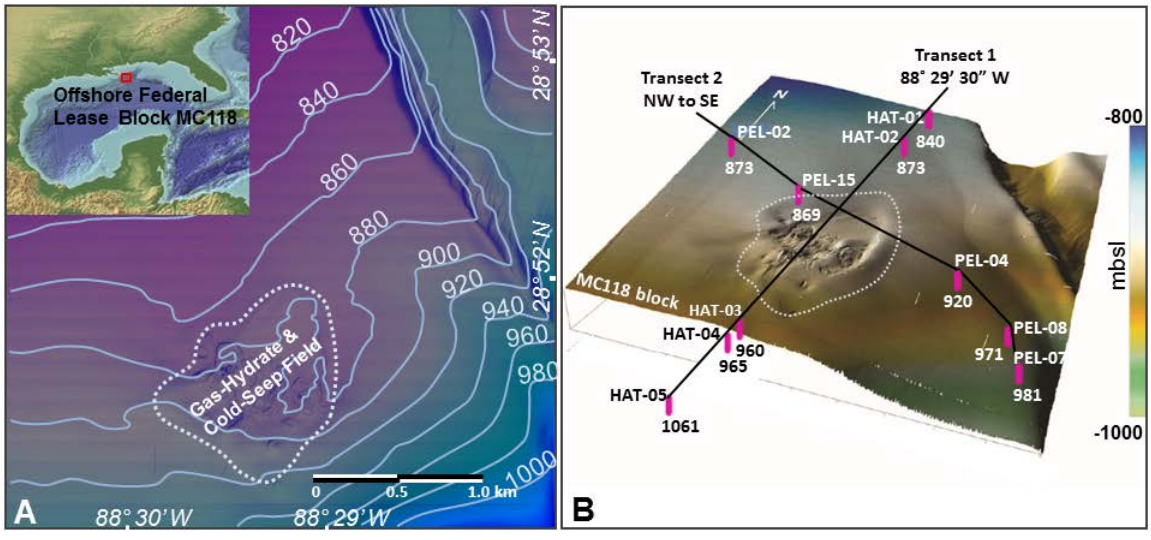

Figure 1. *Panel A*: Bathymetric map of the study area (Block MC118) with labeled contours (light blue) in meters water depth (base map courtesy of Ken Sleeper) with inset digital elevation and bathymetry map (top left; NOAA geophysical data center image) of the Gulf of Mexico Region. Bathymetry provided by the Gulf of Mexico Hydrate Research Consortium, (modified after Sleeper et al., 2006). The location of MC118 offshore federal lease block is indicated by the red box in the inset map. The extent of the studied gas hydrate-cold seep field is outlined by the dashed line and is characterized by an area with gas vents, seafloor pockmark features, petroleum seepage, shallow faults, carbonate hard-grounds and gas hydrate deposits. *Panel B*: Bathymetric map of the study site with the location of cores collected during cruises on the R/V *Hatteras* and R/V *Pelican*; base map image is courtesy of the Gulf of Mexico Hydrate Research Consortium. Cores are indicated as vertical magenta lines, with core identification (above) and water depth (in meters) below the core symbol. The edge of the gas hydrate-cold seep field is outlined by a thin dashed white line, black lines connecting cores indicate transects taken by the R/V *Hatteras* ("Hatteras Transect") and R/V *Pelican* ("Pelican Transect"). The color bar on the far right indicates water depth.

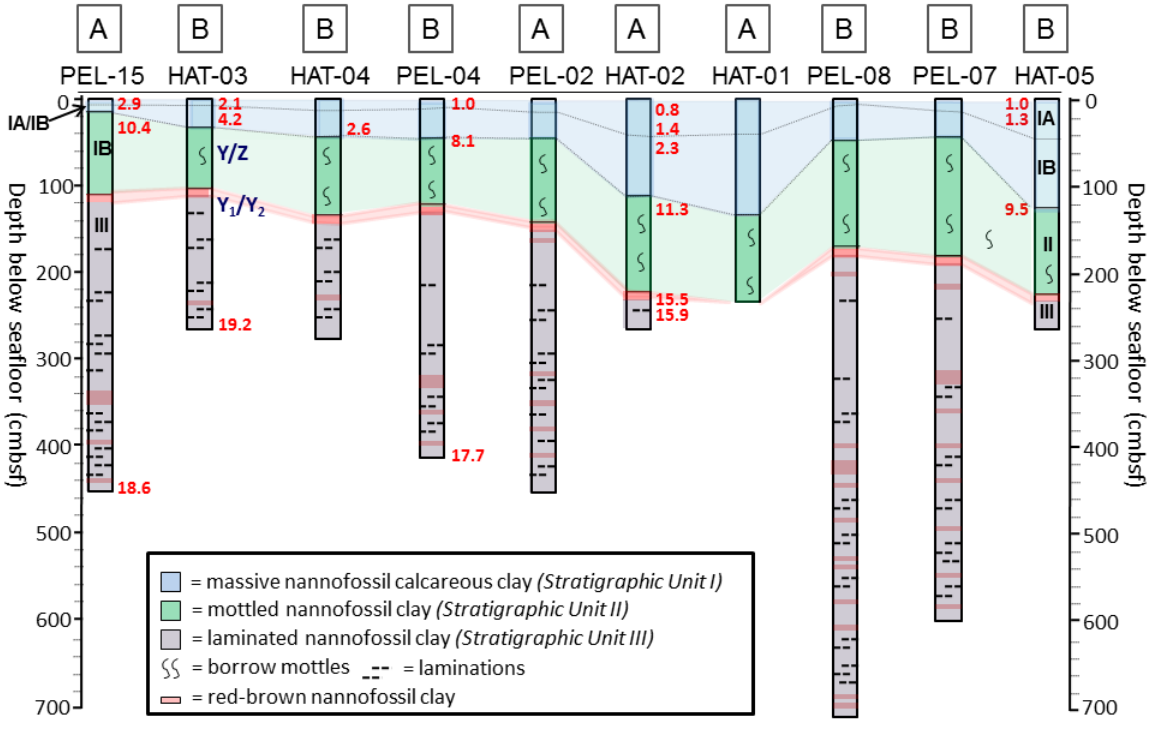

Figure 2. Stratigraphic correlation of marine sediments collected across the MC118 study area. Cores are arranged by increasing distance (left to right) from the gas hydrate-cold seep field. The "A" and "B" designation at the top of each core indicate whether the site is located above or below (respectively) the hydrate/cold-seep field. Dates obtained via AMS radiocarbon analysis of planktonic foraminifera (red, Ka) and foraminiferal biostratigraphic boundaries (dark blue, Y/Z ~ 10 Ka and Y_1/Y_2 ~ 15 Ka) are shown alongside their stratigraphic position; all reported ages are in calendar kilo-years BP. Three distinct stratigraphic units are identified as follows: Unit I (light blue) = massive nannofossil calcareous clay; Unit II (light green) = mottled nannofossil clay; Unit III (gray) = laminated nannofossil clay containing reddish-brown nannofossil clay layers (red lines). A distinct ~5-cm thick reddish clay layer with highly "reworked" (pre-Quaternary) nannofossils defines the top of Unit III.

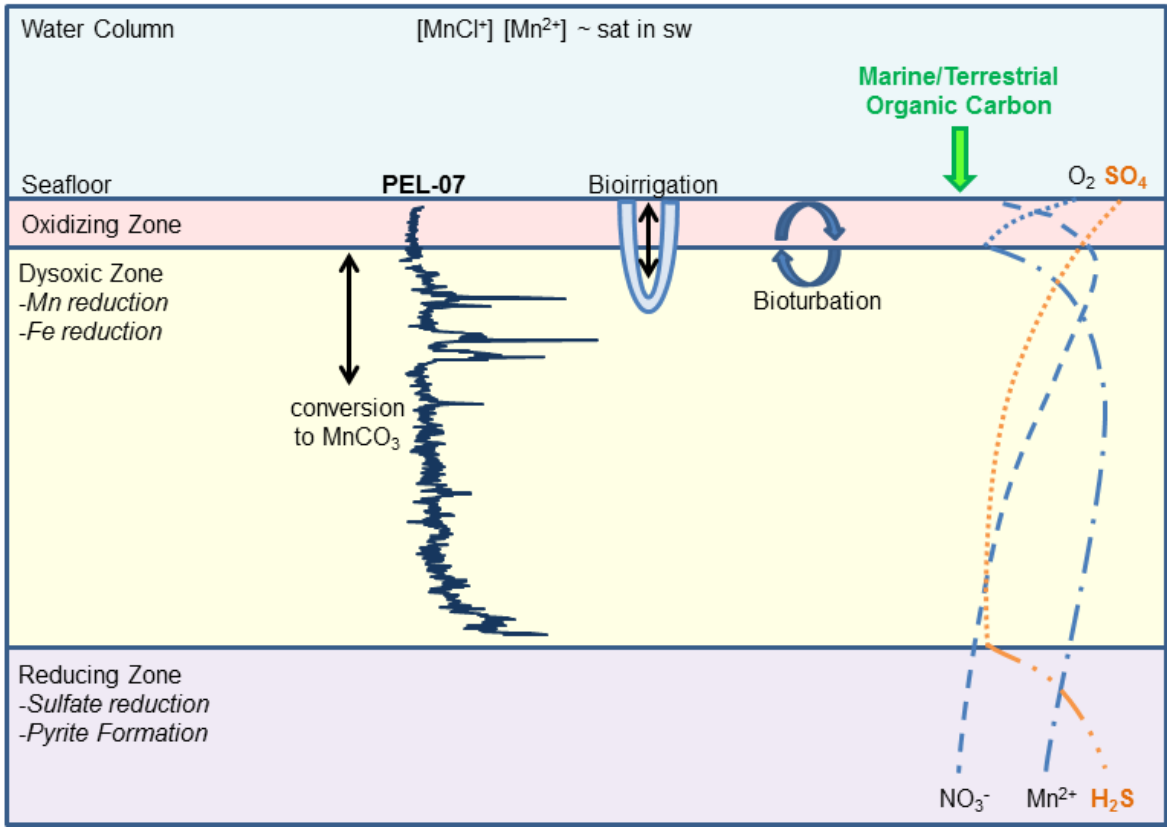

Figure 3. A simplistic conceptual model of manganese cycling and generalized pore-water profiles in oxygenated to reducing marine sediments. The mobility of reactive Mn and its redox chemistry can be summarized by the following (1) burial of Mn-oxides into dysoxic pore waters, (2) reducing MnO_2 (Mn IV) to Mn^{2+} (Mn II), (3) remobilization and upward diffusion of dissolved Mn^{2+}, followed by (4) re-precipitation across a redox front, approximately where oxygen depletes, forming solid-phase authigenic Mn minerals (Froelich et., 1979). Also shown, bioirrigation and bioturbation are important factors in vertically mixing of sediments and pumping of oxygen into dysoxic sediments, facilitating repeated Mn cycling (Aller, 1990). This record (PEL-07 Mn XRF profile) is placed entirely within the dysoxic zone, as all Mn-layers are predominately carbonates (See Results). It is hypothesized (See Discussion) that former authigenic oxides are quickly converted to carbonates where sufficient carbonate exist and when seafloor is above the Calcium Carbonate Compensation depth (such as MC118). This figure is for conceptual purposes only as the (modern) redox boundary and pore-water profiles were not measured. Yet, it is likely that oxygen depletion occurs in very shallow sediments at the site ~5-10 cmbsf (Hu, et al., 2011; Diaz and Trefry, 2006).

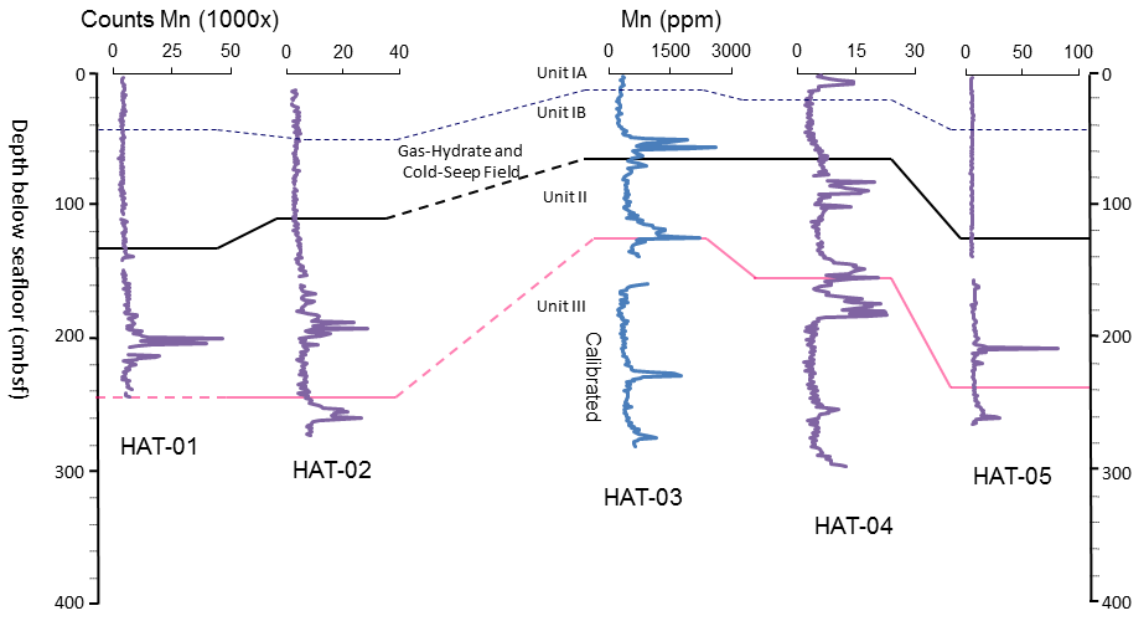

Figure 4. Profiles of down-core concentration and XRF counts of elemental Mn derived from XRF scanning of cores across Transect 1 onboard the *R/V Hatteras* (Figure 1). Core HAT-03 (blue curve) displays Mn concentration (ppm) calculated by calibration of XRF counts to Inductively Coupled Plasma Emission Spectrometry (ICP-ES) Mn-concentration data. All other profiles (purple curves) display Mn counts (1000x). This is an N-S transect from Core HAT-01 (on left) to HAT-05 (on right). The solid black line separates Stratigraphic Unit I from Unit II and is defined by a shift in carbonate content. The thin dashed blue line separates informal stratigraphic units IA and IB, also defined by carbonate content. The light-red line is the depth to the red band, a chronostratigraphic marker (Ingram et al., 2010) defining the base of Stratigraphic Unit II.

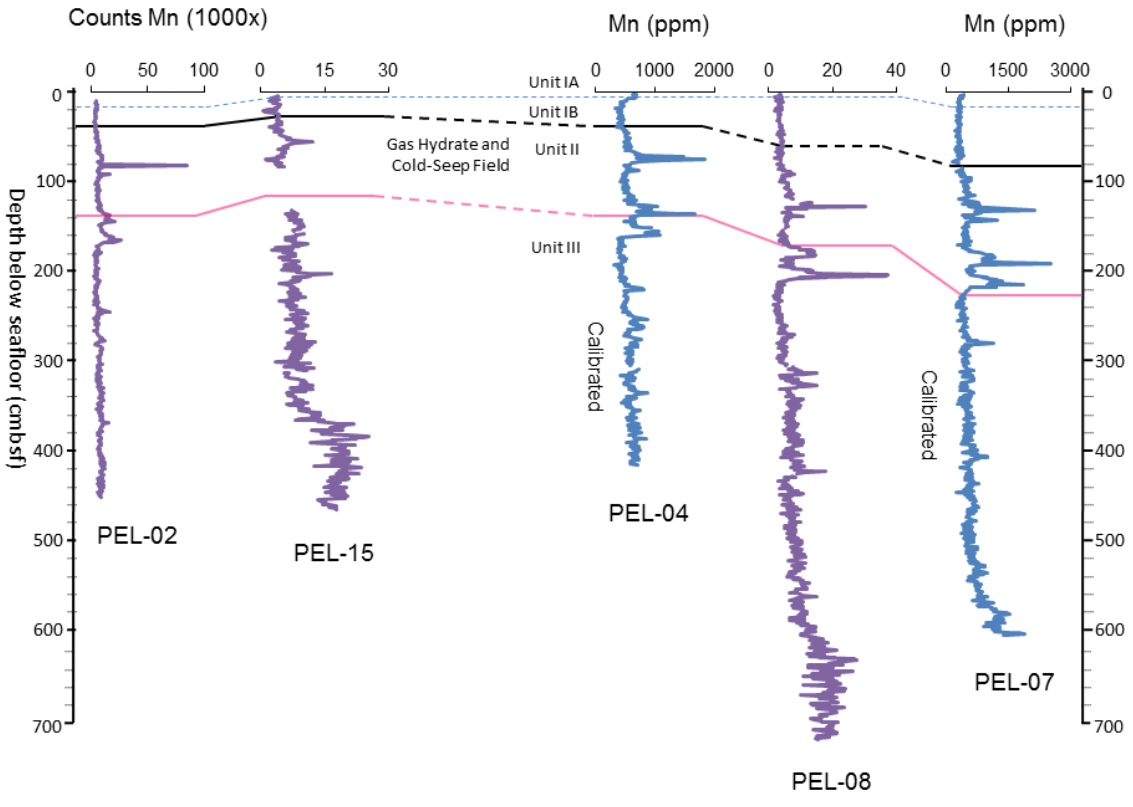

Figure 5. Profiles of down-core concentration and XRF counts of elemental Mn derived from XRF scanning of cores across Transect 2 onboard the *R/V Pelican* (Figure 1). Core PEL-04 and PEL-07 (blue curves) displays Mn concentration (ppm) calculated by calibration of XRF counts to Inductively Coupled Plasma Emission Spectrometry (ICP-ES) Mn-concentration data. All other profiles (purple curves) display Mn counts (1000x). This is a northwest-southeast transect from Core PEL-02 (on left) to PEL-07 (on right). The solid black line separates Stratigraphic Unit I from Unit II and is defined by a pronounced shift in $CaCO_3$ content. The thin dashed blue line separates informal stratigraphic units IA and IB; is also defined by changes in $CaCO_3$ content. The light-red line is the depth to the red band, a visible chronostratigraphic marker (Ingram et al., 2010) defining the base of Stratigraphic Unit II.

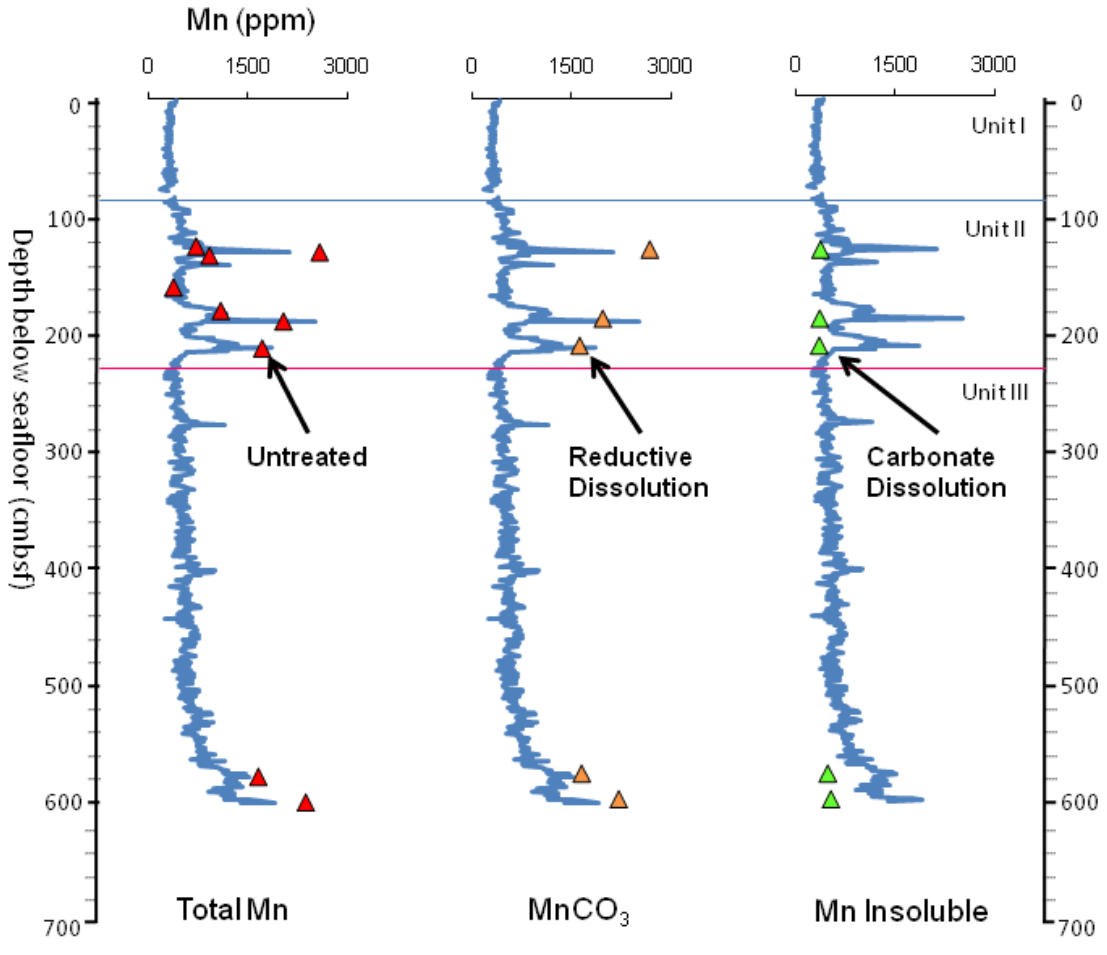

Figure 6. Calibrated XRF-Mn profile (blue curve) for Core PEL-07; manganese concentrations (triangles, same scale) following wet chemistry procedures to operationally determine the likely minerals associated with Mn-layers. From left to right, the red triangles are from untreated sediment samples, orange triangles are following the reductive dissolution step, and the green triangles are following both reductive cleaning and carbonate dissolution steps. Reductive dissolution removes Mn-oxides, hence the remaining concentration comprises insoluble clays and carbonate minerals. The acid-dissolution step removes carbonates, thus only insoluble clay residue remain. The solid blue line and the solid red line are the same as is presented in Figure 4 and 5 (Ingram et al., 2010).

Dissertation Conclusions

Several conclusions are central to one or more of presented studies, yet on a more fundamental level this research seeks to relate local and global events to the depositional environment and geochemistry at MC118. The conclusions formed at this site have broad implications and application to other similar offshore settings, where interactions between sedimentation, geochemistry and seafloor cold seeps are considered important. More specific research themes include linkages, if any, between erosion of the slope at MC118, hydrocarbon expulsion from the seep site and/or seafloor warping from salt diapirism. The first of these topics, linkages of slope erosion to gas hydrates, has received much interest in the scientific community. This concept is considered further by re-visiting the initial goals of this research. The specific conclusion of this research can be summarized into topics, which follow chapter themes (1) sedimentation, (2) sedimentary geochemistry and (3) redox processes.

The original purpose of this research was to obtaining a sedimentary record with sufficient spatial distribution across the MC118 study site to determine if the slope here was influenced by the nearby gas hydrates, cold seeps and/or salt diapirism, which are all associated with MC118. The goal was to document the age of the sediments recovered from coring along a depositional dip orientation across MC118. The reason for this approach was to characterize the sedimentary record upslope and downslope from the MC118 field area (containing gas hydrates, cold seeps and a shallow salt diapir; Figures 1-2 in Chapter 1), and to assess any differences. If considerable variation was discovered (upslope from downslope) then the seafloor here may have been affected by

erosional events perhaps induced connected to the MC118 field, however this was not observed. In fact, there is no evidence in this dataset to support slope destabilization at MC118. There are no apparent "clear" unconformable surface(s), slides, slumps or debris flows from bathymetric and/or core data. Yet, more subtle spatial variations are apparent from the established chronostratigraphy (Chapter 1). However the first study (Chapter 1) demonstrates thinning of sediments adjacent to the field and/or "draping" of over the MC118 bathymetric rise (see Section 1.1).

1.1 Sedimentation at MC118

The results of the first study reveal several conclusions about the depositional history and interactions between the field (with associated salt diapirism) and sedimentation at MC118. As mentioned above, there is no indication of any "major" erosional event or failure of the seafloor originating from the MC118 field. The term "major" is applied here to refer to sufficiently large-scale (10s to 100s of meters) erosional features (permanent scars), visible from bathymetric mapping and/or buried erosional boundaries (unconformities) apparent from seismic and/or core data. This conclusion is based on the observation that the same stratigraphic sequence can be observed upslope (onshore) and downslope (offshore) from the MC118 field. More specifically, the $CaCO_3$-rich Holocene section lies above the late Pleistocene at all core sites (Figures 3-5 in Chapter 1; Figures 5-6 in Chapter 2) and its consistent presence indicates it was not removed after deposition. Hence, a reasonable interpretation is that the seafloor slope and MC118 field was relatively stable from the late Pleistocene to Holocene. However, examining the results of Chapter 1 more closely, there are clear

spatial patterns, which suggest sedimentation is linked to the MC118 field through processes associated with the field such as salt diapirism (see below).

Detailed evaluation of the chronostratigraphy around the study site reveals reduced sedimentation in locations immediately adjacent to the MC118 field. Sediment isopach maps (Figures 7-9 in Chapter 1) demonstrate that greater sediment thicknesses and higher sedimentation rates occur farther from the field. The observed spatial pattern of stratigraphic thinning likely involves complex interactions between subsurface salt deposits, fluid migration and sedimentation processes. It is possible that small-scale sediment remobilization and/or non-deposition occurred in close proximity to the field (or over the elevated mound). Thus, the field itself likely existed at times as a minor bathymetric high (due to the salt), where sediments could "drape" over this raised feature. An elevated bathymetric feature, which sits above the surrounding seafloor, is a higher energy setting where sediments could redistribute off of the high and down the flanks of the mound. In this scenario, sediments should preferentially accumulate farther from the field area. Thus, the MC118 field (including salt diapirism) seems to invoke minor controls on sedimentation as opposed to destabilizing the seafloor. Also documented are changes in bulk geochemistry from Ca/Ti core scans (Figure 4-5 in Chapter 1), reflecting sea-level rise and regional factors such as Mississippi delta lobe switching. This topic is addressed more quantitatively in the second study (Chapter 2), which delineates the chemical components of sedimentation.

1.2 Sedimentary Geochemistry at MC118

Documentation of sedimentary geochemistry was the focus for the second study (Chapter 2). The main goals were to quantitatively define the components of marine sedimentation at MC118 (terrigenous versus pelagic), and to identify the source of organic matter accumulation. This was made possible by interpreting multiple geochemical proxies (Ti, $CaCO_3$, TOC and residual clay), which were used to delineate lithogenic versus pelagic inputs, and relate these results to the depositional history of MC118 (Section 1.2 in Chapter 2). This study makes use of the previously established chronostratigraphy at MC118 (Chapter 1) to interpret the geochemical proxies in a chronological context. Given this, a chemical stratigraphy including burial fluxes, was established for each proxy (listed above) within each of the established stratigraphic units (IA, IB, II and combine units I&II). Together, these data were used to assess sediment provenance at MC118 (terrigenous versus pelagic), which was controlled by global, regional and local geologic controls such as sea-level rise, delta lobe switching and the MC118 field (with associated salt diapirism).

Quantification of sedimentary geochemistry has defined clear changes in composition of MC118 sediments through time, and identified spatial trends in the accumulation of pelagic and terrestrial components as well. Foremost, a distinct shift in geochemistry was observed from markedly clay-rich sediments during the interval from (14 to 9.5 Ka), to substantially more $CaCO_3$-rich during the more recent Holocene (9.5 Ka to present). This shift is attributed to reduction in the clay flux, which is interpreted as linked to sea level and proximity to the Mississippi delta, and importantly is not the result of changes in the pelagic biogenic flux. Study 2 (Chapter 2) carefully documents

this result by demonstration of consistent carbonate accumulation in concert with dramatic changes in sedimentation rate and the clay flux. This reduction in terrigenous inputs (late Pleistocene-Holocene) is attributed to rapid sea level rise during the deglacial and an associated retreating paleo-shoreline. This conclusion is supported by decreased burial of lithogenic inputs Ti and residual clay. While terrigenous sedimentation controls changes in chemical composition, spatial patterns are influenced by local depositional trends associated with the MC118 field and associated salt diapirism (see Chapter 1). Hence spatially, burial fluxes display patterns similar to overall sedimentation.

Organic matter burial at MC118 was also a key topic in the second chapter; results indicate that the flux of TOC is similar to overall sedimentation and to lithogenic inputs (Chapter 2). The MC118 record demonstrates that organic carbon content is much lower in the more recent sediments (9.5 Ka to present) as compared to older sediments (14 - 9.5 Ka). Mass accumulation rates also show that TOC accumulation decreases with time while $CaCO_3$ accumulation remains relatively constant (see Figure 7 of Chapter 2). Given that $CaCO_3$ is a pelagic input (see Section 1.3 in Chapter 2) organic matter burial at MC118 is connected to terrigenous sedimentation; hence just as for lithogenic inputs, organic carbon accumulation is influenced by sea-level change and delta lobe switching.

Additional data from Rock Eval pyrolysis (organic matter typing) was used to support the above conclusion. It was discovered that organic matter from the late Pleistocene interval at MC118 (from Core HAT-03) yielded a terrigenous-dominated

geochemical fingerprint. Conversely, Holocene sediments were shown to contain a mixed type II/III signal (mixed terrigenous and marine organic matter). Based on this result, it is apparent that terrigenous organic matter is present throughout the MC118 sedimentary record, yet Pleistocene-age sediments contain far more terrigenous organic matter. In summary, organic matter typing is consistent with inorganic geochemistry at MC118, which also suggests enhanced terrigenous sedimentation during the interval from 14 to 9.5 Ka, transitioning to more pelagic sedimentation in the later Holocene interval (9.5 Ka to present) primarily due to reduced clay dilution.

In summary, documentation of sedimentary geochemistry at MC118 reveals a clear reduction of terrigenous inputs (terrestrial organics and lithogenic inputs) from the late Pleistocene to the Holocene based on organic and inorganic datasets. This shift in sediment composition with time is also coincident with reduction in organic carbon burial at the site, which in turn is driven by global sea-level rise and marine transgression along the gulf coast. More Recent variability in sediment geochemistry (late Holocene: 2.3 kilo-years to present) is the result of a shifting Mississippi delta, which is best recorded at the site by lithogenic inputs that, in turn, dilutes the biogenic pelagic ($CaCO_3$) inputs.

1.3 Redox Processes at MC118

In the final chapter, redox processes are investigated through documentation of apparent authigenic manganese accumulations. First, it is necessary to establish that highly-enriched manganese layers are formed through *in situ* redox processes at the

MC118 site. These accumulations (Mn-layers) are more than an order of magnitude more concentrated than "background" Mn; more importantly they also occur independently from deposition. Hence, there is no consistent stratigraphic occurrence of the Mn-layers at MC118. Given this, they are interpreted as authigenic deposits. Manganese is a known redox sensitive element in dysoxic sediments, which in the solid-phase (MnO_2) is used as an electron acceptor during early oxidation of organic matter (see Section 1.2 in Chapter 3). The mineralogy and origin of these Mn-layers is considered in detail in this final study (see below).

To understand these authigenic deposits wet-chemistry techniques were used to operationally determine probable composition. The results of this effort indicate that the Mn-layers are predominantly manganese-rich carbonates, Ca-$Mn(CO_3)_2$, and/or rhodochrosite, $Mn(CO_3)$. Given multiple working hypotheses proposed to explain formation of these deposits (see section 1.1 in Chapter 3), several conclusions are possible regarding the Mn-layers. (1) The Mn-layers are authigenic deposits forming *in situ* in association with a variable redox front occurring independently of deposition. (2) The Mn-layers are Mn-rich carbonates, Ca-$Mn(CO_3)_2$, and/or rhodochrosite, $Mn(CO_3)$, which contribute to nearly all "excess" (non siliciclastic) Mn. (3) Mn-layers may (or may not) have initially formed as oxides or oxyhydroxides, yet they are presently carbonates in MC118 sediments. (4) Mn-layers are not "reworked" nor do they originate from the MC118 field. Finally, an important hypothesis is presented, which suggests that Mn-layers at MC118 are sensitive to stability of sedimentation (through redox changes and switching of conditions of non-steady versus steady-state conditions).

Appendix A

Additional Tabulated Data

Numerous tables and data were not included in any of the dissertation chapters and others were included but were reduced in size and thus, not all data was presented. The reason may have been limited space due considerations for preparing the various studies for publication. It is the purpose of this appendix to provide additional tabulated data not available in the previous chapters. XRF measurements are an exception, which include measurement for every cm of scanned core. The immense size of this XRF dataset (over 30,000 discrete measurements) renders it impractical to place into a table(s) or within any single document. Instead, this data is better captured by figures (Appendix B). Data from CO_2 coulometry is also too extensive to include in this section and is summarized with cross plots (also in Appendix B). With respect to the XRF data, average calibrated-XRF concentrations and average burial flux values for each of the defined stratigraphic units are included in other appendices. Error for XRF core scanning is quantified by determining the coefficients of variation (CV), more precisely the CV for each core and element are included here. Tables below may apply to particular chapters and/or results and are compiled in no particular order.

Average calibrated-XRF concentrations

Unit IA	HAT-01	HAT-02	HAT-03	HAT-04	HAT-05
$CaCO_3$ (wt. %)	20.188	17.099	19.216	21.840	20.523
TOC (wt. %)	0.785	0.706	0.365	0.484	1.058
Fe (wt. %)	2.657	3.011	2.984	2.780	2.933
Ba (ppm)	398	410	421	416	406
Ti (wt. %)	0.183	0.193	0.213	0.191	0.202
Mn(ppm)	305	339	342	635	389
Al (wt. %)	5.405	5.074	5.943	5.037	5.204

Unit IA	PEL-02	PEL-15	PEL-04	PEL-08	PEL-07
$CaCO_3$ (wt. %)	13.050	21.189	12.790	26.549	17.000
TOC (wt. %)	1.285	1.271	0.957	1.132	1.132
Fe (wt. %)	3.225	3.351	3.291	2.858	3.240
Ba (ppm)	436	417	484	427	434
Ti (wt. %)	0.247	0.253	0.244	0.225	0.237
Mn(ppm)	476	409	653	414	343
Al (wt. %)	4.940	6.723	6.279	5.853	6.563

Unit IB	HAT-01	HAT-02	HAT-03	HAT-04	HAT-05
$CaCO_3$ (wt. %)	25.557	28.393	26.586	28.173	29.661
TOC (wt. %)	0.658	0.834	0.260	0.546	0.883
Fe (wt. %)	2.671	2.467	2.642	2.640	2.567
Ba (ppm)	404	402	420	429	419
Ti (wt. %)	0.187	0.172	0.201	0.188	0.187
Mn(ppm)	290	314	481	238	388
Al (wt. %)	5.563	4.605	5.930	5.363	5.102

Unit IB	PEL-02	PEL-15	PEL-04	PEL-08	PEL-07
$CaCO_3$ (wt. %)	22.429	26.615	25.393	31.128	23.947
TOC (wt. %)	1.089	0.742	0.813	1.066	1.066
Fe (wt. %)	2.851	3.034	2.844	2.821	2.910
Ba (ppm)	437	433	432	442	426
Ti (wt. %)	0.233	0.246	0.224	0.229	0.226
Mn(ppm)	455	411	430	428	311
Al (wt. %)	5.056	7.140	6.323	5.932	6.531

Unit II	HAT-01	HAT-02	HAT-03	HAT-04	HAT-05
$CaCO_3$ (wt. %)	11.132	11.119	12.560	12.699	13.398
TOC (wt. %)	1.178	1.194	1.198	1.017	1.595
Fe (wt. %)	3.361	3.347	3.451	3.364	3.427
Ba (ppm)	435	437	455	460	475
Ti (wt. %)	0.231	0.230	0.241	0.235	0.237
Mn(ppm)	603	590	614	573	513
Al (wt. %)	6.184	5.637	6.733	6.072	6.097

Unit II	PEL-02	PEL-15	PEL-04	PEL-08	PEL-07
$CaCO_3$ (wt. %)	11.350	9.281	11.068	12.864	12.864
TOC (wt. %)	1.447	0.844	1.374	1.187	1.187
Fe (wt. %)	3.408	3.910	3.509	3.491	3.418
Ba (ppm)	477	454	467	450	477
Ti (wt. %)	0.259	0.290	0.259	0.260	0.250
Mn(ppm)	660	487	607	526	626
Al (wt. %)	5.353	7.942	7.065	6.777	7.211

14 k record	HAT-01	HAT-02	HAT-03	HAT-04	HAT-05
$CaCO_3$ (wt. %)	18.151	16.922	18.948	18.491	20.937
TOC (wt. %)	0.902	0.908	0.737	0.766	1.017
Fe (wt. %)	2.989	3.048	3.088	3.080	3.012
Ba (ppm)	417	423	442	446	442
Ti (wt. %)	0.207	0.208	0.223	0.216	0.212
Mn(ppm)	435	473	545	470	445
Al (wt. %)	5.850	5.259	6.349	5.767	5.564

14 k record	PEL-02	PEL-15	PEL-04	PEL-08	PEL-07
$CaCO_3$ (wt. %)	13.749	13.284	14.670	18.658	17.168
TOC (wt. %)	1.336	0.845	1.104	1.114	1.114
Fe (wt. %)	3.282	3.678	3.335	3.249	3.226
Ba (ppm)	466	448	459	447	456
Ti (wt. %)	0.253	0.278	0.250	0.249	0.240
Mn(ppm)	607	466	565	490	493
Al (wt. %)	5.269	7.740	6.850	6.470	6.927

Table 1. The above tables are display average calibrated-XRF concentrations for each element, TOC and $CaCO_3$ across each of the defined stratigraphic intervals, e.g. units IA, IB, II and combine the complete 14-k record. All concentration values are in wt. %, with the exceptions of the elements Mn and Ba, which are in ppm due to trace concentrations. All values are based on specific ICP-ES calibration to each core, e.g. calibration procedure outlined in Chapter 2 of the dissertation. The exception to the above is for Core PEL-08, which was not calibrated and here concentration values are based on the calibration equation from the nearest offset core, PEL-07.

Density Core PEL-15

	Depth (cm)	wet weight (g)	dry weight (g)	Pore-fluid Mass (g)	Dry Mass (g)	Dry Bulk Density (g/cm^3)
Unit I	10	18.528	8.371	10.526	8.003	1.771
" "	20	16.544	7.456	9.417	7.127	1.581
" "	30	17.701	7.899	10.157	7.544	1.690
Unit II	40	18.920	9.268	10.002	8.918	1.821
" "	50	18.598	9.038	9.906	8.691	1.788
" "	100	17.634	8.101	9.879	7.755	1.688
" "	150	19.070	9.871	9.533	9.537	1.843
" "	200	19.867	10.193	10.025	9.842	1.918
" "	300	18.949	10.722	8.526	10.424	1.842
" "	400	19.449	10.795	8.968	10.481	1.888

Pore-Fluid Mass	Ms =	corrected dry mass
Ms = M - Mf = (Md - s*M)/(1 - s)	M =	total wet mass
	Mf =	pore-fluid mass
Corrected dry mass	Md =	dry mass uncorrected
Ms = M - Mf	s =	salinity (0.035)
	Vs =	volume (10 cm^3)
Density	Pd =	Density (g/cm^3)
Pd = Ms/Vs		

Table 2. Density measurement from Core PEL-15 (top) at each depth in an effort to determine density of the sediments at MC118, the procedure used to determine the dry bulk density of marine sediments corrected for salt is outline by Dadey et al., (1992), and is followed here (Section 2.2 of Chapter 2, e.g. Ingram et al., unpublished). The equation as used by Dadey et al., (1992) is also provided above. Note the average dry bulk density for each interval, e.g. Unit I = 1.716 g/cm^3 and Unit II = 1.828 g/cm^3.

Mass Accumulation Rates

Unit IA	HAT-01	HAT-02	HAT-03	HAT-04	HAT-05
$CaCO_3$	49.704	45.926	5.735	14.665	50.531
TOC	1.932	1.895	0.109	0.325	2.604
Fe	6.543	8.086	0.891	1.867	7.220
Ba	98	110	13	28	100
Ti	0.450	0.517	0.063	0.128	0.497
Mn	75	91	10	43	96
Al	13.308	13.628	1.774	3.382	12.812

Unit IA	PEL-02	PEL-15	PEL-04	PEL-08	PEL-07
$CaCO_3$	6.816	6.323	3.817	7.923	15.220
TOC	0.671	0.379	0.286	0.338	1.014
Fe	1.684	1.000	0.982	0.853	2.901
Ba	23	12	14	13	39
Ti	0.129	0.075	0.073	0.067	0.212
Mn	25	12	20	12	31
Al	2.580	2.006	1.874	1.747	5.876

Unit IB	HAT-01	HAT-02	HAT-03	HAT-04	HAT-05
$CaCO_3$	51.773	40.602	31.048	29.544	58.674
TOC	1.332	1.192	0.304	0.573	1.746
Fe	5.411	3.528	3.086	2.769	5.078
Ba	82	57	49	45	83
Ti	0.379	0.246	0.235	0.197	0.370
Mn	184	141	176	78	240
Al	11.269	6.585	6.925	5.623	10.092

Unit IB	PEL-02	PEL-15	PEL-04	PEL-08	PEL-07
$CaCO_3$	15.502	11.418	19.367	40.062	40.522
TOC	0.753	0.318	0.620	1.372	1.804
Fe	1.970	1.302	2.169	3.630	4.925
Ba	30	19	33	57	72
Ti	0.161	0.106	0.171	0.295	0.382
Mn	98	55	103	173	165
Al	3.494	3.063	4.822	7.634	11.051

Unit II	HAT-01	HAT-02	HAT-03	HAT-04	HAT-05
$CaCO_3$	49.745	55.105	30.614	43.849	60.956
TOC	5.266	5.918	2.919	3.510	7.255
Fe	15.017	16.585	8.412	11.617	15.591
Ba	194	217	111	159	216
Ti	1.033	1.139	0.587	0.810	1.077
Mn	527	572	293	387	457
Al	27.631	27.936	16.412	20.966	27.741

Unit II	PEL-02	PEL-15	PEL-04	PEL-08	PEL-07
$CaCO_3$	47.951	34.307	41.364	57.481	54.869
TOC	6.113	3.119	5.134	5.304	5.063
Fe	14.397	14.453	13.114	15.599	14.578
Ba	201	168	175	201	203
Ti	1.095	1.072	0.968	1.163	1.067
Mn	545	352	444	460	522
Al	22.615	29.359	26.405	30.283	30.756

14 k record	HAT-01	HAT-02	HAT-03	HAT-04	HAT-05
$CaCO_3$	52.527	46.823	27.177	32.389	60.590
TOC	2.612	2.513	1.057	1.342	2.944
Fe	8.651	8.434	4.429	5.396	8.716
Ba	121	117	63	78	128
Ti	0.598	0.575	0.320	0.379	0.613
Mn	766	797	476	501	783
Al	16.931	14.552	9.107	10.101	16.101

14 k record	PEL-02	PEL-15	PEL-04	PEL-08	PEL-07
$CaCO_3$	24.432	19.053	23.834	39.787	40.968
TOC	2.374	1.213	1.793	2.375	2.658
Fe	5.833	5.275	5.419	6.929	7.699
Ba	83	64	75	95	109
Ti	0.450	0.399	0.406	0.531	0.574
Mn	657	407	558	636	716
Al	9.363	11.101	11.128	13.798	16.529

Table 3. Mass Accumulation Rates (burial fluxes) determined for each time interval, Unit IA, IB, II and 14-k record. The dry bulk density (e.g., Table 2: Appendices B), averages for Unit I and II are multiplied by average XRF-calibrated concentration (e.g., Table 1: Appendices B) and multiplied by the thickness in cm, which then divided by years to deposit the respective section of sediment (e.g., Ingram et al., 2010), the established geochronology for the MC118 site. Together these values combine provide the mass accumulation rate, which sometimes referred to as the burial flux and is determined for $CaCO_3$, TOC and several elements (Al, Fe, Ti and Ba). These calculated values determined for each coring site (above tabulated data), and then contoured around the site to generate the burial flux maps for the aforementioned geochemical proxies.

ANALYTE	Al	Ba	Ca	Fe	K	Mn	Ti
METHOD	ICP40B	ICP40B	ICP40B	ICP40B	ICP40B	ICP40B	ICP40B
DETECTION	0.01	1	0.01	0.01	0.01	2	0.01
UNITS	%	PPM	%	%	%	PPM	%
Depth (cm)							
10	6.09	411	10.8	2.8	1.56	323	0.2
10	6.11	408	10.6	2.8	1.54	322	0.21
20	5.2	387	14.2	2.38	1.3	308	0.19
40	5.32	425	14	2.37	1.29	327	0.19
50	7.24	519	5.28	3.22	1.66	545	0.26
60	7.29	494	5.9	3.35	1.61	466	0.27
70	6.57	563	5.7	2.98	1.74	1070	0.24
80	6.96	479	6.26	3.53	1.56	403	0.25
100	7.01	518	5.94	3.48	1.61	487	0.25
120	7.11	473	4.59	3.38	1.68	677	0.25
170	7.87	432	3.52	3.86	1.71	289	0.29
190	7.85	432	3.64	3.88	1.73	298	0.28
230	7.64	444	4	3.79	1.85	378	0.27
250	7.41	466	4.01	3.5	2.13	462	0.27
250	7.27	461	3.94	3.43	2.09	453	0.27

Table 4. ICP results from Core HAT-03 for the elements considered and used to calibrate XRF core scans in this study. Analyses were performed using the ICP40B method and concentration results are reported in weight percent units for the above shown elements with the exception of Ba and Mn, which are reported in ppm concentration units. Note the detection limits for this analytical procedure are generally very high for the elements considered.

ANALYTE	Al	Ba	Ca	Fe	K	Mn	Ti
METHOD	ICP40B	ICP40B	ICP40B	ICP40B	ICP40B	ICP40B	ICP40B
DETECTION	0.01	1	0.01	0.01	0.01	2	0.01
UNITS	%	PPM	%	%	%	PPM	%
Depth (cm)							
1	7.87	448	3.55	3.39	2.39	667	0.27
2	7.84	441	3.4	3.51	2.3	646	0.28
6	7.71	510	3.04	3.69	2.49	572	0.28
10	6.85	432	7.35	3.27	1.91	367	0.25
12	7.89	459	3.87	3.66	2.57	580	0.29
12	7.78	413	3.85	3.66	2.58	580	0.27
13	7.07	406	7.48	3.15	2.03	332	0.23
15	6.36	396	8.24	3.03	1.91	326	0.22
16	6.8	418	9.25	3.08	1.97	324	0.24
20	5.97	401	12.2	2.74	1.68	308	0.21
24	5.56	379	13.3	2.49	1.6	287	0.2
25	5.58	394	13.7	2.52	1.56	299	0.2
26	5.55	359	13.9	2.5	1.56	294	0.2
29	5.71	448	12.8	2.62	1.61	288	0.21
30	5.82	448	12.1	2.62	1.6	294	0.21
50	7.81	515	5.39	3.7	1.96	421	0.28
50	7.54	494	5.32	3.6	1.87	400	0.27
60	7.65	464	5.12	3.59	1.92	422	0.27
66	7.14	586	3.71	3.4	2.15	720	0.27
68	7.52	528	4.21	3.22	2.08	877	0.28
70	6.93	562	3.82	3.27	2.1	894	0.26
72	7	518	4.47	3.14	2.02	908	0.26
73	7.33	471	5.15	3.25	1.93	1010	0.27
74	7.4	508	3.77	3.34	2.06	977	0.29
80	7.59	496	3.74	3.37	2.08	459	0.27
92	7.33	438	6.77	3.65	1.75	389	0.26
100	7.61	485	4.9	3.72	1.86	429	0.28
120	6.85	459	5.08	3.33	1.86	654	0.25
124	7.05	468	4.55	3.38	2.11	1250	0.26
124	6.95	487	4.53	3.37	2.1	1220	0.26
130	7.26	471	4.53	3.61	2.11	1000	0.28
131	7.34	460	4.54	3.45	2.14	1210	0.28
132	7.25	492	3.85	3.44	2.15	1340	0.26
133	7.31	474	4.03	3.47	2.12	1300	0.28
140	7.54	457	5.4	3.63	2	630	0.28
141	6.93	476	5.77	3.62	1.84	583	0.26
142	7.48	437	5.68	3.73	1.96	595	0.26
148	7.21	473	4.78	3.49	2.09	976	0.27

Table 5. ICP results from Core PEL-03 for the elements considered and used to calibrate XRF core scans in this study. Analyses were performed using the ICP40B method and concentration results are reported in weight percent units for the above shown elements with the exception of Ba and Mn, which are reported in ppm concentration units. Note the detection limits for this analytical procedure are generally very high for the elements considered.

Average Coefficient of Variation

XRF Counts	HAT-01	HAT-02	HAT-03	HAT-04	HAT-05
Al	0.078	0.140	0.018	0.113	0.048
Si	0.067	0.110	0.010	0.100	0.043
Ti	0.074	0.079	0.028	0.049	0.040
Fe	0.020	0.023	0.005	0.008	0.006
Ba	0.057	0.049	0.030	0.043	0.059
Ca	0.052	0.071	0.011	0.046	0.019

XRF Counts	PEL-02	PEL-15	PEL-04	PEL-08	PEL-07
Al	0.087	0.073	0.057	0.060	0.034
Si	0.051	0.025	0.020	0.039	0.012
Ti	0.062	0.056	0.070	0.049	0.124
Fe	0.007	0.037	0.034	0.010	0.059
Ba	0.060	0.059	0.040	0.067	0.023
Ca	0.023	0.084	0.036	0.026	0.027

Table 6. Average coefficient of variation ratios for each element all cores except for Core PEL-08 (where destructive samples were not taken); data are based on duplicates from XRF every 10-cm, varying resolution. Note: PEL-08 was the only core where geochemical analyses were not performed for destructive analyses, which was preserved for XRF core scanning only. The one split-half of Core PEL-08 was generously provided by a fellow MC118 consortium member for whom the core belonged.

Manganese Concentration by Core

Core	Net-XRF Scan (cm)	Total Net (ppm)	Avg. Net (ppm)	Max Depth (cmbsf)
HAT-01	212	92611	436	229
HAT-02	244	132325	542	255
HAT-03	249	134274	539	268
HAT-04	279	136565	489	283
HAT-05	245	114533	467	266
PEL-02	440	269775	613	442
PEL-15	402	285623	711	453
PEL-04	396	230696	583	406
PEL-08	698	457105	655	711
PEL-07	592	349986	591	600

Table 7. Average Mn concentrations calculated for each core using calibrated XRF scans, net refers to measured section that was scanned by XRF and does not include gaps in the core.

Time in years to Form Authigenic Mn-layer

HAT-01	HAT-02	HAT-03	HAT-04	HAT-05	PEL-02	PEL-15	PEL-04	PEL-08	PEL-07
1143	*525*	*199*	225	*1044*	*1179*	*117*	192	*388*	*554*
955	*664*	*317*	*376*	*107*	212	185	*343*	*150*	*252*
387	*291*	*140*	*330*	318	290	211	*298*	492	*688*
	168	251	*209*		140	319	*177*	154	*467*
	473	174	302				*270*	153	221
	603	72	406				*373*	198	171
			284				*252*	345	327
			419				386		479
			453				431		
			117				85		
			167						

Table 8. Using a 50 percent cut-off, concentration for each layer is calculated from XRF core scans and used to estimate the time to form the Mn-layer. Calculation of time in years to form a new authigenic Mn-layer following a shift in the redox boundary assumes: (1) constant maximum dissolved Mn gradient, (2) Mn diffusion coefficient $1.5*10^{-6}$ cm^2 sec^{-1} and (3) transport of a 1-cm thick solid-phase layer by diffusion (Froelich et al., 1979). The concentration of Mn at each layer is the only empirical data used from the MC118 to then determine the time to form the authigenic deposit.

Appendix B

Additional Figures

Several figures that convey additional data obtained from MC118 were not included in any of the three dissertation chapters. These figures include cross-sections of XRF profiles of elements (Fe and Al) that were considered in Chapter 2, yet where not presented graphically in an effort reduce the number of figures and to prepare the manuscript for submission to a journal. Those additional figures mentioned in Chapter 2 are included in this appendix, along with other elements such as sulfur, which are considered in the research but not specifically discussed in the various chapters. Cross plots also included in this section, which summarize an immense amount of XRF and coulometry measurements, too numerous to be placed into tables. Trends in the XRF data are apparent by placing a large number of XRF data points (Hatteras transect) into a single cross plot comparison for certain elements and ratios (Ba, Ca, Ti, Fe and Si) along with various other ratios. Cross plots are also constructed for CO_2 coulometry data to relate $CaCO_3$ to TOC. Also note several figures demonstrating burial flux for several elements not included in prior chapters (Al, Fe and Mn).

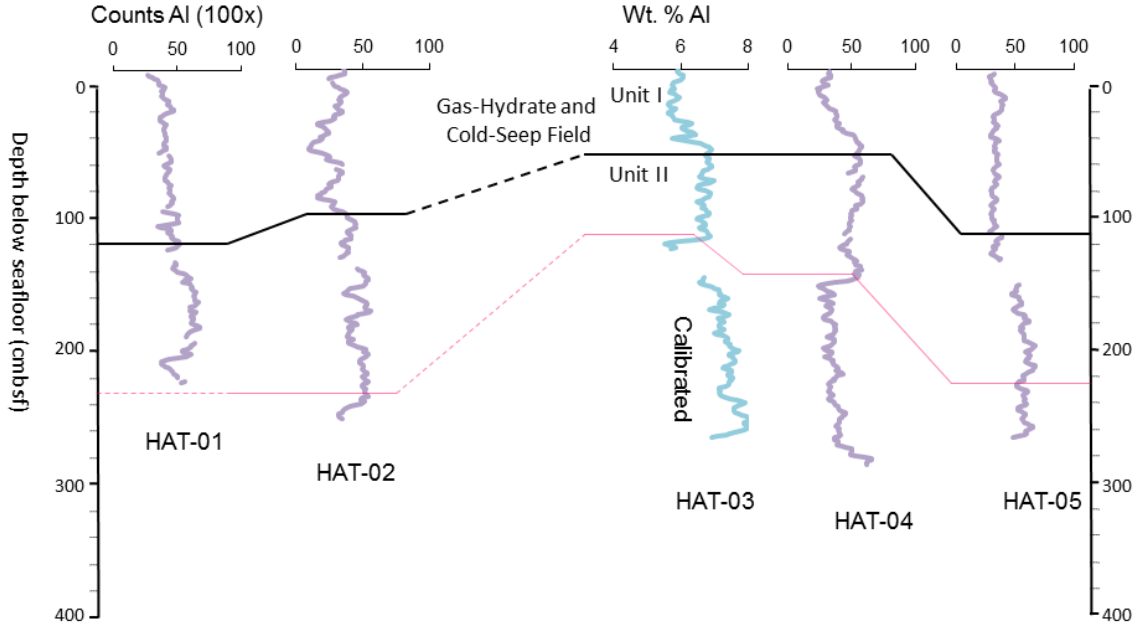

Figure 1. Calibrated (HAT-03) and un-calibrated XRF profiles of Al for cores across Transect 1 onboard the *R/V Hatteras* (Figure 1). Core HAT-03 (blue curve) displays Al concentration (wt. %) calculated by calibration of XRF counts to ICP-ES. All other profiles (purple curves) display Al counts (100x), see Mn profile caption (Figure 4 in Chapter 3) for a more detailed description of the figure and items, which do not pertain to the specific element that is displayed.

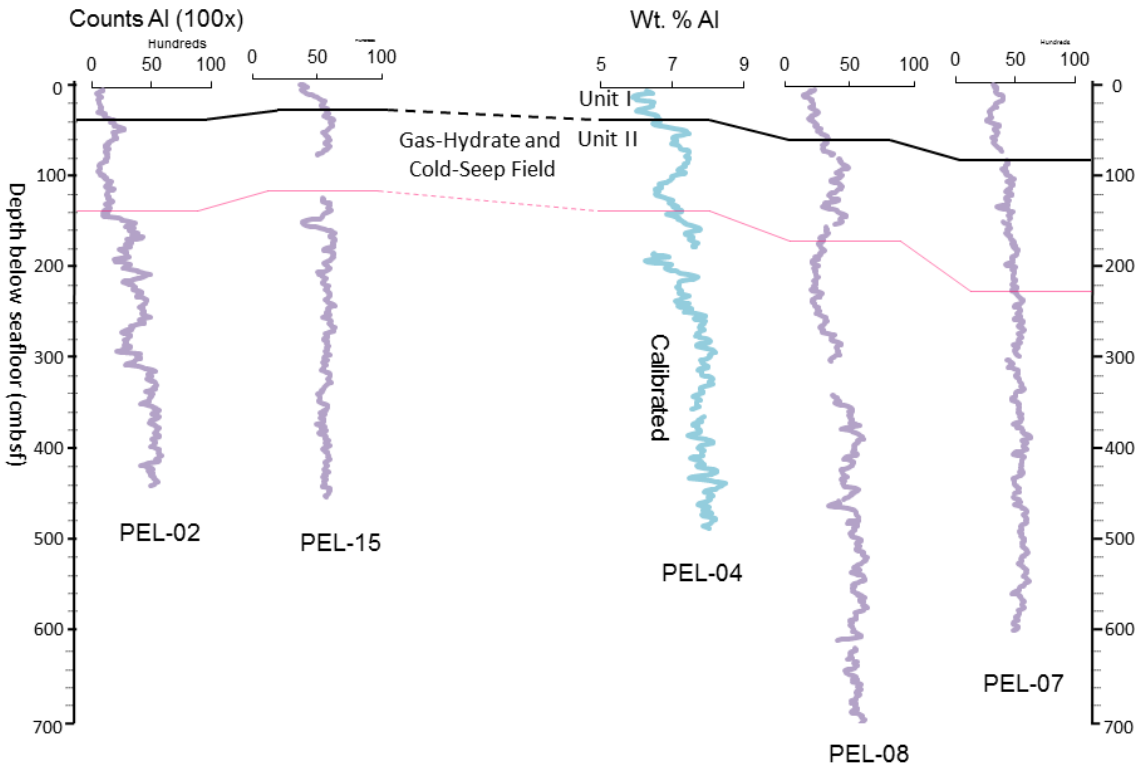

Figure 2. Calibrated (PEL-04) and un-calibrated XRF profiles of Al for cores across Transect 2 onboard the *R/V Pelican* (Figure 1). Core PEL-04 (blue curve) displays Al concentration (wt. %) calculated by calibration of XRF counts to ICP-ES. All other profiles (purple curves) display Al counts (100x), see Mn profile caption (Figure 5 in Chapter 3) for a more detailed description of the figure and items, which do not pertain to the specific element that is displayed.

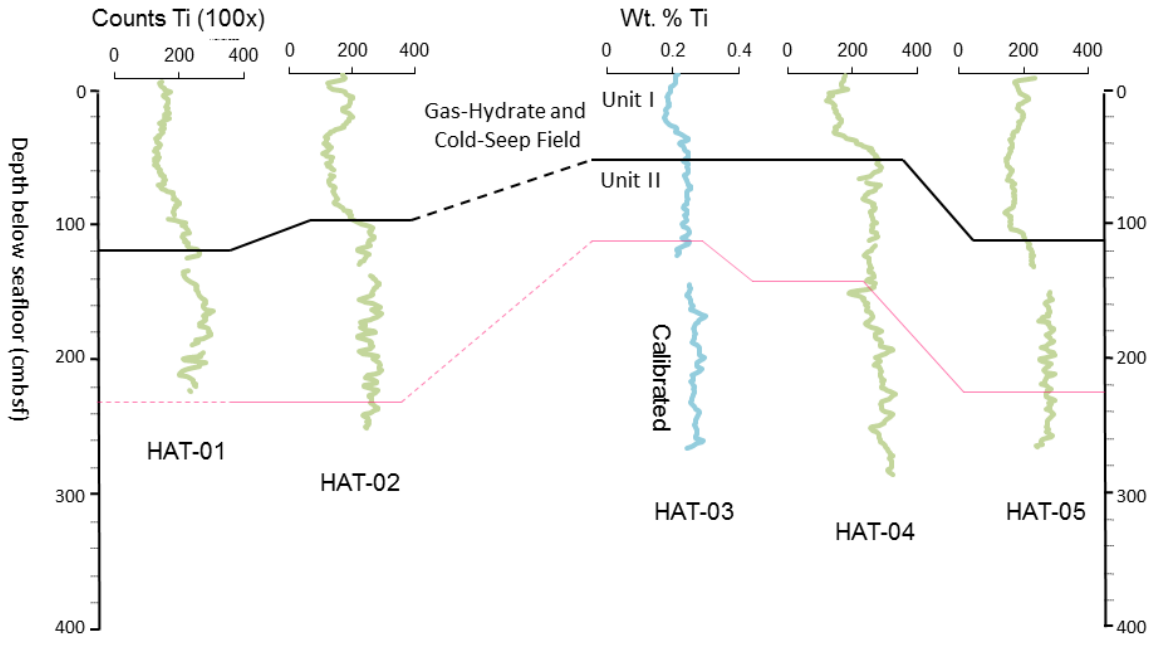

Figure 3. Calibrated (HAT-03) and un-calibrated XRF profiles of Ti for cores across Transect 1 onboard the *R/V Hatteras* (Figure 1). Core HAT-03 (blue curve) displays Ti concentration (wt. %) calculated by calibration of XRF counts to ICP-ES. All other profiles (purple curves) display Ti counts (100x), see Mn profile caption (Figure 4 in Chapter 3) for a more detailed description of the figure and items, which do not pertain to the specific element that is displayed.

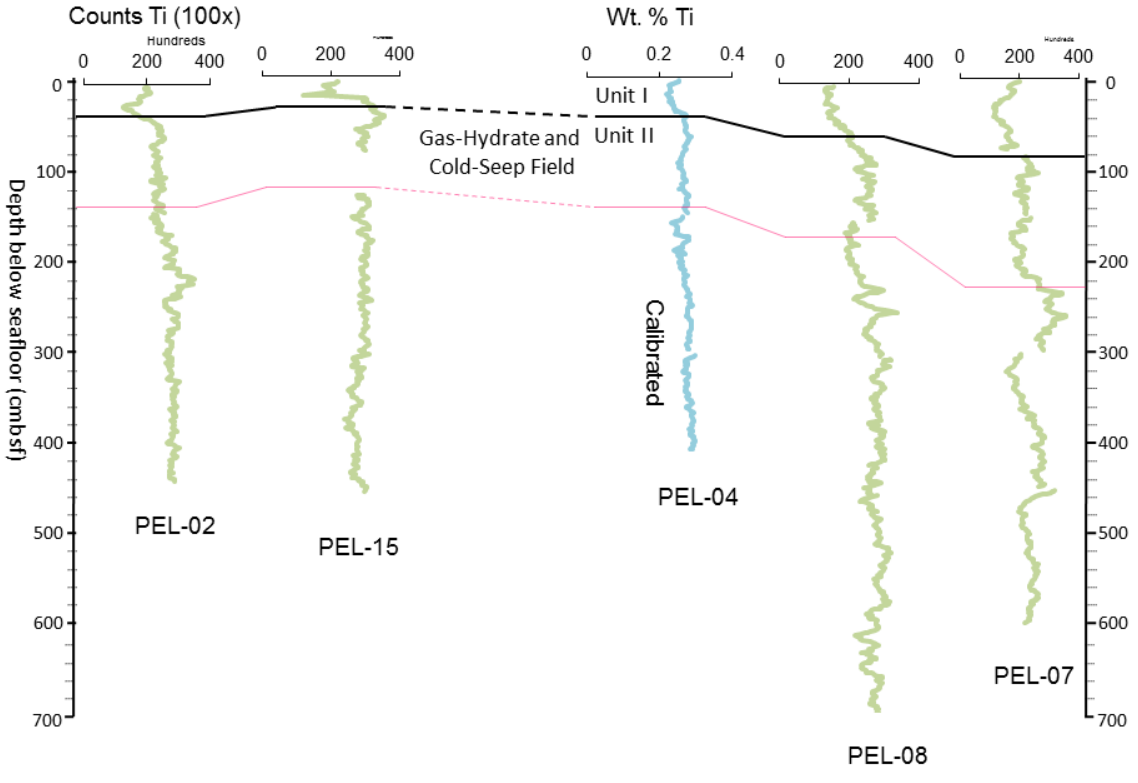

Figure 4. Calibrated (PEL-04) and un-calibrated XRF profiles of Ti for cores across Transect 2 onboard the *R/V Pelican* (Figure 1). Core PEL-04 (blue curve) displays Ti concentration (wt. %) calculated by calibration of XRF counts to ICP-ES. All other profiles (purple curves) display Ti counts (100x), see Mn profile caption (Figure 5 in Chapter 3) for a more detailed description of the figure and items, which do not pertain to the specific element that is displayed.

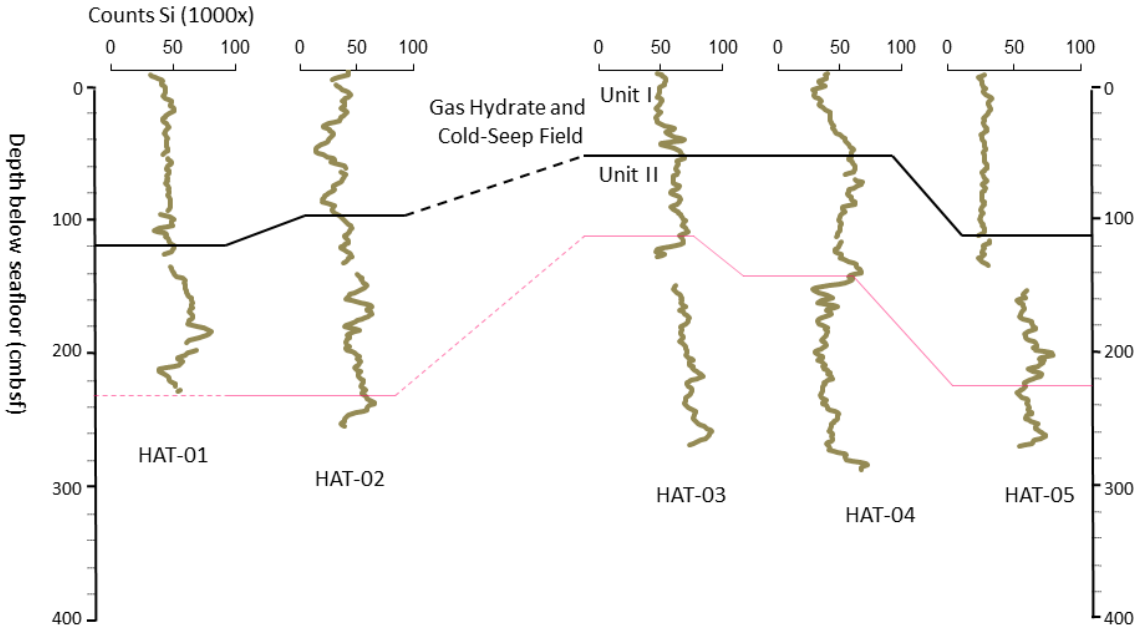

Figure 5. Un-calibrated XRF profiles of Si for cores across Transect 1 onboard the *R/V Hatteras* (Figure 1). Profiles display Ti counts (1000x), see Mn profile caption (Figure 4 in Chapter 3) for a more detailed description of the figure and items, which do not pertain to the specific element that is displayed.

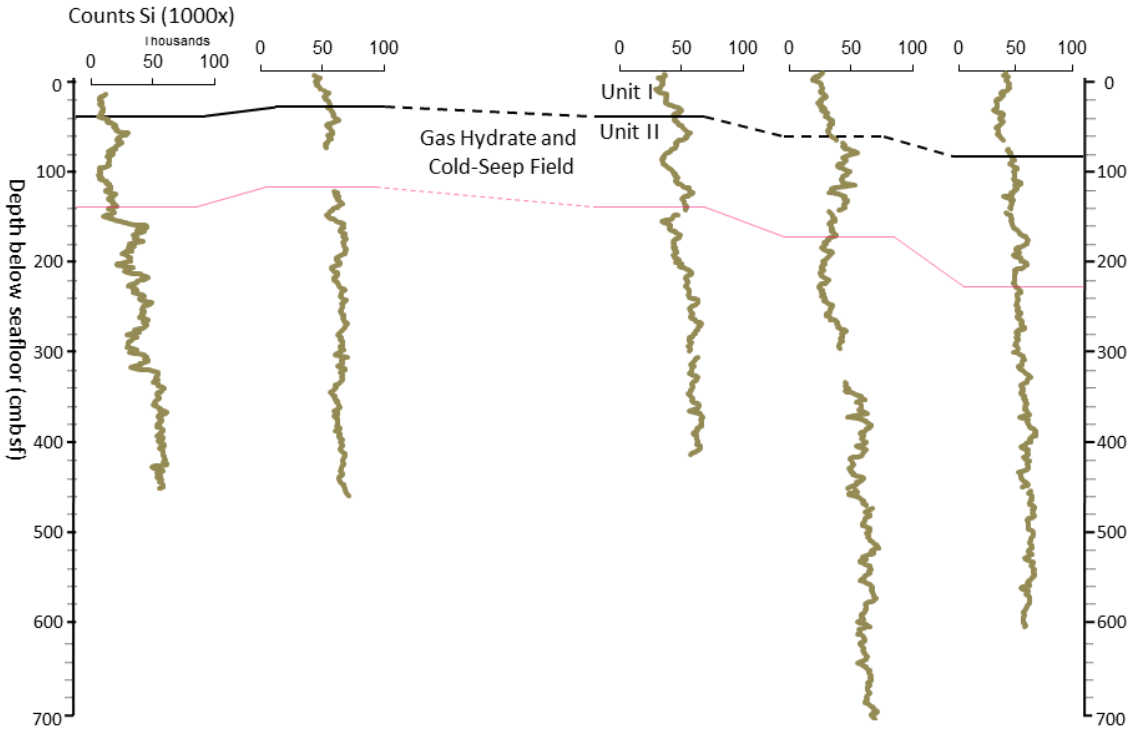

Figure 6. Un-calibrated XRF profiles of Si for cores across Transect 2 onboard the *R/V Pelican* (Figure 1). Profiles display Si counts (1000x), see Mn profile caption (Figure 5 in Chapter 3) for a more detailed description of the figure and items, which do not pertain to the specific element that is displayed.

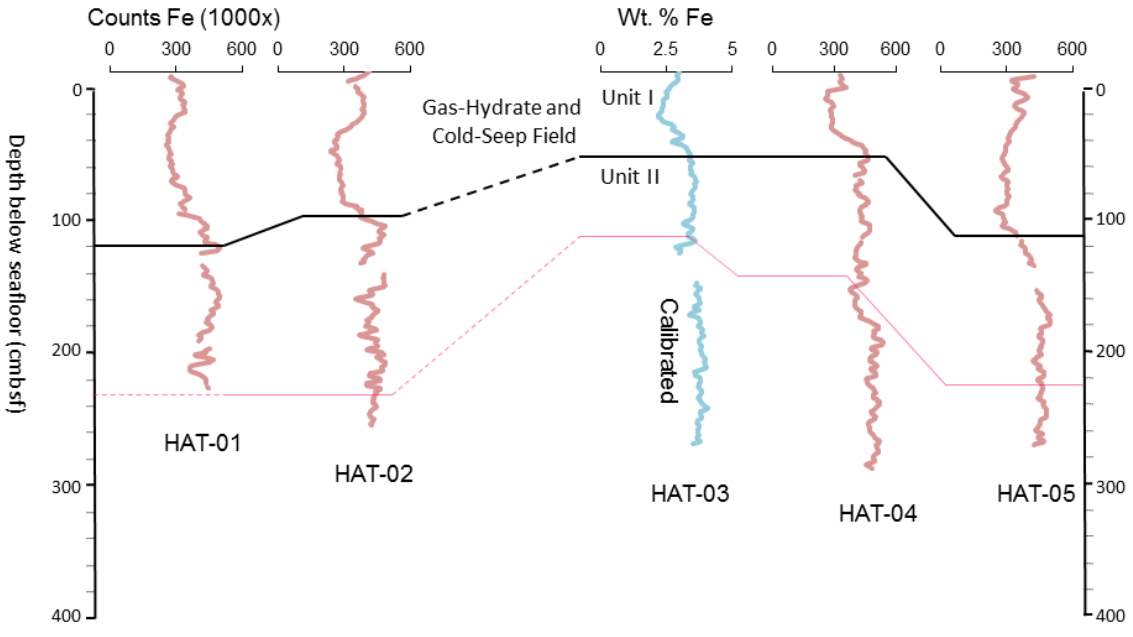

Figure 7. Calibrated (HAT-03) and un-calibrated XRF profiles of Fe for cores across Transect 1 onboard the *R/V Hatteras* (Figure 1). Core HAT-03 (blue curve) displays Fe concentration (wt. %) calculated by calibration of XRF counts to ICP-ES. All other profiles (purple curves) display Fe counts (1000x), see Mn profile caption (Figure 4 in Chapter 3) for a more detailed description of the figure and items, which do not pertain to the specific element that is displayed.

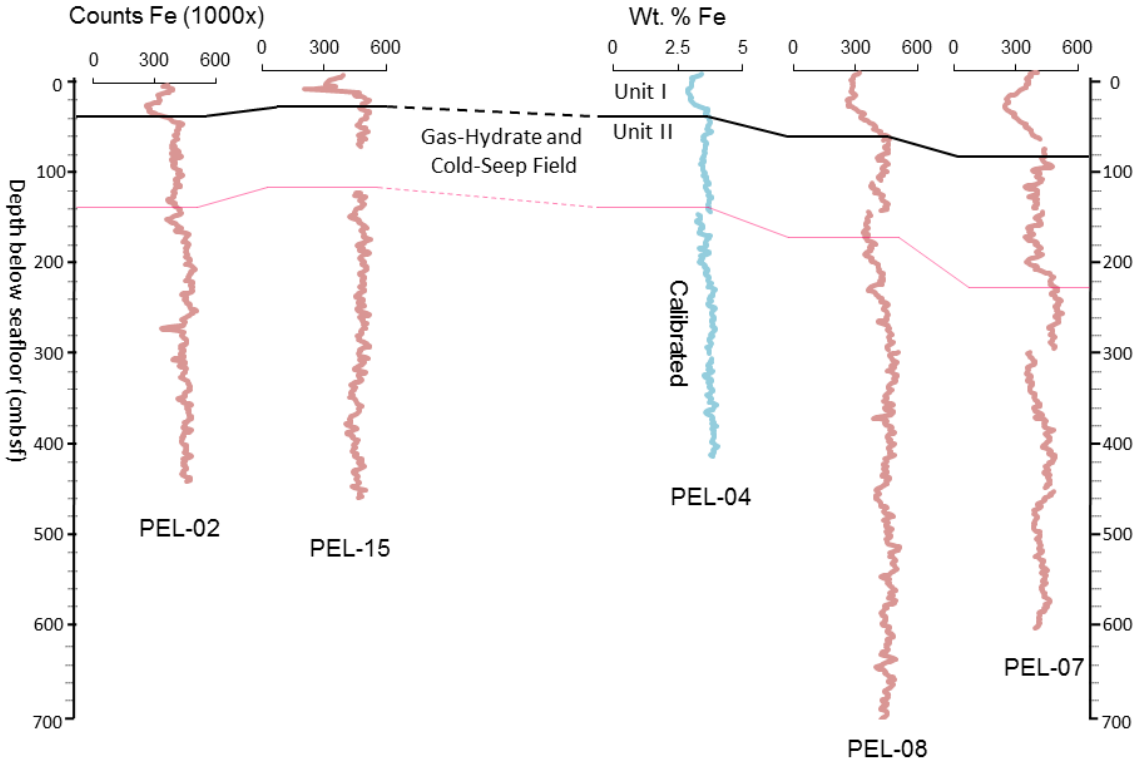

Figure 8. Calibrated (PEL-04) and un-calibrated XRF profiles of Fe for cores across Transect 2 onboard the *R/V Pelican* (Figure 1). Core PEL-04 (blue curve) displays Fe concentration (wt. %) calculated by calibration of XRF counts to ICP-ES. All other profiles (purple curves) display Fe counts (1000x), see Mn profile caption (Figure 5 in Chapter 3) for a more detailed description of the figure and items, which do not pertain to the specific element that is displayed.

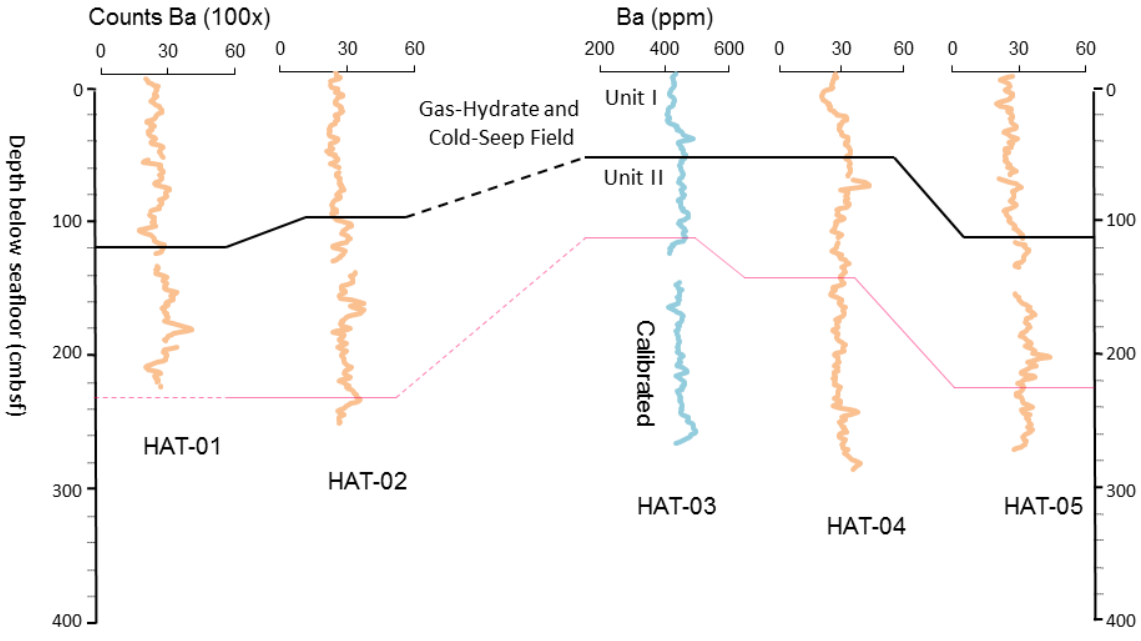

Figure 9. Calibrated (HAT-03) and un-calibrated XRF profiles of Ba for cores across Transect 1 onboard the *R/V Hatteras* (Figure 1). Core HAT-03 (blue curve) displays Ba concentration (ppm) calculated by calibration of XRF counts to ICP-ES. All other profiles (purple curves) display Ba counts (100x), see Mn profile caption (Figure 4 in Chapter 3) for a more detailed description of the figure and items, which do not pertain to the specific element that is displayed.

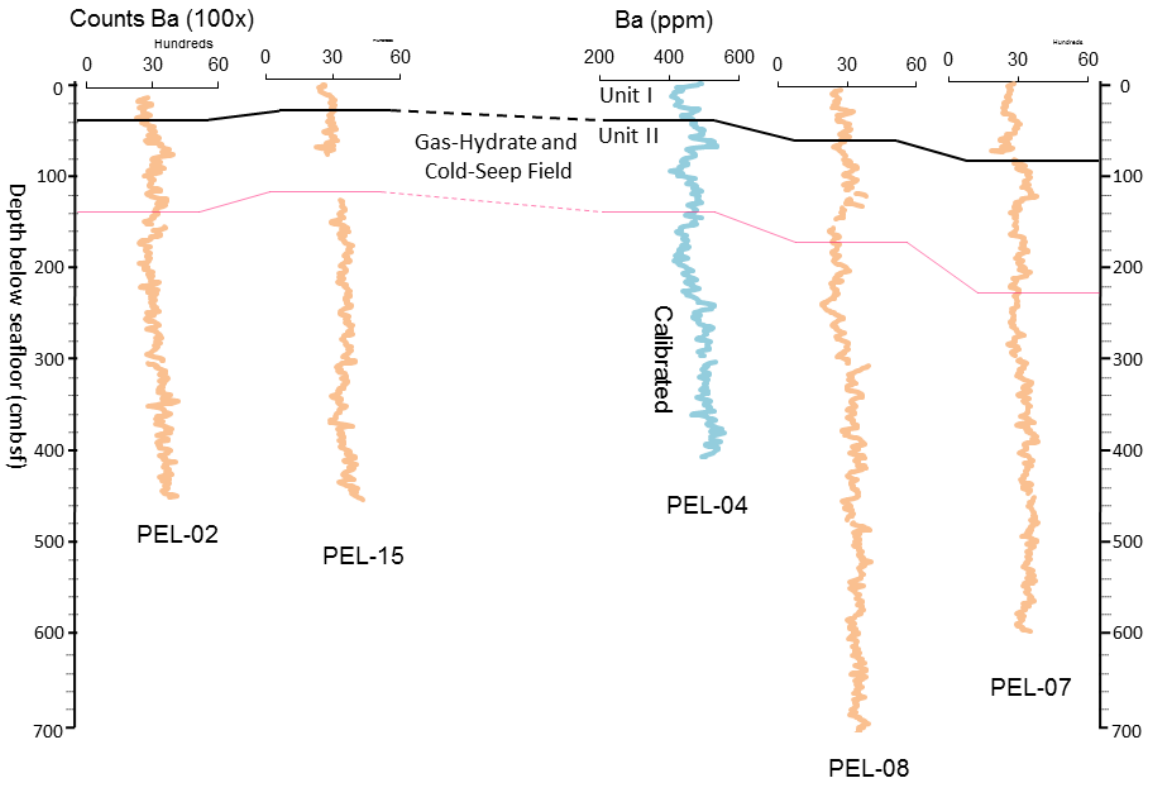

Figure 10. Calibrated (PEL-04) and un-calibrated XRF profiles of Ba for cores across Transect 2 onboard the *R/V Pelican* (Figure 1). Core PEL-04 (blue curve) displays Ba concentration (ppm) calculated by calibration of XRF counts to ICP-ES. All other profiles (purple curves) display Ba counts (100x), see Mn profile caption (Figure 5 in Chapter 3) for a more detailed description of the figure and items, which do not pertain to the specific element that is displayed.

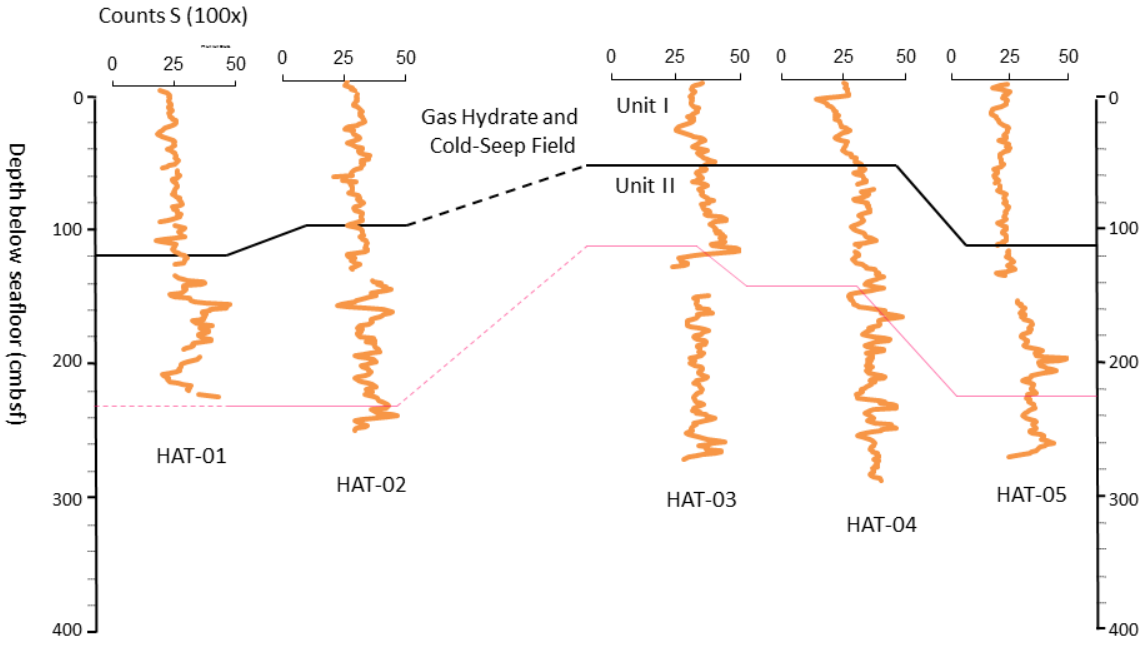

Figure 11. Un-calibrated XRF profiles of S for cores across Transect 1 onboard the *R/V Hatteras* (Figure 1). Profiles display S counts (100x), see Mn profile caption (Figure 4 in Chapter 3) for a more detailed description of the figure and items, which do not pertain to the specific element that is displayed.

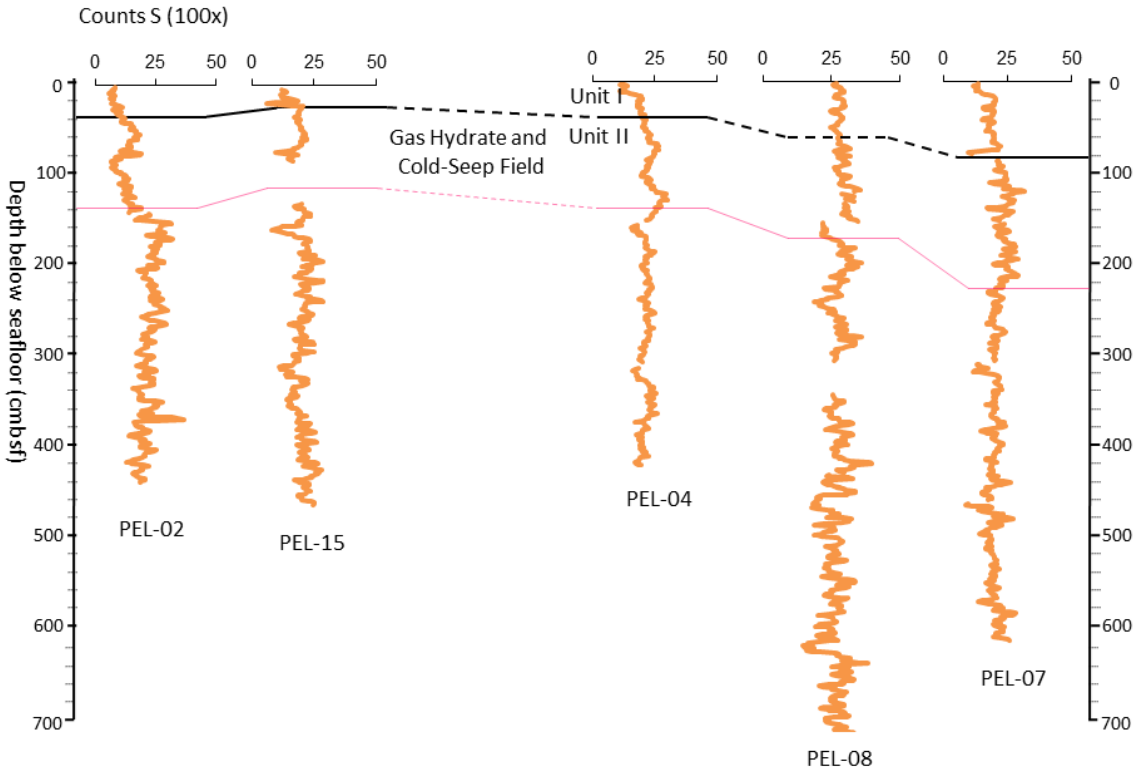

Figure 12. Un-calibrated XRF profiles of S for cores across Transect 2 onboard the *R/V Pelican* (Figure 1). Profiles display S counts (100x), see Mn profile caption (Figure 5 in Chapter 3) for a more detailed description of the figure and items, which do not pertain to the specific element that is displayed.

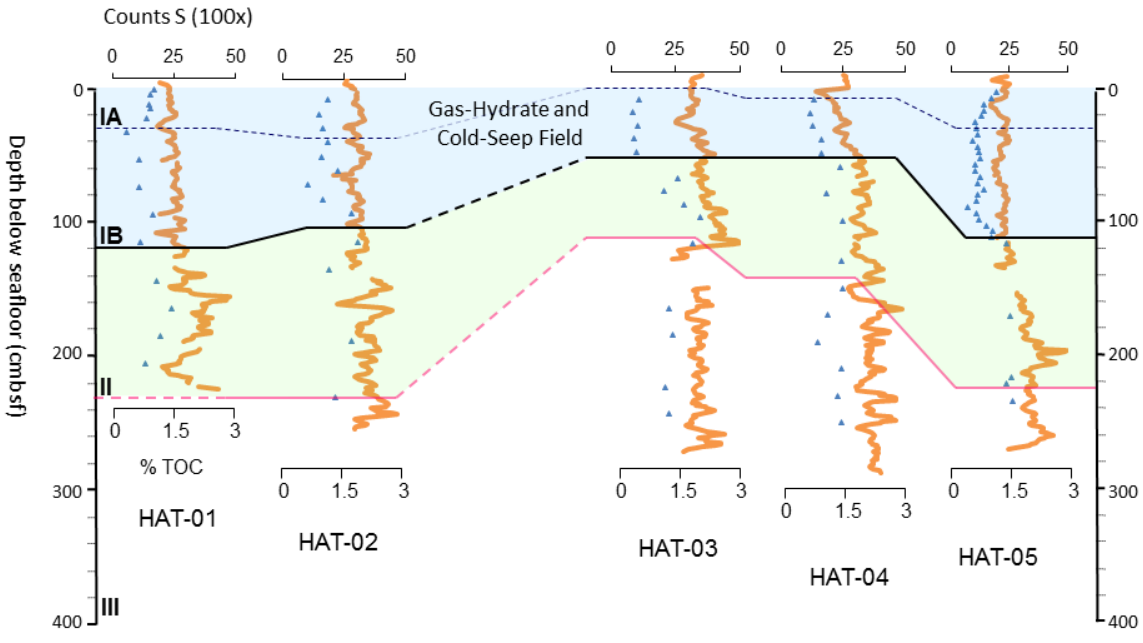

Figure 13. Un-calibrated XRF profiles of S for cores across Transect 1 onboard the *R/V Hatteras* (Figure 1). Weight percent TOC (blue triangles) is plotted (scale on bottom), with profiles of S counts (100x) for each core, see Mn profile caption (Figure 4 in Chapter 3) for a more detailed description of the figure and items, which do not pertain to the specific element that is displayed.

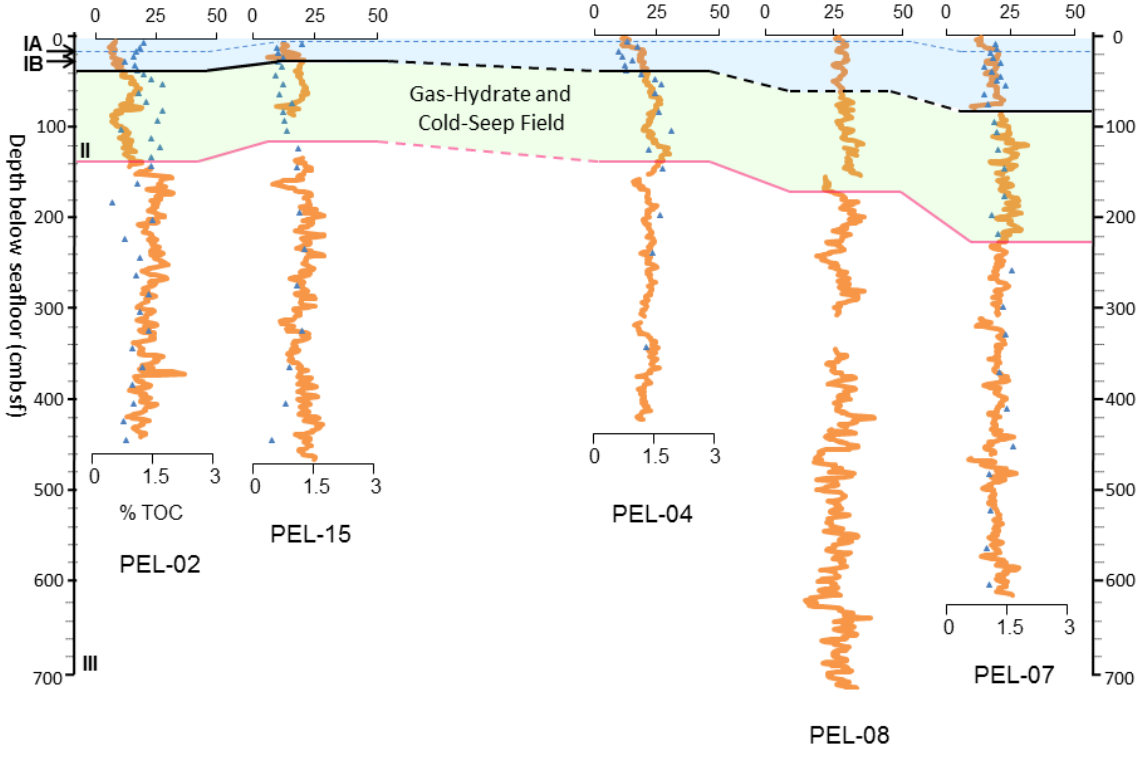

Figure 14. Un-calibrated XRF profiles of S for cores across Transect 2 onboard the *R/V Pelican* (Figure 1). Weight percent TOC (blue triangles) is plotted (scale on bottom), with profiles of S counts (100x) for each core, see Mn profile caption (Figure 5 in Chapter 3) for a more detailed description of the figure and items, which do not pertain to the specific element that is displayed.

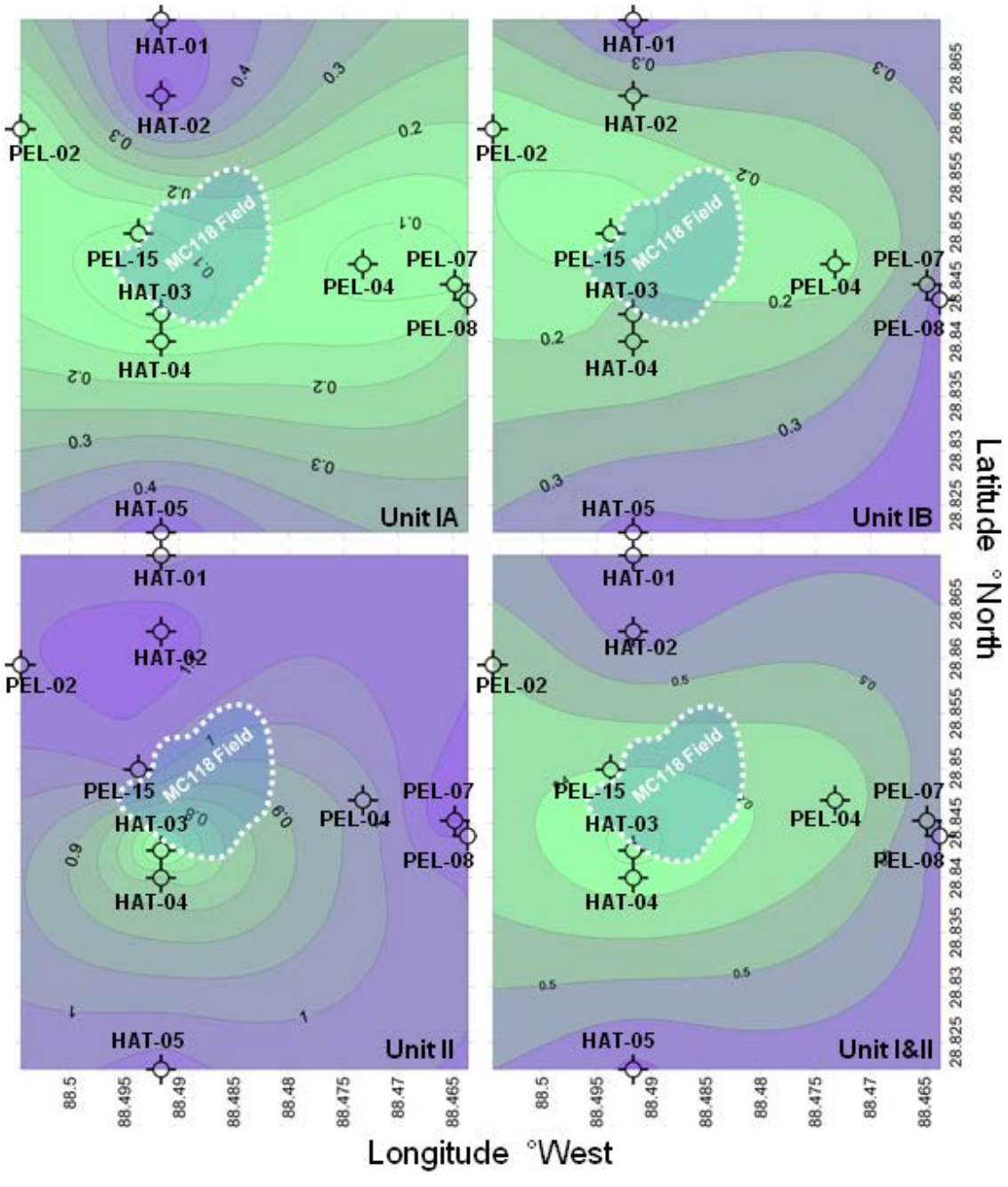

Figure 15. Ti mass accumulation rates (g m-2 yr.-1) calculated for each coring location and contoured over the study area for each stratigraphic unit. Cool colors (blue) represent higher rates and warm colors (lime) represent lower rates. The extent of the studied gas-hydrate and cold-seep field is outlined by the white dashed line and shaded in light blue. Note: overall increased in Fe flux from Unit IB to Unit II across the MC118 study area, see discussion for interpretation.

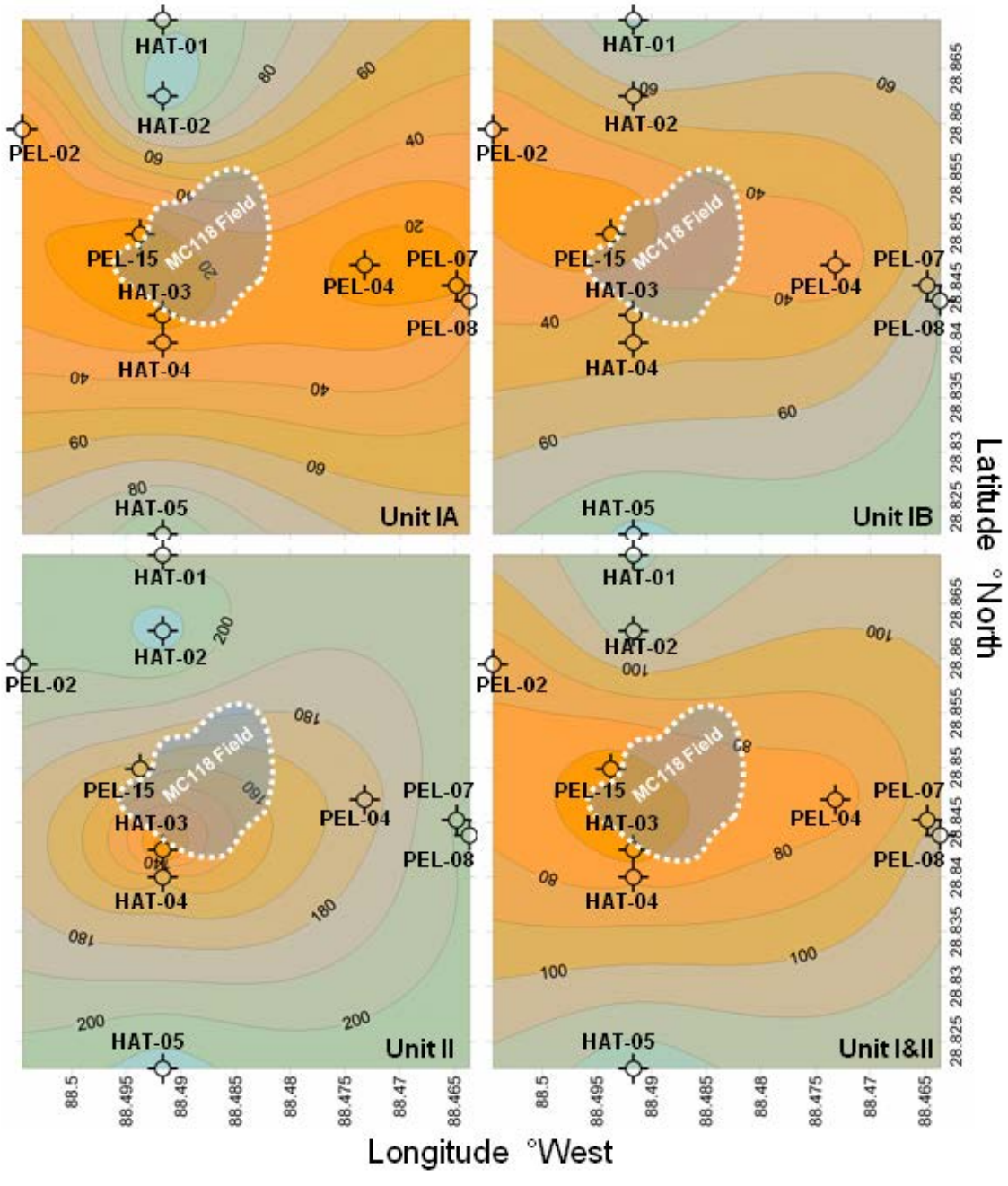

Figure 16. Ba mass accumulation rates (mg m-2 yr.-1) calculated for each coring location contoured over the study area for each stratigraphic unit. Cool colors (blue-green) represent higher rates and warm colors (orange) represent lower rates. The extent of the studied gas-hydrate and cold-seep field is outlined by the white dashed line and shaded in light blue. Note: overall increased in Ba flux from Unit IB to Unit II across the MC118 study area, see discussion for interpretation.

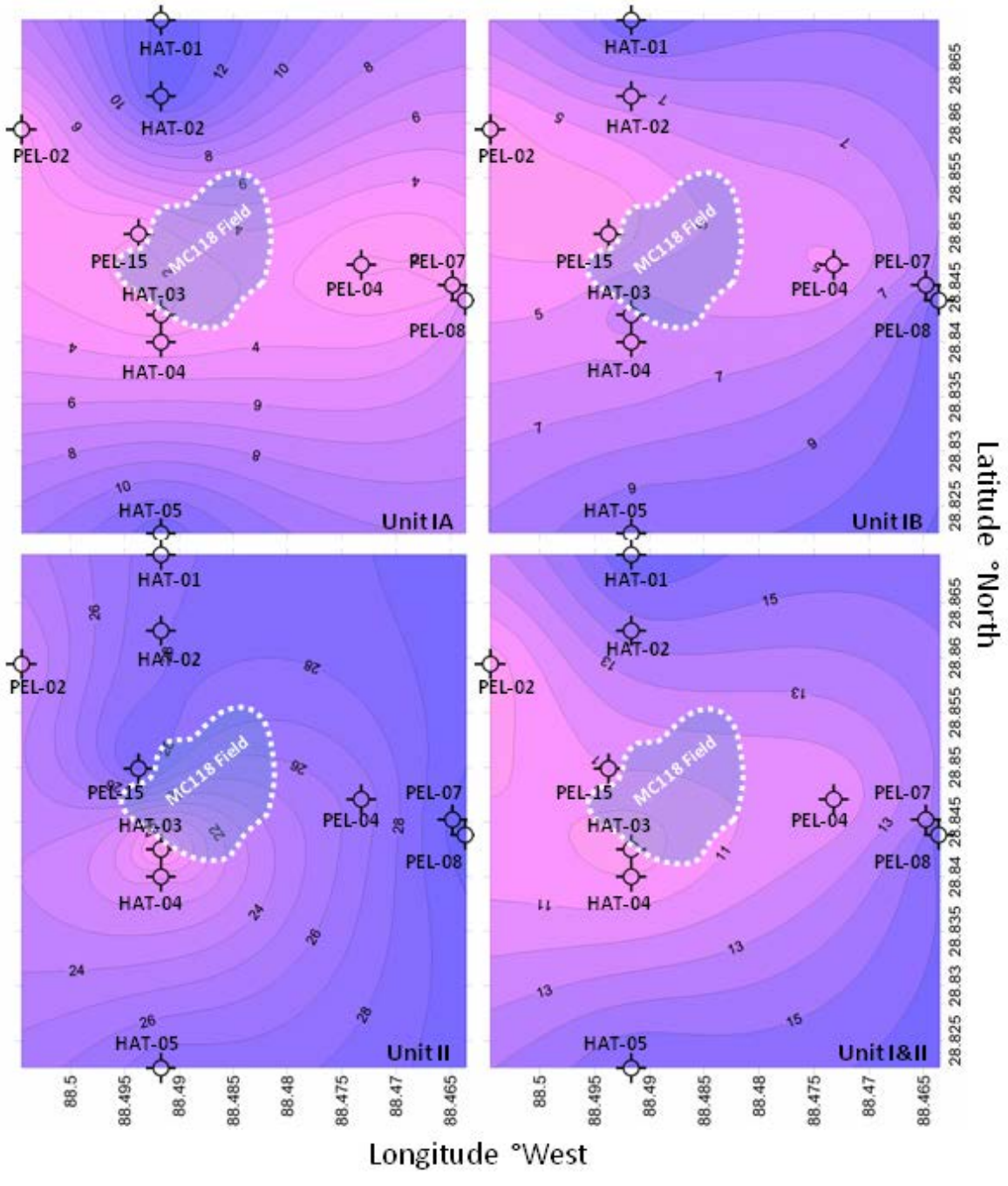

Figure 17. Al mass accumulation rates (g m-2 yr.-1) calculated for each coring location and contoured over the study area for each stratigraphic unit. Cool colors (blue) represent higher rates and warm colors (light purple) represent lower rates. The extent of the studied gas-hydrate and cold-seep field is outlined by the white dashed line and shaded in light blue. Note: overall increase in Al flux from Unit IB to Unit II across the MC118 study area, see discussion in Chapter 2 for interpretation, e.g. Al is considered another "conservative" lithogenic element (Section 1.2 in Appendix A).

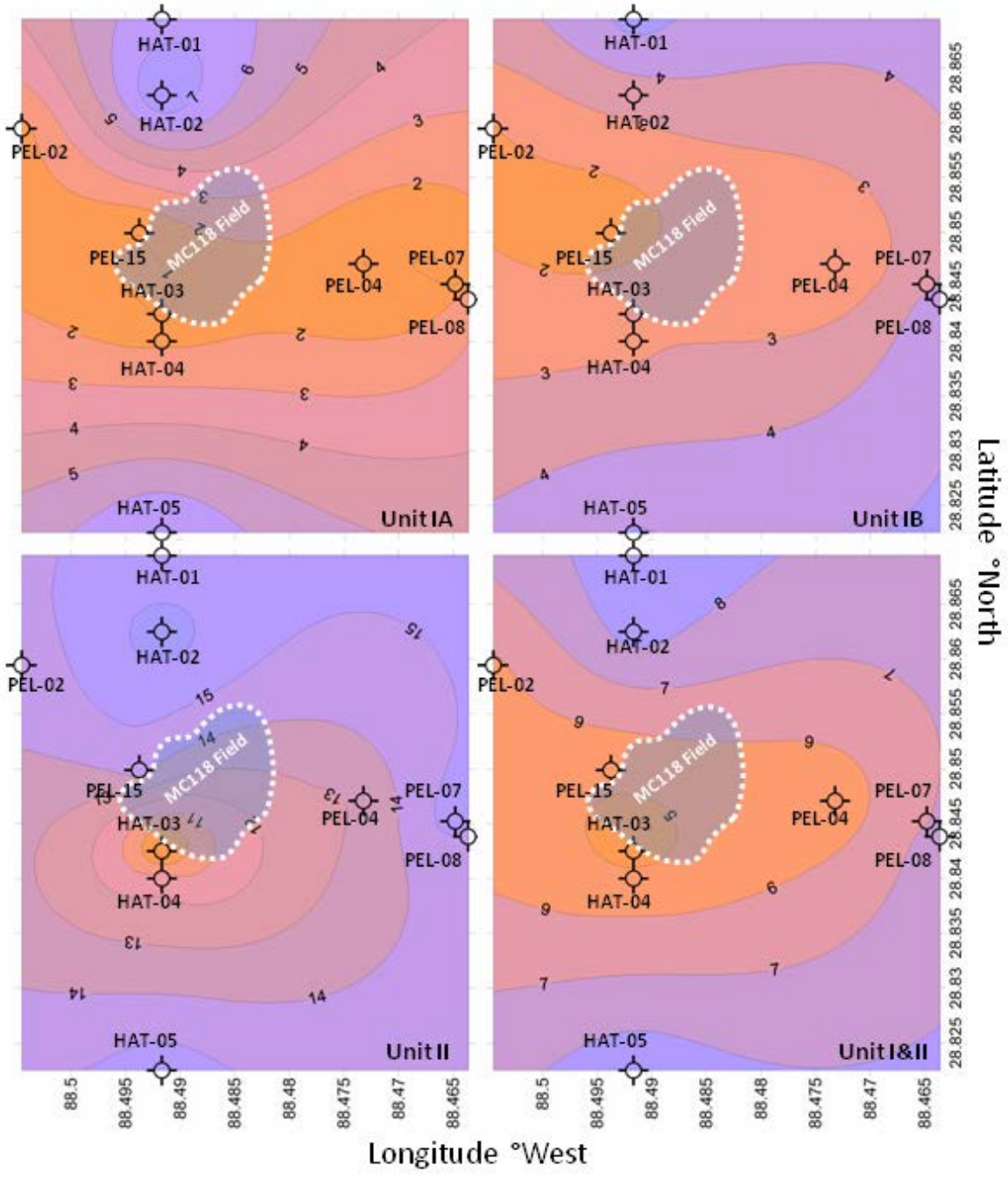

Figure 18. Fe mass accumulation rates (g m-2 yr.-1) calculated for each coring location and contoured over the study area for each stratigraphic unit. Cool colors (light blue) represent higher rates and warm colors (orange) represent lower rates. The extent of the studied gas-hydrate and cold-seep field is outlined by the white dashed line and shaded in light blue. Note: overall increase in Fe flux from Unit IB to Unit II across the MC118 study area, see discussion in Chapter 2 for interpretation, e.g. Fe is considered lithogenic yet may also be authigenic (Section 1.2 in Appendix A).

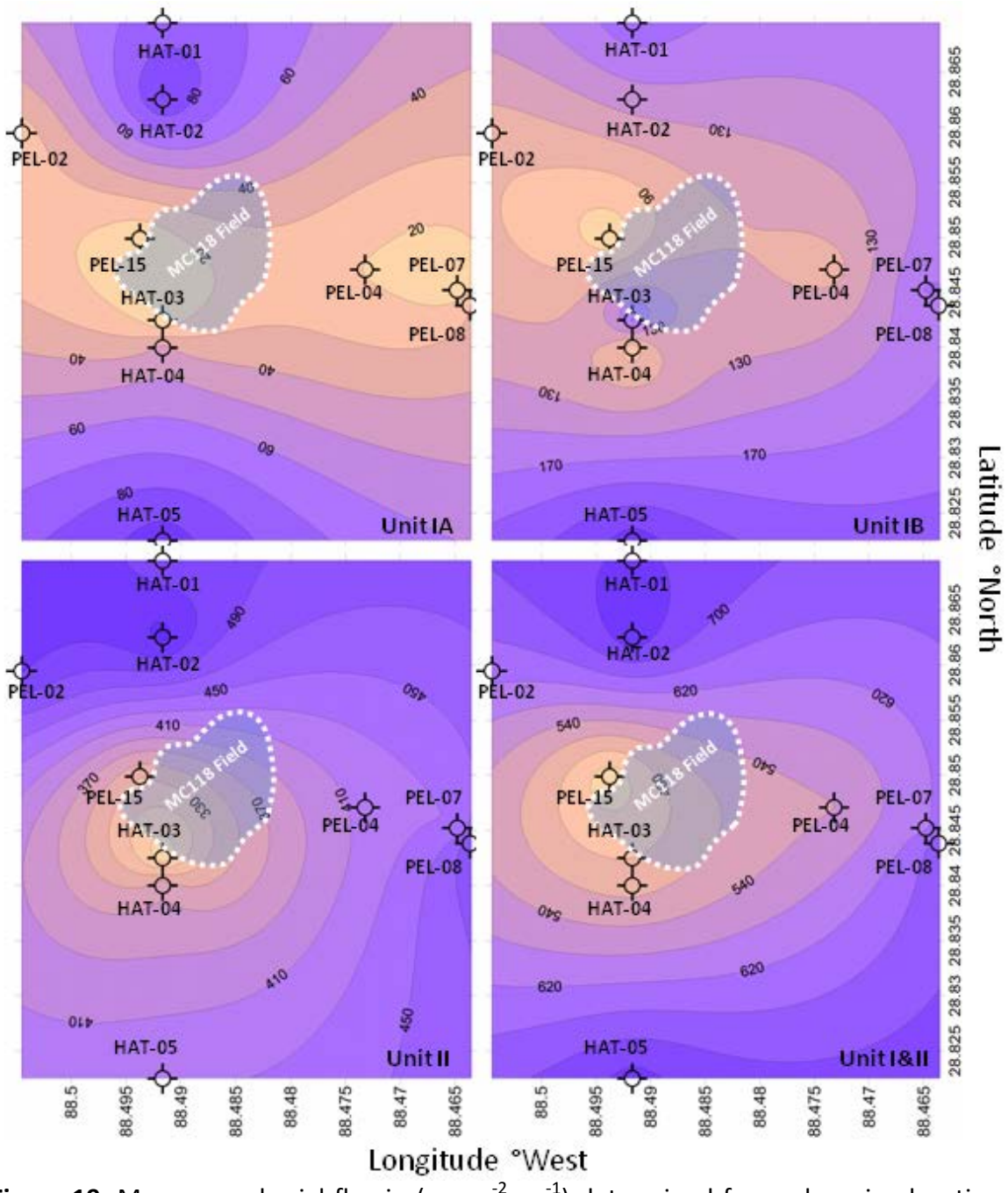

Figure 19. Manganese burial flux in (mg m^{-2} $yr.^{-1}$) determined for each coring location and contoured over the study area for each stratigraphic unit. Cool colors (dark purple) are higher flux and warm colors (yellow-tan) are lower flux. The MC118 gas-hydrate and cold-seep field is outlined by the white dashed line; shaded in light blue. Note: overall increase of Mn flux from Unit IB to Unit II across MC118; abrupt change in burial flux over a short distance from Core HAT-03 to HAT-04, a consequence of authigenic Mn in HAT-03 within Stratigraphic Unit IB, authigenic Mn in Unit II and III is more evenly distributed (Figure 4). Also note, the substantially higher concentration overall in Unit II (Pleistocene) as compared to Unit IB (Holocene), hence the interpretation of "background" manganese as lithogenic (See Results and Discussion in Chapter 2).

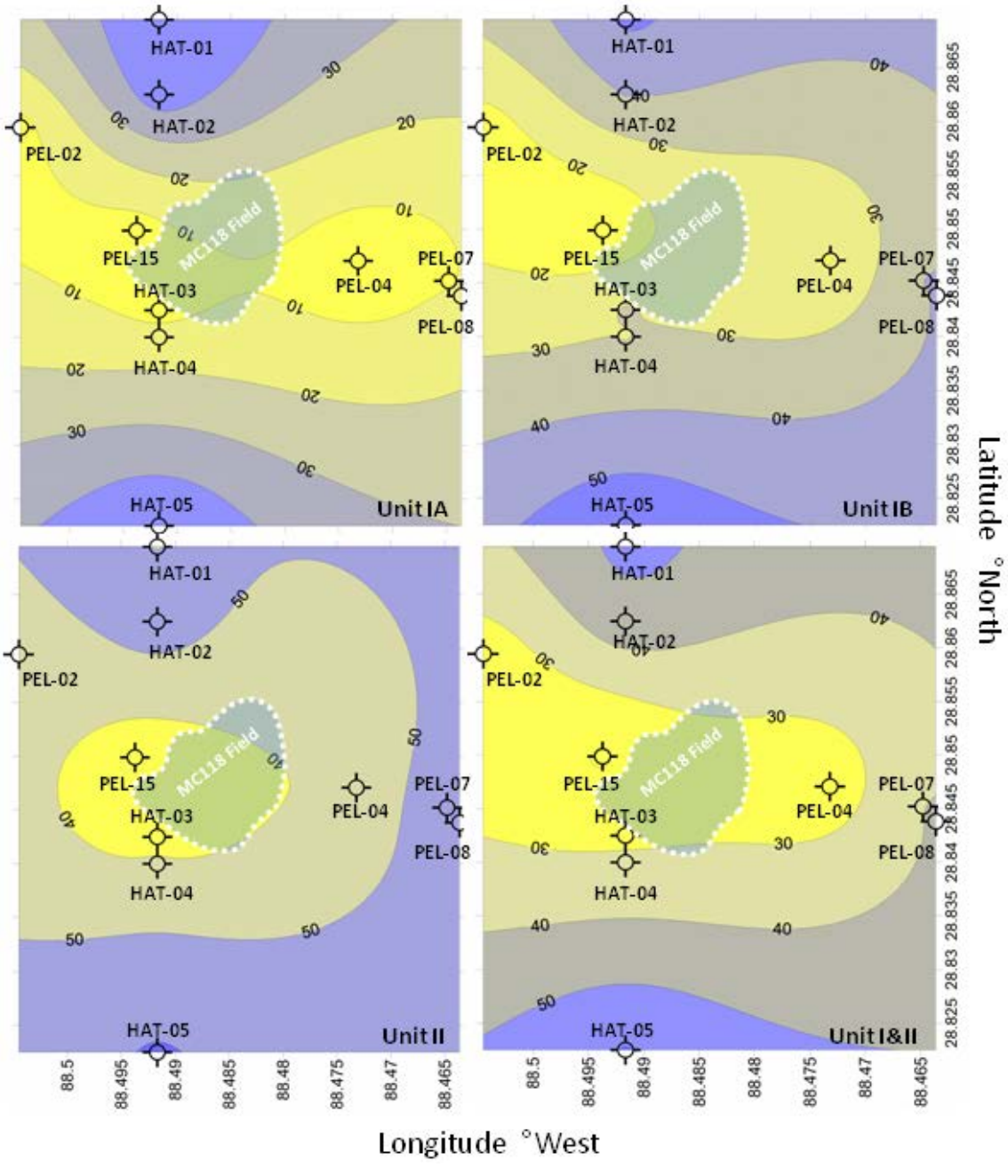

Figure 20. $CaCO_3$ mass accumulation rate (g m-2 yr.-1) calculated for each coring location and contoured over the study area for each stratigraphic unit. Cool colors (blue) represent higher accumulation rates and warm colors (yellow) are lower. The extent of the studied gas-hydrate and cold-seep field is outlined by the white dashed line and shaded in light blue. Note: similar $CaCO_3$ flux seen in some cores (HAT-01, -05) in Unit IB and Unit II across the MC118 study area, see discussion for interpretation.

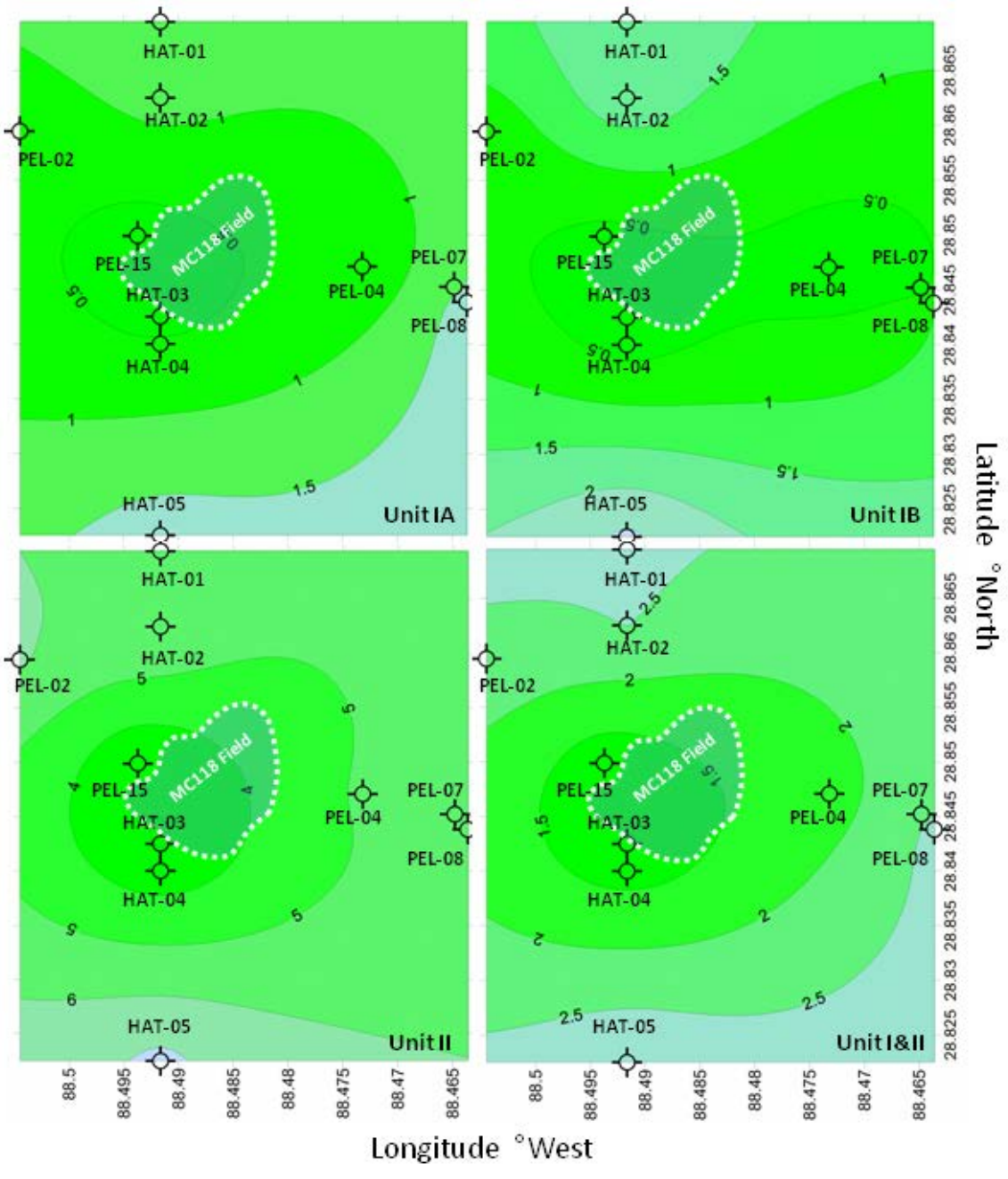

Figure 21. TOC mass accumulation rates (g m-2 yr.-1) calculated for each coring location and contoured over the study area for each stratigraphic unit. Cool colors (blue) represent higher rates and warm colors (green) represent lower rates. The extent of the studied gas-hydrate and cold-seep field is outlined by the white dashed line and shaded in light blue. Note: overall increase in TOC flux from Unit IB to Unit II across the MC118 study area, see discussion for interpretation.

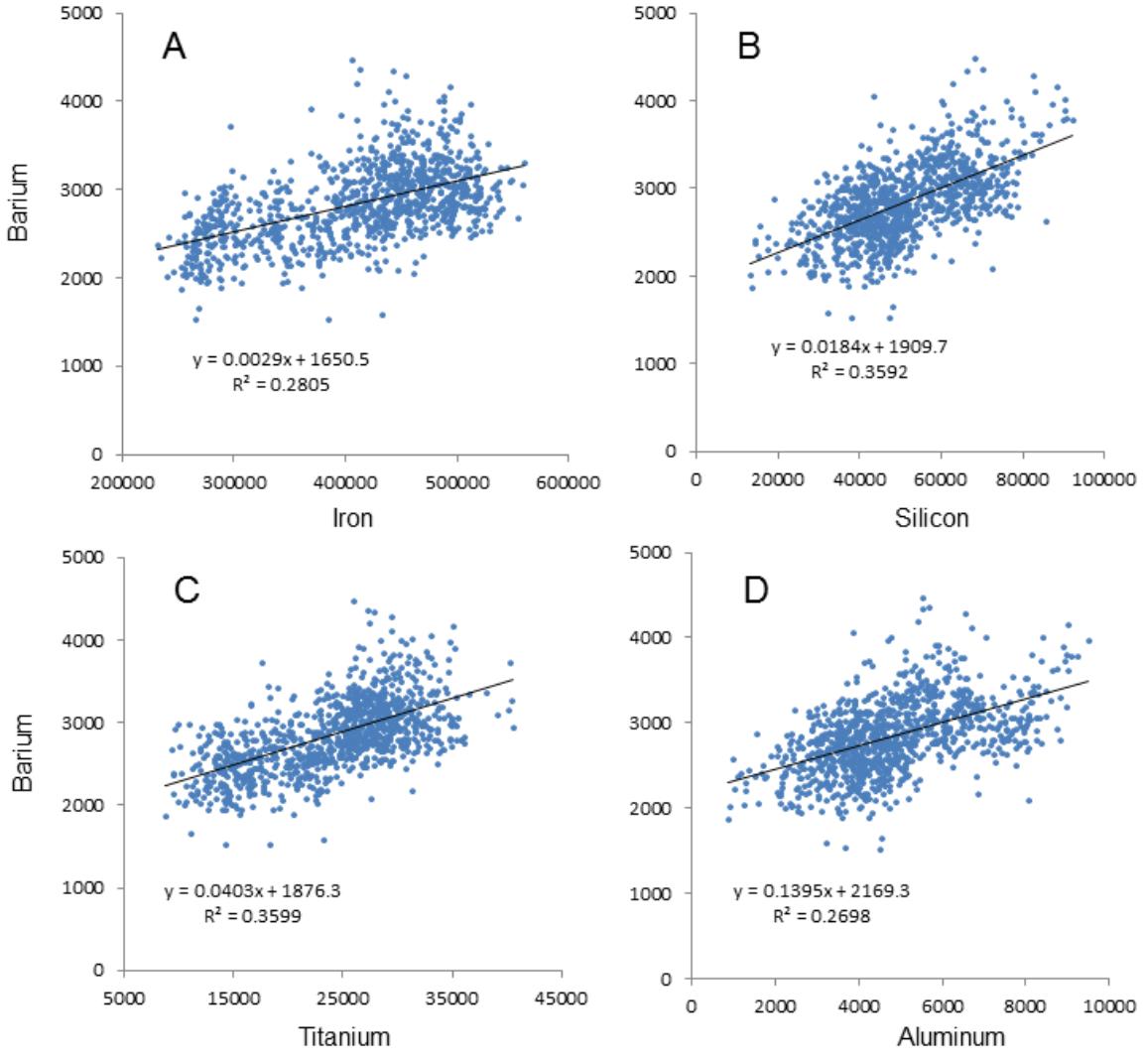

Figure 22. Cross-plots of XRF data from Hatteras cores used to evaluate correlation of barium to lithogenic inputs (e.g., Fe, Si, Ti and Al). Displayed are several plots with equations (least-squares linear fits), which are also provided to quantify the strength of the correlation of Ba to the various lithogenic inputs. These correlations, while not impressive are still significant given the sheer number of data points, with over 3000 individual XRF measurements.

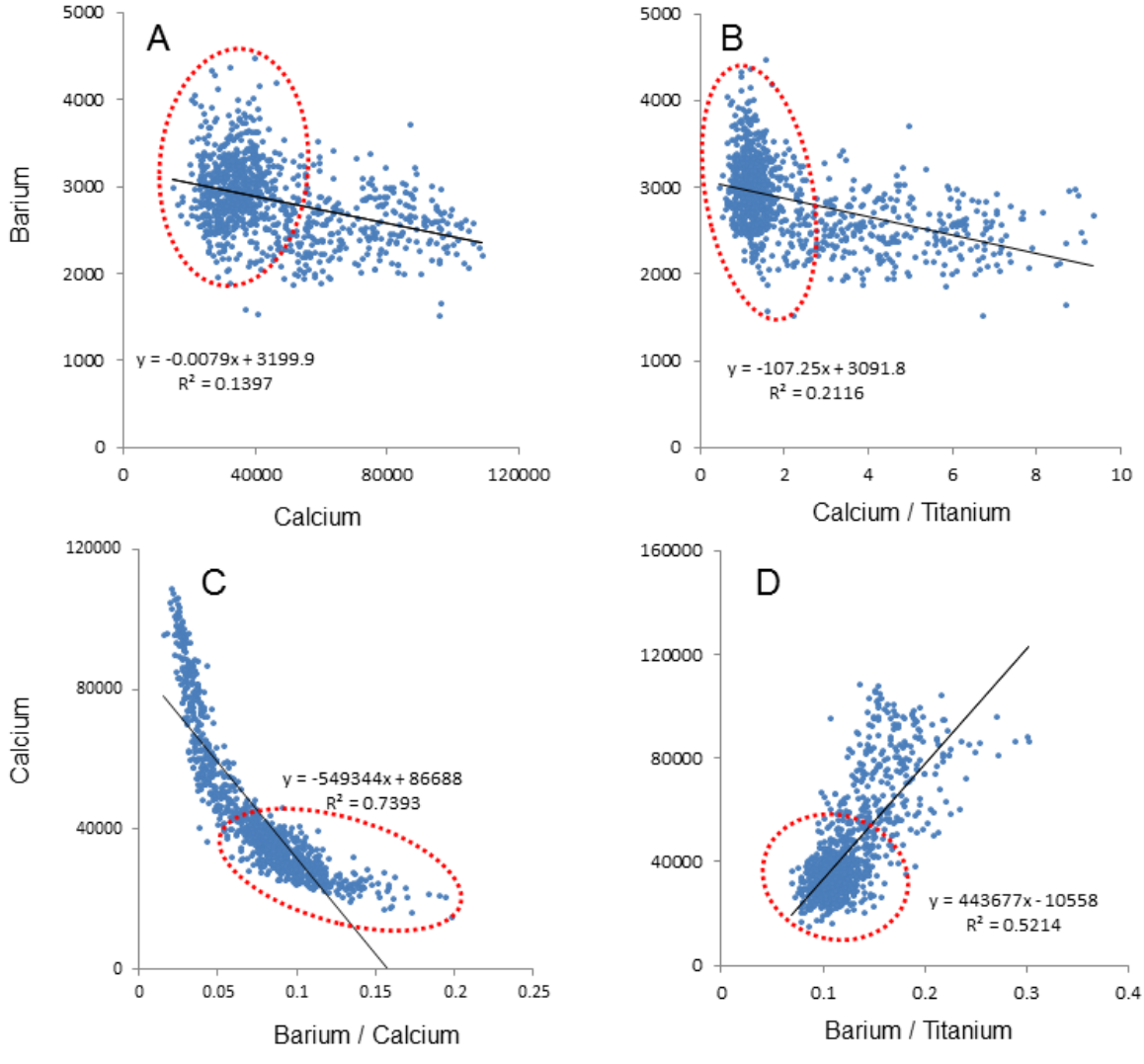

Figure 23. Cross-plots of XRF data from Hatteras cores used to evaluate correlation of barium to other proxies (e.g., Ca, Ca/Ti, Ba/Ca and Ba/Ti). Displayed are several plots with equations (least-squares linear fits), which are also provided to quantify the strength of the correlation. Note the "red and dashed" ellipses identify data points associated with the clay-rich portion of the cores. Also note the high-density cluster of data in plot B demonstrating an increase in Ba with no increase in Ca/Ti ($CaCO_3$ proxy), hence higher Ba counts are typical of a lower Ca/Ti ratio, conversely where the Ca/Ti ratio increases, there is no increase (in fact a slight decrease in Ba), hence Ba is clearly not related to the accumulation of Ca in MC118 sediments. See Figure caption 11 in Chapter 2 for further explanation of element ratios.

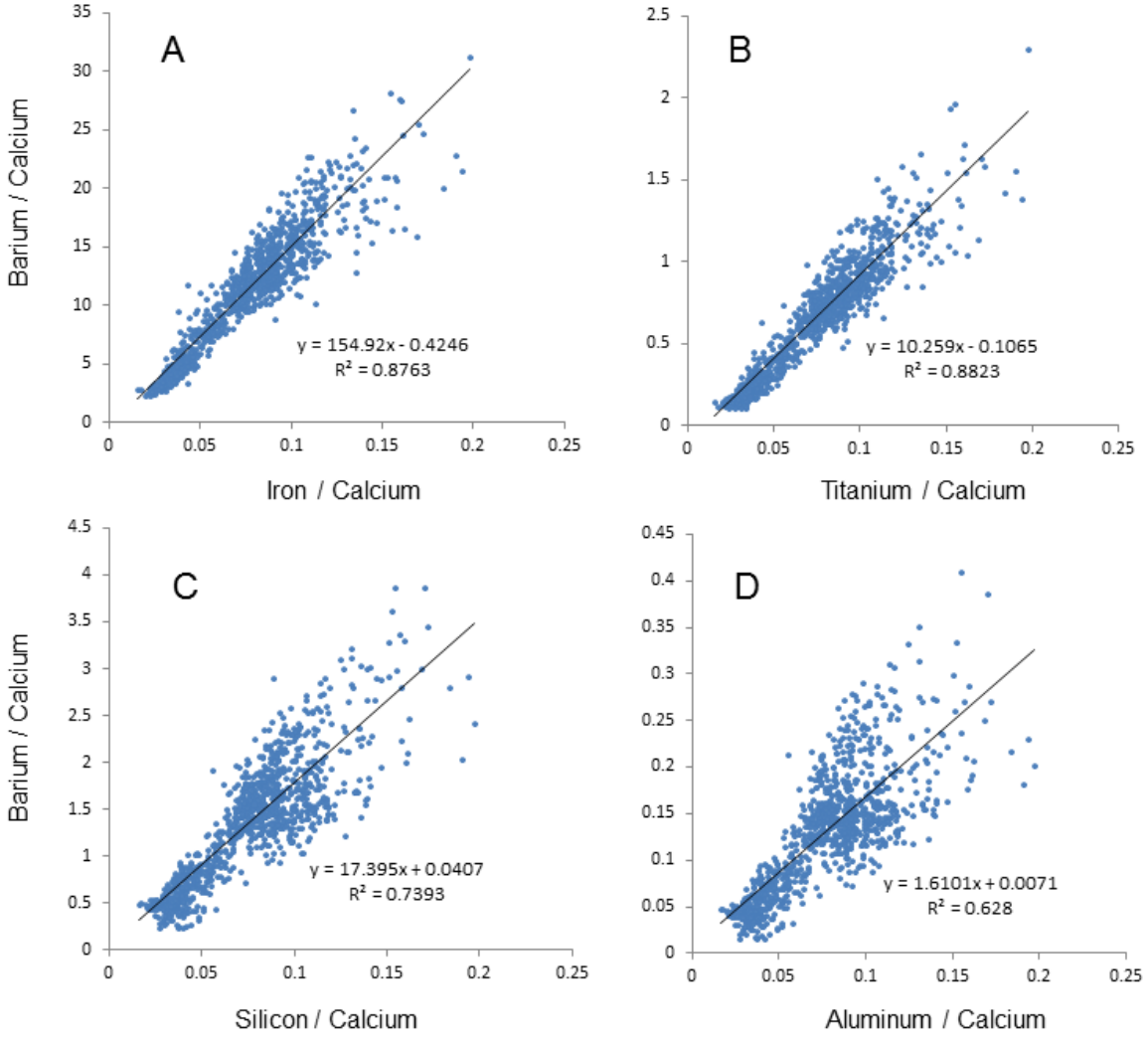

Figure 24. Cross-plots of X-ray fluorescence data from Hatteras cores used to evaluate correlation of barium to lithogenic inputs (e.g., Fe/Ca, Ti/Ca, Si/Ca and Al/Ca). Displayed are several plots with equations (least-squares linear fits) provided to quantify the strength of the correlation of Ba to various indicators. See Figure 11 in Chapter 2 for further explanation of element ratios. Note that the elements shown above are lithogenic inputs, silicon may also be biogenic (e.g., Appendix A). Also note ratio with Ca to remove effects of clay dilution, see Figure caption 11 in Chapter 2 for further explanation of element ratios.

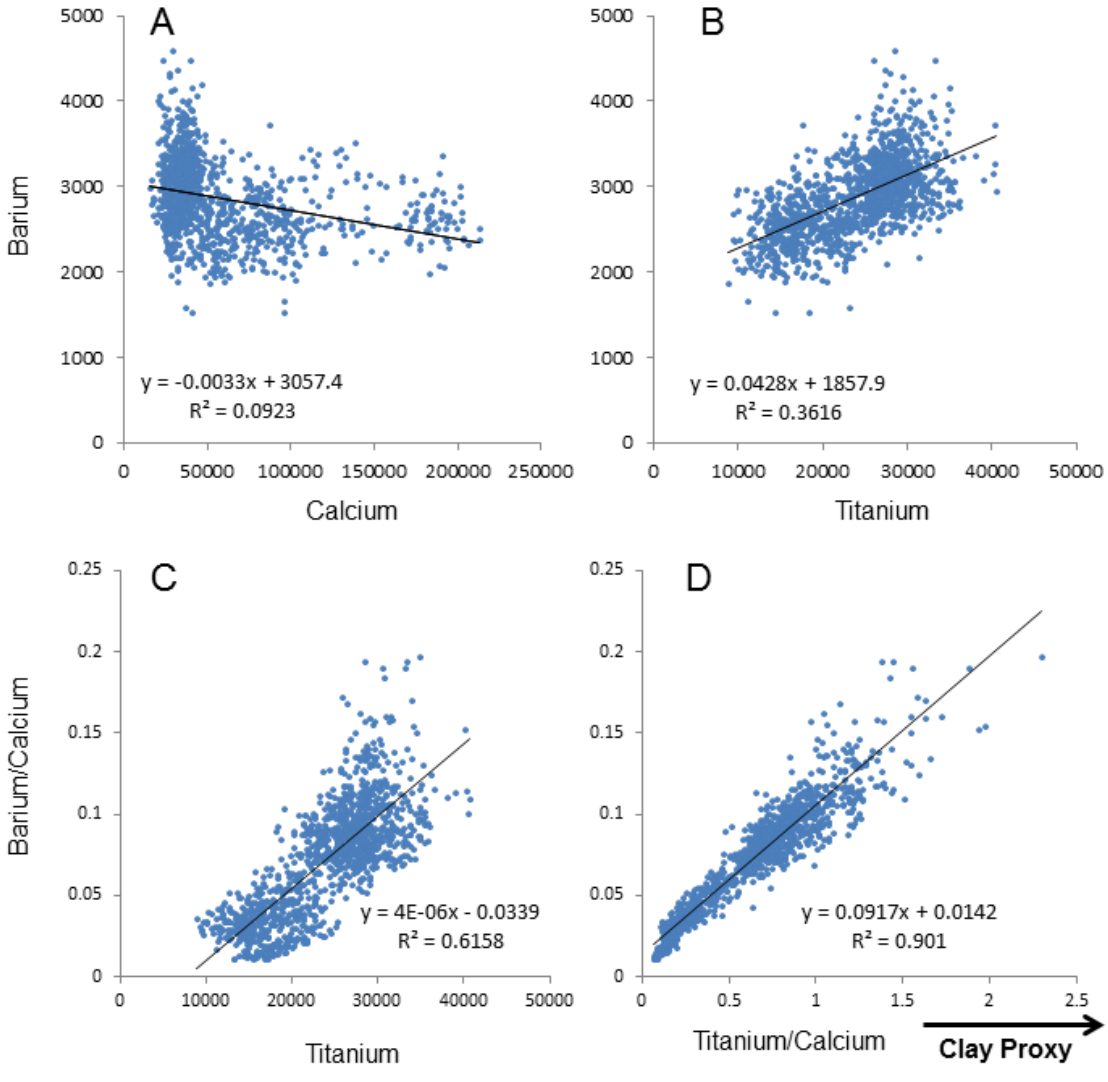

Figure 25. Cross-plots of X-ray fluorescence data from Hatteras transect of cores used to evaluate correlation of barium to biogenic (calcium) and lithogenic (titanium) inputs. Displayed are several plots with equations (least-squares linear fits), which are provided to quantify the strength of the correlation. The relationship of Ba to Ca yields a very poor correlation (0.0923: plot A), while Ba to Ti yields an improved correlation (0.3616: plot B). The ratio of Ba/Ca to Ti further improves the correlation (0.6158: plot C) by correcting for reduction in Ba from clay dilution. The ratio Ba/Ca to Ti/Ca yields a very strong correlation (0.901: plot D). The Ca/Ti ratio (followed closely by the ratio Ca/Fe) was determined to be the best indicator for $CaCO_3$-rich sediments based on calibration of XRF to CO_2 Coulometry (e.g. Figure 6); hence its inverse Ti/Ca is a proxy for clay.

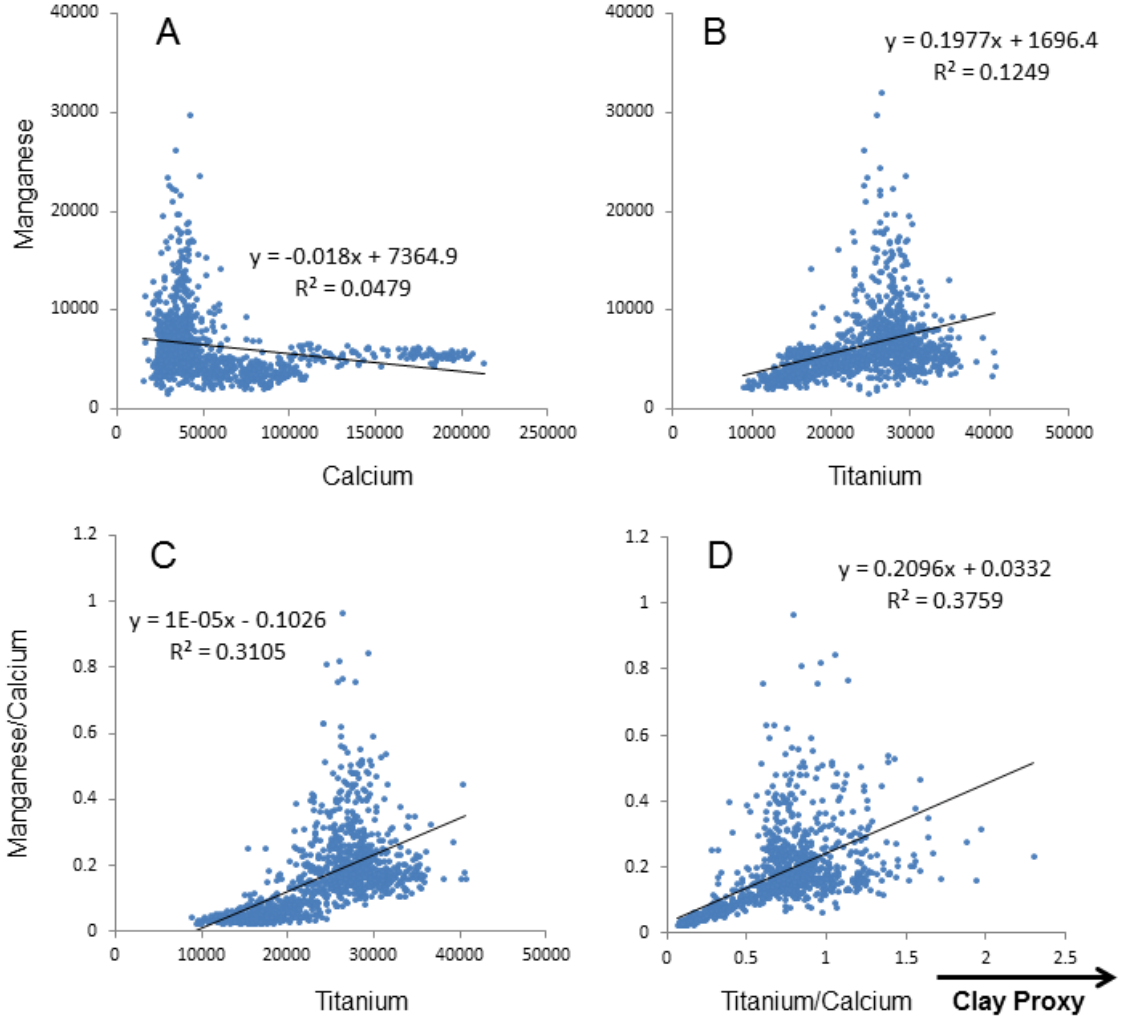

Figure 26. Cross-plots of X-ray fluorescence data from the Hatteras transect of cores used to evaluate correlation of manganese to biogenic (calcium) and lithogenic (titanium) inputs. Displayed are several plots with equations (least-squares linear fits), which are also provided to quantify the strength of the correlation. The relationship of Mn to Ca yields no correlation (0.0479: plot A). Mn to Ti yields an improved correlation (0.1249: plot B). The ratio of Mn/Ca to Ti further improves the correlation (0.3105: plot C) by correcting for reduction in Mn from clay dilution. The ratio Mn/Ca to Mn/Ca yields an even more improved correlation (0.3759: plot D). The Ca/Ti ratio (followed closely by the ratio Ca/Fe) was determined to be the best indicator for $CaCO_3$-rich sediments based on calibration of XRF to CO_2 Coulometry, thus its inverse Ti/Ca is a proxy for clay. While Pearson coefficient values are not high, they are likely significant given the substantial number of data point. Low r^2 values are partially a consequence of the Mn-layers, which have no relation to $CaCO_3$-content. A filter was used to eliminate some of the most concentrated Mn-layers by removing data points more than 20 percent above than a 5-point moving average.

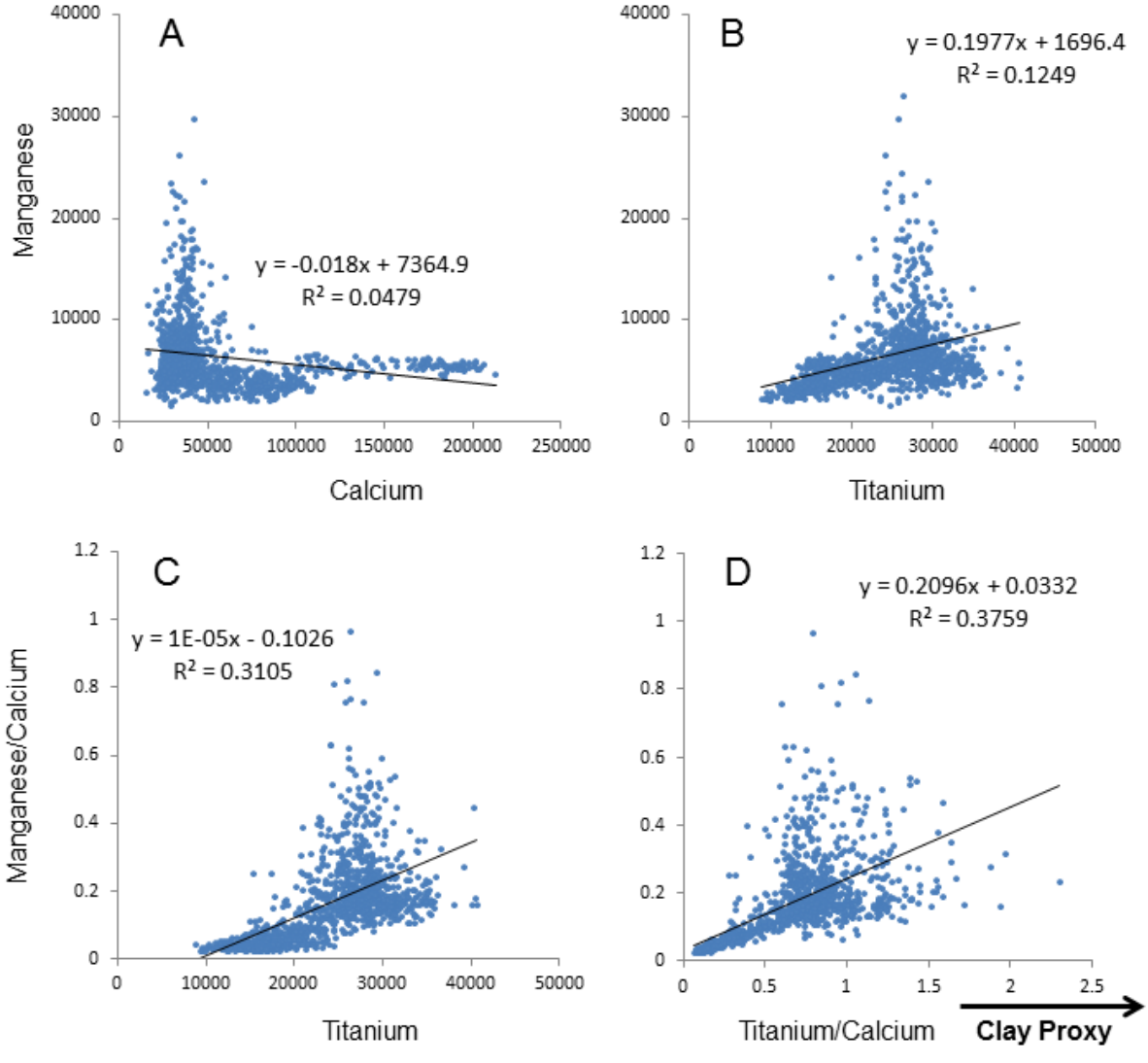

Figure 27. Cross-plots of X-ray fluorescence data from the Hatteras transect of cores used to evaluate correlation of manganese to biogenic (calcium) and lithogenic (titanium) inputs. Displayed are several plots with equations (least-squares linear fits), which are also provided to quantify the strength of the correlation. The relationship of Mn to Ca yields no correlation (0.0479: plot A). Mn to Ti yields a slightly improved correlation (0.1249: plot B). The ratio of Mn/Ca to Ti further improves the correlation (0.3105: plot C) by correcting for reduction in Mn from clay dilution. The ratio Mn/Ca to Mn/Ca yields an even more improved correlation (0.3759: plot D). The Ca/Ti ratio (followed closely by the ratio Ca/Fe) was determined to be the best indicator for $CaCO_3$-rich sediments based on calibration of XRF to CO_2 Coulometry, thus its inverse Ti/Ca is a proxy for clay. Correlations are still not ideal, yet are significant given the substantial number of data point. The low r^2 values are partially a consequence of the Mn-layers, and do not seem to have any relation to $CaCO_3$-content. A filter was used to eliminate some the most concentrated Mn-layers by removing data points more than 20 percent above than a 5-point moving average.

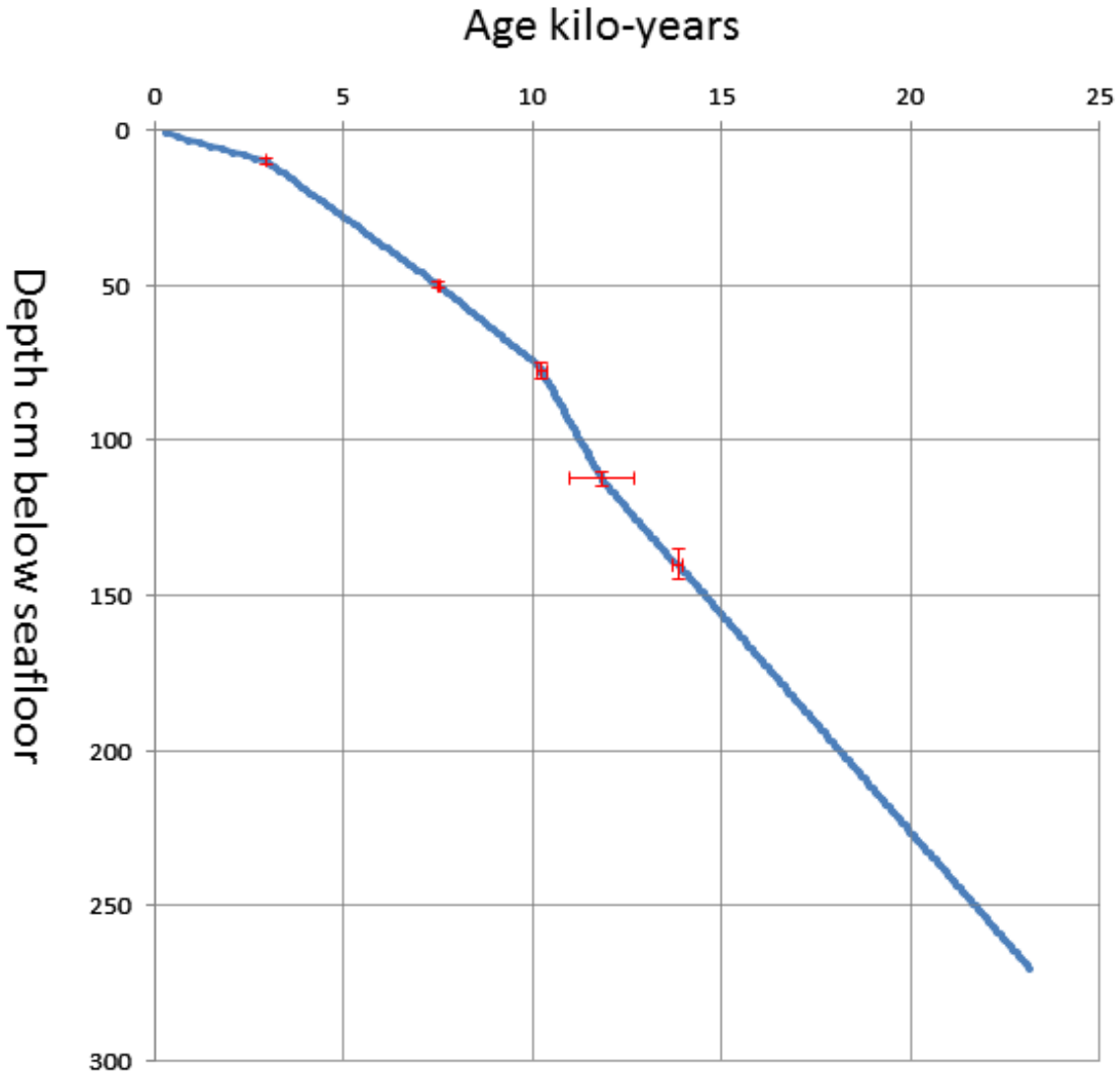

Figure 28. Age-depth plot for Core HAT-03 from transect 1, the plot is constructed using age-control points from numerous methods including foraminiferal and nannofossil biostratigraphy along with several AMS radiocarbon dates measured by NOSAMS. The red error bars represent the full ranges in age and depth possible for that particular point on the plot and vary depending on the method being used, e.g. from biostratigraphy 110 and 115 cm depth range from 11.0 to 12.7 kilo-years. Note that ages are in radiocarbon years and are not converted to calendar years with reservoir correction, see Table 2 in Chapter 1 for conversion of AMS dates to calendar years using a Gulf of Mexico reservoir correction. Also note that the sedimentation rate between the age-control points is assumed to be constant and the age-depth trend line is calculated as such.

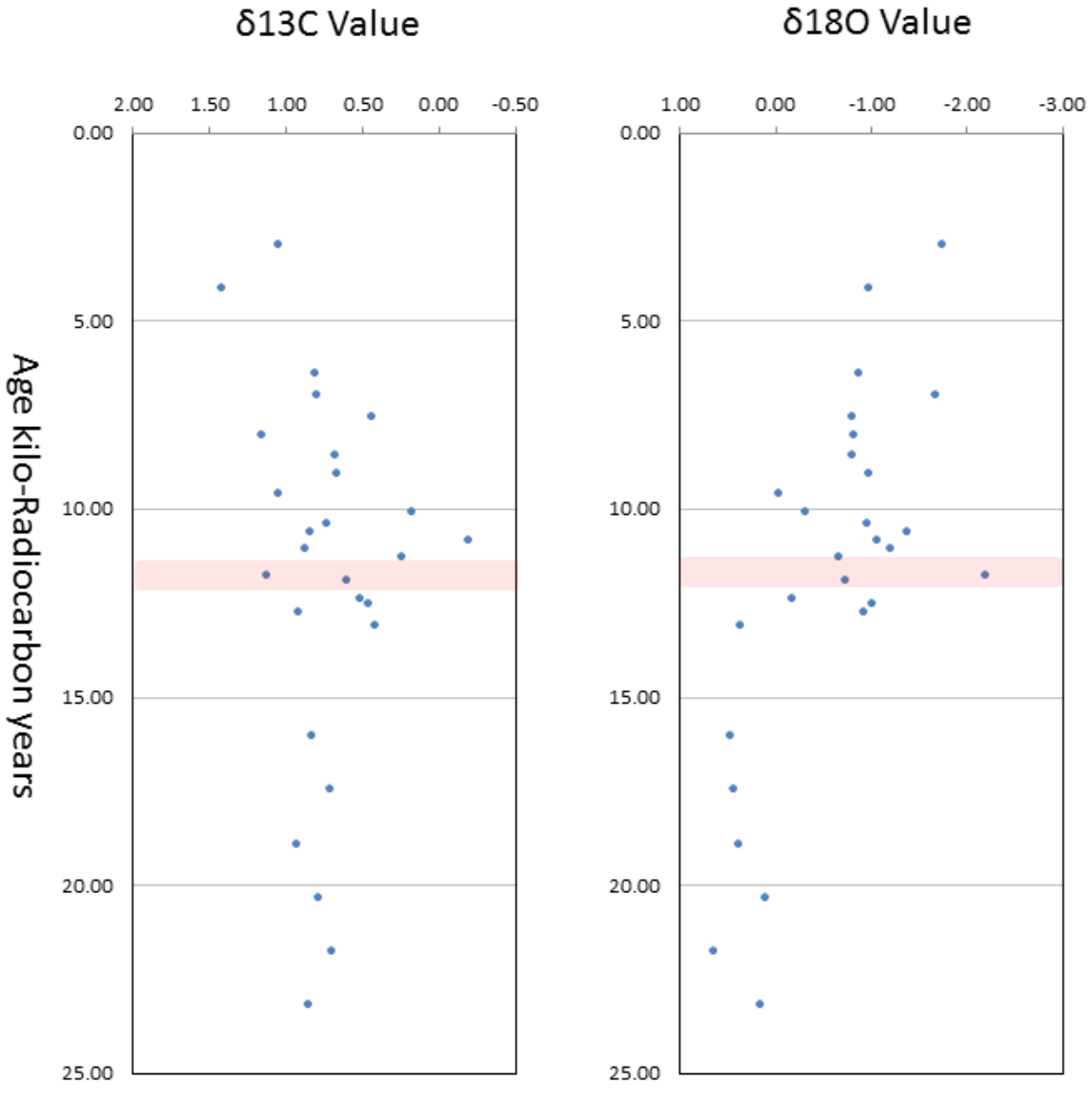

Figure 29. Stable carbon and oxygen isotope results from Core HAT-03, a total of 28 samples span from 10 cm to 270 cm. Depth is converted to radiocarbon years by using an age-depth model (see previous figure) from HAT-03 (e.g., Figure 18 in Appendix C). Sediments samples were prepared from ~5 mg of planktonic foraminiferal tests, mostly the white variety of Globigerinoides ruber that were handpicked from sieved sediment samples and then sonicated in deionized water. This method of preparation of planktic foraminifera follows standard practices and is described in more detailed in Chapter 1 Sections 2.4 and 2.6. Note that the "lightest" $\delta^{18}O$ value falls within the interval described as the "red band" and is shaded in light red. The "red band" is dated between 11,000 and 12,700 radiocarbon years, approximately equivalent to 14,000 - 15,000 calendar years (e.g., Figure 6 in Chapter 1) and interpreted as melt-water pulses into the Gulf of Mexico (e.g., section 5.2 in Chapter 1; Marchitto and Wei, 1995).

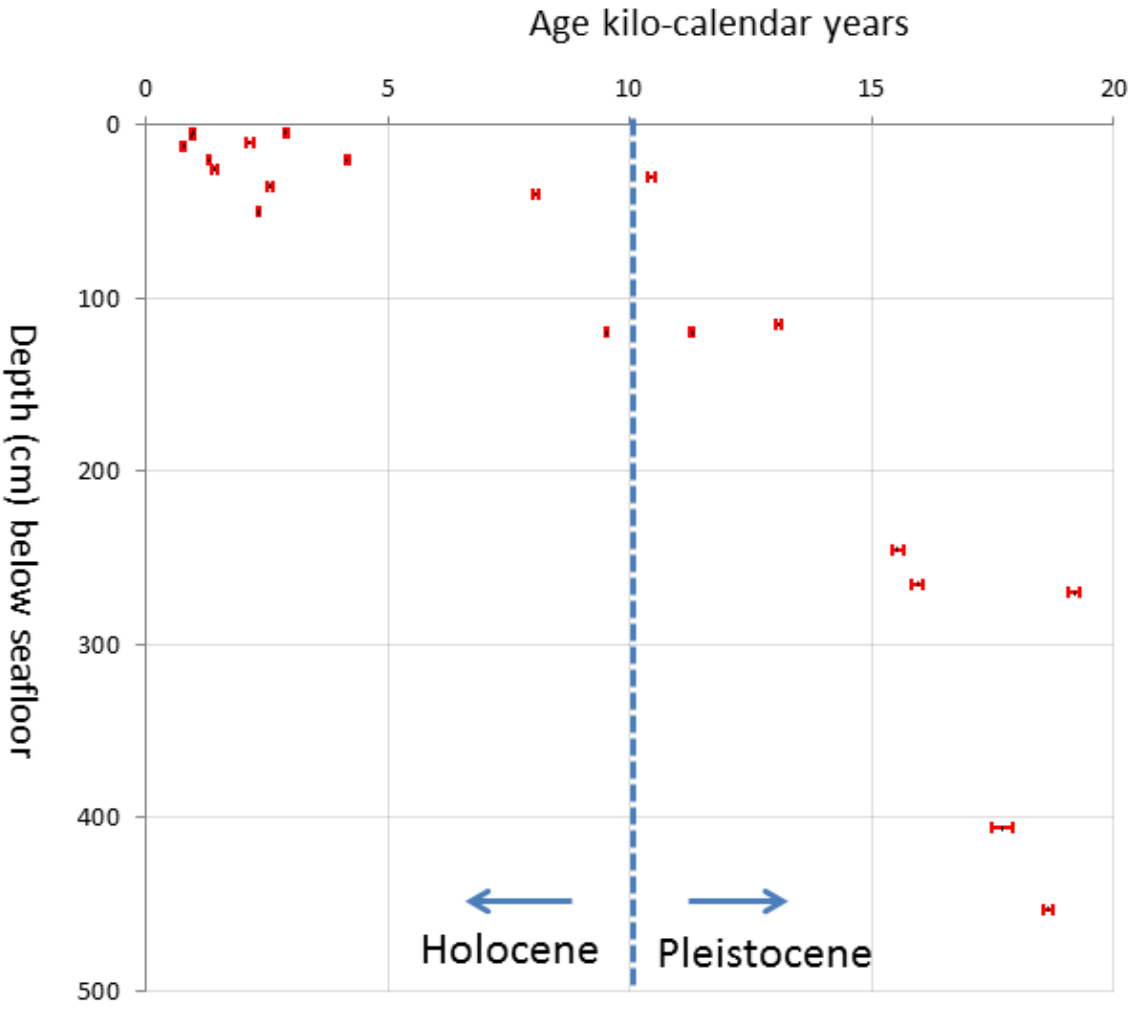

Figure 30. Age-depth plot using all AMS carbon-14 dates (Section 2.6 in Chapter 1), using all cores from transects 1 and 2 (Figure 2 in Chapter 1). AMS radiocarbon dates were measured by NOSAMS. The red error bars represent the potential age error reported for by NOSAMS, the depth error is minimal as sediment samples were selected directly from the core. This is in contrast to biostratigraphic markers where the depth resolution between samples was 5-cm apart, the plot only shows only AMS dates.

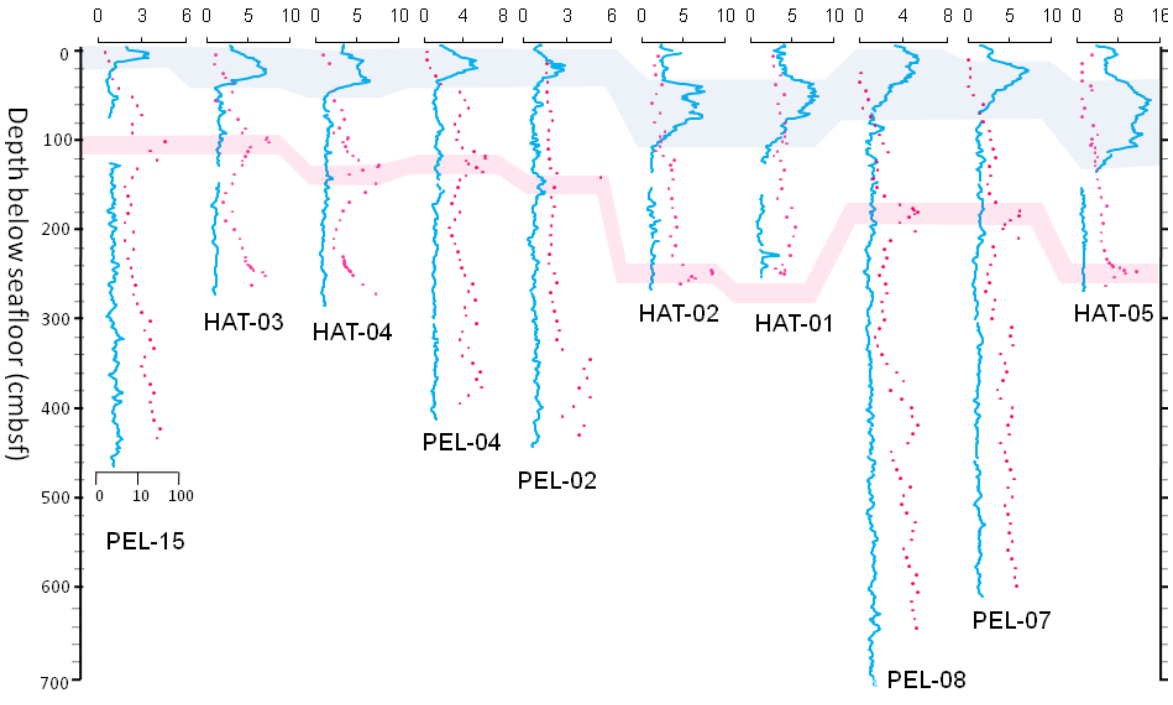

Figure 31. Correlation X-ray fluorescence (XRF) core scans Ca/Ti results (blue line), and the percentage of reworked nannofossils (red dots) across all cores collected from the study area. Cores are arranged by increasing distance (left to right) from the gas-hydrate and cold-seep field. The Ca/Ti data is plotted as a 3-cm moving average, and the reworked nannofossil data are plotted on a log scale (1 to 100%). Two correlative horizons are shown above by shading and are discussed in greater detail in Chapter 1, e.g. $CaCO_3$-rich Holocene (2300–9500 yrs.) in blue and a 5-cm-thick reworked nannofossil interval, late Pleistocene in age (14,000–15,000 yrs.) in red. Note the age of the correlative intervals is in kilo-calendar years.

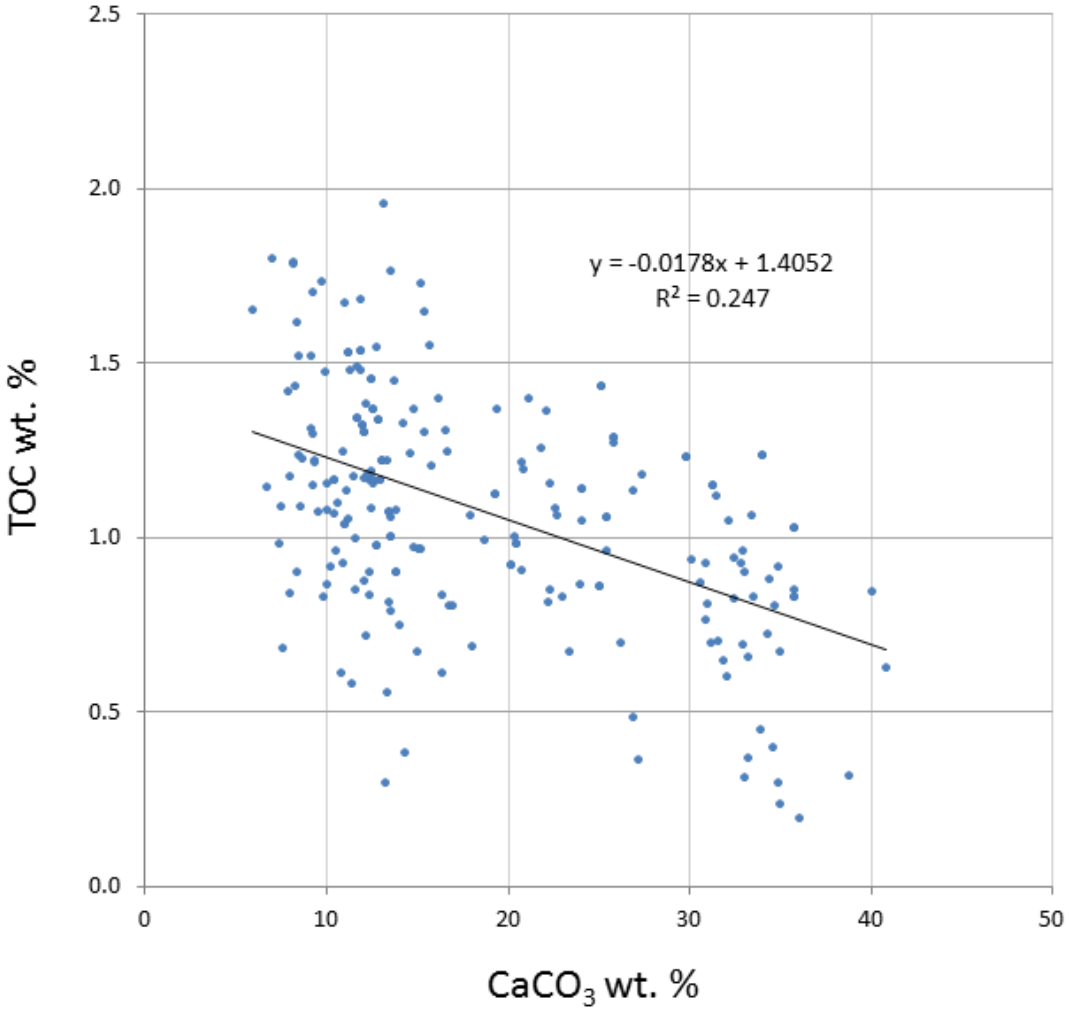

Figure 32. Cross-plot of weight present TOC to $CaCO_3$ determined from CO_2 coulometry, combustion and acid digestion procedures, respectively (e.g., Sections 2.5 in Chapter 2). This plot is based on 217 discrete geochemical data points; hence even with the low r^2 value the correlation is likely still significant. This display and least squares linear fit equation demonstrates that there is negative correlation between TOC and $CaCO_3$ content at MC118.

Aharon, P., 2006. Entrainment of meltwaters in hyperpycnal flows during deglaciation superfloods in the Gulf of Mexico. Earth and Planetary Science Letters 241 (1–2), 260–270.

Aller, R.C., 1990. Bioturbation and manganese cycling at the sediment-water interface. Philos. Trans. R. Soc. London, v. 331, p. 51-68.

Aller, R.C., 1994. The sedimentary cycle in Long Island Sound: Its role as intermediate oxidant and the influence of bioturbation, O_2, and C_{org} flux on diagenetic reaction balances. *Journal of Marine Resources*, v. 52, p. 259-295.

Appelbaum, B.S., Bouma, A.H., 1972. Geology of the upper continental slope in the Alaminos Canyon region. Gulf Cost Association of Geological Societies Transactions 22, 157–164.

Blum, M.D. and Roberts, H.H., 2009. Drowning of the Mississippi Delta due to insufficient sediment supply and global sea-level rise. *Nature Geoscience*, v. 2, p. 488-491.

Bralower, T.J. and Thierstein, H.R., 1987. Organic carbon and metal accumulation rates in Holocene and mid-Cretaceous sediments: paleoceanographic significance. *in* Marine Petroleum Source Rocks (eds. J. Brooks and A.J Fleet), *Geological Society of London Special Publication*, v. 26. p. 345-369.

Broecker, W.S., Andreé, M., Wolfli, W., Oeschger, H., Bonani, G., Kennett, J.P., Peteet, D., 1988. The chronology of the last deglaciation: implications to the causes of the Younger Dryas event. Paleoceanography 3, 1–19.

Broecker, W.S., Kennett, J.P., Flower, B.P., Teller, J.T., Trumbore, S., Bonani, G., Wolfli, W., 1989. Routing of meltwater from the Laurentide ice sheet during the Younger Dryas cold episode. Nature 341, 318–321.

Brunner, C.A., 2007a. Stratigraphy and paleoenvironment of shallow sediments from MC118. Proceedings of the Annual Meeting of the Gulf of Mexico Hydrates Research Consortium, October 10–11, 2007, Oxford, Ms. [one CD].

Brunner, C.A., 2007b. Qualitative planktonic foraminiferal biostratigraphy of core MD02-2570, of late Quaternary age, from the northern Gulf of Mexico. In: Winters, W.J., Lorenson, T.D., Paull, C.K. (Eds.), Initial report of the gas hydrate and paleoclimate cruise on the R/V Marion Dufresne in the Gulf of Mexico, 2–18 July 2002: USGS Open-File Report 2004-1358, one DVD. online at http://www.pubs.usgs.gov/of/2004/1358/.

Bruland, K.W., 1983 1983. Trace elements in sea-water. In: Riley J.P. and Chester, R. (eds.), Chemical Oceanography. Academic Press, London, pp. 157-220.

Burdige, D.J., 1993. The biogeochemistry of manganese and iron reduction in marine sediments. *Earth-Science Reviews*, v. 35, pp. 249-284.

Burdige, D.J., and Gieskes, J.M., 1983. A pore water/solid phase diagenetic model for manganese in marine sediment, *American Journal of Science*, v. 283, p. 29-47.

Calvert, S.E. and Pedersen, T.F, 1993. Geochemistry of recent oxic and anoxic marine sediments: Implications for the geological record, *Marine Geology*, v. 113 (1-2), p. 67-88.

Canfield, D.E., Thamdrup, B. and Hansen, J.W., 1993. The anaerobic degradation of organic matter in Danish coastal sediments: Fe reduction, Mn reduction, and sulfate reduction. *Geochim. Cosmochim. Acta*, 57: 3867-3883.

Castellini, D.G., Dickens, G.D., Snyder, G.T., Ruppel, C.D., 2006. Barium cycling in shallow sediments above active mud volcanoes in the Gulf of Mexico. *Chemical Geology,* v. 226, p. 1–30.

Chappellaz, J., Barnola, J.M.m Raynaud, D., Korotkevich, Y.S. and C. Lorius 1990. Ice-core record of atmospheric methane over the past 160,000 years. *Nature*, v. 345, p. 127-131.

Chun, C.O.J., Delaney, M.L., Zachos, J.C., 2010. Paleoredox changes across the Paleocene-Eocene thermal maximum, Walvis Ridge (ODP Sites 1262, 1263, and 1266): Evidence from Mn and U enrichment factors. *Paleoceanography*, v. 25, p. 1-13.

Claypool, G.E., and Reed, P.R., 1976. Thermal analysis technique for source rock evaluation: quantitative estimate of organic richness and effects of lithologic variation, *AAPG Bulletin*, v.60, pp. 608-626.

Collett, T.S. 1992. Potential of gas hydrates outlined. *Oil and Gas Journal*, v. 9025, p. 84-87.

Collett, T.S. 1993. Natural Gas Hydrates of the Prudhoe Bay and Kuparuk River Area, North Slope, Alaska. *The AAPG Bulletin*, v. 77, no. 5, p. 795-812.

Collett, T.S. 1995. Gas hydrate resources of the United States, in Gautier, D.L., Dolton, G.L., Takahashi, K.I., and Varnes, K.L., (eds.) 1995 National assessment of United States oil and gas resources-results, methodology, and supporting data: U.S. Geological Survey Digital Data Series 30 (on CD-ROM).

Collett, T.S., 2002. Energy resource potential of natural gas hydrates. American Association of Petroleum Geologists, v. 86, no. 11, p. 1971-1992.

Constans, R.E., Parker, M.E., 1986. Calcareous nannofossil biostratigraphy and paleoclimate indices for the Late Quaternary, Deep Sea Drilling Project Leg 96, Gulf of Mexico. In: Bouma, A.H., Coleman, J.M., Meyer, A.W., et al. (Eds.), Initial Reports of the Deep Sea Drilling Project 96. U.S. Government Printing Office, Washington, D.C., pp. 601–630.

Corbett, R.D., McKee, B., Duncan, D., 2004. An evaluation of mobile mud dynamics in the Mississippi River deltaic region. *Marine Geology*, v. 209, p. 91-112.

Cowen, J.P. and Bruland, K.W., 1985. Metal deposits associated with bacteria: implications for Fe and Mn marine geochemistry. *Deep-Sea Research*, 32: 253-272.

Dadey, K.A., Janecek, T., Klaus, A., 1992. Dry-Bulk Density: Its use and determination. Proceedings of the Ocean Drilling Program, *Scientific Results*, v. 126, p. 551-554.

Diaz, R. J. and Trefry, J.H., 2006. Comparison of sediment profile image data with profiles of oxygen and Eh from sediment cores. *Journal of Marine Systems* v. 62, p. 164-172.

DeMaster, D.J., 1981. The supply and accumulation of silica in the marine environment, *Geochimica et Cosmochimica Acta*, v. 45, pp. 1715-1732.

Dickens, G.R., and Owen, R.M., 1993. Global change and manganese deposition at the Cenomanian-Turonian boundary, Marine Georesources Geotechnology, v. 11(1), p. 27–43, doi:10.1080/10641199309379904.

Dickens, G.R., Quinby-Hunt, M.S., 1994. Methane hydrate stability in seawater. Geophysical Research Letters 21, 2115–2118.

Dickens, G.R., O'Neil, J.R., Rea, D.K. and Owen, R.M.(1995. Dissociation of oceanic methane hydrate as a cause of the carbon isotope excursion at the end of the Paleocene. *Paleoceanography*, v. 10, p. 965-971.

Dickens, G.R., Castillo, M.M., Walker, J.C.G., 1997. A blast of gas in the latest Paleocene: simulating first-order effects of massive dissociation of methane hydrate. Geology 25, 259–262.

Diegel, F.A., Karlo, J.F., Schuster, D.C., Shoup, R.C., Tauvers, P.R., 1995. Cenozoic structural evolution and tectono-stratigraphic framework of the northern Gulf Coast continental margin, in: Jackson, M.P.A., Roberts, D.G., Snelson, S., (Eds.), Salt Tectonics: A Global Perspective: American Association of Petroleum Geologist Memoir 65, pp. 109–151.

Dimitrov, L.I., 2002. Mud volcanoes—the most important pathway for degassing deeply buried sediments. Earth Science Reviews 59, 49–76.

Durand, B., 1980. Kerogen. Insoluble organic matter from the sedimentary rocks? Editions Technip., Paris, 519 pp.

Ehrlich, H.L., 1996. *Geomicrobiology*. Marcel Dekker, NY, pp. 719.

Espitalié, J., Deroo, G. and Marquis, F. 1985. La pyrolyse Rock-Eval et ses applications. Rev. Inst. Fr. Pét., v. 40, pp. 755-784.

Fairbanks, R.G., Mortlock, R.A., Chiu, T.-C., Cao, L., Kaplan, A., Guilderson, T.P., Fairbanks,T.W., Bloom, A.L., Grootes, P.M., Nadeau, M.-J., 2005. Radiocarbon calibration curve spanning 0 to 50, 000 years BP based on paired 230Th/234U/238U and 14C dates on pristine corals. Quaternary Science Reviews 24, 1781–1796.

Flower, B.P., Kennett, J.P., 1990. The Younger Dryas cool episode in the Gulf of Mexico. Paleoceanography 5 (6), 949–961.

Froelich, P.N., Klinkhammer, G.P., Bender, M.L., Luedtke, N., Heath, G.R., Cullen, D., Dauphin, P., Hammond, D., Hrtman, B., and Maynard, V., 1979. Early oxidation of organic matter in pelagic sediments of the eastern equatorial Atlantic: suboxic diagenesis. *Geochimica et Cosmochimica Acta*, v. 43, pp. 1075-1090.

Galloway, W.E., Ganey-Curry, P.E., Li, X., Buffler, R.T., 2000. Cenozoic depositional history of the Gulf of Mexico basin. *American Association of Petroleum Geologist Bulletin* v. 84, no. 11, p. 1743-1774.

Gingele, F.X. and Kasten, S., 1994. Solid-phase manganese in southeast Atlantic sediments: Implications for the paleoenvironment, Marine Geology, v. 121, no. 3-4, p. 317-332.

Glasby, G.P., 1988. Hydrothermal manganese deposits in island arcs and related to subduction processes: A possible model for genesis. *Ore Geology reviews*, 4:145-153.

Gordon, E.S., Goni, M.A., 2004. Controls on the distribution and accumulation of terrigenous organic matter in sediments from the Mississippi and Atchafalaya river margin. *Marine Chemistry*, v. 92, p. 331-352.

Haq, B.U., Hardenbol, J. and Vail P.R., 1987. Chronology of fluctuating sea levels since the Triassic (250 million years ago to present), *Science*, v. 235, p. 1156-1167.

Haq, B.U., 1998. Natural gas hydrates: searching for the long-term climatic and slope-stability records. *In*: Henriet, J.P and J. Mienert (eds.) *Gas Hydrates: Relevance to World Margin Stability and Climate Change*. Geological Society, London Special Publications, v. 137, p. 303-318.

Hartnett, H. E., Keil, R.G., Hedges, J.I., Devol, A.H., 1998. Influence of oxygen exposure time on organic carbon preservation in continental margin sediments, *Nature*, v. 391, p. 572– 574.

Heggie, D.T., Kahn, D., and Fischer, K., 1986. Trace metals in metalliferous sediments, MANOP site M: interfacial pore water profiles, *Earth Planetary Science Letters*, v. 80, p. 106-116.

Hem, J.D. 1981. Rates of manganese oxidation in aqueous systems. *Geochemica Cosmochimica Acta*, v. 66, pp. 3811-3826.

Hollander, D.J., McKenzie, J.A., Hsu, K.J., Huc, A.Y. 1993. Application of a eutrophic lake model to the origin of ancient organic-carbon-rich sediments. *Global Biogeochemical Cycles*, v. 7, p. 157-179.

Huffman, E.W.D., Jr., 1977. Performance of a new carbon dioxide coulometer. *Microchemistry Journal* v. 22, p. 567-573.

Hu, X., Cai, W.J., Wang, Y, Guo, X., and Lou, S., 2011. Geochemical environments of continental shelf-upper slope sediments in the northern Gulf of Mexico. *Paleogeography, Paleoclimatology, Paleoecology*, v. 312, p.265-277.

Hunt, J. M., 1972. Distribution of carbon in crust of Earth, *AAPG Bulletin*, v. 56, p. 2273-2277.

Ingram, W.C., Meyers, S.R., Brunner, C.B., Martens, C.S., 2010. Late Pleistocene-Holocene sedimentation surrounding an active seafloor gas-hydrate and cold-seep field on the Northern Gulf of Mexico Slope, *Marine Geology*, v. 278, p. 43-53.

Jackson, M.P.A., 1995. Retrospective Salt Tectonics, in: M.P.A. Jackson, D.G. Roberts, S. Snelson, (eds.), Salt Tectonics: a global perspective. *AAPG Memoir* v. 65, p. 1-28.

Jansen, E., Befring, S., Bugge, T. et al. 1987. Large submarine slides on the Norwegian continental margin: sediments, transport and timing. *Marine Geology*, v. 78, p. 77-107.

Kaiho, K., Arinobu, T., Ishiwatari, R., Morgans, H.E.G., Okada, H., Takeda, N., Tazaki, K., Zhou, G., Kajiwara, Y., Matsumoto, R., Hirai, A., Niitsuma, N. and H. wada (1996), Latest Paleocene benthic foraminiferal extinction and environmental changes at Tawanui, New Zealand: *Paleoceanography*, v. 11, p. 447-465.

Kalhorn, S., and Emerson, S., 1984. The oxidation state of manganese in surface sediments of the deep sea, *Geochemica, Cosmochimica, Acta*, v. 48, p. 897-902.

Katz, M.E., Pak, D.K., Diskens, G.R., Miller, K.G., 1999. The source and fate of massive carbon input during the latest Paleocene thermal maximum. Science 286, 1531–1533.

Kennett, J.P., Huddlestun, P., 1972. Late Pleistocene paleoclimatology, foraminiferal biostratigraphy and tephrochronology, Western Gulf of Mexico. Quaternary Research 2, 38–69.

Kennett, J.P., Elmstrom, K., Penrose, N.L., 1985. The last deglaciation in Orca Basin, Gulf of Mexico: high-resolution planktonic foraminifera changes. Paleogeography, Paleoclimatology, Paleoecology 50, 189–216.

Kennett, J.P., Cannariato, K.G., Hendy, I.L., Behl, R.J., 2000. Carbon isotopic evidence for methane hydrate instability during Quaternary interstadials. Science 288 (5463), 128–133.

Kennett, J.P., Cannariato, K.G., Hendy, I.L., Behl, R.J., 2003. Methane Hydrates in Quaternary Climate Change: The Clathrate Gun Hypothesis. American Geophysical Union, Washington, DC. 216 pp.

Kvenvolden, K.A. 1995. A review of the geochemistry of methane in natural gas hydrate. Organic Geochemistry, v. 23, no. 12, p. 997-1008.

Kvenvolden, K.A. 1998. A primer on the geological occurrence of gas hydrate. *In*: Henriet, J.P and J. Mienert (eds.) *Gas Hydrates: Relevance to World Margin Stability and Climate Change*. Geological Society, London Special Publications, v. 137, p. 9-30.

Lang, T. H. and Wise, S.W. 1987. Neogene and Paleocene-Maestrichtian calcareous nannofossil stratigraphy, Deep Sea Drilling Project Sites 604 and 605, upper continental rise off New Jersey: Sedimentation rates, hiatuses, and correlation with seismic stratigraphy. *Initial Reports of the Deep Sea Drilling Project*, v. 93, p. 661-683.

Lapham, L.L., Chanton, J.P., Martens, C.S., Sleeper, K., Woolsey, J.R., 2008. Microbial activity in surficial sediments overlying acoustic wipeout zones at a Gulf of Mexico cold seep. Geochemistry, Geophysics, Geosystems 9 (4), 1–17.

Lapham, L.L., Chanton, J.P., Chapman, R., Martens, C.S., (in press). Methane undersaturate fluids in deep-sea sediments: implications for gas hydrate stability and rates of dissolution. Manuscript for Earth and Planetary Science Letters

Lerche, I., Bagirov, E., 1998. Guide to gas hydrate stability in various geological settings. Marine and Petroleum Geology 15 (5), 427–437.

Lorius, C., Jousel, J., Raynaud, D., Hansen, J. and H. Le Treut 1990. The ice-core record: climate sensitivity and future greenhouse warming. *Nature*, v. 347, p. 139-145.

Lutken, C.B., Brunner, C.A., Lapham, L.L., Chanton, J.P., Rogers, R., Sassen, R., Dearman, J., Lynch, L., Kuykendall, J., Lowrie, A., 2006. Analyses of core samples from Mississippi Canyon 118, paper OTC 18208, Offshore Technology Conference, American Association of Petroleum Geologist, May 1–4, Houston, TX.

Lynn, D.C. and Bonatti, E. 1965. Mobility of manganese in diagenesis of deep-sea sediments. *Marine Geology*, v. 3, pp. 457-474.

Maslin, M., Mikkelsen, N., Vilela, C. and Haq, B. 1998. Sea-level and gas-hydrate-controlled catastrophic sediment failures of the Amazon Fan. *Geology*, v. 26 no. 12, p. 1107-1110.

Maslin, M., Owen, M., Day, S. and Long, D. 2004. Linking continental-slope failures and climate change: Testing the clathrate gun hypothesis. *Geology*, v. 32, p. 53-56.

Macelloni, L., Caruso, S., Lapham, L., Lutken, C., Brunner, C., Lowrie, A., 2010. Spatial distribution of seafloor bio-geological and geochemical processes as proxy to evaluate fluid-flux regime and time evolution of a complex carbonate/hydrates mound, northern Gulf of Mexico. *Gulf Coast Association of Geological Societies Transactions* v. 60, p. 461-480.

Macelloni, L., Simonetti, A., Knapp, J.H., Knap, C.C., Lutken, C.B. and Lapham, L.L., 2012. Multiple resolution seismic imaging of a shallow hydrocarbon plumbing system, Woolsey Mound, Northern Gulf of Mexico. *Marine and Petroleum Geology*, v. 38, p. 128-142.

Marchitto, T.M., Wei, K-Y., 1995. History of the Laurentide meltwater flow to the Gulf of Mexico during the last deglaciation, as revealed by reworked calcareous nannofossils. *Geology*, v. 23, p. 779-782.

Martin, S.T., 2005. Precipitation and Dissolution of Iron and Manganese Oxides. In: Environmental Catalysis (V.H. Grassian, Ed), CRC Press: Boca Raton, pp. 61-81.

McBride, B.C., 1998. The evolution of allochthonous salt along a megaregional profile across the northern Gulf of Mexico, *AAPG Bulletin*, v. 82, p. 1037-1054.

McGee, T., 2006. A seafloor observatory to monitor gas hydrates in the Gulf of Mexico. *The Leading Edge* v. 25, no. 5, p. 644–647.

McIver, R.D. 1982. Role of naturally occuring gas hydrates in sediment transport. *AAPG Bulletin*, v. 66, p. 789-792.

Milkov, A.V., 2003. Global estimates of hydrate-bound gas in marine sediments: how much is really out there? *Earth-Science Reviews*, v. 66, p. 183-197.

Minert, J., Vanneste, M., Bünz, S., Andreassen, K., Haflidason, H., and Sejrup, H.P 2005. Ocean warming and gas hydrate stability on the mid-Norwegian margin at the Storegga Slide. *Marine and Petroleum Geology*, v. 22, p. 233-244.

Mountain, G.S., Damuth, C.M.G., McHugh, Lorenzo, J.M. and Fulthrope, C.S. 1996. Origin, reburial, and significance of a middle Miocene canyon, New Jersey continental slope. *Proceedings of the Ocean Drilling Program, Scientific Results*, v. 150, no. 15, p. 283-292. Ocean Drilling Program, Texas A&M University, College Station TX, USA

Mountain, G.S. 1987. Cenozoic Margin Construction and Destruction Offshore New Jersey. *Cushman foundation for Foraminiferal Research, Special Publication*, v. 24, 57-83.

Müller, P.J and Seuss, E., 1979. Productivity, sedimentation rate, and sedimentary organic matter in the oceans – Organic carbon preservation. *Deep-Sea Research*, v. 26, p. 1347-1362.

Murray, J. W. and P. G. Brewer (1977). The mechanisms of removal of iron, manganese and other trace metals from seawater. In: Marine Manganese Deposits, G. P. Glasby, ed., Elsevier, Holland, pp. 291- 325.

Murray, R.W., Miller, D.J., and Kryc, K.A., 2000. Analysis of major and trace elements in rocks, sediments, and interstitial waters by inductively coupled plasma-atomic emission spectrometry (ICP-AES). *ODP Technical Note, 29,* [Online] Available from World Wide Web: http://www-opd.tamu.edu/publications/tnotes/tn29/INDEX.HTM [Cited 2002-07-23]

Norris, R.D. and Röhl, U. 1999. Carbon Cycling and chronology of climate warming during the Paleocene-Eocene transition, *Nature*, v. 401, p. 775-778.

Pattan, J.N., Masuzawa, T., Borole1, D.D., Parthiban, G., Jauhari, P., Yamamoto, M., 2005. Biological productivity, terrigenous influence and noncrustal elements supply to the Central Indian Ocean Basin: Paleoceanography during the past » 1 Ma. *Journal of Earth System Science,* v. 114, no. 1, February 2005, p. 63-74.

Paull, C.K., Brewer, P.G., Ussler III, W., Peltzer, E.T., Rehder, G., and Clague, D. 2003. An experiment demonstrating that marine slumping is a mechanism to transfer methane from gas-hydrate deposits into the upper ocean and atmosphere. *Geomarine letters*, v. 22, p. 198-203.

Paull, C.K., Buelow, W.J., Ussler III, W., Borowski, W.S. 1996. Increased continental-margin slumping frequency during sea-level lowstands above gas hydrate-bearing sediments. *Geology*, v. 24, no. 2, p. 143-146.

Pedersen, T.F. and Price, N.B., 1982. The geochemistry of manganese carbonate in Panama Basin sediments, *Geochimica Cosmochimica Acta*, v. 46, no. 1, p. 59-68.

Piper, D.Z., 1994. Seawater as the major source of minor elements in black shales, phosphorites and other sedimentary rocks. Chemical Geology, v. 114, pp. 95-114.

Piper, D.J.W., C. Pirmez, P. L. Manley, D. Long, R.D. Flood, W.R. Normark, and Showers W. 1997. Mass-Transport of the Amazon Fan: Proceedings of the Ocean Drilling Program, Scientific Results, v. 155, p. 109-146. Ocean Drilling Program, Texas A&M University, College Station TX 77845-9547, USA

Prather, B.E., Booth, J.R., Steffens, G.S., Craig, P.A., 1998. Classification, lithologic calibration, and stratigraphic succession of seismic facies of intra-slope basins, deep-water Gulf of Mexico: *American Association of Petroleum Geologists Bulletin*, v. 82, p. 701-728.

Raynaud, D., J. Chappellaz, J. M. Barnola, Y. S. Korotkevich, and C. Lorius 1988. Climatic and CH4 cycle implications of glacial-interglacial CH4 change in the Vostok core, *Nature*, v. 333, p. 655–657.

Reimers, C.E., Jahnke, R.A., and McCorkle, D.C., 1992. Carbon fluxes and burial rates over the continental slope and rise off central California with implications for the global carbon cycle, *Global Biogeochemical Cycles*, v. 6, p. 199-224.

Richter et al., 2006. The Avaatech Core Scanner: Technical description and applications to NE Atlantic sediments. *In*: Rothwell, R.G. (eds.), New ways of looking at sediment core and core data. *Geological Society Special Publication*, London, pp. 39-50.

Roberts, H.H., 1997. Dynamic changes of the Holocene Mississippi river delta plain: the delta cycle. Journal of Coastal Research 13, 605–627.

Rudnick, R. L. and Gao, S. 2003. Composition of the continental crust, in Treatise on Geochemistry, (eds.) Heinrich, D.H. and Karl, K.T., pp. 1–64, Pergamon, Oxford, U. K.

Sageman, B.B., Lyons, T.W., 2004. Geochemistry of Fine-grained Sediments and Sedimentary Rocks, in: MacKenzie, F., (Eds.) Sediments, Diagensis, and Sedimentary Rocks, Treatise on Geochemistry 7, pp. 115-158.

Sassen, R., Sweet, S.T., Milkov, A.V., DeFreitas, D.A., Kennicutt, M.C., 2001. Thermogenic vent gas and gas hydrate in the Gulf of Mexico slope: is gas hydrate decomposition significant? Geology 29 (2), 107–110.

Sassen, R., Roberts, H.H., Jung, W., Lutken, C.B., DeFreitas, D.A., Sweet, S.T., Guinasso Jr., N.L., 2006. The Mississippi Canyon 118 gas hydrate site: a complex natural system. Paper OTC 18132, Offshore Technology Conference, May 1–4, Houston, TX.

Schenau, S. J., Reichart, G.J. and De Lange, G.J., 2002. Oxygen minimum zone controlled Mn redistribution in Arabian Sea sediments during the late Quaternary, Paleoceanography, v. 17(4), p. 1058, doi:10.1029/2000PA000621.

Schulz, H. D., and Zabel, M. (eds.) 2000. Marine Geochemistry, Springer-Verlag, v. 1, 455 p. DM149. ISBN 3-540-66453-X.

Severinghaus, J.P., Sowers, T., Brook, E.J., Alley, R.B. and Bender, M.L. 1998. Timing of abrupt climate change at the end of the Younger Dryas interval from thermally fractionated gases in polar ice. *Nature*, v. 391, p. 141-146.

Shaw, T.J., Gieskes, J.M., Jahnke, R.A., 1990. Early diagenesis in differing depositional environments: the response of transitional metals in pore water, *Geochemica, Cosmochimica, Acta*, v. 54, p. 1233-1246.

Sleeper, K.A., Lowrie, A., Bosman, A., Macelloni, L., Swann, C.T., 2006. Bathymetric mapping and high resolution seismic profiling by AUV in MC 118 (Gulf of Mexico). paper OTC 18133 presented at Offshore Technology Conference, Houston, TX

Sleeper, K.A., Lutken, C., 2008. Activities Report for Cruise GOM1-08-MC118 aboard the R/V Pelican Sampling and Deployment Cruise Mississippi Canyon Federal Lease Block 118 Northern Gulf of Mexico April 22-28, 2008. The Center for Marine Resources and Environmental Technology and the Seabed Technology Research Center, University of Mississippi. http://www.olemiss.edu/depts/mmri/programs/ppt_list.html

Snowdon, L.R., Meyers, P.A., 1992. Source and maturity of organic matter in sediments and rocks from Sites 759, 760, 761 and 764 (Wombat Plateau) and Sites 762 and 763 (Exmouth Plateau). *Proceedings of the Ocean Drilling Program, Scientific Results*, (eds.,) von Rad, U., Haq, B.U., et al., v. 122 pp. 309-315.

Solheim, A., Bryn, P., Berg, K., Mienert, J., 2005. Ormen Lange — an integrated study for the safe development of a deep-water gas field within the Storegga Slide Complex, NE Atlantic continental margin. *Marine and Petroleum Geology* 22 (1–2), 221–318.

Sowers, T., 2006. Late Quaternary Atmospheric CH_4 Isotope Records Suggests Marine Clathrates Are Stable. *Science*, v. 311, p. 838-840.

Stumm W. and Morgan J.J., 1996. *Aquatic Chemistry*. Wiley, New York, 1022 pp.

Stuiver, M., Polach, H.A., 1977. Discussion: reporting of 14C data. Radiocarbon 19, 355–363. Stuiver, M., 1980. Workshop on 14C data reporting. *Radiocarbon* 22, 964–966.

Tissot, B.P. and Welte, D.H., 1984. Petroleum formations and occurrences: Springer and Verlag, Berlin, 2nd edition, 699 pp.

Törnqvist, T.E., Wortman, S.R., Mateo, Z-R.P., Milne, G.A. and Swenson, J.B., 2006. Did the last sea level low stand always lead to cross-shelf valley formation and source to sink sediment flux? *Journal of Geophysical Research*, v. 111, p. 1-13.

Winn Jr., R.D., Roberts, H.H., Kohl, B., Fillon, R.H., Bouma, A.H., Constans, R.E., 1995. Latest Quaternary deposition on the outer shelf, northern Gulf of Mexico: facies and sequence stratigraphy from the Main Pass Block 303 shallow core. *Geological Society of America Bulletin*, v. 107, p. 851-866.

Winkler, C.D., 1996. High Resolution Seismic Stratigraphy of a late Pleistocene submarine fan pounded by salt-withdrawal mini-basins of the Gulf of Mexico continental slope: Offshore technology Conference Proceedings, OTC 8024, pp. 619-628.

Woolsey, J.R., 1984. Exploration for industrial minerals in Mississippi Sound and adjacent offshore territories of Mississippi and Alabama. Mississippi–Alabama Sea Grant Consortium, Project No. R/ER-11, Grant No. NA81AA-D-00050. 22 pp.

Zachos, J.C., Pagani, M., Sloan, L., Thomas, E. and Billups, K. 2001. Trends, Rhythms and Aberrations of in Global Climate 65 Ma to Present. *Science*, v. 292, p. 686-693.